Transmission electron microscopy investigation of growth and strain relaxation mechanisms in GaN (0001) films grown on silicon (111) substrates

DISSERTATION

zur Erlangung des akademischen Grades

doctor rerum naturalium
(Dr. rer. nat.)

im Fach Physik
Spezialisierung: Experimentalphysik

eingereicht an der
Mathematisch-Naturwissenschaftlichen Fakultät
der Humboldt-Universität zu Berlin

von

Dipl.-Phys. Toni Markurt

Präsident der Humboldt-Universität zu Berlin:
Prof. Dr. Jan-Hendrik Olbertz

Dekan der Mathematisch-Naturwissenschaftlichen Fakultät:
Prof. Dr. Elmar Kulke

Gutachter/innen:	1. Prof. Dr. Henning Riechert
	2. Prof. Sir Colin Humphreys
	3. Prof. Dr. Armin Dadgar

Tag der mündlichen Prüfung: 24.08.2015

Kurzzusammenfassung

In dieser Arbeit untersuchen wir die grundlegenden Wachstums- und Relaxationsprozesse, die es erlauben den Verzerrungszustand von GaN (0001) beim Wachstum auf Silizium (111) Substraten einzustellen und die resultierende Dichte an Durchstoßversetzungen (Threading-Versetzungen) zu reduzieren. Zu deren Analyse werden GaN (0001) Schichten, die mittels metallorganischer Gasphasenepitaxy auf Silizium (111), Saphir (0001) und GaN (0001) Substraten abgeschieden worden sind, hauptsächlich mit transmissionselekronenmikroskopischen Methoden untersucht. Unsere Untersuchungen haben im Wesentlichen folgende Ergebnisse hervorgebracht:

(i) Die Einstellung des Verzerrungszustandes von GaN (0001) Filmen mittels $\mathrm{Al_xGa_{1\text{-}x}N}$ Zwischenschichten beruht auf einer Asymmetrie der plastischen Relaxation an den beiden Grenzflächen der $\mathrm{Al_xGa_{1\text{-}x}N}$ Zwischenschicht. Fehlpassungsversetzungsnetzwerke bilden sich zwar an beiden Grenzflächen aus, jedoch ist der mittlere Abstand zwischen Versetzungslinien an der unteren Grenzfläche kleiner, als an der oberen. Dieser Unterschied führt letztendlich zum Aufbau einer kompressiven Verzerrung der aufwachsenden GaN Schicht.

(ii) Plastische Relaxation von verzerrten (0001) Wurtzit Schichten erfolgt im Wesentlichen durch Bildung von a-Typ Fehlpassungsversetzungen im $\frac{1}{3} < 11\bar{2}0 > |\{0001\}$ Gleitsystem. A-Typ Fehlpassungsversetzungen bilden sich aber nur dann, wenn die verzerrten Schichten eine 3-dimensionale Morphologie aufweisen, z.B. durch Inselwachstum oder Rissbildung. Eine quantitative Modellierung dieses Prozesses auf Basis von Rechnungen mit der Methode der finiten Elemente zeigt, dass die kritische Schichtdicke für die Bildung von a-Typ Fehlpassungsversetzungen wesentlich von der Oberflächenmorphologie, sprich vom Wachstumsmodus, bestimmt wird. Für eine gegebene Gitterfehlpassung zwischen Schicht und Substrat erfolgt die Nukleation von a-Typ Versetzungen in Inselecken im Fall von 3-dimensionalem Wachstum bei geringeren Schichtdicken als an der Front von Rissen von ansonsten 2-dimensional gewachsenen Schichten.

(iii) Eine Silizium Delta-Dotierung der GaN (0001) Oberfläche führt zum Wachstum einer kohärenten Sub-Monolage $\mathrm{SiGaN_3}$, die bezüglich des GaN Gitters einer $\sqrt{3} \times \sqrt{3}R30^\circ$ Rekonstruktion entspricht und aus einem Silizium- und Galliumatom, sowie aus einer Galliumvakanz besteht. Da das Wachstum von GaN direkt auf der $\mathrm{SiGaN_3}$-Monolage (in der Literatur häufig als $\mathrm{SiN_x}$-Maske bezeichnet) unterdrückt ist, tritt ein Übergang zu 3-dimensionalem Inselwachstum auf, das zunächst ausschließlich in Löchern der $\mathrm{SiGaN_3}$-Monolage anfängt. Eine hohe Konzentration von Silizium auf der GaN (0001) Oberfläche wirkt also als Anti-Surfactant beim epitaktischen Wachstum von GaN. Rechnungen mittels der Dichtefunktionaltheorie liefern eine Erklärung sowohl für das selbstlimitierte Wachstum der $\mathrm{SiGaN_3}$-Monolage, als auch für das Blocken des Wachstums von GaN auf der $\mathrm{SiGaN_3}$-Monolage.

Abstract

In this work we study the basic growth and relaxation processes that are used for strain and dislocation engineering in the growth of GaN (0001) films on silicon (111) substrates. To analyse these processes, dedicated samples, grown by MOVPE onto silicon (111), sapphire (0001) and GaN (0001) substrates, were investigate by means of transmission electron microscopy. Our investigations have revealed the following main results:

(i) Strain engineering in GaN (0001) films by means of $Al_xGa_{1\text{-}x}N$ interlayer is based on an asymmetry in plastic relaxation between the two interfaces of the $Al_xGa_{1\text{-}x}N$ interlayer. Although misfit dislocation networks form at both interfaces of the interlayer, the average spacing of dislocation lines at the lower interface is smaller than that at the upper one. This difference finally leads to a build-up of compressive strain in the subsequent GaN layer.

(ii) Plastic relaxation of strained (0001) wurtzite films is caused mainly by formation of a-type misfit dislocations in the $\frac{1}{3} < 11\bar{2}0 > | \{0001\}$ slip-system. These a-type misfit dislocations form once the strained films undergo a transition to a 3-dimensional surface morphology, e.g. by island growth or cracking. Quantitative modelling of this process, based on finite element simulations, reveals that the critical thickness for nucleation of a-type misfit dislocations depends next to the lattice mismatch mainly on the surface morphology, i.e. the growth mode, of the film. For a given lattice mismatch, nucleation of a-type dislocations in the corners of islands for 3-dimensional growth occurs already at lower layer thickness than at the front of cracks in 2-dimensionally grown layers.

(iii) Silicon delta-doping of the GaN (0001) surface leads to the growth of a coherent sub-monolayer of $SiGaN_3$ that corresponds with respect to the GaN lattice to a $\sqrt{3} \times \sqrt{3}R30^\circ$ reconstruction and consists of a silicon and gallium atom and a gallium vacancy. Since growth of thick GaN layers directly on top of the $SiGaN_3$-monolayer (commonly called SiN_x-mask in the literature) is inhibited a transition towards 3-dimensional island growth occurs, whereby GaN islands exclusively nucleate at openings in the $SiGaN_3$-monolayer. A high concentration of silicon on the GaN (0001) surface thus acts as an anti-surfactant in the epitaxial growth of GaN. Our density functional theory calculations provide an explanation for both the self-limited growth of the $SiGaN_3$-monolayer, as well as for the blocking of GaN growth on top of the $SiGaN_3$-monolayer.

Contents

1. Introduction **1**

1.1. Outline of this thesis 3

2. Theoretical background and experimental methods **5**

2.1. Dislocations and slip-systems in the wurtzite lattice 5

2.2. Sample growth by metal-organic vapour phase epitaxy 8

2.2.1. Thermodynamic framework of vapour phase epitaxy 8

2.2.2. Basic principle of metal-organic vapour phase epitaxy 9

2.2.3. Experimental details and sample structure 10

2.3. Transmission electron microscopy 12

2.3.1. Basic principle of structural imaging by transmission electron microscopy 12

2.3.2. High resolution transmission electron microscopy 16

2.3.3. Diffraction contrast imaging 20

2.3.4. STEM-HAADF imaging 21

2.3.5. Experimental setup 24

2.4. X-ray diffraction 25

2.5. In-situ laser reflectometry 27

3. Strain-engineering with $Al_xGa_{1-x}N$ interlayer - build-up of compressive strain **29**

3.1. Aim of this chapter 29

3.2. Experimental results 29

3.2.1. Structural characterisation of $Al_xGa_{1-x}N$ interlayer by TEM . 29

3.2.2. Analysis of the misfit dislocation networks 35

3.2.3. Macroscopic strain measurements 45

3.3. Discussion 51

3.3.1. Phenomenological model for the build-up of compressive strain by $Al_xGa_{1-x}N$ interlayer 51

3.3.2. Modelling of TEM results 51

3.3.3. Comparison with macroscopic strain measurements 55

3.4. Summary of this chapter 59

4. Growth and relaxation mechanism of (0001)-oriented III-nitride heterostructures **61**

4.1. Aim of this chapter 61

4.2. Experimental results 62

4.2.1. Analysis of the dislocation structure in the GaN film 62

4.2.2. Initial stages of growth and relaxation at $Al_xGa_{1-x}N$/GaN and GaN/$Al_xGa_{1-x}N$ heterostructures 64
4.2.3. Summary of experimental results 73
4.3. Quantitative modelling of the strain relaxation process 73
4.3.1. Identification of the relevant relaxation mechanism 74
4.3.2. Finite Element Calculations 75
4.3.3. Nucleation of a-type dislocation half-loops 79
4.3.4. Glide of a-type dislocations 84
4.4. Discussion 88
4.4.1. Microscopic model for the growth and strain relaxation mechanism of (0001)-oriented III-nitride heterostructures 88
4.4.2. Influence of the growth mode on the plastic relaxation process 89
4.4.3. Asymmetry of plastic relaxation at the interfaces of (0001)-oriented $Al_xGa_{1-x}N$ interlayers 94
4.4.4. Influence of the growth conditions of $Al_xGa_{1-x}N$ interlayers on the strain engineering process 97
4.4.5. Alternative plastic relaxation mechanisms 97
4.5. Conclusions - Optimised growth schema for strain engineering with $Al_xGa_{1-x}N$ interlayers 99

5. Anti-surfactant effect of Si in GaN (0001) epitaxy 101
5.1. Aim of this chapter 101
5.2. Experimental results 102
5.2.1. Transition towards 3-dimensional growth 102
5.2.2. HR(S)TEM investigation of the SiN_x-interlayer 103
5.3. The atomic structure of the SiN_x-interlayer 105
5.4. Discussion 110
5.4.1. Growth of the $SiGaN_3$-interlayer 110
5.4.2. Anti-surfactant effect of Si in the growth of GaN 112

6. Summary and conclusions 115

7. Acknowledgements 119

A. Coherent elastic scattering 133

B. Details of the finite element calculation 135

C. Analysis of the $Al_xGa_{1-x}N$ interlayer composition 139
C.1. Strain analysis from high resolution (S)TEM lattice images 139
C.2. Quantitative analysis of STEM-HAADF image intensities 140

D. Nucleation of dislocations 143

E. Density functional theory calculations 147

Publications 151

Selbständigkeitserklärung **155**

List of Figures

2.1. Possible slip-systems in the wurtzite lattice 6
2.2. Simplified scheme of MOVPE growth process 10
2.3. Schematic representation of the structure of samples studied in this work 11
2.4. Schematic representation of the basic principle of image formation in a TEM 13
2.5. Transfer function of a 300 kV TEM 17
2.6. Effect of aberration correction on HRTEM imaging 19
2.7. Schematic representation of diffraction contrast imaging 21
2.8. Schematic representation of the image formation process in a STEM . 22
2.9. Schematic representation of X-ray diffraction methods used in this work 26
2.10. Schematic representation of the experimental setup for the X-ray diffraction experiments 26
2.11. Schematic representation of the wafer curvature measurement by insitu laser reflectometry 27

3.1. Cross-sectional weak beam dark field TEM micrographs of $Al_xGa_{1-x}N$ interlayers in GaN films grown on Si (111) substrates 30
3.2. Cross-sectional bright field TEM images of $Al_xGa_{1-x}N$ interlayer in GaN films grown on Si (111) substrates 31
3.3. Cross-sectional weak beam dark field TEM micrographs of $Al_xGa_{1-x}N$ interlayer in GaN films grown on sapphire and GaN (0001) substrates 34
3.4. Cross-sectional bright field TEM images of $Al_xGa_{1-x}N$ interlayer in GaN films grown on sapphire and GaN (0001) substrates 34
3.5. Plan view weak beam dark field TEM analysis of the interface between a 35 *nm* thick high temperature $Al_{0.75}Ga_{0.25}N$ interlayer and the GaN buffer underneath 36
3.6. Magnified view of the centre region of Fig. 3.5 38
3.7. Schematic illustration of the misfit dislocation networks observed at the interfaces of $Al_xGa_{1-x}N$ interlayer 38
3.8. Aberration corrected HRTEM images of perfect a-type misfit dislocations at the $Al_xGa_{1-x}N$ interlayer/GaN buffer interface 40
3.9. Aberration corrected HRTEM images of a dissociated a-type misfit dislocation at the $Al_xGa_{1-x}N$ interlayer/GaN buffer interface 41
3.10. Aberration corrected HRTEM images of a dissociated a+c-type misfit dislocation at the interfaces of $Al_xGa_{1-x}N$ interlayer 42
3.11. Plan view weak beam dark field TEM images of the misfit dislocation network at the interfaces of different $Al_xGa_{1-x}N$ interlayers 44
3.12. In-situ wafer curvature measurements for samples with different $Al_xGa_{1-x}N$ interlayers 45

3.13. Reciprocal space maps of the GaN $(11\bar{2}4)$ reflection 48
3.14. High resolution XRD $\theta/2\theta$-scans of the symmetric GaN reflection . . 49
3.15. High resolution XRD $\theta/2\theta$-scans of the GaN (0006) reflection from different positions of a sample, which was prepared as a wedge 50
3.16. Schematic illustration of the build-up of compressive strain due to an asymmetry in plastic relaxation between the interfaces of $Al_xGa_{1-x}N$ interlayers 52
3.17. Schematic representation for the calculation of the average spacing between misfit dislocation lines from the observed spacing in TEM images 54

4.1. Cross-sectional weak beam dark field TEM micrographs of GaN films with $Al_xGa_{1-x}N$ interlayers grown on Si (111) and GaN (0001) substrates, respectively 63
4.2. First growth stage of a high temperature $Al_{0.75}Ga_{0.25}N$ interlayer . . . 65
4.3. First growth stage of a low temperature $Al_{0.75}Ga_{0.25}N$ interlayer . . . 66
4.4. Second stage of the growth of a high temperature $Al_{0.75}Ga_{0.25}N$ interlayer 67
4.5. Second stage of the growth of a thin low temperature $Al_{0.75}Ga_{0.25}N$ interlayer 69
4.6. Second stage of the growth of a thick low temperature $Al_{0.75}Ga_{0.25}N$ interlayer 69
4.7. First growth stage of the GaN overlayer on top of a relaxed high temperature $Al_{0.75}Ga_{0.25}N$ interlayer 70
4.8. First growth stage of the GaN overlayer on top of a relaxed low temperature $Al_{0.75}Ga_{0.25}N$ interlayer 72
4.9. Results of finite element calculations for the in-plane strain and strain energy density 76
4.10. The effect of elastic relaxation as a function of the width-to-height aspect ratio for island and crack geometries 77
4.11. Results of finite element calculations for the shear stress on the basal planes 77
4.12. Distribution of the shear stress on the basal plane as function of the width-to-height aspect ratio 78
4.13. Schematic representation of different possible sites for nucleation of dislocation half-loops in the (0001) plane 80
4.14. Schematic representation of the different contributions to the total energy for the dislocation nucleation process 81
4.15. Energetical barrier for dislocation half-loop nucleation as function of the layer thickness and critical thickness for spantaneous nucleation of an a-type dislocation half-loop 82
4.16. Simulated lateral arrangement of misfit dislocations in the $Al_{0.75}Ga_{0.25}N/GaN$ heterointerface between 2 adjacent cracks 87
4.17. Effect of the growth mode of (0001)-oriented strained wurtzite films on the plastic relaxation process 89

4.18. Comparison of theoretically predicted critical thickness values and experimental results for strain relaxation of (0001)-oriented III-nitride heterostructures 92
4.19. Schematic illustration of possible growth modes of the GaN overlayer on top of an $Al_xGa_{1-x}N$ interlayer 96

5.1. Growth mode transition due to SiN_x-interlayer 103
5.2. Aberration corrected HRTEM and STEM-ADF images of the SiN_x-interlayer in the $\langle 11\bar{2}0 \rangle$ projection 104
5.3. Aberration corrected HRTEM, the phase of an exit wave reconstruction and STEM-ADF images of the SiN_x-interlayer in the $\langle 1\bar{1}00 \rangle$ projection 105
5.4. Ball-and-stick model of the SiN_x-interlayer 106
5.5. Ball-and-stick representation of the relaxed structure models of the SiN_x-interlayer 107
5.6. Comparison of experimental and simulated images of the 5 assumed structure models for the SiN_x-interlayer 109
5.7. Relative surface energies for a variety of considered GaN (0001) surface reconstructions 111
5.8. Relative surface energies versus number of GaN overlayers on top of the $SiGaN_3$ monolayer 113

A.1. Schematic representation of diffraction of a plane wave at a crystal . . 134

B.1. Models used for finite element calculations 135

C.1. Quantitative composition analysis of an $Al_xGa_{1-x}N$ interlayer by means of strain mapping by geometric phase analysis 140
C.2. Quantitative composition analysis of an $Al_xGa_{1-x}N$ interlayer by means of the STEM-HAADF image intensity 141

D.1. Schematic representation of the total energy for nucleating a dislocation half-loop as a function of the half-loop radius and resolved shear stress 144

List of Tables

2.1. Properties of various slip-systems in the wurtzite lattice 7

3.1. Average spacing of misfit dislocations at the interfaces of $Al_xGa_{1-x}N$ interlayer as determined from cross-sectional TEM images 35
3.2. Summary of results from in-situ wafer curvature measurements 46
3.3. Summary of results from the ex-situ X-ray diffraction measurements . 50
3.4. Comparison of results of the quantitative analysis of the strain relaxation in $Al_xGa_{1-x}N$ interlayers (δ_{AlGaN}) and the build-up of compressive strain in GaN overlayers ($\Delta\varepsilon$) 58

5.1. Possible structures for the SiN_x-interlayer 107

B.1. Overview about the considered parameter range of the finite element analysis 137

E.1. Considered GaN (0001) surface reconstructions 149

1. Introduction

GaN-based devices for solid state lighting (e.g. light emitting diodes, LEDs) and power electronics (e.g. high electron mobility transistors, HEMTs) have become commercially available in the past years and with further price reduction an increase of their market share is expected for the future. Since bulk GaN substrates with low dislocation densities are still expensive and only available in small size and small quantities [1], the majority of GaN based device structures are grown heteroepitaxially on either sapphire (0001), silicon carbide (0001) or silicon (111) substrates. Growth of GaN on silicon substrates (GaN-on-Si) has attracted great interest in the past years [2, 5, 3, 4, 6, 7, 8], mainly because of the potential to reduce the costs of device fabrication [9] by utilizing larger area and cheaper substrates in comparison to established technologies based on sapphire or SiC substrates. However, two major challenges have to be overcome to realise high quality GaN-on-Si devices. On the one side, the large lattice parameter mismatch between GaN film and silicon substrate ($+20.4\%$) leads to a high dislocation density limiting the performance of devices. This is, however, not a particular problem for GaN-on-Si but occurs in general for heteroepitaxial growth with considerable lattice mismatch (mismatch for GaN films on sapphire/silicon carbide substrates is $-13.9\%/-3.6\%$, respectively). On the other side, a particular challenge for the case of GaN-on-Si is the large difference in the coefficients of thermal expansion between substrate and film, which results in a tensile strain in GaN film upon cool-down after the epitaxial growth[1]. This tensile strain typically leads to cracking of the GaN film if its thickness exceeds a value of about 1 μm [13].

Appropriate strategies to overcome both these problems have been proposed based on intuition and/or experimental trial. Typically an *in-situ* Si/N treatment (exposure of the GaN (0001) surface to a silicon flow while the gallium flow is off) is used for defect density control [14, 15, 16, 17, 18, 19, 20, 21] and $Al_xGa_{1-x}N$ interlayers [13, 22, 23, 24, 25, 26, 27, 28, 29] are inserted into the film structure for strain-engineering. Though combining both concepts results in thick crack-free GaN (0001) films on silicon (111) a basic understanding that would allow to tailor the growth process with respect to obtain thick layers with minimum dislocation density is actually missing to large extend.

(i) Strain-engineering with $Al_xGa_{1-x}N$ interlayers

As regards the cracking issue due to tensile thermally induced strain, Amano et al. [22] were the first to show that inserting low temperature AlN interlayers into the film structure prevents cracking. The general strain-engineering concept of Amano has later been applied by Dadgar et al. [13, 23] to the particular case of GaN-on-Si to counterbalance the tensile thermal strain arising during cool-down. Again this approach has been found based on experience and intuition, while a basic understanding of the mechanisms that would allow to tailor the strain management concept is still missing. In literature it is assumed that the $Al_xGa_{1-x}N$ interlayer is (partly) relaxed, while the subsequent GaN layer on top grows coherently on the $Al_xGa_{1-x}N$ interlayer and thus is compressively strained [23, 27, 28, 29]. Amano et al. [22] proposed that relaxation of the interlayer is due to formation of small $Al_xGa_{1-x}N$ crystallites that grow incoherently on the film underneath. Bläsing et al. [28] and Reiher et al. [29] studied the influence of growth temperature of $Al_xGa_{1-x}N$ interlayer on the compensation of tensile strain. They found by means of X-ray diffraction that AlN interlayers grown at low temperature (below 900 $°C$) are partially relaxed and thus induce compressive strain in the subsequent GaN layer, while their counterparts deposited at high temperature (1145 $°C$) grow pseudomorphic. Thus a decoupling of the GaN layer separated by the interlayer is not observed. Other authors, however, have in contrast to the results of Bläsing et al. [28] and Reiher et al. [29] demonstrated that strain-engineering is possible also with high temperature $Al_xGa_{1-x}N$ interlayers [24, 25, 26]. If we leave the discrepancy of the influence of growth conditions on the strain relaxation process aside, there is an even more intriguing question. It is far from intuitive that a thin (approximately 10 nm) AlN interlayer relaxes plastically, while a much thicker (typically 1 μm and more) GaN layer grows coherently strained on top of the relaxed AlN interlayer. These apparent inconsistencies have their common origin in the more general problem that plastic relaxation of (0001)-oriented wurtzite heterostructures is not well understood at a quantitative level until now. In literature there exist models for plastic relaxation of (0001)-oriented strained wurtzite films that consider the important aspect of how misfit dislocation are formed, e.g. by a *"cooperative mechanism"* [30, 31, 32] or by a *"punch out mechanism"* [33]. However, they all describe the process only qualitatively. Quantitative models presented in literature so far, e.g. Holec et al. [34], however, neglect the kinetics of misfit dislocation formation and do not agree with experimental results.

---

[1] For a cool-down from typical deposition temperatures of 1000-1100°C to room temperature the strain due to the thermal mismatch amounts for GaN on Si to approximately $\varepsilon^{silicon}_{thermal} = +0.19\%$ (tensile strain) and for GaN on sapphire to $\varepsilon^{sapphire}_{thermal} = -0.18\%$ (compressive strain) [10, 11, 12].

(ii) The anti-surfactant effect of silicon in the epitaxial growth of (0001)-oriented GaN films

A commonly applied method to reduce the threading dislocation density in GaN films is a kind of nanoscopic lateral overgrowth that takes place after an *in-situ* Si/N treatment of the GaN (0001) growth surface (exposure of the GaN (0001) surface to a silicon flow while the gallium flow is off) [14, 15, 16, 17, 18, 19, 20, 21]. The fact that this *in-situ* Si/N treatment causes a transition from 2-dimensional towards 3-dimensional growth [15, 16, 17, 18, 19, 20] has often be assigned to an anti-surfactant effect of Si in the epitaxial growth of GaN [15, 16, 35, 36]. The transition towards 3-dimensional growth in case of a high silicon surface coverage has been attributed in literature to a partial "masking"' of the GaN (0001) growth surface by Si (commonly called "SiN_x-mask"). While Tanaka et al. [16] considered a sub-monolayer coverage with Si-N bonds to cause this masking of the surface, Rosa et al. [36, 37] showed with the help of ab-initio calculations that for Si-rich and N-rich growth conditions the GaN (0001) surface is thermodynamically unstable against the formation of β-

Si_3N_4 islands, which chemically passivate GaN surfaces. However, so far there is no direct experimental proof in literature neither for the SiN_x model proposed by Tanaka et al. [16] nor for the Si_3N_4 model by Rosa et al. [36, 37]. A TEM analysis by Kuwano et al. [38] has indeed shown that the "SiN_x-mask" is a thin crystalline layer (thickness less than $1\,nm$), which shows an epitaxial relationship with the GaN lattice and contains a certain amount of silicon. However, because aberration correction TEM was not common at that time, the exact atomic structure of the "SiN_x-mask" remained unsolved so far. Consequently, any explanation on the physical or chemical mechanism of how the "SiN_x-mask" prevents growth of GaN growth on top of it remained speculative.

1.1. Outline of this thesis

In this thesis we develop, based on transmission electron microscopy studies of dedicated samples, a predictive quantitative model for strain relaxation in the epitaxial growth of in (0001)-oriented wurtzite heterostructures. We investigate growth and relaxation of $Al_xGa_{1\text{-}x}N$ on GaN and the overgrowth of GaN on $Al_xGa_{1\text{-}x}N$ step by step for different growth temperatures. Furthermore, we analyse the effect of Si as an anti-surfactant in the epitaxial growth of GaN (0001) by a combined effort of transmission electron microscopy studies and ab-initio theory provided from the Max-Planck-Institut für Eisenforschung.

The thesis is organised as follows. In chapter 2 we will give a short overview on the main experimental techniques that we use for our studies. We then will present results, modelling and discussion of our experimental work. We will start with an investigation of the strain-engineering process with $Al_xGa_{1\text{-}x}N$ interlayer in chapter 3. In this chapter our aim is to explain the build-up of compressive strain in GaN films by $Al_xGa_{1\text{-}x}N$ interlayers on a purely phenomenological basis. In the following chapter 4 we will then focus on the microscopic mechanisms leading to plastic strain relaxation at the interfaces of $Al_xGa_{1\text{-}x}N$ interlayers. With the help of our experimental results and finite element method calculations we will derive a quantitative model for the growth and plastic relaxation mechanism. This model, however, is not limited to the case of $Al_xGa_{1\text{-}x}N$ interlayer but can be applied to any (0001)-oriented strained wurtzite heterostructure. Finally, in chapter 5 we will study the anti-surfactant effect of Si in GaN (0001) epitaxy.

2. Theoretical background and experimental methods

2.1. Dislocations and slip-systems in the wurtzite lattice

In this section we give a brief overview on dislocations and slip-systems in the wurtzite lattice. For a more detailed introduction into the theory of dislocations, we refer the reader to respective textbooks by e.g. Hirth and Lothe [132] or Hull and Bacon [178].

The III-nitrides (AlN, GaN and InN) crystallise in the wurtzite structure. In this crystal structure 3 different types of perfect dislocations are possible: (i) a-type dislocations, which have a Burgers-vector of $\vec{b} = \frac{1}{3} < 11\bar{2}0 >$ corresponding to an in-plane a-lattice vector lying in the basal plane, (ii) c-type dislocations with a Burgers-vector of $\vec{b} =< 0001 >$, i.e. a c-lattice vector in the wurtzite lattice, and (iii) a+c-type dislocations with $\vec{b} = \frac{1}{3} < 11\bar{2}3 >$. In case of (0001)-oriented strained III-nitride thin films, however, only a-type and a+c-type dislocations can contribute to plastic relaxation of lattice mismatch at heterointerfaces. This is because only these two dislocation types have a component of their Burgers-vector, which would lie in the interface of a strained heterostructure (only such component is able to relax misfit strain). The process of plastic relaxation itself proceeds by formation of misfit dislocations at the interface by motion of dislocations (either pre-existing or new nucleated dislocations) into the heterointerface. Motion of dislocations in the crystal lattice occurs typically under the influence of shear stresses by glide on slip-planes. Possible slip-systems[1] of a-type and a+c-type dislocations in the wurtzite lattice are schematically shown in Fig. 2.1.

Parameters, which are relevant for the discussion of the plastic relaxation process, such as the interplanar spacing of the slip planes, the modulus of the Burgers-vector, the line direction of the dislocation in the interfacial plane, the Schmid factor and the Peierls stress at typical growth temperatures are summarised for all considered slip-systems in Table 2.1. The line direction of the dislocation in the interfacial plane is given by the line of intersection of the slip plane and the heterointerface. The Schmid factor S defines for a given slip geometry the magnitude of the resolved shear stress acting on a dislocation due to the misfit stress [179]. It is given by

$$S = \cos\alpha \cdot \cos\beta \ , \tag{2.1}$$

where α is the angle between the Burgers-vector and the direction in the strained interface, perpendicular to the dislocation line and β is the angle between the slip plane

---

[1] A Slip-system is given by the combination of a slip-direction and a set of slip-planes for which dislocation motion occurs [178].

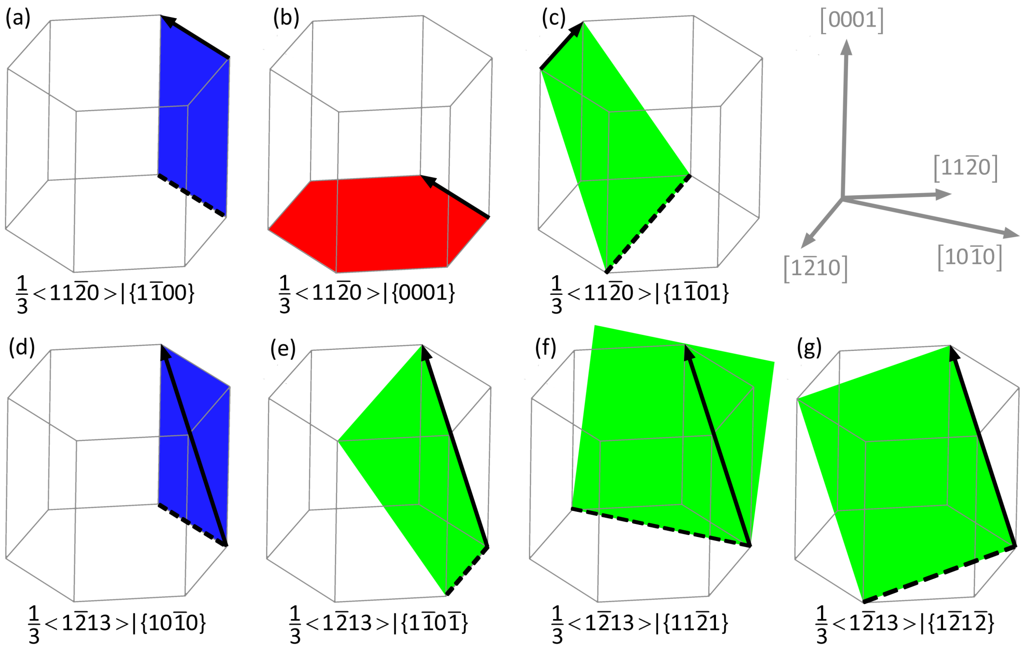
(a)
(b)
(c)
[0001]
[11$\bar{2}$0]
[1$\bar{2}$10]
[10$\bar{1}$0]
$\frac{1}{3}$<11$\bar{2}$0>|{1$\bar{1}$00}
$\frac{1}{3}$<11$\bar{2}$0>|{0001}
$\frac{1}{3}$<11$\bar{2}$0>|{1$\bar{1}$01}
(d)
(e)
(f)
(g)
$\frac{1}{3}$<1$\bar{2}$13>|{10$\bar{1}$0}
$\frac{1}{3}$<1$\bar{2}$13>|{1$\bar{1}$0$\bar{1}$}
$\frac{1}{3}$<1$\bar{2}$13>|{11$\bar{2}$1}
$\frac{1}{3}$<1$\bar{2}$13>|{1$\bar{2}$1$\bar{2}$}

Figure 2.1.: Possible slip-systems in the wurtzite lattice. Blue, red and green shaded planes denote prismatic, basal and pyramidal slip planes, respectively. Solid and dashed black arrows indicate the Burgers-vector of the dislocation and the resulting dislocation line direction in the interfacial (0001) plane for each slip-system, respectively.

and the normal of the strained interface. The Peierls stress can be considered as a lattice frictional force that the dislocation has to overcome during its motion on the slip plane through the periodic potential of the crystal [132]. In the original form in the framework of the Peierls-Nabarro dislocation model [133, 134] the Peierls stress σ_P is derived from a purely phenomenological consideration and depends essentially on the ratio of the interplanar spacing of the slip planes and the modulus of the Burgers-vector $\frac{d}{b}$ [132]. Chidambarrao et al. [135] have presented a modification, which includes also a temperature dependency of the Peierls stress σ_P. For a pure edge dislocation the Peierls stress is given by

$$\sigma_P = \frac{2\mu}{1-\nu}\,\omega\,\exp\left(-\frac{d}{b}\,\frac{2\pi}{1-\nu}\,\omega\right), \tag{2.2}$$

$$\omega = \exp\left(\frac{4\pi^2 N}{5\mu}\,kT\right), \tag{2.3}$$

where μ is the shear modulus, ν is Poisson's ratio, N is the number of atoms per unit cell volume, k is the Boltzmann constant and T is the temperature.

Table 2.1.: Properties of various slip-systems in the wurtzite lattice

slip system	interplanar spacing [nm]	modulus Burgers-vector [nm]	line direction of misfit segment	α [2]	β [3]	Schmid-factor S	in-plane edge component	Peierls-stress σ_P at 1000°C [GPa]
$\frac{1}{3} < 11\bar{2}0 > \vert \{1\bar{1}00\}$	0.276	0.3189	$< 11\bar{2}0 >$	90°	0°	0	0	0.14
$\frac{1}{3} < 11\bar{2}0 > \vert \{0001\}$	0.259	0.3189	n/a[4]	n/a[4]	90°	0	n/a[4]	0.18
$\frac{1}{3} < 11\bar{2}0 > \vert \{1\bar{1}01\}$	0.244	0.3189	$< 11\bar{2}0 >$	90°	28.1°	0	0	0.23
$\frac{1}{3} < 1\bar{2}13 > \vert \{10\bar{1}0\}$	0.276	0.6087	$< 11\bar{2}0 >$	90°	0°	0	0	7.1
$\frac{1}{3} < 1\bar{2}13 > \vert \{1\bar{1}0\bar{1}\}$	0.244	0.6087	$< 11\bar{2}0 >$	63.0°	28.1°	0.40	0.866 a[5] (60° disl.)	10.9
$\frac{1}{3} < 1\bar{2}13 > \vert \{11\bar{2}1\}$	0.152	0.6087	$< 10\bar{1}0 >$	74.8°	17.1°	0.25	0.5 a[5] (30° disl.)	37.3
$\frac{1}{3} < 1\bar{2}13 > \vert \{1\bar{2}1\bar{2}\}$	0.136	0.6087	$< 10\bar{1}0 >$	58.4°	31.6°	0.45	a[5] (90° disl.)	49.2

---

[2] α is the angle between the Burgers-vector and the direction in the strained interface, perpendicular to the dislocation line

[3] β is the angle between the slip plane and the normal of the strained interface

[4] line direction of misfit segment not defined because the dislocation can move and proceed along any direction on the (0001) plane

[5] a is here the in-plane lattice parameter of the wurtzite lattice

2.2. Sample growth by metal-organic vapour phase epitaxy

The samples studied in this work have been grown by metal-organic vapour phase epitaxy (MOVPE). MOVPE is a technique to grow epitaxially[2] thin crystalline films on a crystalline substrate. In the following section we will give a brief introduction about the thermodynamic framework and basic principle of metal-organic vapour phase epitaxy. Further details of MOVPE and on epitaxial growth in general can be found in specialised literature (see e.g. Ref [40, 41, 42, 43]). Finally, we will very briefly describe the experimental setup for the sample growth and give an overview about the sample structure.

2.2.1. Thermodynamic framework of vapour phase epitaxy

Very simplified, epitaxial growth from the vapour phase can be described as a phase transition of species from their vapour to their solid phase. We can apply basic concepts of thermodynamics to describe this phase transition. In case of homoepitaxy, where film and substrate material are the same, the vapour-solid system is in thermodynamic equilibrium if the condition

$$\Delta\mu = \mu^i_{vapour} - \mu^i_{solid} = 0 \,, \tag{2.4}$$

is satisfied [40]. The terms $\mu^i_{vapour,solid}$ are the chemical potentials of material i in the vapour and in the solid phase, respectively. However, at thermodynamic equilibrium no net crystal growth occurs. To induce a net crystal growth an excess Gibbs free energy (ΔG) due to supersaturation of the growth relevant species at the growth front is necessary [40]

$$\Delta G = \Delta\mu > 0 \,. \tag{2.5}$$

For an ideal gas the difference in the chemical potential is given by [40]

$$\Delta\mu = RT\, ln\frac{p}{p_0} \,, \tag{2.6}$$

where R is the gas constant, T is the temperature, p is the partial pressure of the gas and p_0 is the equilibrium or saturated vapour pressure at the temperature of the solid, respectively. Hence, epitaxial growth will occur if the partial pressure of the gas is higher than p_0, i.e. if there is a supersaturation of the vapour phase at the surface of the solid.

In case of heteroepitaxy, where the film and substrate material are different, one has additionally to consider the change in surface free energy $(\Delta\gamma)$ and the contribution of elastic energy due to a possible lattice mismatch strain (E_{strain}) [44]

---

[2] The word epitaxy comes from the Greek words epi and taxis meaning above in an ordered manner. Epitaxial growth thus refers to the continuation of the crystallographic alignment of atoms in the crystalline substrate into the crystal film [39].

$$\Delta G = \Delta\mu - \Delta\gamma - E_{strain} \text{ , with} \tag{2.7}$$

$$\Delta\gamma = \gamma_{film} - \gamma_{substrate} + \gamma_{interface} \text{ ,} \tag{2.8}$$

where $\gamma_{substrate}$and γ_{film} are the surface free energies of the substrate and the film, respectively, and $\gamma_{interface}$ is the interfacial energy. Note that the elastic energy due to strain scales linear with the thickness t of the film and with the square of the strain ε, i.e. $E_{strain} \sim t \cdot \varepsilon^2$. Consequently, eq. (2.7) and (2.8) imply that the driving force for crystal growth of a heteroepitaxial film might depend in addition to the supersaturation also on the difference of the surface energies between substrate and film, the magnitude of the strain and thickness of the film. For example, there might be a situation that the driving force for epitaxial growth vanishes despite of the fact that the vapour is supersaturated. This will be the case if the lattice mismatch between film and substrate is too large (if changes in the surface free energy are negligible: $E_{strain} > \Delta\mu$). On the other hand, if strain is negligible and the surface free energy of the film is lower than that of the substrate and the interfacial energy together, the film might grow even for an undersaturated vapour $\left(\text{if } \gamma_{film} - \gamma_{substrate} + \gamma_{interface} > \Delta\mu\right)$.

2.2.2. Basic principle of metal-organic vapour phase epitaxy

The basic processes of epitaxial growth by means of metal-organic vapour phase epitaxy are schematically depicted in Fig. 2.2. The growth process can be divided into the following steps [40]:

1. Mass transport of volatile precursor molecules (molecules consisting of one white and two black balls in Fig. 2.2) to the substrate/film surface by a carrier gas.
2. Pyrolysis (decomposition at elevated temperatures) of the precursor to ad-atoms, either homogeneous in the gas phase or heterogeneous at the substrate/film surface.
3. Adsorption of ad-atoms (white balls in Fig. 2.2) and precursor molecules on the growth surface.
4. Diffusion of ad-atoms and precursor molecules on the surface.
5. (a) Incorporation of ad-atoms into the film at proper growth sites (surface steps and kinks), (b) nucleation of new islands or (c) desorption of ad-atoms into the vapour phase.
6. Mass transport of reaction by-products and desorbed species to the gas exhaust.

From this scheme it can be deduced that the MOVPE process is not only governed by thermodynamical factors but also by the growth kinetics. The main effects are the chemical kinetics of the precursors, i.e. the pyrolysis of them, the surface diffusion of ad-atoms and the desorption rate of ad-atoms. All these phenomena typically show

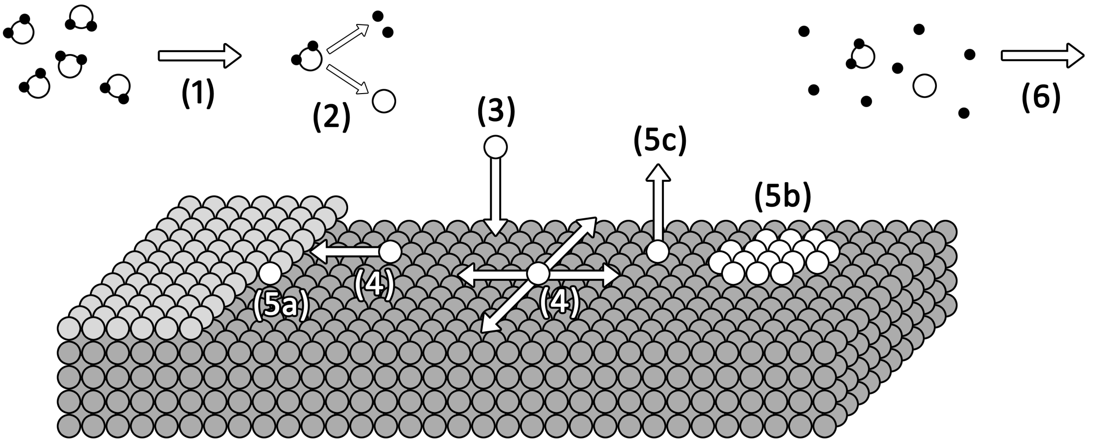

Figure 2.2.: Simplified scheme of MOVPE growth process. For explanation of individual steps see text.

an Arrhenius like behaviour meaning that their rates increase exponentially with the temperature. The growth process and the resulting surface morphology and film quality thus depend substantially on the deposition temperature. For more details on this topic see e.g. Ref. [40, 41].

2.2.3. Experimental details and sample structure

The samples studied in this work have been provided by Philipp Drechsel and Peter Stauss [45] (Osram Opto Semiconductors, Regensburg, Germany), Armin Dadgar (Otto von Guericke University Magdeburg, Germany) and the former AZZURRO Semiconductors company (Magdeburg and Dresden, Germany).

All samples have been grown by metal-organic vapour phase epitaxy using commercially available growth reactors from Aixtron and Veeco. For the III-nitride epitaxial growth the group III elements are supplied in form of metal-organic precursors: trimethyl- or triethylgallium (TMGa or TEGa), trimethylaluminium (TMAl) and trimethylindium (TMIn). The nitrogen (group V element) as well as silicon as the donor of choice in GaN are supplied as hydrides, i.e. ammonia (NH_3) and silane (SiH_4). Either hydrogen (H_2) or nitrogen (N_2) have been used as carrier gas. Epitaxial films have been deposited on either 2-, 4- and 6-inch Si (111), 4-inch sapphire (0001) or 2-inch GaN (0001) substrates. Their thickness are 300 μm (for 2-inch Si wafer), $1.0\,mm$ (for 4- and 6-inch Si wafer), 650 μm (for sapphire wafer) and 300 μm (for GaN wafer), respectively. In order to heat the substrates, they are mounted on a temperature controlled susceptor. Epitaxial growth has been performed typically at a substrate temperatures of about $1000-1100\,^{\circ}C$ if not otherwise stated.

The structure of the studied samples is schematically shown in Fig. 2.3. In case of heteroepitaxial growth of the nitride films on either Si (111) or sapphire (0001) substrates, we have used a similar template structure in order to have comparable samples. The growth starts with an AlN nucleation layer[3] deposited within a temperature range

---

[3] In case of MOVPE growth of GaN on a Si substrate the AlN nucleation layer is mandatory to avoid

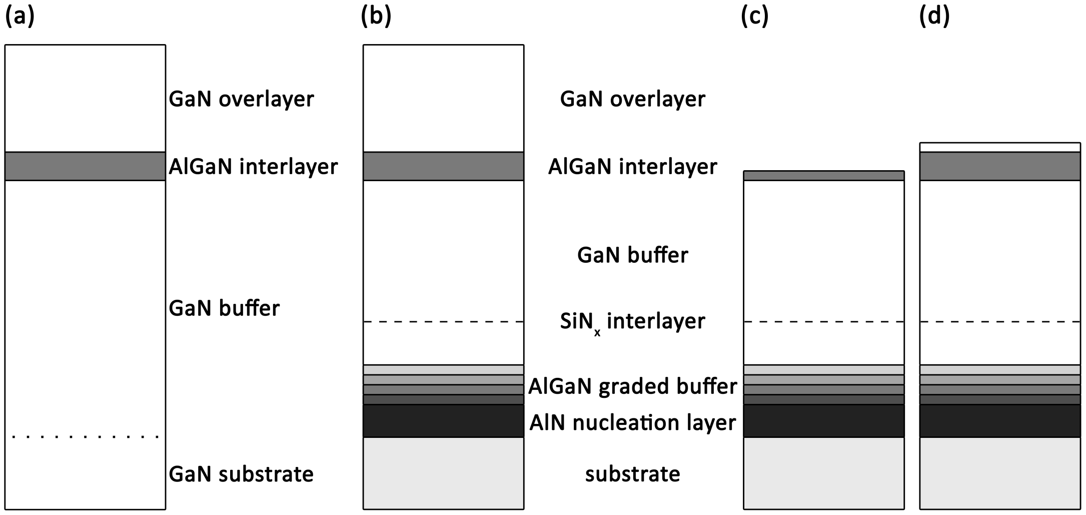

Figure 2.3.: Schematic representation of the sample structure of GaN films with $Al_xGa_{1-x}N$ interlayer grown (a) homoepitaxially on a GaN (0001) substrate and (b)-(d) heteroepitaxially on Si (111) or sapphire (0001) substrates, respectively. (a) and (b) schematically represent samples with a full layer structure, (c) and (d) depict the structure of samples for which the deposition of $Al_xGa_{1-x}N$ interlayer and GaN overlayer, respectively, has been stopped during the initial stages of growth (experiments in chapter 4.2.2).

of 1000–1100 $^\circ C$ at a low reactor pressure of 50 $mbar$ and a V/III ratio of 300. On top of the nucleation layer, a graded $Al_xGa_{1-x}N$ buffer[4] is grown at the same temperature while steadily increasing the amount of gallium. Subsequently, a first $100-200$ nm thick GaN layer has been deposited at a temperature and V/III ratio of 1050 $^\circ C$ and 1500, respectively. Finally, a SiN_x-interlayer[5], grown by exposing the GaN (0001) surface at a temperature of 1030 $^\circ C$ for two minutes to a silane flow of approximately 400 $\frac{nmol}{min}$ while the Ga precursor (TMGa) has been switched off, completes the heteroepitaxial template structure. Although there are some variations in the thickness and composition of the layers forming the template structure between different investigated samples, the key parameters, relevant for the strain relaxation process of subsequent layers grown on top of this template, are comparable. These are the threading dislocation density (in the range of $1-2\times10^9$ cm^{-2}), the distribution among Burgers-vectors of the threading dislocations (i.e. the ratio of a-type vs. a+c-type threading dislocations is about 2:1) and the residual biaxial strain (during the growth the GaN buffer is typically slightly compressively strained with $\varepsilon \approx -0.001$).

On top of this template structure a GaN buffer layer is grown whose thickness ranges from $1000-1500$ nm. Growth temperature and V/III ratio are again 1050 $^\circ C$ and 1500, respectively. No intentional doping has been applied. In case of homoep-

---

so called melt-back etching [46, 47].

[4] It has been shown in literature that a graded $Al_xGa_{1-x}N$ buffer effectively reduces the threading dislocation density in the film [48, 49, 50, 51].

[5] The purpose of the SiN_x-interlayer is to further reduce the threading dislocation density [16, 17, 18].

itaxy the AlN nucleation layer, the graded $Al_xGa_{1-x}N$ buffer and the SiN_x-interlayer are omitted and the GaN buffer has been grown directly on the GaN substrate (see Fig. 2.3). Subsequently, an $Al_xGa_{1-x}N$ interlayer has been deposited at a reactor pressure of 100 *mbar* and a nominal V/III ratio of 430. Thickness and growth temperature have been systematically varied. If not stated otherwise, the aluminium content of the $Al_xGa_{1-x}N$ interlayers in this work is approximately $x \approx 75\%$. The composition of $Al_xGa_{1-x}N$ interlayers has been quantitatively determined by combining several TEM methods (see details in appendix C). Finally, a $1-2\ \mu m$ thick GaN overlayer has been grown on top of the $Al_xGa_{1-x}N$ interlayer. The growth parameters of the GaN overlayer are same as before for the GaN buffer.

2.3. Transmission electron microscopy

The main characterisation technique employed in this work is transmission electron microscopy (TEM). In particular we use TEM to study the dislocation structure in the films and at interfaces, the dislocation formation process, the atomic structures of defects and the composition and morphology of heterostructures. For this purpose we apply mainly 3 techniques: diffraction contrast imaging (bright field and weak beam dark field imaging), aberration corrected high resolution transmission electron microscopy (HRTEM) and scanning transmission electron microscopy (STEM) using a high angle annular dark field (HAADF) detector. Latter technique is also known as STEM Z-contrast imaging. In the following we want to give a brief overview about the basic principles of image and contrast formation for the relevant imaging techniques used in this work. For a more detailed introduction into transmission electron microscopy we would like to refer to respective textbooks by Williams and Carter [52], Fultz and Howe [53], Bethge and Heydenreich [54] and Pennycook and Nellist [55].

2.3.1. Basic principle of structural imaging by transmission electron microscopy

The basic design and optical path of a transmission electron microscope (TEM) is schematically depicted in Fig. 2.4. Electrons are generated by a source (in our case a field emission source) and accelerated by a high voltage applied to an anode. According to the de Broglie relation, the wavelength of an electron accelerated by a voltage U is given by [52]

$$\lambda = \frac{h}{\sqrt{2m_0eU\left(1+\frac{eU}{2m_0c^2}\right)}}, \tag{2.9}$$

where h is the Planck constant, m_0 is the electron mass, e is the elementary charge and c is the speed of light. For an acceleration voltage of 300 kV used throughout this work, the electron wavelength is 1.97 pm $\left(0.0197\ \text{Å}\right)$. A condenser system then forms the beam, which illuminates the specimen. In conventional TEM typically a parallel

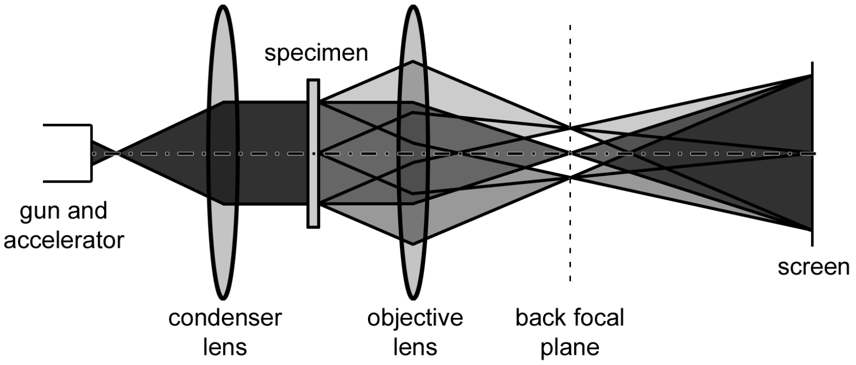

Figure 2.4.: Schematic representation of the basic principle of image formation in a TEM. The horizontal dashed-dotted line denotes the optical axis of the microscope.

illumination is used, and the incident electrons are described as a plane wave according to

$$\Psi_0 = A_0 \exp\left[2\pi i\left(\vec{k_0}\cdot\vec{r}\right)+\phi_0\right], \tag{2.10}$$

where A_0 is the amplitude (for simplicity normalised to 1 in the following), $\vec{k_0}$ ($\left|\vec{k_0}\right| = \frac{1}{\lambda}$) is the wave vector and ϕ_0 is the phase offset of the incident electron wave. This wave is then transmitted through the electron transparent specimen (typical thickness is in the range of a few nm up to some hundred nm). The electron wave interacts with the electrostatic potential of the specimen, which results in coherent (elastic) scattering, incoherent (quasi-elastic) scattering and inelastic scattering of the electrons. In the latter case the electrons transfers energy to the specimen, e.g. they excite photons, phonons or plasmons or ionise atoms. Through spectroscopic analyses of these characteristic energy transfer processes by electron energy loss spectroscopy (EELS) or by analysis of secondary processes that result from these, e.g. emission of element specific X-rays detected by energy dispersive X-ray spectroscopy (EDXS), one can gain useful analytical information on the composition of the specimen. Structural imaging, however, is based on elastic scattering[6]. In this case the energy of the incident and scattered electrons and thus also their wavelengths stay unchanged. The process of elastic scattering of a plane electron wave at a crystalline specimen is considered in more detail in appendix A. The main result is that coherent elastic scattering of electrons by the periodic potential of a crystal results in an electron wave at the exit surface (Ψ_{exit}) that has a discrete spectrum in the Fourier space according to [54]

$$\Psi_{exit}(\vec{r}) = \sum_g \Psi_g(\vec{r}) = \sum_g A_g \exp\left[2\pi i\left(\vec{k_g}\cdot\vec{r}+\phi_g\right)\right], \tag{2.11}$$

where A_g and ϕ_g are the amplitude and the phase offset of the diffracted waves, respectively. The discrete components in the Fourier space correspond to the respective diffracted waves Ψ_g for which the condition

---

[6] Inelastically scattered electrons are due to (i) their different energy compared to that of elastically scattered electrons and (ii) chromatic aberration of the objective lens not focussed on the image plane and thus mainly produce a diffuse background.

$$\vec{k}_g - \vec{k}_0 = \vec{g}, \tag{2.12}$$

where $\vec{g}$ is a reciprocal lattice vector, is satisfied. The analogue of eq. (2.12) in real space is the well known Bragg's law

$$2d \sin\theta = n\lambda, \tag{2.13}$$

whereθ is the scattering angle and $|\vec{g}| = \frac{1}{d}$ with d being the interplanar spacing of the diffracting lattice planes. The exit wave then passes through the objective lens and in its back focal plane the diffraction pattern with focussed diffraction spots is obtained. With the help of a suitable aperture one can then select in the back focal plane of the objective lens appropriate diffracted waves which should contribute to the image formation. The electron wave function in the back focal plane of the objective lens can be expressed by [54]

$$\Psi'(q) = \mathscr{F}\left(\Psi_{exit}(\vec{r})\right) \cdot T(q), \tag{2.14}$$

where q is the spatial frequency (for small scattering angles the spatial frequency is related to the scattering angle by the equation $q = \frac{\theta}{\lambda}$), $\mathscr{F}$ denotes a Fourier transformation and $T(q)$ is the transfer function of the objective lens. The transfer function basically describes the impact of the lens on the exit wave as a function of the spatial frequency. Mathematically the transfer function can be expressed by [52]

$$T(q) = A(q) \cdot E(q) \cdot \exp(i\chi(q)), \tag{2.15}$$

where $A(q)$ is a top hat function describing the objective aperture, which cuts off all spatial frequencies above $q_{aperture}$

$$A(q) = \begin{cases} 1 & \text{for } 0 \leq q \leq q_{aperture} \\ 0 & \text{for } q > q_{aperture} \end{cases}, \tag{2.16}$$

$\chi(q)$ is the aberration function and $E(q)$ is the envelope function. Because spherical aberration and defocus are the most dominant aberrations in a TEM, $\chi(q)$ is typically written as [52]

$$\chi(q) = \pi\lambda q^2 \Delta f + \frac{\pi}{2}\lambda^3 q^4 C_S, \tag{2.17}$$

where Δf and C_S denote the defocus and spherical aberration[7] parameter of the objective lens, respectively. From eq. (2.15) and (2.17) one can see that lens aberrations induce a spatial frequency dependent phase shift (between -π and +π) to the electron wave as it passes through the objective lens. The envelope function in eq. (2.15) takes values between 0 and 1 and describes the attenuation of the electron wave as a function of the spatial frequency due to limited coherence. The envelope function can be expressed as a product of separate terms, which attribute limited spatial ($E_S(q)$) and temporal coherence ($E_T(q)$), specimen drift ($E_D(q)$) and vibration ($E_V(q)$) [52]

---

[7] Spherical aberration means that a monochromatic wave emitted from a point on the optical axis of a lens is not focussed by it again into a point because of the stronger refraction of rays, which pass further away from the optical axis of the lens. The same holds for a parallel wave, whose wave vector is aligned with the optical axis of the lens.

$$E(q) = E_S(q) E_T(q) E_D(q) E_V(q)\,. \tag{2.18}$$

Neglecting the latter two and assuming parallel illumination (i.e. perfect spatial coherence) the damping at higher spatial frequencies is caused by limited temporal coherence. This is in turn due to chromatic aberration of the objective lens in combination with the energy spread of the electron wave emitted from the gun, instabilities in the acceleration voltage and lens currents (compare with the terms under the square root in eq. (2.20)), respectively. In this case the envelope function is given by [52]

$$E(q) = \exp\left[-\left(\pi\lambda\frac{\Delta}{2}\right)^2 q^4\right], \text{ with} \tag{2.19}$$

$$\Delta = C_C\sqrt{\left(\frac{\Delta E}{E}\right)^2 + \left(\frac{\Delta U}{U}\right)^2 + 4\left(\frac{\Delta I}{I}\right)^2}\,, \tag{2.20}$$

where Δ is the focal spread and C_C is the chromatic aberration[8] parameter of the objective lens. From eq. (2.19) one can see that especially electron waves scattered into higher angles (corresponding to higher spatial frequencies q) are strongly attenuated. Thus the envelope function limits the achievable resolution of the microscope. The spatial frequency at which the envelope function has dropped to a value of $\frac{1}{e^2}$ is typically defined as the information limit of the microscope and amounts for the TEM used in this work to approximately 12.5 nm^{-1} corresponding to a resolvable spacing of 0.8 Å (for state-of-the-art TEMs an information limit of 20 nm^{-1} has been reported [56]).

After propagation of the electron wave from the back focal plane to the imaging device (typically either fluorescence screen or CCD camera) the wave function in the image plane is given by an inverse Fourier transformation

$$\Psi_{image}(x,y) = \mathscr{F}^{-1}\left(\Psi'(q)\right). \tag{2.21}$$

What we finally measure is an intensity distribution in the image plane, i.e. the modulus squared of the electron wave function

$$I_{image}(x,y) = \left|\Psi_{image}(x,y)\right|^2. \tag{2.22}$$

---

[8] Chromatic aberration means that waves of different wavelength emitted from a point source are not focussed again into a point.

2.3.2. High resolution transmission electron microscopy

Origin and interpretation of lattice fringe images

For high resolution transmission electron microscopy one typically investigates thin specimens. In this case one can consider the specimen as a phase object, meaning that interaction of the electron wave with the periodic potential of the crystal leads only to a small shift of the phase of the electron wave. The electron wave at the exit surface of the specimen can then be expressed by [52]

$$\Psi_{exit}(x,y) = \Psi_0 \exp\left(-i\sigma V_t\left(x,y\right)\right) \ , \tag{2.23}$$

where $\sigma = \frac{\pi}{\lambda E}$ is called the interaction constant and

$$V_t\left(x,y\right) = \int_0^t V\left(x,y,z\right) dz \tag{2.24}$$

is the projected atomic potential for a specimen thickness of t. For very thin specimens (thickness of only a few nanometers) $\sigma V_t\left(x,y\right)$ becomes much smaller than 1 and the exponential term in eq. (2.23) can be developed according to

$$\Psi_{exit}\left(x,y\right) = \Psi_0 \exp\left(-i\sigma V_t\left(x,y\right)\right) \approx 1 - i\sigma V_t\left(x,y\right), \tag{2.25}$$

with the normalisation $\Psi_0 = 1$. Eq. (2.25) is the so called weak phase object approximation [52]. In this case all the information about the atomic structure of the specimen is stored in the phase of the electron wave at the exit surface of the specimen. During imaging with an ideal lens, see eq. (2.22), the phase information of the electron wave in the image plane is, however, lost and in the weak phase object approximation the image intensity would be the same everywhere. However, we can still obtain phase contrast in the final image by taking advantage of the phase shift that the electron wave experiences as it is transferred through the objective lens. An ideal microscope for phase contrast imaging would shift the phase of the scattered wave by $\pm\frac{\pi}{2}$ so that the electron wave in the image plane would be given by

$$\Psi_{image}^{phase\,contrast}\left(x,y\right) = 1 \pm \sigma V_t\left(x,y\right) \ , \tag{2.26}$$

respectively. Interference of all waves in the image plane thus produces a lattice image which reveals information about the atomic structure of the specimen. However, the interpretation of conventional HRTEM images in terms of assigning an intensity minima/maxima to positions of atomic columns is typically not straight forward. This is because aberrations of the objective lens lead to a non-homogeneous phase shift as electron waves pass through the objective lens, i.e. the phase shift depends on the spatial frequency of the electron waves. As we have seen before, the phase shift can be expressed by the transfer function of the objective lens (see eq. (2.15) and (2.17)). In case the weak phase object approximation (WPOA) applies and neglecting non-linear contributions to the HRTEM image formation process the transfer function simplifies and is given by [52]

$$T_{WPOA}\left(q\right) = A\left(q\right) \cdot E\left(q\right) \cdot 2\sin\left(\chi\left(q\right)\right). \tag{2.27}$$

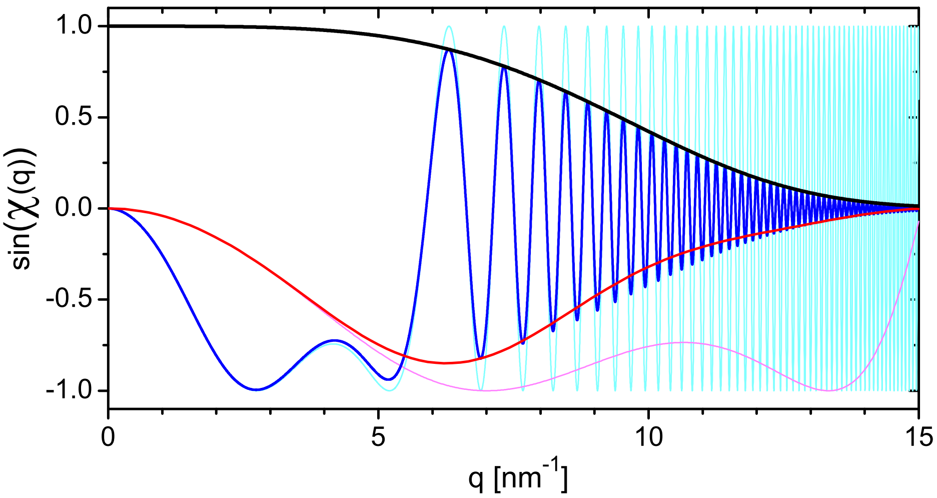

Figure 2.5.: Transfer function of a 300 kV TEM in the weak phase object approximation at Scherzer defocus. The black solid line denotes the envelope function (eq. (2.19)) for a focal spread of $\Delta = 3\ nm$ corresponding to an information limit of approximately 12.5 nm^{-1} $\left(0.8\ \text{Å}\right)$. Red and magenta (blue and cyan) curves are the contrast transfer function with and without the effect of the envelope function $E\left(q\right)$ for a spherical aberration parameter of $C_S = 15\ \mu m$ ($C_S = 0.64\ mm$) respectively.

The transfer function of a conventional 300 kV TEM having a spherical aberration parameter of $C_S = 0.64\ mm$ (one of the lowest value for non-corrected lenses) and for an optimum defocus value, the so called Scherzer defocus [57], is shown as cyan/blue curve in Fig. 2.5. For this condition the transfer function amounts close to -1 for a broad range of spatial frequencies. This means that waves within this band of spatial frequencies experience an almost constant phase shift of $-\frac{\pi}{2}$ which results for thin samples (i.e. the weak phase object approximation applies) in a dark atom contrast in the interference image. For higher values of q the transfer function then starts to oscillate rapidly, which means that waves with higher spatial frequencies (corresponding to smaller distances in the image) are transferred with either positive or negative phase shift through the objective lens. This causes image artefacts and inhibits direct interpretation of the HRTEM pattern. The first zero crossing of the transfer function essentially limits the minimum interpretable spacing, which is commonly defined as the point resolution of the microscope. For the aforementioned parameters of 300 kV and $C_S = 0.64\ mm$ (they apply e.g. for a Philips CM300 TEM) the point resolution equals to approximately 1.7 Å corresponding to the zero crossing of $\sin\left(\chi\left(q\right)\right)$ at $q = 5.9\ nm^{-1}$ (see Fig. 2.5).

Aberration corrected HRTEM

As we have just seen, optical aberrations of the image forming lens, especially the spherical aberration, which is typically the most detrimental aberration of TEM lenses, limit the resolution of the microscope. One possibility to overcome this problem is to use aberration correctors. It has been shown by Rose [58, 59] that a post objective lens unit consisting of several multi-pole elements is able to correct C_S and other aberrations of the objective lens like axial coma, 3-fold astigmatism, star aberration and 4-fold astigmatism, respectively (for an overview of the aberration function including all contributions up to higher orders aberrations see e.g. Ref. [60]). As a result of aberration correction, the point resolution of the microscope can be extended up to the information limit of the microscope (see magenta curve in Fig. 2.5). For a corrected 300 kV TEM with a spherical aberration parameter of $C_S = 15\ \mu m$ and Scherzer defocus the transfer function of the objective lens has no zero crossing up to the assumed information limit of 12.5 nm^{-1}. This means that an interpretable resolution of approximately 0.8 Å is achieved. The effect of aberration correction on HRTEM imaging of GaN crystals is illustrated in Fig. 2.6. While in the case of an aberration corrected TEM, neighbouring Ga and N atomic columns of a GaN crystal seen along the $\langle 11\bar{2}0\rangle$ projection (their projected distance is approximately 1.1 Å) are clearly identified (see Fig. 2.6 (c) and (d)) they can not be resolved in the case of a non-corrected microscope (see Fig. 2.6 (b)). Thus, aberration corrected HRTEM images are much easier to interpret in terms of the projected atomic structure than conventional HRTEM micrographs.

Another important benefit of aberration correction is the reduced contrast delocalisation R[9] which is given by [61]

$$R = max\left|\frac{1}{2\pi}\frac{\partial\chi(q)}{\partial q}\right| \text{ for } q \text{ within the interval } [0, q_{max}], \tag{2.28}$$

where q_{max} is either given by the objective aperture cut-off or the information limit of the microscope. In case of an aberration corrected TEM with $C_S = 15\ \mu m$ and Scherzer defocus the contrast delocalisation amounts to approximately 0.6 Å compared to several Å for a non-corrected microscope. This effect is impressively illustrated in Fig. 2.6. While in the case of conventional HRTEM imaging one can observe some artificial contrast also in the vacuum region more than 1 nm above the GaN (0001) surface (making it impossible to identify the surface structure), there is an abrupt contrast at the interface between vacuum and the GaN crystal underneath in the aberration corrected HRTEM image (compare Fig. 2.6 (b) with (c) or (d)).

A third advantage, which the utilisation of aberration correctors offers, is that one can tune the aberration parameters (e.g. C_S) intentionally to any desired value. This allows for a completely new imaging method, namely negative spherical aberration imaging or NCSI [62, 63]. In conventional TEMs the spherical aberration parameter C_S is a positive value which is determined by the design of the objective lens. With a proper underfocus this leads for thin specimens to atomic columns appearing dark (see

---

[9] Note that contrast delocalisation in HRTEM should not be understood as an incoherent blurring leading to a diffuse background. Instead it means that the wave function emitted from a point at the exit surface of the specimen is delocalised in the image plane. At a given position in the image delocalised waves from several points from the specimen will superimpose coherently.

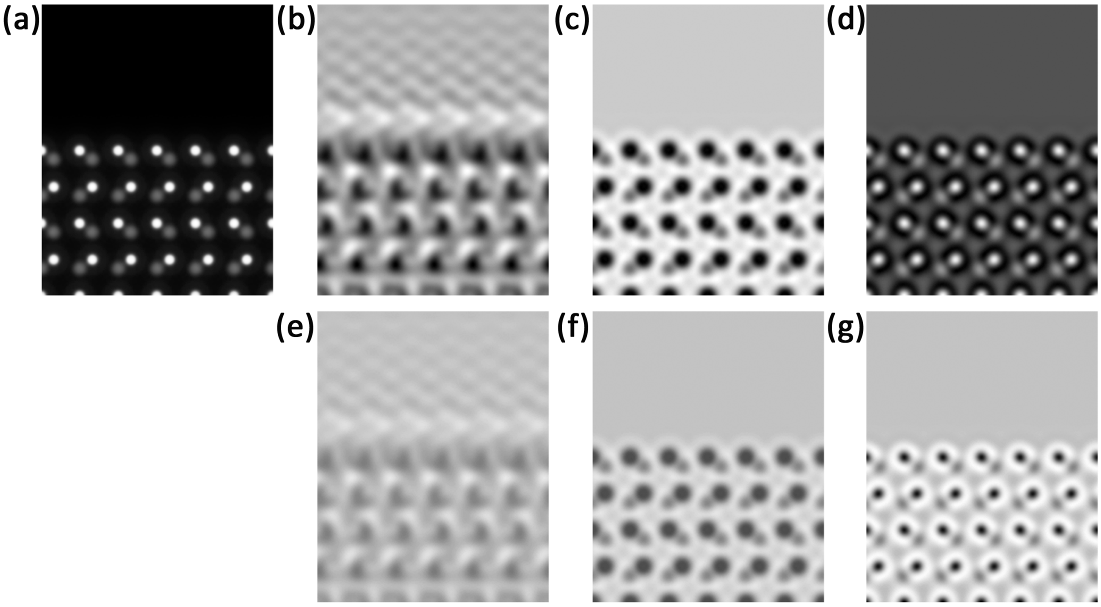

Figure 2.6.: Effect of aberration correction on HRTEM imaging for the example of a GaN crystal with a Ga-terminated (0001) surface: (a) projected potential along the $\left[11\bar{2}0\right]$ direction (Ga atomic columns appear brighter than N atomic columns). (b) and (e) HRTEM multislice simulation[10] for a conventional microscope with $C_S = 0.64\ mm$ and Scherzer defocus $\Delta f = -43\ nm$. (c) and (f) HRTEM simulation for an aberration corrected microscope with $C_S = 15\ \mu m$ and Scherzer defocus $\Delta f = -6.5\ nm$. (d) and (g) HRTEM simulation for an aberration corrected microscope with $C_S = -15\ \mu m$ and Scherzer defocus $\Delta f = +6.5\ nm$. Note that the intensity scale in image (g) has been inverted relative to that of image (d). Images in the lower row have been displayed on the same intensity scale (adjusted to that of image (g)) to illustrate the differences in image contrast.

Fig. 2.6 (b) for a conventional TEM and Fig. 2.6 (c) for a corrected objective lens with a small residual positive C_S). In contrast to that, for thin specimens atomic columns will show up bright with respect to the mean intensity if a small negative spherical aberration in combination with a slight overfocus is used [67] (see Fig. 2.6 (d)). The main advantage of NCSI is, however, the strong increase of the absolute contrast of atomic columns compared to the case of HRTEM imaging with a positive C_S [67]. This effect is illustrated in the lower row of Fig. 2.6. To understand this phenomenon, one has to consider next to the linear also non-linear contributions to the image formation process. In the case of HRTEM imaging with a positive/negative spherical aberration and Scherzer defocus, i.e. a proper underfocus/overfocus, the objective lens adds to the scattered waves a phase shift of approximately $\mp\frac{\pi}{2}$, respectively, so that the electron wave function in the image plane is given by

---

[10] HRTEM image simulations have been performed with a self developed software using a multislice approach [64, 65]. The phase plates and Fresnel propagator have been calculated with the EMS program package [66].

$$\Psi_{image}(x,y) = 1 \mp \sigma V_t(x,y)\,. \tag{2.29}$$

Including next to the linear also the second order contributions the image intensity leads to [62]

$$I(x,y) = 1 \mp 2\sigma V_t(x,y) + (\sigma V_t(x,y))^2\,. \tag{2.30}$$

While the sign of the second order term is always positive it depends for the linear term on the chosen imaging conditions. For a negative spherical aberration and positive Scherzer defocus (i.e. overfocus) the phase shift due to the objective lens amounts to $+\frac{\pi}{2}$, which leads to a constructively addition of linear and second order contributions and therefore to an increased contrast of atomic columns [62]. As shown by Jia et al. [62, 63], the negative C_S imaging technique thus significantly improves the detection limit of atoms.

2.3.3. Diffraction contrast imaging

Another TEM technique for structural characterisation of the specimen is diffraction contrast imaging. In this case only one beam in the back focal plane of the objective lens is selected with the objective aperture. Depending on whether one selects the transmitted or the diffracted beam in the objective aperture, i.e. a beam with wave vector $\vec{k_0}$ or $\vec{k_g}$ passes the aperture, either a bright field or dark field image is formed (see Fig. 2.7). To obtain strong diffraction contrast, the specimen is typically tilted relatively to the incident electron beam in such a way that in the ideal case only one set of lattice planes is in Bragg condition (typically called two beam condition).

Any lattice defect causing locally a bending of the respective lattice planes used for imaging will therefore affect the diffraction condition and thus the intensity of the diffracted beam. This will finally manifest in a contrast in the image around the lattice defect. Since dislocations induce distortions to the crystal lattice one can visualise them in the specimen by performing diffraction contrast imaging. Comparing several images, which have been recorded with different diffracted beams, one can furthermore determine also the Burgers-vector of dislocations. Therefore, one has to find lattice planes, for which the respective diffraction vectors $\vec{g}$ are perpendicular to the Burgers-vector of the dislocation (this is called the $\vec{g} \cdot \vec{b} = 0$ criterion). For this condition dislocation lines are out of contrast in the image. This is because the corresponding lattice planes are not affected by the strain field of the dislocations. Note that for dislocations having an edge component there will be still a weak residual contrast if $\vec{g} \cdot \vec{b} = 0$ but $\vec{g} \cdot \left(\vec{b} \times \vec{l}\right) \neq 0$, where $\vec{l}$ is the line direction of the dislocation. Latter condition corresponds to the local buckling in the vicinity of the dislocation core of those lattice planes, which are perpendicular to the inserted half-plane and include the dislocation line.

Under regular bright field / dark field conditions not only the strongly bended region around the dislocation core but also the long ranged strain fields around dislocations significantly affect the intensity of the un-/diffracted beam. Therefore, the contrast of a dislocation is rather blurred and extends up to several 10 *nm* under such imaging

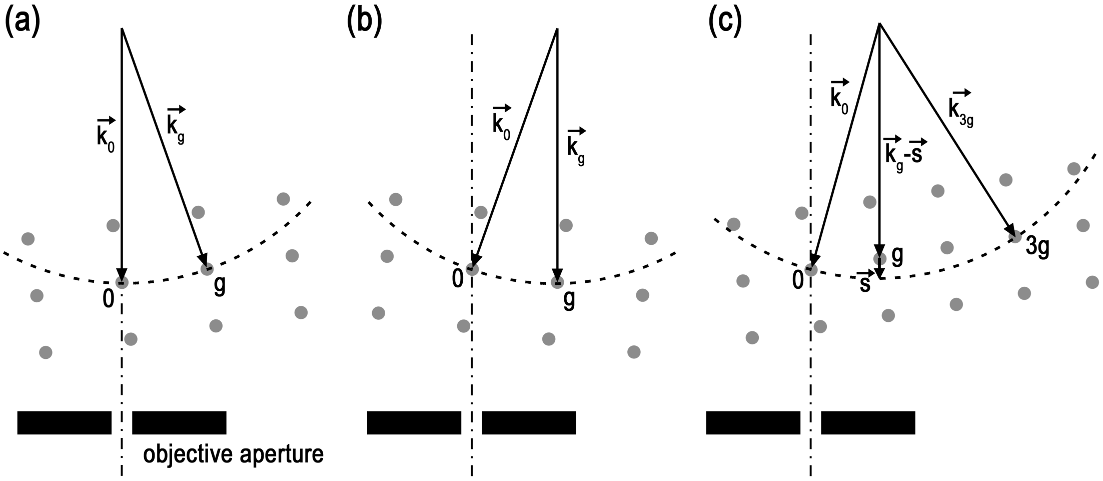

Figure 2.7.: Schematic representation of diffraction contrast imaging. Grey spheres denote the reciprocal lattice with its origin being labeled with "0". Black arrows indicate the wave vectors of the incident $\left(\vec{k}_0\right)$ and diffracted beam $\left(\vec{k}_g\right)$, respectively. The dashed and dashed-dotted black lines are the Ewald sphere and the optical axis of the microscope, respectively. (a) Bright field TEM under two beam conditions with the reflex **g** being in Bragg condition (i.e. it is cut by the Ewald sphere). (b) Dark field TEM under two beam conditions (with the reflex **g** being in Bragg condition) and tilted incident beam. (c) Weak beam dark field TEM under **g-3g** weak beam conditions (with the reflex **3g** being in Bragg condition while the **g** reflex is not cut be the Ewald sphere and a small deviation parameter $\vec{\mathbf{s}}$ exists) and tilted incident beam.

conditions. To obtain a more localised contrast, one can select with the objective aperture a diffracted beam for imaging, for which the corresponding lattice planes are not exactly in Bragg condition (this corresponds in the Fourier-space to a certain distance between the Ewald sphere and the respective reciprocal lattice spot, which is given by the so called deviation parameter $\vec{\mathbf{s}}$ (see Fig. 2.7 (c)). Because in this case the diffracted beam has only little intensity this method is called weak beam dark field imaging. It was shown by Cockayne et al. [68], that imaging with a large deviation parameter results in very localised contrast closely around the dislocation (in the range of a few nanometer).

2.3.4. STEM-HAADF imaging

The principle of image formation in a scanning transmission electron microscope (STEM) is fundamentally different from that of the TEM techniques mentioned above. In STEM mode a convergent focussed electron beam, or probe, is formed, which is scanned across the specimen (see Fig. 2.8). In STEM mode an image of the scanned specimen area is built up by sequentially collecting with an appropriate detector for

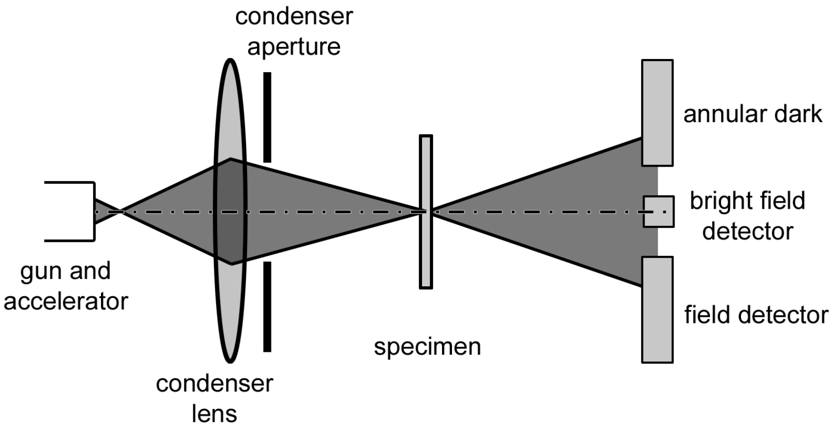

Figure 2.8.: Schematic representation of the image formation process in a STEM. The horizontal dashed-dotted line denotes the optical axis of the microscope.

each scanning point a signal, generated by interaction of the focused electron beam with the sample. This signal could either be due to primary electrons, scattered into low angles with respect to the optic axis (bright field imaging) [55], or electrons being scattered into higher angles (dark field imaging). In addition a secondary signal, excited through inelastic interaction, such as the intensity of secondary electrons, X-ray (EDXS) or other lower energetic photons (cathodoluminescence) can be detected. One of the advantage of STEM is that these signals can be detected simultaneously, using e.g. a concentric bright field and annular dark field detector and an energy dispersive X-ray (EDX) spectrometer, respectively.

One of the most commonly used STEM techniques is high angle annular dark field imaging (STEM-HAADF). In this case an annular detector is used, which collects only electrons scattered into higher angles (inner semi-acceptance angle of the detector amounts typically to several 10 *mrad* for a 300 kV STEM). As pointed out by Howie [69], the amplitude of coherently (Bragg) scattered electrons becomes weak for high scattering angles and the HAADF signal is then dominated by thermal diffuse scattering (TDS). The origin of TDS is vibration of atoms (known as phonons) around their equilibrium positions in the crystal lattice leading to a perturbation of the instantaneous crystal potential $V(\vec{r},t)$ according to

$$V(\vec{r},t) = V_0(\vec{r}) + \Delta V(\vec{r},t)\,. \tag{2.31}$$

In eq. (2.31) the first term represents the time averaged crystal potential causing the Bragg reflections. The second term is the perturbation due to thermal vibrations. As shown by Wang and Cowley [70, 71], ΔV is considerably narrower than V_0 meaning that TDS is a highly localised scattering process. Consequently, HAADF imaging is capable of displaying individual atomic columns [71]. Because the perturbation ΔV is not necessarily periodic, diffuse scattering of electrons leads to intensity in the Fourier space also between Bragg reflections [70]. According to Hall and Hirsch [72] the TDS intensity is given by

$$I^{TDS}(s) = \left(f^{e}(s)\right)^{2}\left[1 - \exp\left(-2M(s)\right)\right], \tag{2.32}$$

where $M(s)$ is the Debye-Waller-factor

$$M(s) = 2\pi^{2}s^{2}\overline{u}^{2}, \tag{2.33}$$

$\overline{u}^{2}$ is the temperature dependent mean square displacement of the respective atom and s is the scattering parameter, which is related to the scattering angle θ by $s = \frac{\sin\theta/2}{\lambda}$. In eq. (2.32) $f^{e}(s)$ denotes the atomic scattering factor for electrons, which is given by [73]

$$f^{e}(s) = \frac{m_0 e^2}{8\pi\varepsilon_0 h^2}\frac{Z - f^{x}(s)}{s^2} \approx \frac{m_0 e^2}{8\pi\varepsilon_0 h^2}\frac{Z}{s^2} \text{ for large } s, \tag{2.34}$$

where m_0 is the electron mass, e is the elementary charge, ε_0 is the vacuum permittivity, h is the Planck constant, Z the atomic number of the specimen material and $f^{x}(s)$ is the atomic scattering factor for X-rays.

What makes HAADF technique so valuable for structural analysis is the fact that HAADF images show, as can be inferred from eq. (2.32) and (2.34), a strong atomic number contrast. Atomic columns with a higher mean atomic number thus appear in most cases brighter than those with a lower mean atomic number. Due to the high inner acceptance angle of the HAADF detector, Bragg scattered electrons are not registered and diffraction contrast is typically suppressed. Therefore, this method is also called STEM Z-contrast. However, the image intensity of individual atomic columns does not simply scale with their atomic number squared (Z^2, corresponding to unscreened Rutherford scattering) but depends also on the strength of atomic vibrations (i.e. the Debye-Waller-factor, see eq. (2.32)) [70] and on the electron channelling behaviour[11]. Consequently, any lattice distortion which influences electron channelling, will also affect the HAADF intensity and thus complicate composition analysis. This phenomenon will become particularly pronounced if the specimen is observed along a low index zone axis where the effect of electron channelling is typically strong. The reason for this is that lattice distortions like e.g. static atomic displacements in alloys [75, 76, 77], strain gradients around dislocations [75, 78] or at the surface of the TEM specimen in regions of strained heterostructure interfaces [75, 79] disturb the periodicity of the lattice and therefore may, on the one side, give rise to additional diffuse scattering [80] and, on the other side, cause dechannelling which reduces the scattering probability [75]. A simple quantitative analysis of HAADF images is thus in many cases not possible and a precise quantitative composition evaluation requires a comparison with image simulations.

Another advantage of STEM-HAADF imaging is that it is supposed to be incoherent. The image intensity at any probe position $\vec{r}$ can therefore be expressed by

---

[11] In STEM electron channelling describes the effect that the electron beam is self-focussed onto an atomic column as the electrons propagates through the crystal. Electrons focussed onto atomic columns pass closer to atomic nuclei and thus have an increased probability for high angle scattering [74].

$$I_{HAADF}\left(\vec{r}\right) = P\left(\vec{r}\right) \otimes O\left(\vec{r}\right), \tag{2.35}$$

which is a convolution of the probe intensity $P\left(\vec{r}\right)$ and the object function $O\left(\vec{r}\right)$. This implies that, unlike as in the case of HRTEM, there are no contrast reversals with defocus and the STEM-HAADF image intensity increases monotonically with the specimen thickness. The incoherent nature of HAADF images can be explained in principle by the incoherent thermal diffuse scattering process itself [70]. However, incoherent scattering is not a necessary prerequisite for incoherent imaging [81, 82]. It was shown that even for coherent dynamical scattering from a hypothetical non-vibrating lattice (i.e. no TDS), annular dark-field imaging in a scanning transmission electron microscope provides an incoherent image of the crystal structure [81]. Thus the signal detection process, namely the integration of the scattered intensity by the HAADF detector over a large interval in k-space/Fourier-space, ensures the incoherent nature of STEM-HAADF images [55, 71, 81, 83]. This phenomenon can be understood by employing the principle of reciprocity[12]. A large detector in STEM mode is equivalent to a conical - and thus incoherent - illumination source in a TEM [81, 83, 85]. A detailed theoretical consideration of this problem is given e.g. in Ref. [55].

Let us finally consider the spatial resolution, which we can achieve in STEM-HAADF experiments. Looking on eq. (2.35) one can see that the probe intensity $P\left(\vec{r}\right)$ has the role of a point spread function, i.e. it corresponds to the response of the imaging system to a point object. The probe intensity is given by the inverse Fourier transform of the autocorrelation of the condenser system transfer function $T\left(q\right) = A\left(q\right) \cdot \exp\left(i\chi\left(q\right)\right)$:

$$P\left(\vec{r}\right) = \mathscr{F}^{-1}\left\{\int T\left(q\right) T^{*}\left(q+q'\right) dq\right\}. \tag{2.36}$$

The aperture function $A\left(q\right)$ (here the condenser aperture) and aberration function $\chi\left(q\right)$ are defined as before in eq. (2.16) and (2.17). From eq. (2.35) and (2.36) one can conclude that the spatial resolution in STEM-HAADF imaging is limited by the opening angle of the aperture and the aberrations of the probe forming lens. For optimum conditions [86] we obtain for a 300 kV STEM and a spherical aberration of the probe forming lens of $C_S = 1.2\,mm$ (as it is the case for the microscope used in this work) a spatial resolution of 1.3 Å.

2.3.5. Experimental setup

(S)TEM measurements have been performed with an FEI Titan 80-300 operated at an acceleration voltage of 300 kV ($\lambda = 1.97\,pm$). The microscope is equipped with an aberration corrector for the objective lens and a field emission gun (FEG) as electron source. The information limit of our microscope is approximately $12.5\,nm^{-1}$, thus we are able to resolve details with a spacing of about 0.8 Å. Images have been recorded with an Eagle 2k HR charge coupled device (CCD) camera, which has 2048×2048 pixels and achieves a sampling of $17.1\ \frac{pm}{pixel}$ at the highest used magnification. The modulation transfer function of the CCD camera has been determined according to the method suggested by Van den Broek et al. [87] and amounts to approximately 0.25 at half of the Nyquist frequency.

---

[12] Consider the following situation. A wave I is emitted from a source located in point A, then scattered at a point S and arrives at point B. The principle of reciprocity states that if the source is moved to point B and emits a wave II which is also scattered in point S then the amplitude of wave II in point A will be equal to the amplitude of wave I in point B [84].

For HRTEM imaging we tune with the help of the corrector the spherical aberration of the objective lens typically to a small negative value of about $C_S \approx -15\ \mu m$. Other lens aberrations have been corrected to a minimum. In TEM mode a parallel beam with a semi-convergence of smaller than approximately $\alpha \leq 0.4\ mrad$ and a beam current in the range of $100\ pA - 1\ nA$[13] has been used. STEM imaging has been performed with a focussed, convergent beam with a semi-convergence angle of $\alpha = 9.0\ mrad$. The spherical aberration parameter of the probe forming lens is approximately $C_S = 1.2\ mm$, which limits the spatial resolution to a value of about 1.3 Å (in the experiment it is possible to resolve the well known dumbbell structure in the $[110]$ projection of silicon, which has a spacing of 1.36 Å). Typically we have a probe current in the range of $1 - 2\ pA$. STEM-HAADF images have been recorded with a Fishione model 3000 annular detector (16 bit dynamical range) with a typical dwell time of approximately $50\ \mu s$ per scanning point.

2.4. X-ray diffraction

Ex-situ X-ray diffraction (XRD) has been used in this work to evaluate the strain state of the GaN films and $Al_xGa_{1-x}N$ interlayers after the growth at room temperature on a macroscopic scale. For this purpose we have, on the one hand, performed symmetric $\theta/2\theta$-scans of the (0002) and (0006) reflection. On the other hand, we have also acquired reciprocal space maps around the asymmetric $\left(11\bar{2}4\right)$ reflection. Latter technique has the advantage that by scanning the reciprocal space in two dimension around a reflection, which has an in-plane and an out-of plane scattering component, it is possible to determine both the in-plane and out-of-plane reciprocal lattice parameter q_x and q_z. A schematic representation of both measurement techniques is shown in Fig. 2.9.

The basic principle of kinematic X-ray diffraction at crystalline specimens can be described by coherent elastic scattering (for more details see appendix A). The main result is that an X-ray beam will be diffracted at a crystal lattice only if the Bragg condition is satisfied:

$$2d_{hkl} \sin\theta = n\lambda, \tag{2.37}$$

where d_{hkl} is the interplanar spacing of the diffracting lattice planes, θ is the angle between the incident/diffracted beam and the diffracting lattice planes and λ is the wavelength of the X-rays.

---

[13] This current leads for HRTEM imaging where an area of typically $100 \times 100\ nm^2$ is illuminated by the beam to a current density of less than $10\ \frac{A}{cm^2}$. According to literature reports [88] for such a current density GaN and III-nitride heterostructures are at least for a typical timeframe of image recording (a few seconds to one minute) stable under the electron beam before beam damage can be observed.

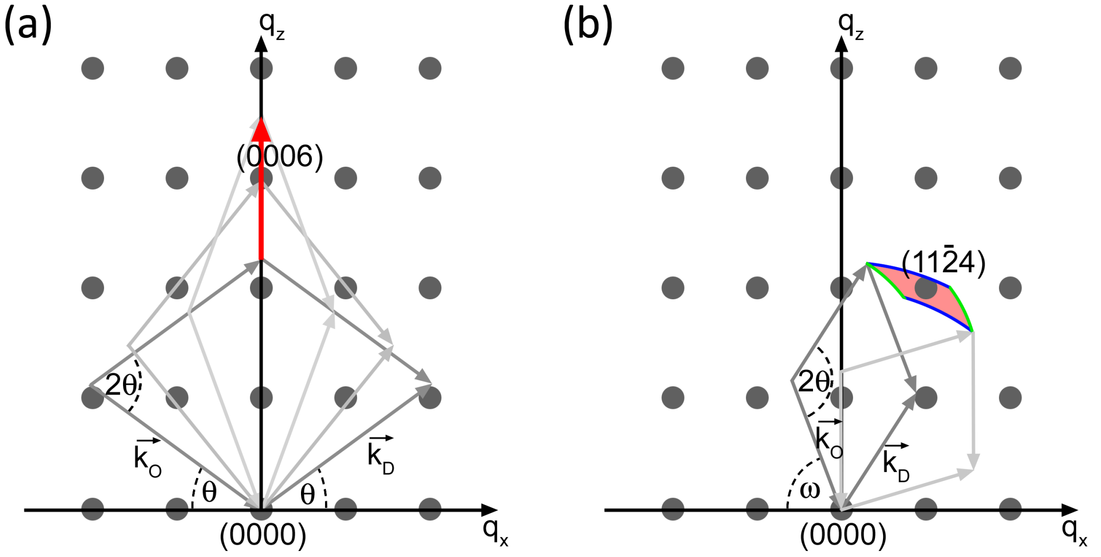
(a)
q_z
(0006)
2θ
$\vec{k}_O$
θ
θ
$\vec{k}_D$
(0000)
q_x
(b)
q_z
$(11\bar{2}4)$
2θ
$\vec{k}_O$
$\vec{k}_D$
ω
(0000)
q_x

Figure 2.9.: Schematic representation of (a) a $\theta/2\theta$-scan around the (0006) reflection and (b) a reciprocal space map around the asymmetric $\left(11\bar{2}4\right)$ reflection. Grey spheres and arrows represent reciprocal lattice points and wave vectors of incident/diffracted beam $\left(\vec{k_{0/D}}\right)$. The red arrow indicates the $\theta/2\theta$-scan. Blue/green curves denote the direction of an ω- / $\theta/2\theta$-scan, respectively. The red shaded area corresponds to the acquired reciprocal space map.

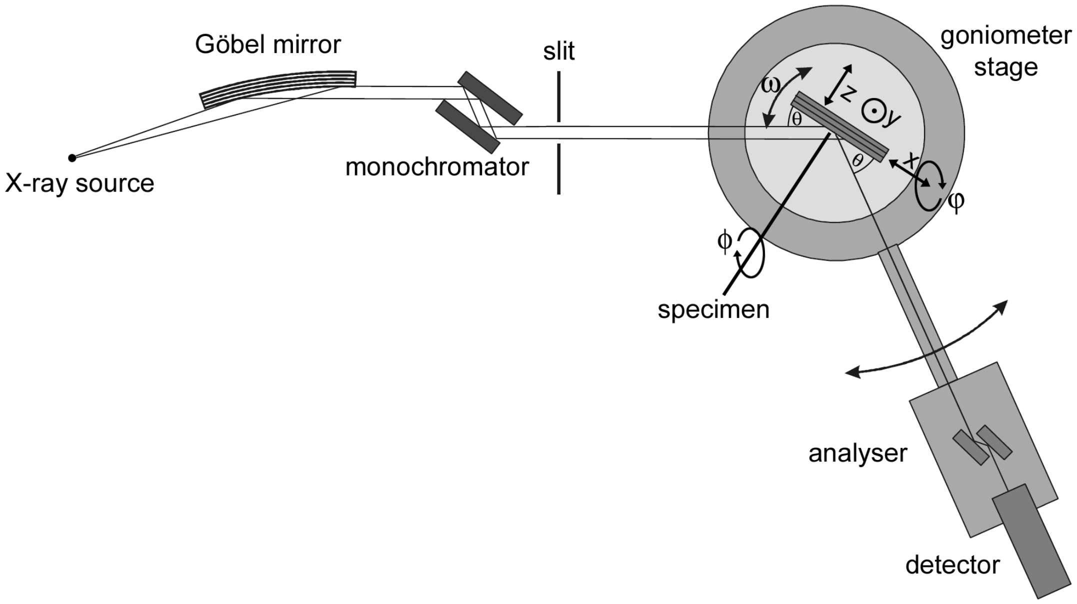
Göbel mirror
X-ray source
monochromator
slit
goniometer stage
ω
z
y
θ
θ
x
φ
ϕ
specimen
analyser
detector

Figure 2.10.: Schematic representation of the experimental setup for the X-ray diffraction experiments.

The basic set-up of the XRD experiment is schematically depicted in Fig. 2.10. The XRD measurements have been performed with a Seifert XRD Master HR diffractometer using a copper anode to generate the X-rays. A Göbel mirror (bowed multilayer stack with a lateral layer thickness gradient) and a two-bounce channel cut monochromator consisting of two Ge (220) crystals then collimate (the residual beam divergence is approximately 0.005°) and monochromate the beam (Cu-Kα_1 radiation with a wavelength of $\lambda = 1.540593$ Å has been selected). A slit can be introduced into the beam to limit the size of the X-ray spot on the specimen. The specimen itself is mounted on a goniometer stage which allows movement along x-, y- and z-directions and a ω-, ϕ- and φ- tilt (see Fig. 2.10). For high resolution X-ray diffraction (HRXRD) measurements the angular resolution of the diffractometer can be enhanced by placing either an analyser crystal or an aperture just before the detector (angular resolution in our experiment was about 0.006°). In case of X-ray reciprocal space maps we utilised a position sensitive line detector which simultaneously records a 5.9° wide 2θ-range with an accuracy of approximately 0.01° per channel.

2.5. In-situ laser reflectometry

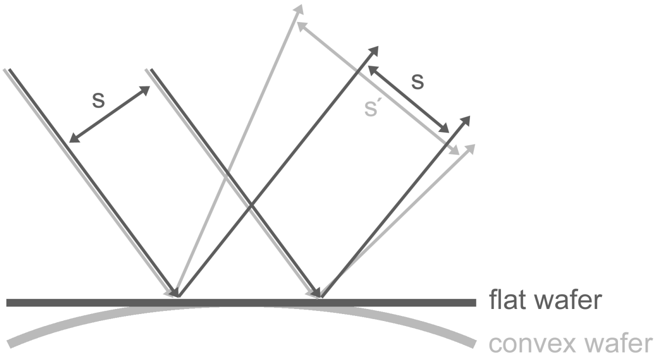

Figure 2.11.: Schematic representation of the wafer curvature measurement by in-situ laser reflectometry.

Another method to determine the strain state of an epitaxial film at a macroscopic scale is in-situ laser reflectometry. In contrast to ex-situ XRD this technique provides complementary in-situ information about the strain state of the film during the growth. The operating principle is rather simple (see schematic representation in Fig. 2.11). Basically, one monitors the wafer curvature κ as a function of the growth time by analysing the spacing s of two (or more) laser beams reflected at the growth surface of the sample. Because the initially parallel incident laser beams are shifted relative to each other, a change of the wafer curvature will directly translate into a change of the spacing of the reflected beams. Based on the geometry of the system, the wafer curvature can be calculated from the spacing s. If Fabry-Perot oscillations occur, one can additionally evaluate the thickness and thus the growth rate of the film at any time of the growth. Using the well-known Stoney equation [89] the film strain ε is calculated according to

$$\kappa = 6\frac{M_f}{M_s}\frac{t_f}{t_s^2}\varepsilon \ , \tag{2.38}$$

where $M_{f,s}$ and $t_{f,s}$ are the biaxial modulus and the thickness of the film and the substrate, respectively. A change of the slope $\frac{\partial\kappa}{\partial t_f}$ thus can be interpreted as a change of the film strain ε, e.g. due to a build-up of compressive strain in the GaN film by an $\mathrm{Al_xGa_{1\text{-}x}N}$ interlayer. However, in order that the Stoney equation can be applied several requirements have to be satisfied [90]: (i) Both the film and substrate thicknesses have to be small compared to their lateral dimensions, i.e. plane stress conditions apply. (ii) The film has to be much thinner than the substrate (approximately 100 times thinner). (iii) The substrate material is homogeneous, isotropic and linearly elastic. The film material is isotropic. (iv) Edge effects near the rim of the substrate can be neglected and (v) the strains and rotations are infinitesimally small. In our case all requirements are met.

3. Strain-engineering with $Al_xGa_{1-x}N$ interlayer - build-up of compressive strain

3.1. Aim of this chapter

The main objective of this chapter is to explain the build-up of compressive strain in GaN films by $Al_xGa_{1-x}N$ interlayers on a purely phenomenological basis. For this purpose we study a series of samples where $Al_xGa_{1-x}N$ interlayers of different thickness and deposition temperature have been grown on GaN buffers on Si, sapphire and GaN substrates. The aim is to investigate, how the resulting compressive strain in the top GaN layer depends on (i) the growth parameters of the $Al_xGa_{1-x}N$ interlayer (thickness and deposition temperature) and by (ii) the thermal stress arising during cool-down after the growth.

In a first step we will examine the microstructure of $Al_xGa_{1-x}N$ interlayers with the help of TEM. In particular, we will analyse the misfit dislocation networks at the interfaces between the GaN layers and the $Al_xGa_{1-x}N$ interlayer in detail in terms of the average line spacing of misfit dislocations, their Burgers-vector and the geometry of the misfit dislocations networks. Later we will use this data to quantify the degree of strain relaxation at the interfaces of the $Al_xGa_{1-x}N$ interlayer. In a second step we will evaluate ex-situ X-ray diffraction and in-situ wafer curvature measurements to validate the significance of our TEM results, gained at a more microscopic scale, by strain measurements at macroscopic scale.

3.2. Experimental results

3.2.1. Structural characterisation of $Al_xGa_{1-x}N$ interlayer by TEM

3.2.1.1. Influence of thickness and deposition temperature of $Al_xGa_{1-x}N$ interlayers on the strain relaxation process

In a first experiment we study plastic relaxation of thin $Al_xGa_{1-x}N$ interlayers as dependent on layer thickness. The $Al_xGa_{1-x}N$ layers are grown at low deposition temperature ($\approx$ 800°C) and high deposition temperature ($\approx$ 1050°C), respectively, on top of thick GaN buffers on Si (111) substrates and are subsequently covered by a GaN overlayer. We will start with a purely qualitative analysis of the relaxation process.

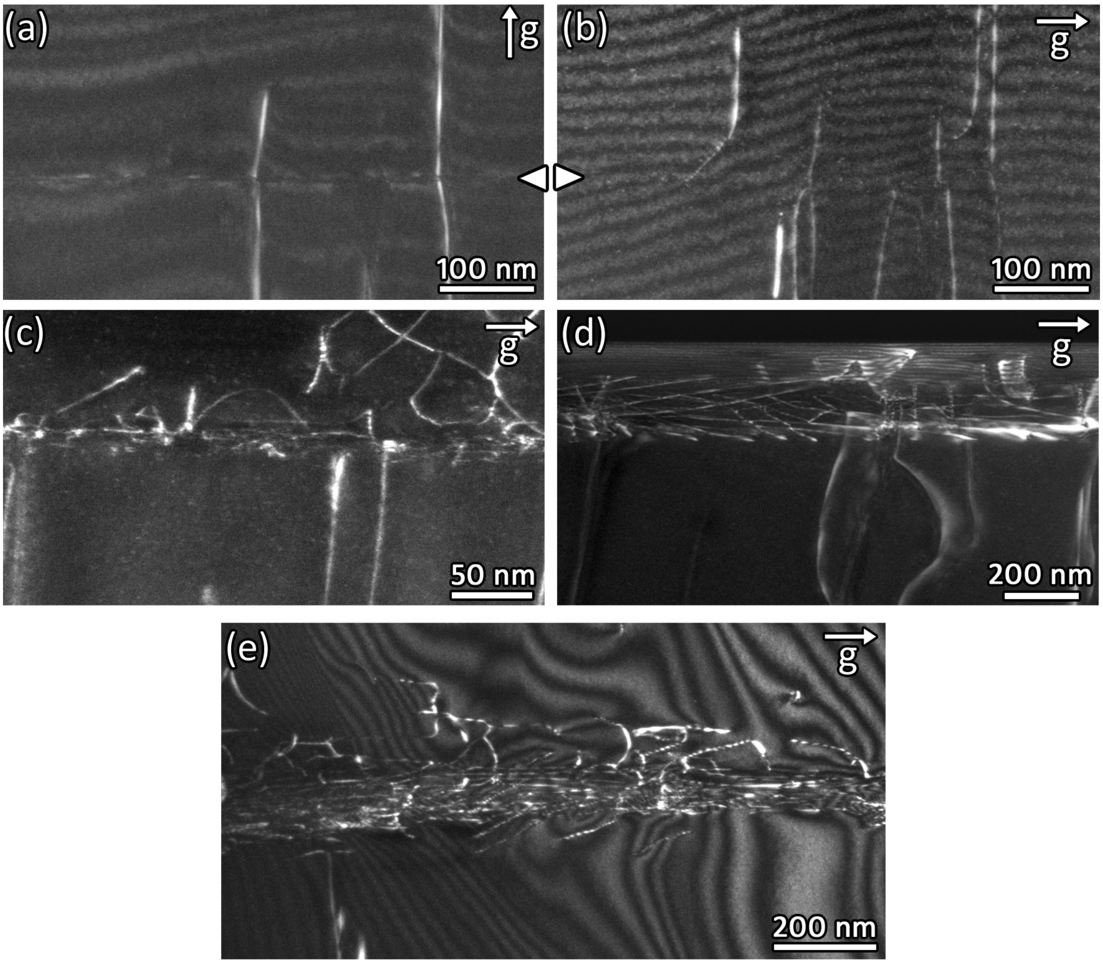

Figure 3.1.: Cross-sectional weak beam dark field TEM micrographs of $Al_xGa_{1-x}N$ interlayers in GaN films grown on Si (111) substrates. The images are recorded under (a) $\mathbf{g} = 0002$ and (b)-(e) $\mathbf{g} = \bar{1}100$ $\mathbf{g(3g)}$ weak beam conditions, respectively. (a) and (b) same region of a 5 *nm* thin low temperature $Al_{0.65}Ga_{0.35}N$ interlayer, (c) 10 *nm* thin low temperature $Al_{0.75}Ga_{0.25}N$ interlayer, (d) 26 *nm* thick low temperature $Al_{0.75}Ga_{0.25}N$ interlayer between GaN buffer and a 120 *nm* GaN cap and (e) 35 *nm* thick high temperature $Al_{0.75}Ga_{0.25}N$ interlayer. In (a) and (b) the position of the 5 *nm* thin low temperature $Al_{0.65}Ga_{0.35}N$ interlayer is indicated by white triangles.

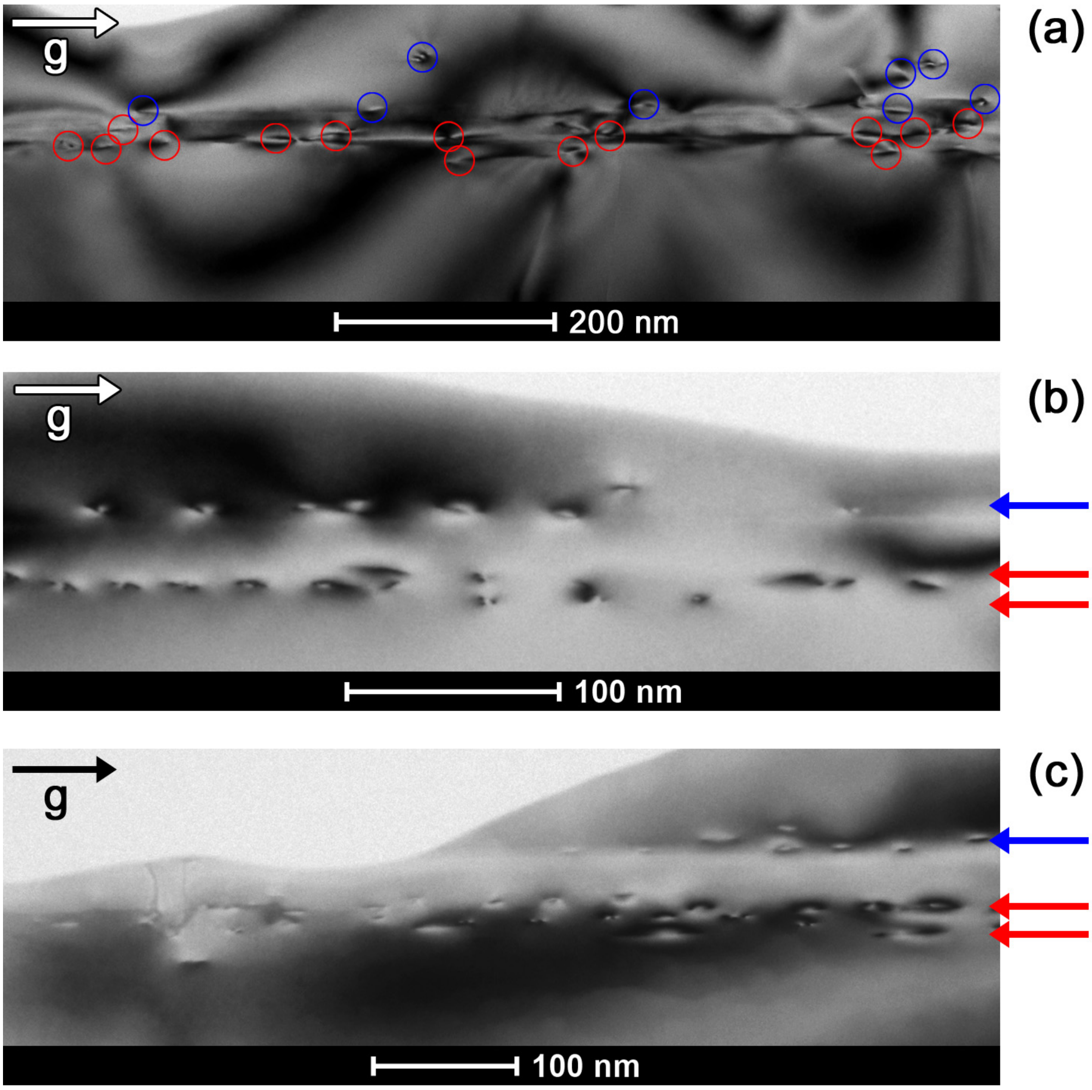

Figure 3.2.: Cross-sectional bright field TEM images for two beam conditions of $Al_xGa_{1-x}N$ interlayer in GaN films grown on Si (111) substrates. (a) 18 *nm* low temperature $Al_{0.75}Ga_{0.25}N$ interlayer, (b) 26 *nm* low temperature $Al_{0.75}Ga_{0.25}N$ interlayer and (c) 35 *nm* high temperature $Al_{0.75}Ga_{0.25}N$ interlayer, respectively. Misfit dislocations at the lower and upper interface of $Al_xGa_{1-x}N$ interlayers are indicated by red and blue arrows and circles, respectively.

The cross-sectional weak beam dark field TEM image of a 5 *nm* thin low temperature $Al_{0.65}Ga_{0.35}N$ interlayer[1] recorded under $\mathbf{g} = 0002$ $\mathbf{g}(3\mathbf{g})$ weak beam conditions (Fig. 3.1 (a)) shows only a weak diffuse contrast at the $Al_{0.65}Ga_{0.35}N$ interlayer due to fluctuating strain. Imaging with $\mathbf{g} = \bar{1}100$ $\mathbf{g}(3\mathbf{g})$ weak beam conditions (Fig. 3.1 (b)), however, reveals no misfit dislocations at the interfaces of the $Al_{0.65}Ga_{0.35}N$ interlayer to the surrounding GaN, but a-type and a+c-type threading dislocations penetrating it. In the case of a sample with a 10 *nm* thin $Al_{0.75}Ga_{0.25}N$ interlayer grown at low temperature, few misfit dislocations are observed at the interfaces of the interlayer (see Fig. 3.1 (c)). At a thickness of the low temperature $Al_{0.75}Ga_{0.25}N$ interlayer of 26 *nm*, a network of misfit dislocations is present at the interface between interlayer and GaN (Fig. 3.1 (d)). To distinguish individual misfit dislocations of the dense network we tilt the TEM specimen by approximately 20° out of the $\left[11\bar{2}0\right]$ zone axis towards $[0001]$ so that the network is seen in oblique view. A similar dense network of misfit dislocations is also observed in the case of a 35 *nm* thick high temperature $Al_{0.75}Ga_{0.25}N$ interlayer (see Fig. 3.1 (e)). In this case the further increased density of misfit dislocations in the network does not allow to distinguish individual dislocation lines anymore.

Comparing the cross-sectional weak beam dark field TEM images of these samples, it is obvious that, on the one hand, the misfit dislocation network becomes denser with increasing thickness of the $Al_xGa_{1-x}N$ interlayer. On the other hand, we do not see qualitative differences between samples with low temperature or high temperature $Al_xGa_{1-x}N$ interlayer with respect to plastic relaxation at the interfaces of the $Al_xGa_{1-x}N$ interlayer.

To quantify our results we evaluate the projected line density of misfit dislocations at the interfaces of $Al_xGa_{1-x}N$ interlayers. Therefore, the same sample series has been studied by bright field imaging close to the $\left[1\bar{1}00\right]$ zone axis using a $\mathbf{g} = 11\bar{2}0$ diffraction vector. Under this condition all dislocations with an a-component are in contrast and appear by their projected line segment in the interface. Representative images are shown in Fig. 3.2 and statistically representative results[2] of the quantitative analysis are summarised in Table 3.1. The accuracy is mainly limited by the statistical uncertainty due to fluctuations of the dislocation spacings and is in the range of 10-15%.

First of all we find that $Al_xGa_{1-x}N$ interlayer ($x \geq 0.75$), which are thicker than approximately 10 *nm*, exhibit misfit dislocations at both interfaces of the $Al_xGa_{1-x}N$ interlayer. The quantitative analysis, however, reveals a systematic asymmetry in plastic relaxation between the two interfaces. The misfit dislocation line spacing is higher at the upper interface of the $Al_xGa_{1-x}N$ interlayer than at the lower one. The ratio of the misfit dislocation line spacings at the upper interfaces to that of the lower interface is typically in the range of 1.8...2.2. These results are found in all samples independently of the thickness of the $Al_xGa_{1-x}N$ interlayer. The absolute values of the spacings as seen qualitatively above, however, decrease as the thickness of the $Al_xGa_{1-x}N$ interlayer increases. All quantitatively analysed samples having an $Al_{0.75}Ga_{0.25}N$ interlayer, irrespective whether grown at low or high temperature, fit in the overall trend that the average spacing of misfit dislocation lines decreases with increasing thickness of the $Al_xGa_{1-x}N$ interlayer.

---

[1] The composition of $Al_xGa_{1-x}N$ interlayers has been quantitatively determined by combining several TEM methods (see details in appendix C).

[2] To obtain statistically significant results, we evaluated the misfit dislocation line spacings from cross-sectional bright field TEM images that cover a lateral field of view of several *µm* and thus include typically $50 - 150$ dislocations.

It is worth noting is that not all misfit dislocations are located exactly at the interfaces of the interlayer, but are spread vertically up to 50 *nm* around the interfaces. Especially at the lower interface of the $Al_xGa_{1-x}N$ interlayer the misfit dislocations tend to align vertically in 2 planes (indicated by 2 red arrows in Fig. 3.2).

3.2.1.2. Influence of the thermal stress during cool-down on the strain relaxation process

In the following we study the possible influence of thermally induced strain, arising during cool down, on the relaxation of the $Al_xGa_{1-x}N$ interlayers. Therefore, we compare samples where GaN films with $Al_xGa_{1-x}N$ interlayers have been deposited on Si (111), sapphire (0001) and GaN (0001) substrates resulting in tensile, compressive and nominal no thermal stress, respectively.

Fig. 3.3 shows cross-sectional weak beam dark field TEM images of samples grown on sapphire (0001) and GaN (0001) substrates. For both samples we observe a network of misfit dislocations at the interfaces of the $Al_xGa_{1-x}N$ interlayer. Cross-sectional bright field TEM imaging of these samples (see Fig. 3.4) reveals, as in the case of samples grown on Si (111) substrates, the presence of misfit dislocations at both interfaces of the $Al_xGa_{1-x}N$ interlayer. The quantitative evaluation of the line spacings for both samples are given in Table 3.1. As in the previous samples on Si, the ratio of the misfit dislocation line spacing at the upper compared to that at the lower interface lies for all three samples between $1.8 \ldots 2.2$ and thus in the same range. Compared to the samples deposited on silicon, the sample with the 23 *nm* thin $Al_{0.75}Ga_{0.25}N$ interlayer grown on the sapphire substrate fits well into the trend of an decreasing dislocation spacing with increasing thickness of the $Al_xGa_{1-x}N$ interlayer. Though the thickest $Al_xGa_{1-x}N$ layer (grown on a GaN substrates) seems to make an exception, i.e. the misfit dislocation line spacings are larger for the thicker interlayer, this is explained by a lower Al content of the $Al_xGa_{1-x}N$ interlayer (approximately $x = 50\%$) than that of all other samples (typically $x = 75\%$).

In summary, our TEM results show that the thermal stress after the growth does not significantly influence the relaxation of $Al_xGa_{1-x}N$ interlayers. Misfit dislocation networks at the both interfaces of $Al_xGa_{1-x}N$ interlayers, however, with an asymmetry in the dislocation line spacing between the upper/lower interface, have been observed in all samples, irrespective of the used substrate (silicon, sapphire or GaN) and the respective thermally induced stress during cool-down, i.e. tensile, compressive or no thermal stress.

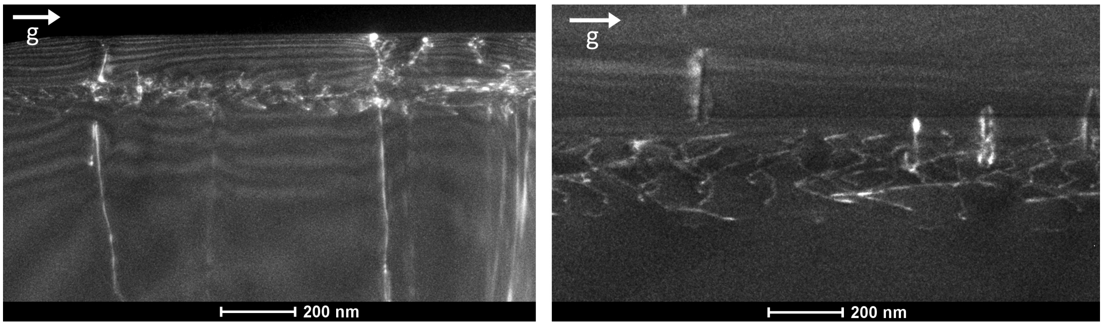

Figure 3.3.: Cross-sectional weak beam dark field TEM micrographs of (a) a 23 *nm* thick low temperature $Al_{0.75}Ga_{0.25}N$ interlayer between the GaN buffer and a 120 *nm* GaN cap grown on a sapphire (0001) substrate, (b) a 45 *nm* thick high temperature $Al_{0.5}Ga_{0.5}N$ interlayer in a GaN film grown on a GaN (0001) substrate. Both images have been recorded under $\mathbf{g} = \bar{1}100$ **g(3g)** weak beam conditions.

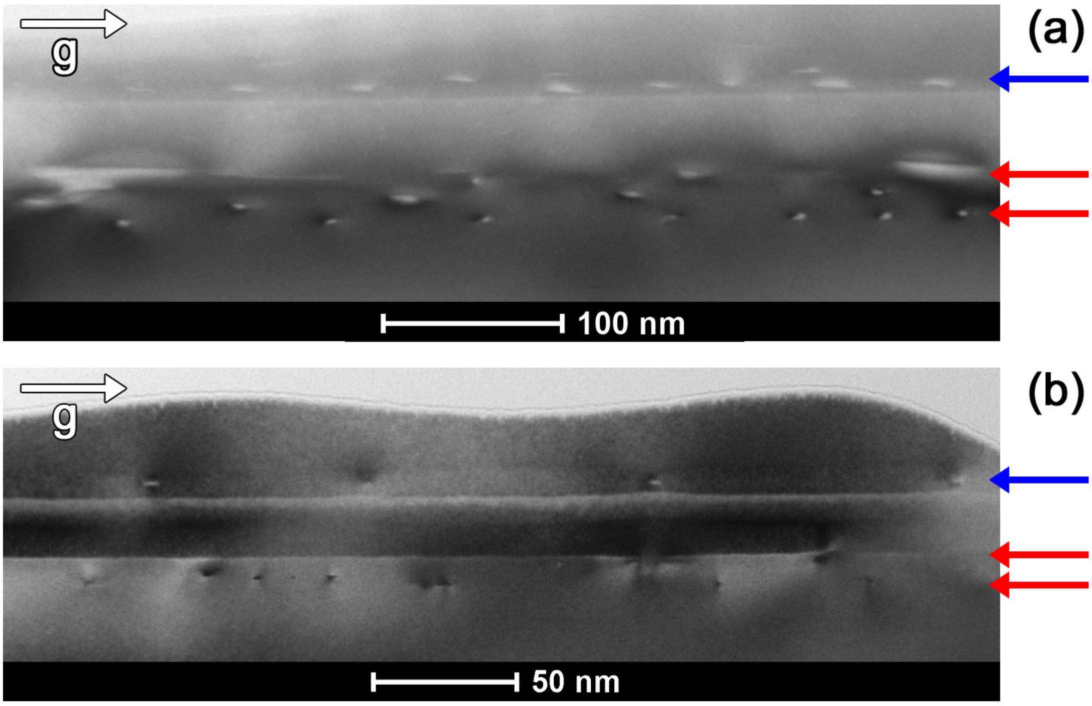

Figure 3.4.: Cross-sectional bright field TEM images for $\mathbf{g} = 11\bar{2}0$ two beam conditions of (a) a 23 *nm* thick low temperature $Al_{0.75}Ga_{0.25}N$ interlayer between the GaN buffer and a 120 *nm* GaN cap grown on a sapphire (0001) substrate, (b) a 45 *nm* thick high temperature $Al_{0.5}Ga_{0.5}N$ interlayer in a GaN film grown on a GaN (0001) substrates. Misfit dislocations at the lower and upper interface of the $Al_xGa_{1\text{-}x}N$ interlayer are indicated by red and blue arrows, respectively.

Table 3.1.: Average spacing of misfit dislocations at the interfaces of $Al_xGa_{1-x}N$ interlayer as determined from cross-sectional TEM images

sample	mean misfit dislocation line spacing lower interface $d_{image}^{lower\,IF}$ [nm]	 upper interface $d_{image}^{upper\,IF}$ [nm]
45 nm high temperature $Al_{0.50}Ga_{0.50}N$ interlayer in GaN film on GaN substrate	34 ± 4	61 ± 8
35 nm high temperature $Al_{0.75}Ga_{0.25}N$ interlayer in GaN film on Si substrate	21 ± 2	38 ± 5
26 nm low temperature $Al_{0.75}Ga_{0.25}N$ interlayer in GaN film on Si substrate	36 ± 5	73 ± 10
23 nm low temperature $Al_{0.75}Ga_{0.25}N$ interlayer in GaN film on sapphire substrate	45 ± 6	98 ± 15
18 nm low temperature $Al_{0.75}Ga_{0.25}N$ interlayer in GaN film on Si substrate	63 ± 8	121 ± 20

3.2.2. Analysis of the misfit dislocation networks

To quantify the amount of mismatch relaxation in the $Al_xGa_{1-x}N$ interlayer and the build-up of compressive strain in the subsequent GaN layer, we will now characterise the misfit dislocation networks at the interface between GaN buffer and $Al_xGa_{1-x}N$ interlayers in more detail. More specific, we aim to gather all necessary information about misfit dislocation networks, i.e. their lateral arrangement, their Burgers-vector and their line direction. To obtain unambiguous results, we use in addition to conventional diffraction contrast imaging in plan view TEM also cross-sectional aberration corrected HRTEM. To achieve statistical significance in our HRTEM investigation, we have typically analysed more than 20 dislocations for each sample. All samples considered in the following have been grown on Si (111) substrates.

3.2.2.1. Plan view TEM analysis

Fig. 3.5 shows plan view weak beam TEM images recorded under different excitation conditions of the same region of a sample with a 35 *nm* thick high temperature $Al_{0.75}Ga_{0.25}N$ interlayer, which has no GaN cap. Consequently, we see only the misfit dislocation network at the interface between the $Al_{0.75}Ga_{0.25}N$ layer and GaN buffer. A closer look reveals that the misfit dislocations can be grouped into two types of networks.

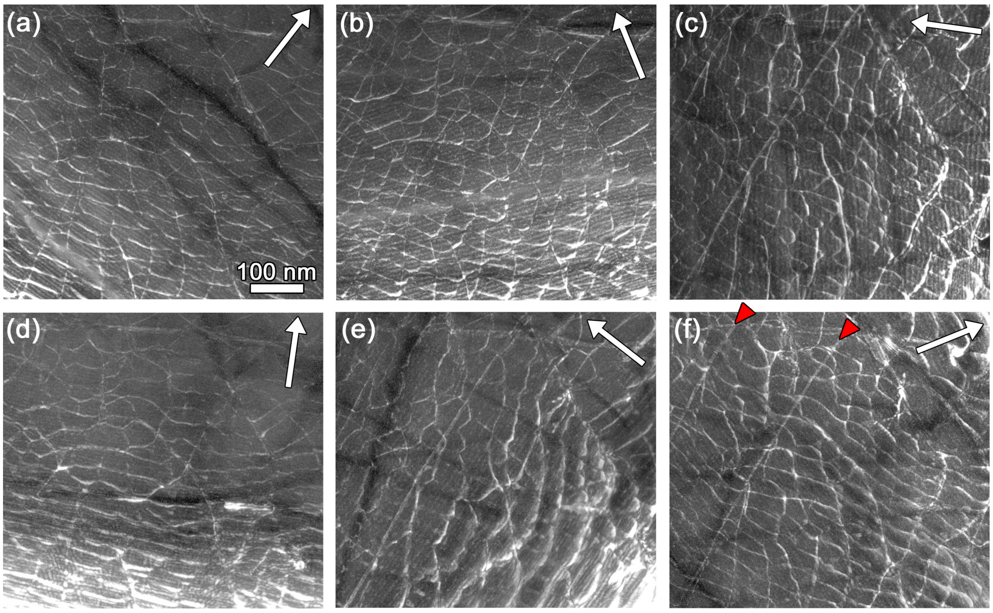

Figure 3.5.: Plan view weak beam dark field TEM analysis of the misfit dislocation network, which has formed at the interface between a 35 *nm* thick high temperature $Al_{0.75}Ga_{0.25}N$ interlayer and the GaN buffer underneath. The sample has no GaN capping. Images (a)-(f) depict all the same specimen area and have been recorded under (a) $\mathbf{g} = 11\bar{2}0$, (b) $\mathbf{g} = \bar{1}2\bar{1}0$, (c) $\mathbf{g} = \bar{2}110$, (d) $\mathbf{g} = 01\bar{1}0$, (e) $\mathbf{g} = \bar{1}100$ and (f) $\mathbf{g} = 10\bar{1}0$ **g(3g)** weak beam conditions. Red triangles in (f) indicate dislocations having straight line directions.

Misfit dislocation network type 1

The majority of misfit dislocations forms a dense network[3] with a spacing of dislocation lines in the range of 30-50 nm. The most distinctive feature of this type of network is, however, that their dislocation lines are bowed. A closer inspection of these dislocations in Fig. 3.6 (which is a magnified view of the centre of Fig. 3.5) shows that they appear as perfect as well as dissociated dislocations. Latter ones are split into 2 partial dislocations, which are typically separated by only a few nm. In some cases dissociated dislocations form stacking fault nodes whose lateral extension are about 20 nm. An example of such an extended stacking fault node is indicated by yellow triangles in Fig. 3.6.

The geometry and Burgers-vector of respective dislocation lines are schematically represented in Fig. 3.7 (a). Dislocation lines spanning the stacking fault node are each out of contrast for a different $\mathbf{g} = 11\bar{2}0$-type diffraction vector meaning that these three partial dislocations have a $\frac{1}{3} < 1\bar{1}00 >$ in-plane component in their Burgers-vector. Further away from the stacking fault node the dislocation lines are extinguished by a $\mathbf{g} = 1\bar{1}00$-type diffraction vector corresponding effectively to a $\frac{1}{3} < 11\bar{2}0 >$ in-plane component of the Burgers-vector. The individual lines of the dissociated dislocation also cannot be separated anymore. This can either be explained by the fact that (i) the partial dislocations are too close to each other so that the individual strain fields cannot be sufficiently resolved by weak beam imaging, or (ii) because the dislocations (in-plane components of them) are not dissociated anymore and merged again to a perfect dislocation according to

---

[3] Actually, the misfit dislocation networks are pseudo networks because, as we have seen from cross-section TEM before, not all misfit dislocations are located exactly at the interfaces of the interlayer, but are spread vertically around the interfaces. Thus, misfit dislocation lines intersecting each other in the projected plan view image do not necessarily lie in the same plane and cross each other. This has to be kept in mind. In terms of the amount of strain relaxation on a macroscopic scale, however, this makes no big difference. Therefore, in the following we will for simplicity describe the pseudo networks just as misfit dislocation networks.

$$\frac{1}{3}\left[10\bar{1}0\right] + \frac{1}{3}\left[01\bar{1}0\right] \to \frac{1}{3}\left[11\bar{2}0\right]. \tag{3.1}$$

On the other hand lines of perfect dislocations like those indicated by blue triangles in Fig. 3.6 (b) are each out of contrast for one of the three crystallographic equivalent in-plane $\mathbf{g} = 1\bar{1}00$-type vectors (e.g. the aforementioned dislocation line is not visible in Fig. 3.6 (e)). According to the $g \cdot b = 0$ extinction criterion this means that there are 3 arrays of perfect dislocations each having a $\frac{1}{3} < 11\bar{2}0 >$ in-plane component in their Burgers-vector (compare also the different images in Fig. 3.5). In order to determine if these dislocations have also a c-component (out-of-plane component), we have used dark field imaging with a $\mathbf{g} = 1\bar{1}01$ vector by tilting the specimen from the $< 0001 >$ zone axis by approximately 30° close to the $< 1\bar{1}02 >$ pole. Unfortunately, this analysis did not give unambiguous results (not shown here).

As the misfit dislocations of this type of network are not straight, one cannot specify a uniform angle between the dislocation line and the in-plane component of the Burgers-vector. For example, for the dislocation line indicated in Fig. 3.6 (b) by the blue triangle the angle changes along the dislocation line from the left to the right part of the image on a length scale of about 150 nm from approximately 30° over 90° back to 60°. Therefore, we consider the angle between dislocation line and Burgers-vector for this type of misfit dislocation network as a statistically distributed quantity and we find typically an average value of approximately 60° and a standard deviation of 15°.

Misfit dislocation network type 2

In addition, we observe a widely spaced trigonal network, formed of straight dislocations having $< 11\bar{2}0 >$ line directions (see dislocations indicated by red triangles in Fig. 3.5 (f)). Misfit dislocations of this type are always dissociated into two partial dislocations, which are separated by approximately $5 - 10\ nm$ (see dislocation indicated by red triangles in Fig. 3.6 (e)). Using different diffraction vectors we find the following behaviour: (i) Both partial dislocations are out of contrast simultaneously for one of the $\mathbf{g} = 1\bar{1}00$-type diffraction vectors (for the given example see Fig. 3.6 (d)). (ii) for the other two remaining $\mathbf{g} = 1\bar{1}00$-type vectors typically both partials are visible (Fig. 3.6 (e) and (f)). (iii) For one of the $\mathbf{g} = 11\bar{2}0$-type diffraction vectors both partial dislocations are in contrast (Fig. 3.6 (c)) while (iv) for the other two $\mathbf{g} = 11\bar{2}0$-type diffraction vectors one of the partial dislocation line is extinguished (Fig. 3.6 (a) and (b)).

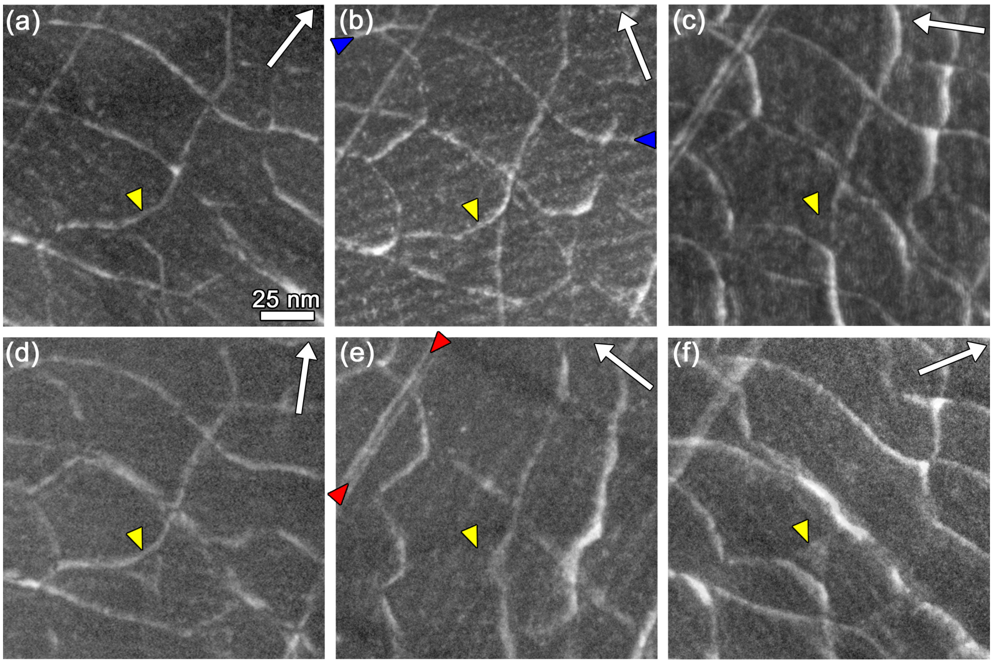

Figure 3.6.: Magnified view of the centre region of Fig. 3.5. The plan view weak beam dark field TEM images depict all the same specimen area and have been recorded under (a) $\mathbf{g} = 11\bar{2}0$, (b) $\mathbf{g} = \bar{1}2\bar{1}0$, (c) $\mathbf{g} = \bar{2}110$, (d) $\mathbf{g} = 01\bar{1}0$, (e) $\mathbf{g} = \bar{1}100$ and (f) $\mathbf{g} = 10\bar{1}0$ $\mathbf{g(3g)}$ weak beam conditions. Yellow triangles point towards an extended stacking fault node formed by dissociated a-type dislocations. Blue triangles in (b) and red triangles in (e) indicate a bowed perfect a-type dislocation and a dissociated a+c-type dislocation, respectively.

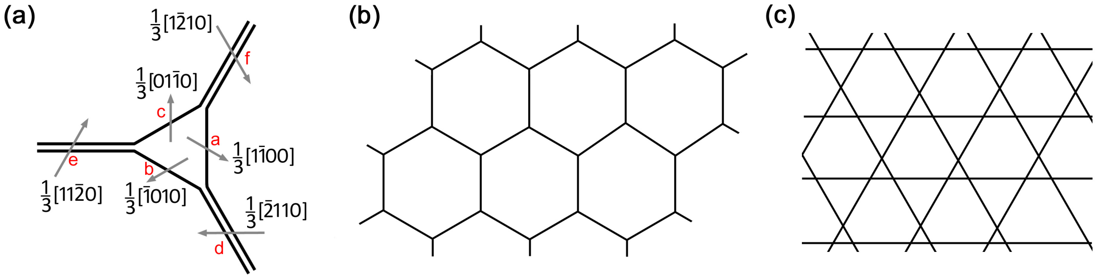
(a)
$\frac{1}{3}[1\bar{2}10]$
f
$\frac{1}{3}[01\bar{1}0]$
c
a
$\frac{1}{3}[1\bar{1}00]$
e
b
$\frac{1}{3}[11\bar{2}0]$
$\frac{1}{3}[\bar{1}010]$
$\frac{1}{3}[\bar{2}110]$
d
(b)
(c)

Figure 3.7.: (a) Schematic illustration of the extended stacking fault node indicated in Fig. 3.6 by yellow triangles. Grey arrows denote Burgers-vectors of the dislocations and red letters next to the Burgers-vectors indicate the images in Fig. 3.6 in which the respective dislocation lines are out of contrast. (b) and (c) Schematic representation of misfit dislocation networks having a hexagonal honeycomb and "Star of David" geometry, respectively.

This can be explained if the in-plane component of the considered dislocation is dissociated according to

$$\frac{1}{3}\left[2\bar{1}\bar{1}0\right] \rightarrow \frac{1}{3}\left[1\bar{1}00\right] + \frac{1}{3}\left[10\bar{1}0\right] \tag{3.2}$$

and if one bears in mind that in the case of $\mathbf{g} = 01\bar{1}0$ (Fig. 3.6 (d)) the overlapping strain fields of both partial dislocations appear as a perfect dislocation in the far field. Diffraction contrast analysis of other misfit dislocations reveals that this type of network also consist of 3 sets of dislocations corresponding to the three crystallographic equivalent in-plane Burgers-vectors in the wurtzite lattice. In contrast to the first type of network the dislocations of the trigonal network have a constant angle of 60° between their line direction and the in-plane component of their Burgers-vector (in the case one considers the perfect dislocation). However, due to the wide spacing of misfit dislocations of the trigonal network in the range of several 100 *nm* their contribution to mismatch relaxation is insignificant.

3.2.2.2. Aberration corrected HRTEM analysis

Fig. 3.8 and 3.9 show typical examples for aberration corrected HRTEM images of misfit dislocations at the interface of a 35 *nm* thick high temperature $Al_xGa_{1\text{-}x}N$ interlayer to the GaN buffer. This analysis reveals the major part of misfit dislocations to be of a-type. However, individual a-type misfit dislocations differ from each other with regard to their core structure, perfect or dissociated dislocations, and their character, mixed- or edge-type. We have observed at least 3 different groups of a-type dislocations: mixed-type and edge-type perfect dislocations as well as dissociated mixed-type dislocations. This is consistent with our plan-view analysis that revealed that the network formed by the majority of misfit dislocations has an inhomogeneous appearance with varying line direction and with simultaneous presence of perfect as well as dissociated dislocations.

Fig. 3.8 (c) shows an example for an edge-type (90°) perfect a-type dislocation recorded along the $< 1\bar{1}00 >$ projection in which it is identified as a 90° perfect a-type dislocation by the presence of the two inserted $\left\{1\bar{1}20\right\}$ half-planes. In case of a mixed-type (e.g. 60°) perfect a-type dislocation only one inserted $\left\{1\bar{1}20\right\}$ half-plane is seen in the $< 1\bar{1}00 >$ projection (Fig. 3.8 (b)). In addition, dissociated mixed-type a-type misfit dislocations are found and an example is shown in the HRTEM image recorded in the $< 11\bar{2}0 >$ projection in Fig. 3.9 (a). The dissociated a-type dislocation is easily identified by its characteristic *AB AB* ***ABCA*** *CA CA* stacking sequence (commonly called I_2-basal stacking fault in literature [91, 92]) between the two Shockley partial dislocations. The I_2-basal stacking faults typically extend in the range from $2-20$ *nm*. A closer inspection of the pair of partial dislocations bounding the stacking fault (Fig. 3.9 (b) and (c)) reveals a good agreement with core structure models of a 90° single period and a 30° double Shockley partial dislocation in the glide set configuration. According to Belabbas et al. [93] this combination is the energetically most favourable one for the dissociation of a 60° a-type dislocation into two Shockley partials ($\frac{1}{3}\left\langle 11\bar{2}0\right\rangle \rightarrow \frac{1}{3}\left\langle 10\bar{1}0\right\rangle + \frac{1}{3}\left\langle 01\bar{1}0\right\rangle$). Another detail visible in our HRTEM images of a-type misfit dislocations is the displacement field of atoms along $[0001]$ due

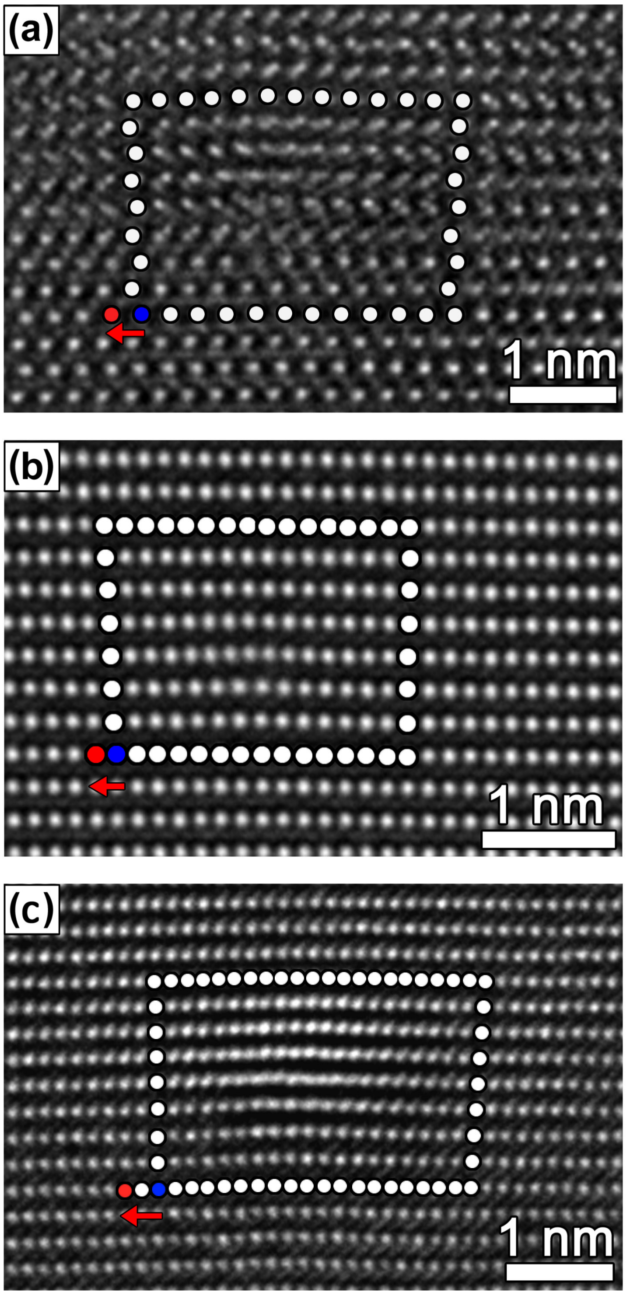

Figure 3.8.: Aberration corrected HRTEM images of perfect a-type misfit dislocations at the Al$_x$Ga$_{1-x}$N interlayer/GaN buffer interface recorded along the (a) $< 11\bar{2}0 >$ and (b), (c) $< 1\bar{1}00 >$ projection. The images were recorded with a negative C_s and a small overfocus so that atomic columns appear bright. White circles indicate the Burgers-circuit, whereby start and finish points of the right handed circuit are coloured blue and red, respectively. The projected edge component of the Burgers-vector is indicated by a red arrow.

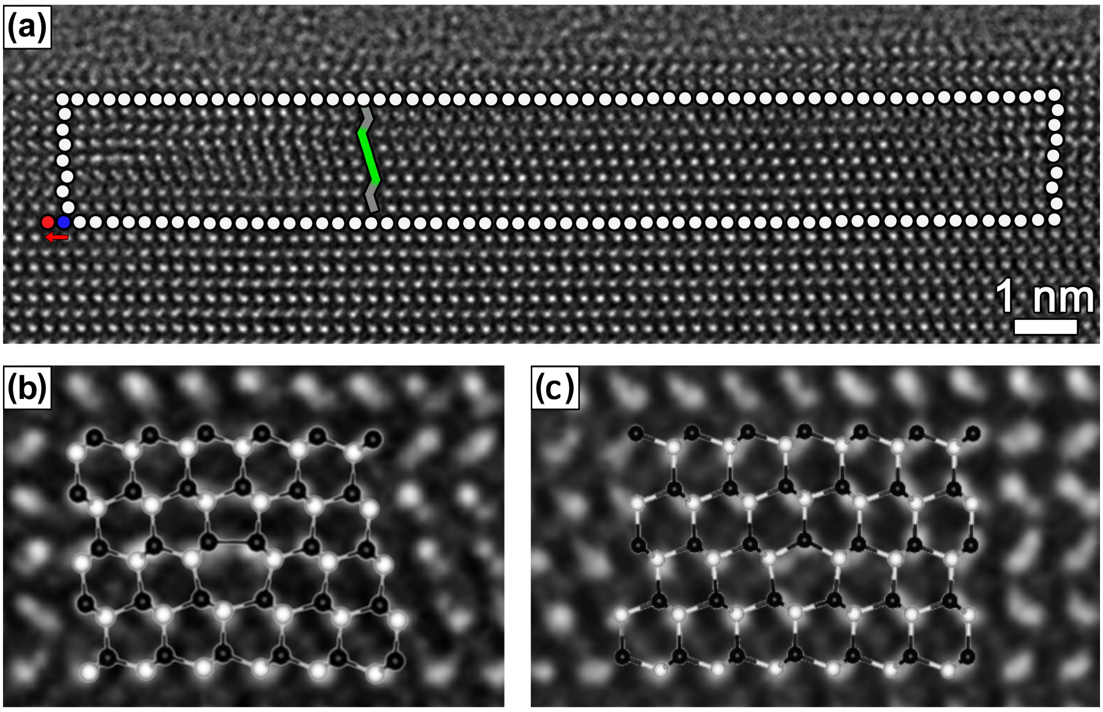

Figure 3.9.: Aberration corrected HRTEM images of a dissociated a-type misfit dislocation at the $Al_xGa_{1\text{-}x}N$ interlayer/GaN buffer interface recorded along the $< 11\overline{2}0 >$ projection. The image was recorded with a negative C_s and a small overfocus so that atomic columns appear bright. The Burgers-circuit is indicated by white circles, whereby start and finish points of the right handed circuit are coloured blue and red, respectively. The projected edge component of the Burgers-vector is represented by a red arrow. The AB AB hexagonal close-packed stacking of the wurtzite lattice and the I_2-basal stacking fault (AB $\underline{\boldsymbol{ABCA}}$ CA stacking sequence) between the two Shockley partials are indicated by a grey and green bar, respectively. (b) and (c) show a magnified view of the partial dislocations from (a) overlayed with a ball-and-stick model (black balls: Ga, white balls: N) of the dislocation core structure for a (b) 90° single period and (c) 30° double period Shockley partial dislocation with a glide set configuration, respectively (core structure models are taken from Belabas et al. [93, 94]).

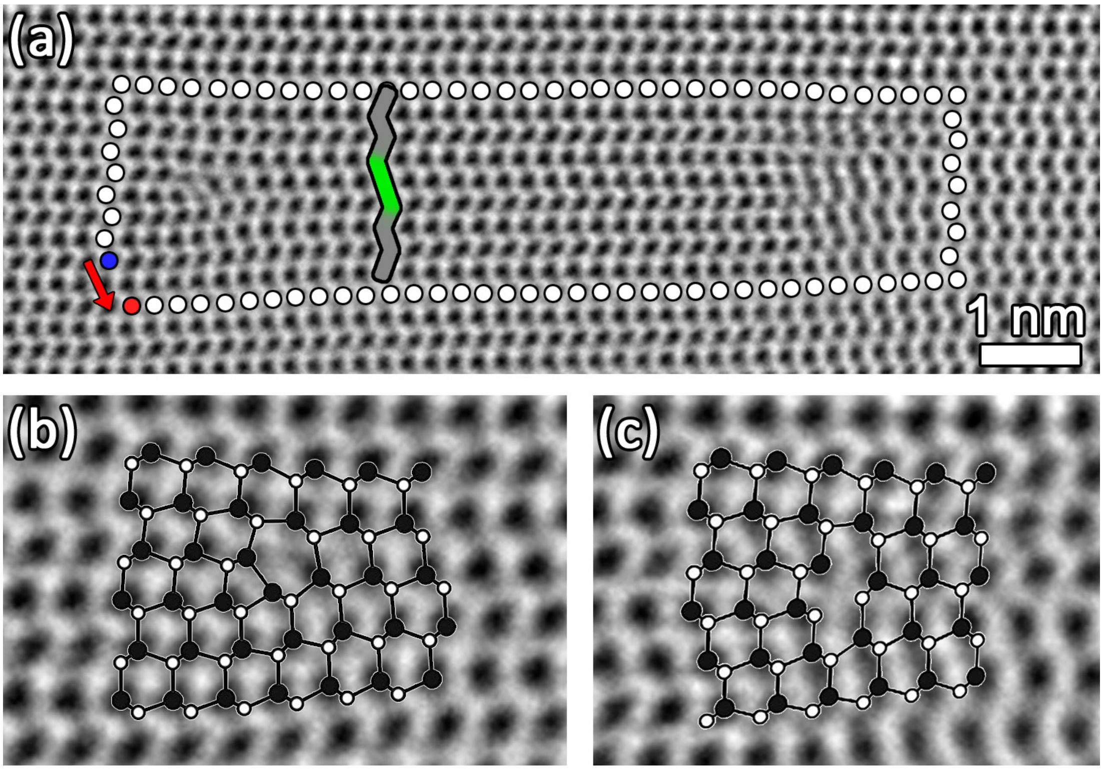

Figure 3.10.: Aberration corrected HRTEM images of a dissociated a+c-type misfit dislocation at the $Al_xGa_{1-x}N$ interlayer interface recorded along the projection. The image was recorded with $C_s \approx 0$ and a small underfocus so that atomic columns appear dark. The Burgers-circuit is indicated by white circles, whereby start and finish points of the right handed circuit are coloured blue and red, respectively. The projected edge component of the Burgers-vector is represented by a red arrow. In (a) the AB AB hexagonal close-packed stacking of the wurtzite lattice and the I_1-basal stacking fault (AB ***ABC*** BC stacking sequence) between the two Frank-Shockley partials are indicated by a grey and green bar, respectively. (b) and (c) show a magnified view of the partial dislocations from (a) overlayed with a ball-and-stick model (black balls: Ga, white balls: N) of the dislocation core structure for a (b) 5/7 atom rings edge-type and (c) 12 atom ring mixed-type Frank-Shockley partial dislocation, respectively (core structure models are taken from Kioseoglou et al. [95] and Komninou et al. [96]).

to elastic relaxation around the dislocation core (see e.g. Fig. 3.8 (b)). This causes the residual contrast of a-type misfit dislocation networks in cross-sectional weak beam dark field images using the (0002) diffraction vector (e.g. in Fig. 3.1 (a)) despite the fact that the $g \cdot b = 0$ criterion for contrast extinction is fulfilled in this case.

In addition to a-type dislocations we also find a few a+c-type misfit dislocations (see Fig. 3.10). However, compared to the density of a-type misfit dislocations the latter ones occur typically at least 10 times less frequent. All observed a+c-type misfit dislocations are dissociated into two Frank-Shockley partials, which are typically separated by 5 *nm* and span a characteristic stacking fault with an *AB AB* $\underline{\textbf{\textit{ABC}}}$ *BC BC* stacking sequence (commonly called I_1-basal stacking fault in literature [91, 92]) between them. To gain more information we have compared experimental images of a pair of partial dislocations with core structure models of Frank-Shockley partials of a dissociated mixed-type a+c-type dislocation having a $< 11\bar{2}0 >$ line direction. For one of the partials (Fig. 3.10 (b)) the best agreement is found for an edge-type dislocation involving 5/7 atom rings while for the other partial dislocation (Fig. 3.10 (c)) a mixed-type partial with a 12 atom ring yields the best match. According to literature reports [95, 96] both core models are energetically favourable structures among the 12 possible edge-type and 12 possible mixed-type configurations, respectively.

Combining our plan view and high resolution TEM results we conclude that the first misfit dislocation network consists of a-type dislocations while the second (trigonal) network is built up of a+c-type misfit dislocations.

3.2.2.3. Lateral homogeneity of the misfit dislocation networks

A comparison of plan view images from different regions of the same sample reveals that the general appearance of the networks is spatially rather inhomogeneous in terms of the geometry and arrangement of misfit dislocation lines. It varies on a length-scale in the order of 10 *µm*. This fluctuation is exemplarily seen, when comparing Fig. 3.11 (a) with (b) or Fig. 3.11 (c) with (d). In Fig. 3.11 (b) and 3.11 (d) the misfit dislocation networks appear to be more ordered and have in some regions, as one might expect for wurtzite crystals, similarities with a “Star of David” pattern and/or with a hexagonal honeycomb structure (compare with schematic illustration of these types of network geometries in Fig. 3.7).

On the other side, comparing samples with different thickness as well as growth temperature of $Al_xGa_{1-x}N$ interlayers (compare Fig. 3.11 (a) with (c) and (e)) shows that the misfit dislocation networks at the interfaces of $Al_xGa_{1-x}N$ interlayers look qualitatively very similar with respect to the following features: (i) The presence of the two types of networks, one of which is formed by bowed a-type dislocations having in average an angle between Burgers-vector and line direction of approximately 60° and the other consists of straight a+c-type dislocations oriented along $< 11\bar{2}0 >$. (ii) The dominance of a-type misfit dislocations and (iii) the spatially rather inhomogeneous appearance of the misfit dislocation networks.

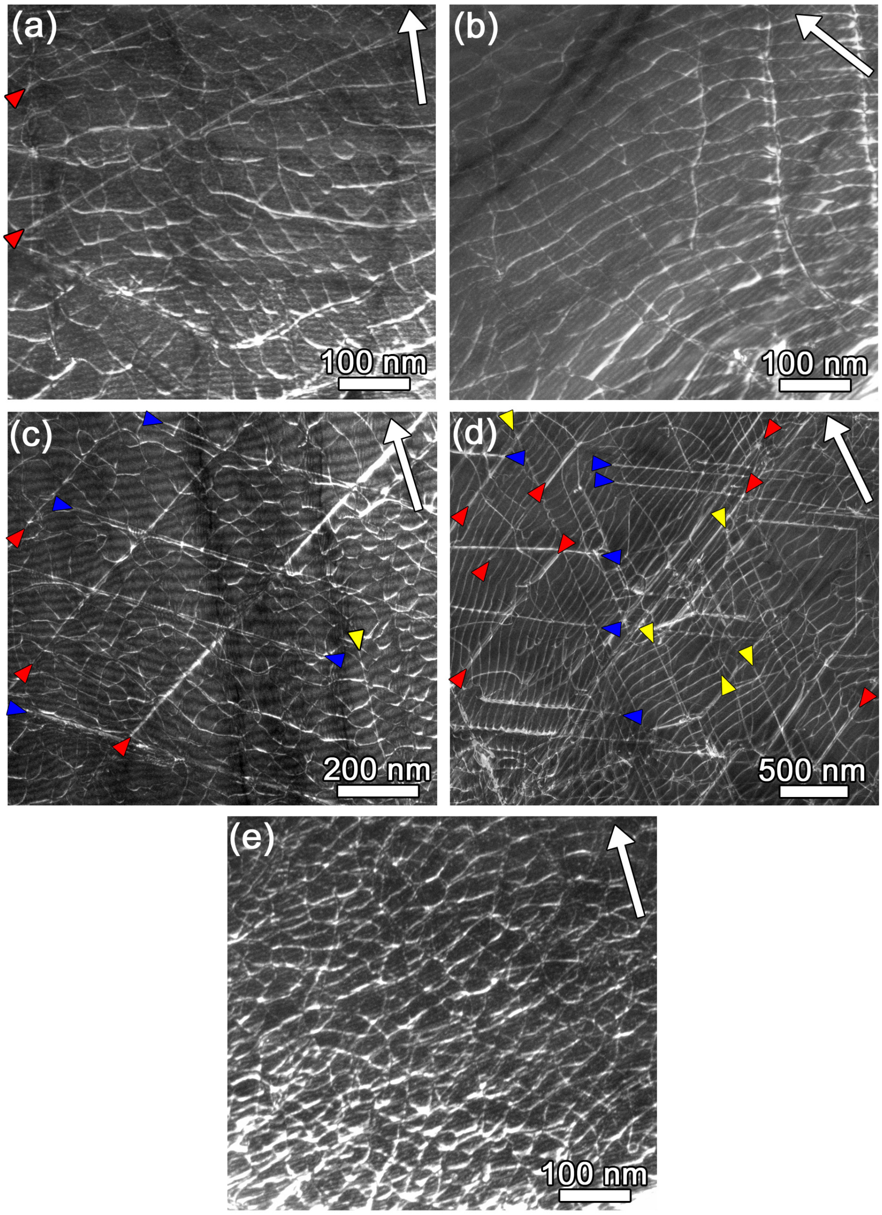

Figure 3.11.: Plan view weak beam dark field TEM images of the misfit dislocation network at the interface between $Al_xGa_{1-x}N$ interlayer and GaN buffer. All images have been recorded under $\mathbf{g} = 11\bar{2}0$ **g(3g)** weak beam conditions. (a) and (b) show different regions of a sample with a 35 *nm* thick high temperature $Al_{0.75}Ga_{0.25}N$ interlayer without GaN capping, (c) and (d) show different regions of a sample with a 26 *nm* thin low temperature $Al_{0.75}Ga_{0.25}N$ interlayer and 120 *nm* GaN capping and (e) is a plan-view from a sample with a 70 *nm* thick low temperature $Al_{0.75}Ga_{0.25}N$ interlayer without GaN capping. Red, blue and yellow triangles denote selected a+c-type dislocations having a straight line direction along $< 11\bar{2}0 >$.

3.2.3. Macroscopic strain measurements

We will now quantify the degree of strain relaxation in $Al_xGa_{1-x}N$ interlayers and the strain state of the GaN buffer and the GaN overlayer on a macroscopic scale by ex-situ XRD and in-situ wafer curvature measurements. On the one side we will use these data later in the discussion part to confirm the macroscopic validity of our results obtained from the microscopic TEM analysis. On the other side we will measure the effect of thermally induced stress that arises during the cool-down on the built up compressive strain in the GaN overlayer $\Delta\varepsilon$ (difference of strain state GaN overlayer and GaN buffer) by comparing in-situ wafer curvature measurements with ex-situ X-ray measurements. The analysis will be done exemplarily for 3 samples which have been grown on Si (111) substrates and have a comparable buffer structure but different $Al_xGa_{1-x}N$ interlayers (18 *nm* low temperature, 26 *nm* low temperature and 35 *nm* high temperature $Al_{0.75}Ga_{0.25}N$ interlayer).

3.2.3.1. In-situ wafer curvature monitoring

Figure 3.12 shows the change of wafer curvature with increasing film thickness in-situ, i.e. during the growth at the deposition temperature for the 3 samples mentioned above. The graphs can be separated into 3 distinct parts: the stages where the GaN buffer is grown on top of the silicon substrate, the second stage where the $Al_xGa_{1-x}N$ interlayer is grown and the final stage where the GaN overlayer is grown on top of the

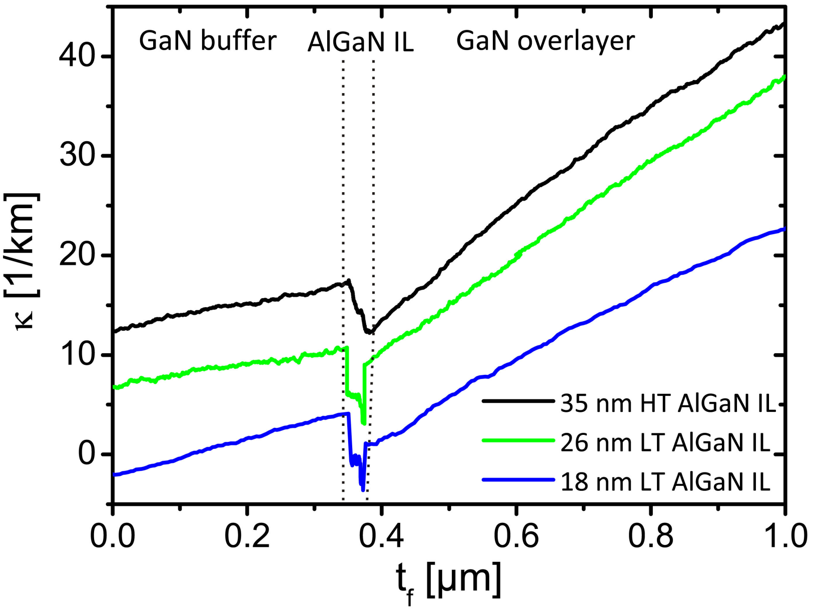

Figure 3.12.: In-situ wafer curvature measurements for 3 samples grown on Si (111) substrates with different thickness and depostion temperature of the $Al_xGa_{1-x}N$ interlayer (see legend in the graph). The curves are shifted vertically for clearness. The black dotted lines indicate the different layer, i.e. the GaN buffer layer, $Al_xGa_{1-x}N$ interlayer, and the GaN overlayer. A positive slope denotes compressive strain.

Table 3.2.: Summary of results from in-situ wafer curvature measurements

sample	GaN buffer average slope $\left[\frac{1}{km\ \mu m}\right]$	GaN overlayer initial slope[8] $\left[\frac{1}{km\ \mu m}\right]$	GaN overlayer average slope[9] $\left[\frac{1}{km\ \mu m}\right]$
35 nm high temperature $Al_{0.75}Ga_{0.25}N$ interlayer [5]	11 ± 2	60 ± 2	38 ± 1
26 nm low temperature $Al_{0.75}Ga_{0.25}N$ interlayer [6]	10 ± 2	50 ± 2	42 ± 1
18 nm low temperature $Al_{0.75}Ga_{0.25}N$ interlayer [7]	14 ± 2	42 ± 2	34 ± 1

interlayer. For the first stage we observe for all 3 samples a similar constant positive slope of the curvature $\left(\frac{\partial\kappa}{\partial t_f}\right)$. According to the Stoney equation this means that the GaN buffer, while being deposited, is under moderate compressive strain[4]. During the growth stage of the $Al_xGa_{1\text{-}x}N$ interlayer, the wafer curvature exhibits overall a negative slope corresponding to the tensile strain state of the $Al_xGa_{1\text{-}x}N$ interlayer. As soon as the GaN overlayer is grown on top of the $Al_xGa_{1\text{-}x}N$ interlayer the wafer curvature increases again with the film thickness. However, for the initial growth stage of the GaN overlayer the slope of the wafer curvature is higher than that during the growth of the GaN buffer. According to equation (2.38) this indicates the build-up of an additional compressive strain $\Delta\varepsilon$ in the GaN overlayer. By comparing the 3 samples in Fig. 3.12 we find that with increasing thickness of the $Al_xGa_{1\text{-}x}N$ interlayer also the change of the slope increases, i.e. more compressive strain is initially built up in the GaN overlayer. During the further growth of the GaN overlayer, however, the slope of the wafer curvature decreases again gradually indicating an effective relaxation of the built up compressive strain. Quantitative results of the analysis of the in-situ curvature measurements are summarised in Table 3.2. An evaluation of the strain state of the layers and a comparison with results of the other methods will be given in section 3.3.3.

---

[4] This is because the GaN buffer is deposited on a AlN nucleation layer/$Al_xGa_{1\text{-}x}N$ buffer, which typically leads to a small amount of compressive strain.

[5] sample with a 1.7 μm GaN overlayer

[6] sample with a 1.0 μm GaN overlayer

[7] sample with a 0.7 μm GaN overlayer

[8] average slope for the first 100 nm of the GaN overlayer

[9] average slope for the full thickness of the GaN overlayer

3.2.3.2. Ex-situ X-ray diffraction

In the following we will evaluate X-ray diffraction data, which have been obtained ex-situ. These measurements capture the strain state of the layers after growth, i.e. at room temperature.

We start with X-ray reciprocal space maps (RSM) recorded around the asymmetric $(11\overline{2}4)$ reflection. To identify the individual peaks in the reciprocal space map, we have measured three samples from a growth series: the first one is a reference sample without the $Al_xGa_{1-x}N$ interlayer and GaN overlayer (Fig. 3.13 (a)), the second has additionally a 35 *nm* thick high temperature $Al_{0.75}Ga_{0.25}N$ interlayer (Fig. 3.13 (b)), and the third sample corresponds to a full structure with additionally a 1.7 µ*m* thick GaN overlayer on top of a 35 *nm* thick high temperature $Al_{0.75}Ga_{0.25}N$ interlayer (Fig. 3.13 (c)). The most intense peak in the reciprocal space maps is due to the GaN layers. The other peaks in the reciprocal space maps at higher q_x and q_z originate from the step-graded $Al_xGa_{1-x}N$ buffer, $Al_xGa_{1-x}N$ interlayer and AlN nucleation layer, respectively. The signal of the $Al_xGa_{1-x}N$ interlayer (see dashed white circle in Fig. 3.13) is identified by comparing the reciprocal space map of the first sample with that of the second/third one. Although the signal is very weak it is possible to apply 2D Gaussian fitting routines and to extract the in-plane reciprocal lattice parameter of the $Al_xGa_{1-x}N$ interlayer. The results (also from two other samples, which are not shown here) are listed in Table 3.3.

A closer look of the GaN peak in Fig. 3.13 (d) for a full structure, i.e. a sample with a GaN buffer and a GaN overlayer on top of a $Al_xGa_{1-x}N$ interlayer, reveals that the GaN peak is composed of two separate peaks, a main peak and a shoulder at smaller q_x-values (both are aligned approximately along the dotted line in Fig. 3.13 (d)). These two peaks originate from the GaN buffer and GaN overlayer, respectively, having a different strain state. However, due to the strong broadening of the peaks almost along that direction in the reciprocal space, which corresponds to pairs of $(q_x,\ q_z)$ of GaN under a varying strain state, an unambiguous determination of the q_x-values for both GaN layers from the reciprocal space maps of the asymmetric $(11\overline{2}4)$ reflection is not possible.

Therefore, we have performed high resolution $\theta/2\theta$-scans of symmetric reflections. Measurements for the 3 samples (same samples as in the in-situ wafer curvature graphs in Fig. 3.12) are shown in Fig. 3.14. A separation of the GaN (0002) and (0006) reflection, respectively, into 2 peaks can be recognized even with the naked eye. The best agreement with the measured data is obtained by fitting the curve, however, with 3 peaks: 2 main peaks which correspond to GaN under tension and compression, respectively, and another broad shoulder at lower 2θ-values that is caused by diffraction at even more compressively strained GaN. Fitting results are given in Table 3.3.

In order to identify the contributions from the different layers to the 3 peaks we have measured a sample, which has been prepared as a wedge similar as depicted schematically in Fig. 3.15 (b). The sample has been prepared with a very shallow angle of $\theta_{wedge} = 0.1^\circ$ by mechanical polishing with diamond lapping foils (first 1 µ*m* then 0.1 µ*m* grain size) and finally chemo-mechanical polishing (colloidal silica slurry with average particle size of 35 nm and pH of 10) to reduce the thickness of the preparation related surface damage layer. By measuring at different x-positions on the bevelled part

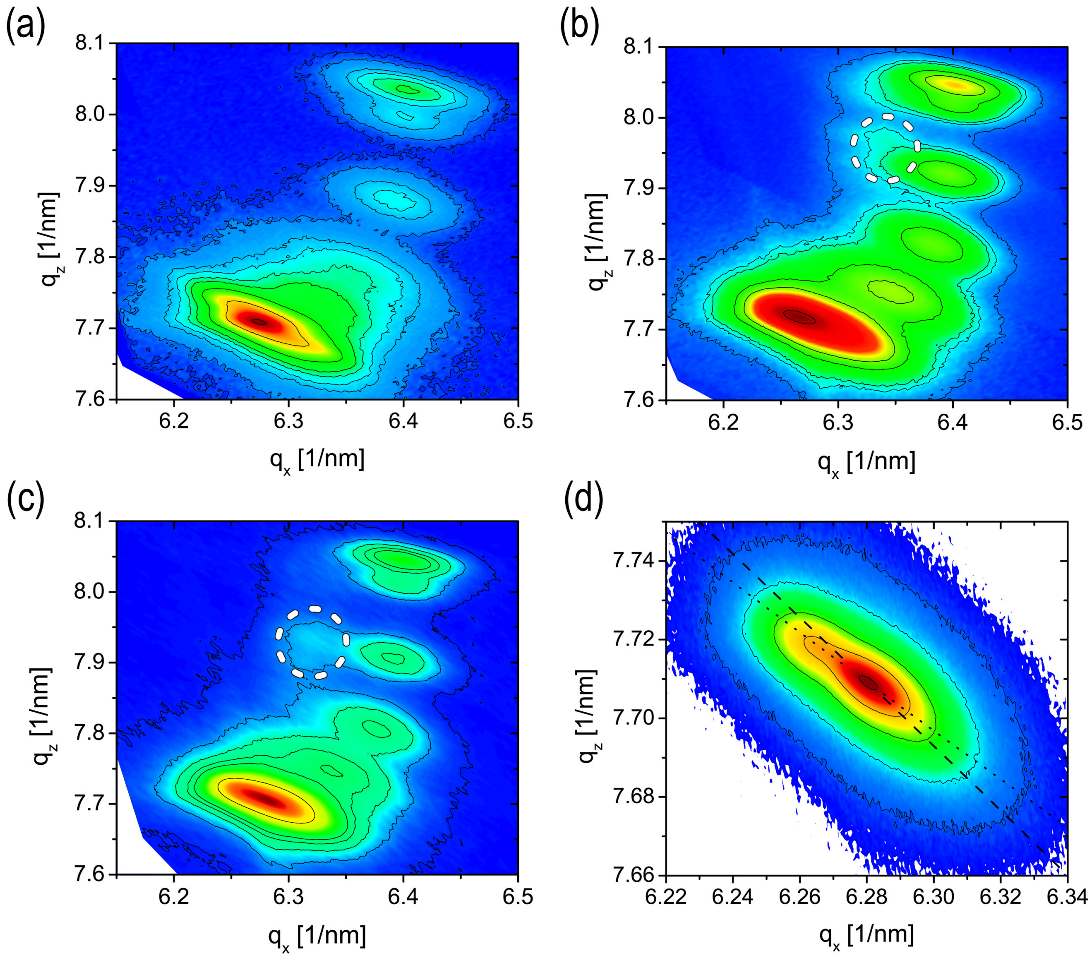

Figure 3.13.: Reciprocal space maps of the $(11\bar{2}4)$ reflection from a sample series where the growth was stopped after (a) the GaN buffer, (b) a 35 *nm* thin high temperature $Al_{0.75}Ga_{0.25}N$ interlayer on top of the GaN buffer and (c) after an additional $1.7\mu m$ thick GaN overlayer, respectively. White dashed cirles highlight the signal from the $Al_{0.75}Ga_{0.25}N$ interlayer. In (d) a magnified view of the GaN peak. The dashed black line denotes the direction in the reciprocal space, which is perpendicular to the diffraction vector and is the main direction of peak broadening (typically denoted as mosaic spread in literature). The dotted black line corresponds to pairs of (q_x, q_z), which are reciprocal lattice parameters of GaN under varying biaxial strain.

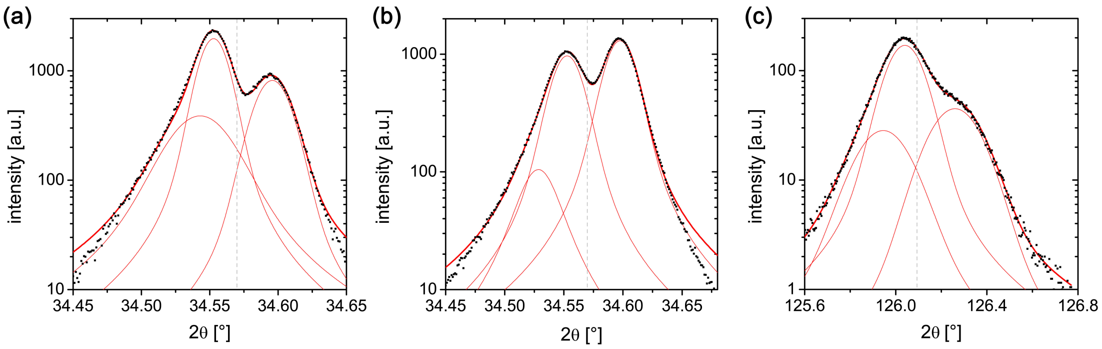

Figure 3.14.: High resolution XRD $\theta/2\theta$-scans of samples with (a) 35 *nm* thick high temperature, (b) 26 *nm* low temperature and (c) 18 *nm* low temperature $Al_{0.75}Ga_{0.25}N$ interlayer, respectively. The $\theta/2\theta$-scans were carried out for the (a) and (b) GaN (0002), (c) GaN (0006) reflection, respectively. Black symbols denote experimental data and simulations are shown in red. The dashed grey lines indicates the 2θ-values of relaxed GaN.

of the sample we obtain depth integrated XRD signals, which correspond to different effective thicknesses of the film. The depth-resolution Δz is limited by the finite size of the X-ray beam ($d_{beam} = 0.1$ mm), the wedge angle θ_{wedge} and the incident angle $\theta_{incident}$ ($\approx 63°$ for the used (0006) reflection) of the X-rays according to

$$\Delta z = \frac{d_{beam}}{\sin \theta_{incident}} \cdot \tan \theta_{wedge} \tag{3.3}$$

and amounts for the given parameters to approximately 200 *nm*. The experiment yields two important results, which are visible in Fig. 3.15 (a). (i) A peak at higher 2θ-values, corresponding to tensile strained GaN, appears as soon as the X-ray beam hits the film wedge. Thus, this peak must originate from the lower part of the film, i.e. from the GaN buffer. The 2θ-value of this peak does not change with the x-positions of the measurement implying that the strain state of the GaN buffer is constant along the vertical direction. (ii) A second peak at a lower 2θ-value, corresponding to compressively strained GaN, arises as the sample is moved further relative to the X-ray beam and the thickness of the film increases, i.e. also the GaN overlayer gets illuminated by the beam. In contrast to the first peak the second one shifts continuously towards higher 2θ-values for increasing thickness of the film (corresponding to an increasing x-position of the measurement). This means that there is a vertical strain gradient in the GaN overlayer, whereby the part directly above the $Al_xGa_{1-x}N$ interlayer exhibits the highest compressive strain and consequently causes the shoulder at lower 2θ-values in the $\theta/2\theta$-measurements.

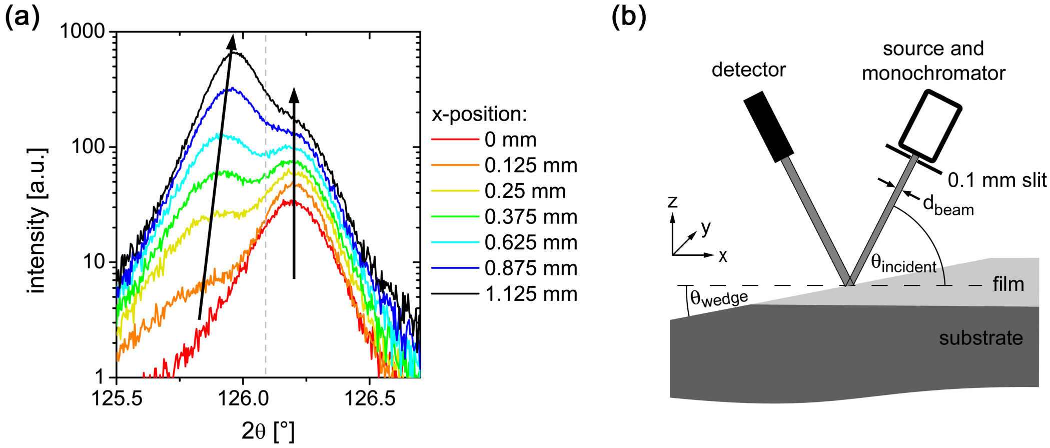

Figure 3.15.: (a) High resolution XRD $\theta/2\theta$-scans of the GaN (0006) reflection from different x-positions of a sample which was prepared as a wedge. The sample is the same one as in Fig. 3.14 (b). The 2 black arrows are a guide to the eye and represent the change of the peak position for the 2 main peaks for increasing values of the x-position. The dashed grey line indicates the 2θ-value of relaxed GaN. (b) Schematic representation of the experimental setup. x=0 corresponds to the horizontal position where the GaN (0006) reflection has just sufficient intensity to be detected, i.e. close to the edge of the GaN film wedge.

Table 3.3.: Summary of results from the ex-situ X-ray diffraction measurements

sample	$\theta/2\theta$-scans		$(11\bar{2}4)$ RSM
	$c_{GaN\,buffer}$ [Å]	$c_{GaN\,overlayer}$ [Å]	q_x^{AlGaN} $\left[\frac{1}{nm}\right]$
35 nm high temperature $Al_{0.75}Ga_{0.25}N$ interlayer [10]	5.1813 (5)	5.1875 (5)[13]	6.321 (5)[13]
26 nm low temperature $Al_{0.75}Ga_{0.25}N$ interlayer [11]	5.1810 (5)	5.1875 (5)[13]	6.297 (5)[13]
18 nm low temperature $Al_{0.75}Ga_{0.25}N$ interlayer [12]	5.1811 (5)	5.1862 (5)[13]	6.291 (5)[13]

---

[10] sample with a 1.7 μm GaN overlayer

[11] sample with a 1.0 μm GaN overlayer

[12] sample with a 0.7 μm GaN overlayer

[13] The number in brackets denotes the error of the lattice parameter determination due to uncertainties in the peak fitting

3.3. Discussion

In the following we will discuss our experimental results in terms of the build-up of compressive strain in the GaN overlayer. In the first part we will give a phenomenological explanation why strain engineering with $Al_xGa_{1-x}N$ interlayer works and how it is possible to generate compressive strain in the subsequent layer. In the second part we will perform a quantitative evaluation of the strain-engineering process on the basis of our TEM observations. Finally, we will compare results from the different strain measurement techniques (i) to prove our microscopic TEM model to be valid also on a macroscopic scale and (ii) to discuss the influence of the thermal stress on the strain relaxation process.

3.3.1. Phenomenological model for the build-up of compressive strain by $Al_xGa_{1-x}N$ interlayer

Our in-situ wafer curvature measurements have clearly shown that the compressive strain starts to build up once GaN is grown top of the $Al_xGa_{1-x}N$ interlayer. This is true for all samples described above, though the amount of compressive strain depends on the detailed growth parameters of the $Al_xGa_{1-x}N$ layer such as thickness and Al content. According to our TEM results the build-up of compressive strain is caused by an effective plastic relaxation of the $Al_xGa_{1-x}N$ interlayer due to formation of misfit dislocation networks. Cross-sectional TEM imaging also reveals that misfit dislocation networks form at both interfaces of the $Al_xGa_{1-x}N$ interlayer. While the misfit dislocations located at the lower interface between $Al_xGa_{1-x}N$ interlayer and GaN buffer relaxes the $Al_xGa_{1-x}N$ interlayer by introducing extra half-planes (as can be seen e.g. in Fig. 3.8) those at the upper interface of the $Al_xGa_{1-x}N$ interlayer relieve the lattice mismatch between the GaN overlayer and the $Al_xGa_{1-x}N$ interlayer by retracting half-planes in the GaN overlayer.

However, since the spacing of misfit dislocations at the upper interface of the $Al_xGa_{1-x}N$ interlayer is always higher than at the lower interface, the GaN overlayer grows compressively strained. The schematic drawing in Fig. 3.16 demonstrates this phenomenon. A detailed analysis of the strain relaxation mechanisms that induce this favourable imbalance will be the focus of chapter 4. Also the effect of the $Al_xGa_{1-x}N$ interlayer thickness on the generated compressive strain will be discussed in this chapter.

3.3.2. Modelling of TEM results

In the following we will quantitatively estimate the amount of strain relaxation of the $Al_xGa_{1-x}N$ interlayer and the resulting build-up of compressive strain in the GaN overlayer with the help of the information we have gained from our TEM investigation. We will use a similar approach for the calculation as presented by Moran et al. [97]. Before we begin with the modelling, we want to briefly summarise to relevant results.

We have seen that strain relaxation occurs at both interfaces of the $Al_xGa_{1-x}N$ interlayer mainly by formation of a-type misfit dislocation networks. A systematic difference between the average spacing of dislocation lines at the upper and lower interface

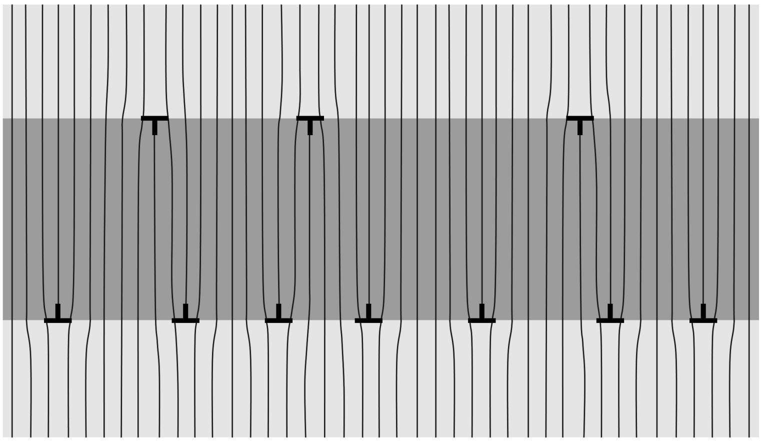

Figure 3.16.: Schematic illustration of the build-up of compressive strain due to as asymmetry in plastic relaxation between the interfaces of $Al_xGa_{1-x}N$ interlayers. Black lines represent vertical lattice planes. The two GaN layers (buffer and overlayer) and the $Al_xGa_{1-x}N$ interlayer are depicted as light and dark grey shaded areas, respectively. The "T" symbols designate misfit dislocations, whereby the vertical element points towards the inserted half-plane.

of the $Al_xGa_{1-x}N$ interlayer finally leads to the build-up of compressive strain in the GaN overlayer.

From our HRTEM and plan-view TEM investigation we have seen that (i) the geometry of the a-type misfit dislocation networks is spatially rather inhomogeneous and varies on a 10 μm scale. In some regions of the interfaces of the $Al_xGa_{1-x}N$ interlayer the misfit dislocation network has similarities with a “Star of David” or hexagonal honeycomb geometry as one might expect for wurtzite crystals [98, 99, 100, 101] or as it has been reported also for other materials like Si/Ge (111)[102, 103] and InAs/GaAs (111) [104]. ii) On the other hand we have seen that the a-type misfit dislocations appear as perfect as well as dissociated dislocations and their line direction varies on a 100 nm scale between 30-90°. Therefore, we have to consider for our analysis the statistical average of the networks, i.e. the average effective dislocation line spacing and the average line direction. We assume in the following that the misfit dislocation networks consist of 3 arrays of dislocations, whose effective line direction has in average an angle of 60° with the Burgers-vector $\vec{b} = \frac{1}{3}\left\langle 11\bar{2}0\right\rangle$. Since in our case partial dislocations always appear as pairs of a dissociated perfect dislocations (in contrast to a network formed only of partials as reported by Zhang et al. [101]) this consideration holds independent on the fact whether on a local scale the dislocations are perfect 60° dislocations or split into 30° and 90° Shockley partials. For the latter case the strain fields of the 2 partials simply add up to that of an undissociated dislocation and the amount of lattice relaxation is the same. The amount of misfit, which has been accommodated by a network of misfit dislocations can be expressed in general by,

$$\delta = \frac{\left|\vec{b_{IF}}\right| \sin\varphi}{d_{array}} \alpha_{geo} , \tag{3.4}$$

where $\left|\vec{b_{IF}}\right|$ is the modulus of the component of the Burgers-vector that lies in the interfacial plane, φ is the angle between $\vec{b_{IF}}$ and the line direction and d_{array} is the average spacing between dislocations of an array. The factor α_{geo} implies the geometry of the misfit dislocation network. For a hexagonal as well as trigonal network consisting of 3 arrays of misfit dislocations the factor equals to $\alpha_{geo} = \frac{3}{2}$ [97]. In principle d_{array} can be easily determined directly from plan view images. However, in case of overlapping misfit dislocation networks from both interfaces of the $\mathrm{Al_xGa_{1\text{-}x}N}$ interlayer and also in case of samples, which have a thick GaN overlayer, an evaluation of d_{array} from plan view images is not suitable or even not possible at all (e.g. TEM specimen would be to thick to be electron transparent). Therefore, we have estimated the average spacing of misfit dislocations from cross-sectional images considering the fact that one observes a projection of several dislocation arrays (see Fig. 3.17). For a network consisting of 3 arrays of misfit dislocations, d_{array} can be calculated from the average spacing of misfit dislocations in the projected cross-sectional TEM image d_{image} according to

$$d_{image} = \frac{L}{\#_1 + \#_2 + \#_3} = \frac{L}{\frac{L \cdot \cos\theta_1}{d_{array}} + \frac{L \cdot \cos\theta_2}{d_{array}} + \frac{\varphi L \cdot \cos\theta_3}{d_{array}}} \tag{3.5}$$

$$d_{array} = d_{image} \cdot (\cos\theta_1 + \cos\theta_2 + \cos\theta_3) , \tag{3.6}$$

where L is a arbitrary unit length, $\#_i$ is the number of dislocations of array i seen per unit length L and θ_i is the angle between the viewing direction and the average line direction of dislocations of array i (see Fig. 3.17).

In order to account for the inhomogeneous appearance of the network and the non-straight line direction, we modify eq. (3.6) by introducing a random fluctuation (Gaussian distribution $f(\sigma, \theta^*)$) of the line direction from its average value

$$\begin{aligned} d_{array} = d_{image} \cdot \Bigg[& \int |\cos(\theta_{TEM} + \theta^*)| \cdot f(\sigma, \theta^*)\, d\theta^* \\ & + \int |\cos(\theta_{TEM} + 60^\circ + \theta^*)| \cdot f(\sigma, \theta^*)\, d\theta^* \\ & + \int |\cos(\theta_{TEM} - 60^\circ + \theta^*)| \cdot f(\sigma, \theta^*)\, d\theta^* \Bigg], \text{ with} \end{aligned} \tag{3.7}$$

$$f(\sigma, \theta^*) = \frac{1}{\sqrt{2\pi}\sigma} \exp\left[- \left(\frac{\theta^*}{\sigma} \right)^2 \right] , \tag{3.8}$$

where θ_{TEM} denotes the angle between the electron beam and the average direction of one array of the dislocation lines and σ is the standard deviation of the line direction

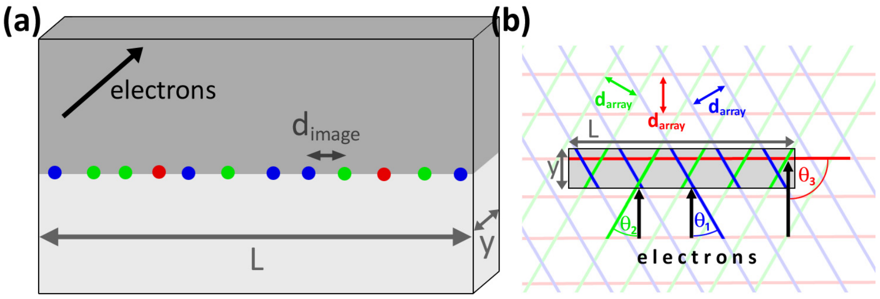

Figure 3.17.: Schematic representation for the calculation of the average spacing between misfit dislocation lines of an array d_{array} from the measured average spacing of all misfit dislocations seen in cross-sectional TEM images d_{image}. (a) shows a side view of a cross-sectional TEM specimen with a misfit dislocation network at an interface and (b) shows a top view of the cross-sectional TEM specimen. In (b) the grey shaded area represents the TEM specimen. Red, blue and green (a) dots and (b) lines denote the 3 arrays of misfit dislocations where each of them has an average spacing of their dislocation lines of d_{array}. Black arrays indicate the viewing direction (direction of electrons in the TEM) and θ_{1-3} are the angles between the viewing direction and the dislocation lines.

from its average value. In eq. (3.7) we have also made use of the crystal symmetry and the fact that in average the 3 dislocation arrays should be equivalent after rotation by 120°. Thus, we can reduce the number of parameters to one value θ_{TEM}. E.g. for imaging close to the $<1\bar{1}00>$ zone axis and the aforementioned geometry (average line direction along $<11\bar{2}0>$) we have $\theta_{TEM} = 30°$. In combination with the standard deviation of $\sigma = 15°$ we obtain

$$d_{array} = d_{image} \cdot 1.88\,. \tag{3.9}$$

Because of the curved line direction, we average the $\sin\varphi$ term (φ is in average approximately 60°) in eq. (3.4) as just before

$$\delta = \frac{\left|\vec{b}\right|}{d_{array}}\alpha_{geo} \cdot \int \sin\theta^* \cdot f(\sigma,\,\theta^*)\,d\theta^* = \frac{\left|\vec{b}\right| \cdot 0.84}{d_{array}}\alpha_{geo}\,. \tag{3.10}$$

In order to calculate the resulting compressive strain in the GaN overlayer, an effective misfit dislocation spacing according to

$$d_{effective} = \left(\frac{1}{d_{lower\,IF}} - \frac{1}{d_{upper\,IF}}\right)^{-1} \tag{3.11}$$

has to be considered because of the opposite effect of lattice relaxation by misfit dislocations at the lower and upper interface of the $Al_xGa_{1-x}N$ interlayer, respectively. Finally, combining eq. (3.9-3.11) we obtain for the amount of strain relaxation in the $Al_xGa_{1-x}N$ interlayer

$$\delta^{TEM}_{AlGaN} = \frac{\left|\vec{b}\right| 0.84}{1.88 \cdot d^{lower\,IF}_{image}} \cdot \frac{3}{2} \tag{3.12}$$

and for the build-up of compressive strain in the GaN overlayer

$$\Delta\varepsilon^{TEM} = \frac{\left|\vec{b}\right| 0.84}{1.88 \cdot d^{effective}_{image}} \cdot \frac{3}{2} \,. \tag{3.13}$$

Together with the average misfit dislocation spacings at the interfaces of $Al_xGa_{1-x}N$ interlayers, which we have determined in sub-section 3.2.1 (see Table 3.1), we can now calculate both values using eq. (3.12) and (3.13). In Table 3.4 we summarise the results from our TEM modelling for the amount of strain relaxation in $Al_xGa_{1-x}N$ interlayers and for the resulting build-up of compressive strain in GaN overlayers for 3 samples.

3.3.3. Comparison with macroscopic strain measurements

First we will perform a quantitative analysis of the macroscopic strain measurements and discuss briefly limitations and problems of both techniques. Afterwards we will then compare the results from the different strain measurement techniques.

3.3.3.1. In-situ waver curvature monitoring

The strain state of the GaN buffer and GaN overlayer *during the growth* has been evaluated for the 3 samples shown in Fig. 3.12 (18/26 *nm* low temperature and 35 *nm* high temperature $Al_{0.75}Ga_{0.25}N$ interlayer in a GaN film grown on Si (111)) from in-situ wafer curvature measurements with the help of the Stoney equation. As the slope $\frac{\partial\kappa}{\partial t_f}$ is approximately constant for all 3 considered samples within the last 300 *nm* before the $Al_xGa_{1-x}N$ interlayer, the calculation of the strain state of the GaN buffer is straightforward. However, as the curvature κ does not increase linearly with the film thickness during the growth of the GaN overlayer, the strain analysis becomes more complicated. This problem was address by Krost et al. [105]. The gradual decrease of the curvature during the growth can be explained in 2 ways. In the first case it is assumed that the strain varies vertically in the layer while in the second case it is assumed that the strain in the layer is homogeneous along the growth direction but varies as a function of the layer thickness, i.e. a gradual relaxation process occurs at the interface between the layers and changes the strain state of the entire top layer. Following the work of Krost et al. [105], in the first case the strain can be calculated at each depth of the layer by the slope of the curvature

$$\varepsilon(t_f) \sim \frac{\partial\kappa}{\partial t_f} \,, \tag{3.14}$$

while in the second case the strain of the layer is given by the secant

$$\varepsilon \sim \frac{\Delta\kappa}{\Delta t_f} . \tag{3.15}$$

However, from the in-situ curvature measurement alone it is neither possible to distinguish, which of both method is the correct one nor one can reveal the mechanism behind this strain relaxation phenomenon. Using the secant for the strain analysis, however, will give in any case the thickness averaged strain state of the layer. The build-up of compressive strain $\Delta\varepsilon$ is then calculated simply by subtracting of the strain state of the GaN overlayer and GaN buffer

$$\Delta\varepsilon^{curvature} = \varepsilon_{overlayer} - \varepsilon_{buffer} . \tag{3.16}$$

The results are given in Table 3.4. Unfortunately, strong fluctuations of the wafer curvature during the growth of the $Al_xGa_{1-x}N$ interlayer (caused probably by changes e.g. of the wafer temperature and/or reactor pressure) prevent a reliable evaluation of the strain state of the the $Al_xGa_{1-x}N$ interlayer.

3.3.3.2. XRD measurements

To determine the strain state of the GaN layers and the amount of relaxation of $Al_xGa_{1-x}N$ interlayers *after the growth* we use the XRD results given in Table 3.3. The easiest way to obtain the built up compressive strain in the GaN overlayer is to compare the out-of-plane lattice parameters from $\theta/2\theta$-scans and then to calculate from this difference $\left(\Delta\varepsilon_{zz}^{XRD}\right)$ the build-up of compressive strain by assuming tetragonal distortion

$$\Delta\varepsilon^{XRD} = -\frac{C_{33}}{2C_{13}}\Delta\varepsilon_{zz}^{XRD} = -\frac{C_{33}}{2C_{13}}\left(\frac{c_{GaN\,overlayer}}{c_{GaN\,buffer}} - 1\right) . \tag{3.17}$$

The amount of strain relaxation of $Al_xGa_{1-x}N$ interlayers can be calculated via the in-plane lattice parameters, which have been obtained from asymmetric $\left(11\bar{2}4\right)$ reciprocal space maps, according to

$$\delta_{AlGaN}^{XRD} = \frac{a_{AlGaN\,interlayer}}{a_{GaN\,buffer}} - 1 . \tag{3.18}$$

However, due to the overlap of the 2 GaN peaks in the reciprocal space maps, the evaluation of the in-plane lattice parameter of the GaN buffer is not directly possible and we have to choose a similar approach as just before by using again the out-of-plane lattice parameter and assuming tetragonal distortion of the GaN buffer

$$\delta_{AlGaN}^{XRD} = \frac{2\cdot\left(q_x^{AlGaN}\right)^{-1}}{a_{GaN\,buffer}} - 1 \text{ with} \tag{3.19}$$

$$\begin{aligned} a_{GaN\,buffer} &= a_{relaxed\,GaN} \cdot \left(1 + \varepsilon_{xx\,buffer}\right) \\ &= a_{relaxed\,GaN} \cdot \left(1 - \frac{C_{33}}{2C_{13}}\,\varepsilon_{zz\,buffer}\right) \\ &= a_{relaxed\,GaN} \cdot \left(1 - \frac{C_{33}}{2C_{13}} \left(\frac{c_{GaN\,buffer}}{c_{relaxed\,GaN}} - 1\right)\right). \end{aligned} \tag{3.20}$$

The results are listed in Table 3.4 for the same 3 samples as in the case of the TEM- and in-situ wafer curvature strain analysis .

Let us now briefly address an important point that has to be considered particularly for the interpretation of the XRD strain measurements for the samples under investigation. Our XRD measurement of the wedge sample has revealed a vertical strain gradient in the GaN overlayer[14]. Because of the depth integrating character of the XRD technique, one has to keep in mind, that the peak position of the GaN overlayer will, however, correspond rather to the average strain state of this layer.

3.3.3.3. Comparison of results

Table 3.4 summarises the values for the build-up of compressive strain in the GaN overlayer and the amount of strain relaxation for $Al_xGa_{1-x}N$ interlayers obtained from the different calculation methods (TEM analysis, ex-situ XRD and in-situ wafer curvature measurements) for 3 different samples with $18/26\ nm$ low temperature and $35\ nm$ high temperature $Al_{0.75}Ga_{0.25}N$ interlayers in a GaN films grown on Si (111). The comparison of the results reveals that within the accuracy of our TEM model the calculated values for the build-up of compressive strain in the GaN overlayer as well as the relaxation of $Al_xGa_{1-x}N$ interlayers are in good agreement with the macroscopic strain measurements. The accuracy of our TEM method is mainly limited by the statistical error due to fluctuations in the dislocation line spacing. The accuracy becomes better as the degree of relaxation (i.e. the number of misfit dislocations per unit length) increases. Our microscopic model, i.e. the asymmetry in plastic relaxation at both interfaces of the $Al_xGa_{1-x}N$ interlayer, thus correctly describes the strain-engineering process and is valid to explain the macroscopic effect of the build-up of compressive strain by $Al_xGa_{1-x}N$ interlayers. Our experimental observations and our phenomenological model are furthermore consistent with previous reports in literature about the origin for the build-up of compressive strain by $Al_xGa_{1-x}N$ interlayer. Bläsing et al. [28] and Reiher et al. [29] have studied thin AlN interlayer by XRD and observed a decoupling of GaN layers separated by low temperature AlN interlayer. They proposed that thin low temperature AlN interlayer grow incoherent and thus would induce a compressive strain in the subsequent GaN layer. In contrast to that they found that

---

[14] This observation is fully consistent with reports in literature on a gradual relief of the built up compressive strain in the GaN overlayer [106, 107, 108, 109, 110, 111] and is explained by the inclination of a-type threading dislocations from the growth direction towards $< 1\bar{1}00 >$. We have also observed the inclination of threading dislocations in TEM micrographs (e.g. see Fig. 4.1 (d) and (f) in the next chapter) but we do not want to go into detail of this mechanism as it has already been intensively discussed in literature [106, 107, 108].

Table 3.4.: Comparison of results of the quantitative analysis of the strain relaxation in $Al_xGa_{1-x}N$ interlayers (δ_{AlGaN}) and the build-up of compressive strain in GaN overlayers ($\Delta\varepsilon$). Number in brackets denote the errors.

sample	δ_{AlGaN} [%]		$\Delta\varepsilon$ [%]			
			first 100 nm		average	
	TEM	XRD	TEM	curvature	curvature	XRD
35 nm high temperature $Al_{0.75}Ga_{0.25}N$ interlayer [14]	-1.02 (10)	-0.92 (9)	-0.46 (17)	-0.42 (3)	-0.23 (2)	-0.23 (2)
26 nm low temperature $Al_{0.75}Ga_{0.25}N$ interlayer [15]	-0.59 (9)	-0.55 (9)	-0.30 (12)	-0.34 (3)	-0.27 (2)	-0.25 (2)
18 nm low temperature $Al_{0.75}Ga_{0.25}N$ interlayer [16]	-0.34 (5)	-0.45 (9)	-0.17 (7)	-0.24 (3)	-0.17 (2)	-0.19 (2)

---

[15] sample with a 1.7 μm GaN overlayer

[16] sample with a 1.0 μm GaN overlayer

[17] sample with a 0.7 μm GaN overlayer

thin high temperature AlN interlayers with the same nominal thickness grow pseudomorphic and do not produce compressive strain. Our results and reports from several other authors [24, 25, 26, 112], however, demonstrate that high temperature $Al_xGa_{1-x}N$ interlayers relax as well and thus induce also compressive strain into the subsequent GaN layer, very similar to the case of low temperature $Al_xGa_{1-x}N$ layers. The reason for this open discrepancy will be investigated in detail in the next chapter.

Let us finally compare the results of the ex-situ (XRD and TEM) and in-situ (wafer curvature monitoring) methods. One the one side, as mentioned just before, the additional built up compressive strain $\Delta\varepsilon$ during the initial growth stage of the GaN overlayer, as determined from the in-situ wafer curvature measurement (slope of the curve), agrees well with the value obtained from ex-situ TEM data. One the other hand, the results for the average built up compressive strain in the GaN overlayer from ex-situ XRD and in-situ curvature measurement (secant of the curve) also agree well. Furthermore, our TEM investigation of samples grown on silicon, sapphire and GaN substrates show no difference in the microstructural features, which are relevant for the strain relaxation process (misfit dislocation networks are present at the both interfaces of $Al_xGa_{1-x}N$ interlayers, however, with an asymmetry in the dislocation line spacing between the upper/lower interface). All these findings indicate that $Al_xGa_{1-x}N$ interlayers relax during growth and that the thermally induced stress during the cool-down does not affect the strain relaxation process, at least within the precision of our measurements.

3.4. Summary of this chapter

In this chapter we have shown that strain-engineering with $Al_xGa_{1-x}N$ interlayers, i.e. the build-up of compressive strain in the subsequent layer, is based on an asymmetry in plastic strain relaxation between the interfaces of $Al_xGa_{1-x}N$ interlayers. Misfit dislocation networks consisting of mainly a-type dislocations occur at both interfaces. However, the line spacing of misfit dislocations is always higher (i.e. the amount of plastic relaxation is smaller) at the upper interface of $Al_xGa_{1-x}N$ interlayers than at the lower one. This difference finally leads to the build-up of compressive strain in the layer grown on top of the $Al_xGa_{1-x}N$ interlayer. Our studies reveal that this phenomenon occurs qualitatively independently on growth parameters of the $Al_xGa_{1-x}N$ interlayer like the thickness and deposition temperature. Also the choice of the substrate where the film is grown on and thus the thermal stress during cool-down after the growth does not significantly affect the strain relaxation process. However, with increasing thickness of the $Al_xGa_{1-x}N$ interlayer also the amount of the generated compressive strain increases.

4. Growth and relaxation mechanism of (0001)-oriented III-nitride heterostructures

4.1. Aim of this chapter

Although plastic relaxation of strained heterostructures in (0001)-oriented III-nitride wurtzite films has been widely studied in literature, see e.g. reports about relaxation of $Al_xGa_{1-x}N$ on AlN [97, 107, 113, 114, 115, 116], $Al_xGa_{1-x}N$ on GaN [30, 114, 117, 118, 119] and $In_xGa_{1-x}N$ on GaN [31, 33, 120], several questions remain unsolved so far. For example: (i) Why can compressively strained layers be grown up to ten times as thick as tensile strained layers before plastic relaxation occurs (compare e.g. Ref. [116] with [119])? (ii) Why are $Al_xGa_{1-x}N$ interlayers grown at lower temperature (partly) relaxed but deposition at higher temperature results in pseudomorphic growth [29, 105]?

Moreover, there is so far no quantitative model in the literature, which considers the dislocation formation mechanism, i.e. nucleation and glide of dislocations[1]. This is, however, a particular intricate problem for (0001)-oriented strained III-nitride wurtzite heterostructures under plane stress conditions (i.e. thin 2-dimensional layers), since in this case the resolved shear stresses, as driving force for dislocation nucleation and glide, are zero for the primary slip-systems (see chapter 2.1 for an overview about the slip-systems in wurtzite films). Plastic relaxation of (0001)-oriented strained III-nitride wurtzite films is thus typically inhibited and basic concepts for modelling plastic relaxation like the Matthews-Blakeslee critical thickness model [122] do not give meaningful results.

The aim of this chapter is therefore to gain a deeper quantitative understanding about the microscopic mechanism behind the plastic relaxation process of (0001)-oriented strained III-nitride wurtzite films. As a first step we will sort out the dominant mechanism for formation of misfit dislocations at the interfaces of $Al_xGa_{1-x}N$ interlayers - bending of existing threading dislocations or nucleation of new dislocations. For this purpose we will compare the dislocation structure in the GaN layers above and below $Al_xGa_{1-x}N$ interlayers buffer in samples, which have been grown either heteroepitaxially on a Si (111) substrate or homoepitaxially on a bulk GaN (0001) substrate[2] resulting in different threading dislocation density in the GaN buffer. In the second part of the experimental section we study the initial stages of growth and plastic relaxation of high temperature as well as low temperature $Al_xGa_{1-x}N$ interlayers and GaN overlayers on top of relaxed $Al_xGa_{1-x}N$ interlayers. Therefore, series of dedicated samples where growth of the $Al_xGa_{1-x}N$ interlayer and the subsequent GaN overlayer has been stopped at different stages of the growth will be investigated by TEM and atomic force microscopy (AFM). Using these experimental results together with finite element method calculations we will establish a quantitative model for the plastic relaxation mechanism of $Al_xGa_{1-x}N$ interlayers as dependent on growth, which also includes the dislocation formation kinetics. Thereby we will develop generalised framework that is applicable for any (0001)-oriented strained III-nitride heterostructure. Finally, we will discuss the implications of the $Al_xGa_{1-x}N$ interlayer growth parameters on the strain engineering process.

---

[1] Holec et al. [34, 121] have indeed quantitatively treated plastic relaxation of (0001)-oriented strained III-nitride films using an energy minimisation approach (as shown by Freund and Suresh [39] this approach gives same results as the Matthews-Blakeslee-model [122]), but they have neglect the dislocation formation process. The agreement between theoretically predicted and experimentally observed critical thickness values is also rather poor: Vennegues et al. [30] determined for the case of AlN on GaN experimentally a critical thickness range for formation of a-type misfit dislocations of $3.5-8\ nm$, while the energy minimisation approach [34] predicts for the $\frac{1}{3} < 11\bar{2}0 > |\{0001\}$ slip-system (i.a. a-type misfit dislocations) a critical thickness of approximately $0.7\ nm$ $(2-3$ monolayers).

4.2. Experimental results

4.2.1. Analysis of the dislocation structure in the GaN film

Fig. 4.1 shows weak beam dark field TEM images of GaN films with $Al_xGa_{1-x}N$ interlayer grown on Si (111) and HVPE GaN (0001) substrates. Hardly surprising the density of threading dislocations in the GaN buffer ($\approx 10^9\,cm^{-2}$) below the $Al_xGa_{1-x}N$ interlayer and especially in the nucleation layer and step-graded $Al_xGa_{1-x}N$ buffer ($\approx 10^{11}\,cm^{-2}$) is much higher in the heteroepitaxially grown film than in the sample grown on the HVPE GaN substrate ($\leq 10^7\,cm^{-2}$). A comparison of micrographs recorded with different diffraction vectors of the same specimen region reveals, that almost all threading dislocations are visible in the weak beam dark field image recorded under $\mathbf{g} = \bar{1}100$ $\mathbf{g}(3\mathbf{g})$ weak beam conditions (right images), while a part of them are simultaneously visible also in the $\mathbf{g} = 0002$ $\mathbf{g}(3\mathbf{g})$ weak beam dark field images. This means that there are mainly a-type and a+c-type threading dislocations in the GaN film. In the case of the heteroepitaxially grown structure on a Si (111) substrate the ratio of a-type vs. a+c-type-dislocations in the GaN buffer below the $Al_xGa_{1-x}N$ interlayer is approximately 2 : 1, whereby the threading dislocation density in this layer is in the range of $1-2\cdot10^9\,cm^{-2}$.

Regarding the dislocation structure in the GaN layer grown on top of the $Al_xGa_{1-x}N$ interlayer we find 3 distinct differences compared to the GaN buffer: (i) We observe in all investigated samples initially an increase of the overall dislocation density in the GaN overlayer directly above the $Al_xGa_{1-x}N$ interlayer (especially in the first 200 *nm*). This becomes particularly evident for the sample grown on the GaN substrate (see

---

[2] We have used a commercially available bulk GaN substrate, which has been grown by hydride vapour phase epitaxy (HVPE) on a sapphire (0001) substrate.

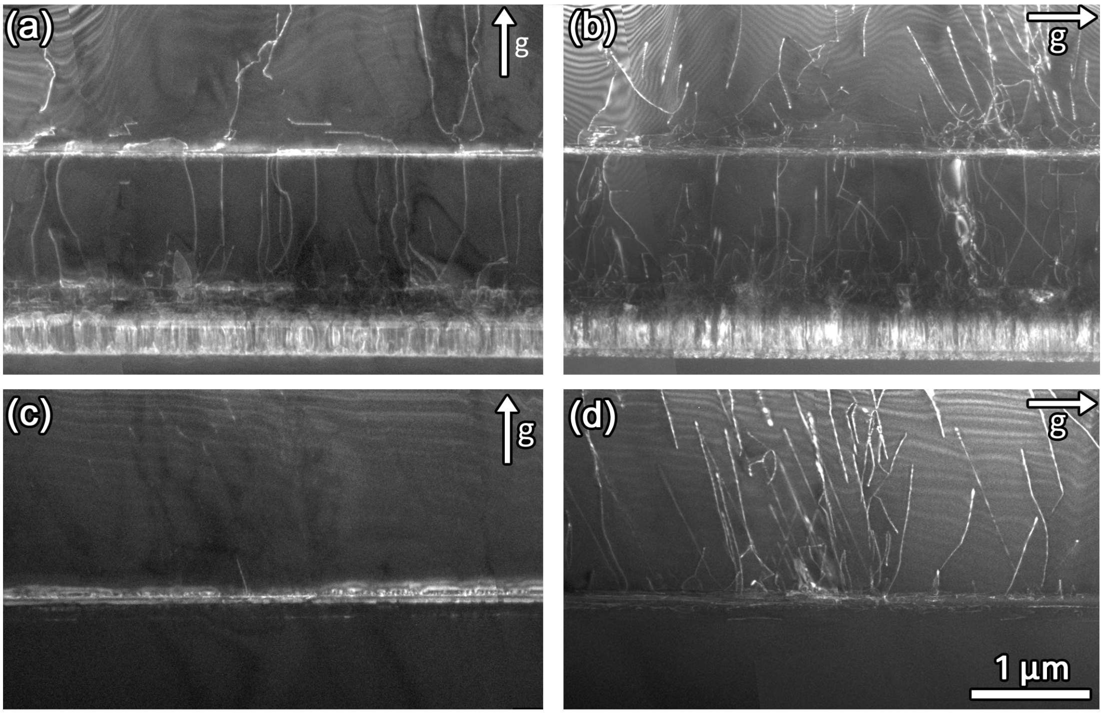

Figure 4.1.: Cross-sectional weak beam dark field TEM micrographs of GaN films with $Al_xGa_{1-x}N$ interlayers grown on (a) and (b) a Si (111) and (c) and (d) a GaN (0001) substrate, respectively. Images on the left/right side show the same regions of the respective specimens but are recorded under $\mathbf{g} = 0002$/$\mathbf{g} = \bar{1}100$ **g(3g)** conditions, respectively. All images are on the same scale.

Fig. 4.1 (d)). From a $g \cdot b$ analysis we find that these new threading dislocations are all a-type dislocations. (ii) In contrast to that, the density of dislocations having a c-component decreases from the GaN buffer to the GaN overlayer. Interestingly, especially threading dislocation having a c-component tend to bend into the basal plane at the interface between the GaN buffer and the $Al_xGa_{1-x}N$ interlayer. On the other hand, formation of new a+c-type dislocations at the $Al_xGa_{1-x}N$ interlayer is observed much less frequently than of a-type dislocations. Consequently the ratio of a-type vs. a+c-type dislocations changes from the GaN buffer to the GaN overlayer from 2:1 to 5:1-10:1 in the case of the heteroepitaxially grown films. For the sample grown on the GaN substrates there are in both GaN layers almost only a-type threading dislocations. (iii) Another interesting results is that most of the threading dislocations in the GaN overlayer do not proceed along the growth direction (as it is approximately the case in the GaN buffer) but are initially inclined from the $[0001]$ direction by approximately 25°.

4.2.2. Initial stages of growth and relaxation at $Al_xGa_{1-x}N$/GaN and GaN/$Al_xGa_{1-x}N$ heterostructures

4.2.2.1. First growth stage of a high temperature $Al_xGa_{1-x}N$ interlayer

Figure 4.2 shows the first growth stage of a high temperature $Al_xGa_{1-x}N$ interlayer ($x \approx 0.75$, growth temperature$\approx$ 1050°C) where the growth has been stopped after deposition of approximately 11 *nm*. Under the given conditions the high temperature $Al_xGa_{1-x}N$ interlayer grows 2-dimensionally. The layer, however, is cracked. Cross-sectional STEM-HAADF imaging (Fig. 4.2 (a)) reveals, on the one side, that the cracks tips are atomically sharp and, on the other side, that the cracks do not only propagate through the high temperature $Al_xGa_{1-x}N$ interlayer but extend also a few nm into the GaN buffer. In average the depth of the cracks is 1.2 times the thickness of the $Al_xGa_{1-x}N$ interlayer. The crack pattern has been further investigated by SEM imaging (Fig. 4.2 (b)). We find that the cracks extend mainly along the $< 11\bar{2}0 >$- directions, but they do not necessarily form a closed network where each crack is bound by another one. Some of the cracks begin/end somewhere in the film. According to Hutchinson and Suo [123] such pattern corresponds to "surface cracks", i.e. cracks that are the nuclei for an extended crack network. The average spacing of adjacent parallel cracks is approximately 300 *nm*. Atomic force microscopy reveals that the surface of the high temperature $Al_xGa_{1-x}N$ interlayer between the cracks is atomically flat (monolayer steps can be seen in Fig. 4.2 (d)) and the width of the flat terraces is in the range of $50-100$ *nm*. Interestingly, the crack network appears in AFM topography images as an "elevation" with a z-height of approximately 0.5 *nm* above the mean value of the surrounding surface (corresponding to the bright lines in Fig. 4.2 (d)).

However, the absence of a dense misfit dislocation network in plan view TEM (Fig. 4.2 (c)) shows that at this growth stage plastic relaxation has not occurred yet. The contrast in the plan view weak beam dark field image arises from local lattice distortions caused by the cracks. Another interesting finding is the existence of a thin layer in the high temperature $Al_xGa_{1-x}N$ interlayer after a thickness of approximately 8 *nm*, which appears darker in the STEM-HAADF image than the $Al_xGa_{1-x}N$ interlayer matrix. This layer is found across the entire lateral range (several 100 μm) of the cross-sectional specimen, which was thin enough to be observed in the TEM. This points to an local increase of the Al concentration in the $Al_xGa_{1-x}N$ layer.

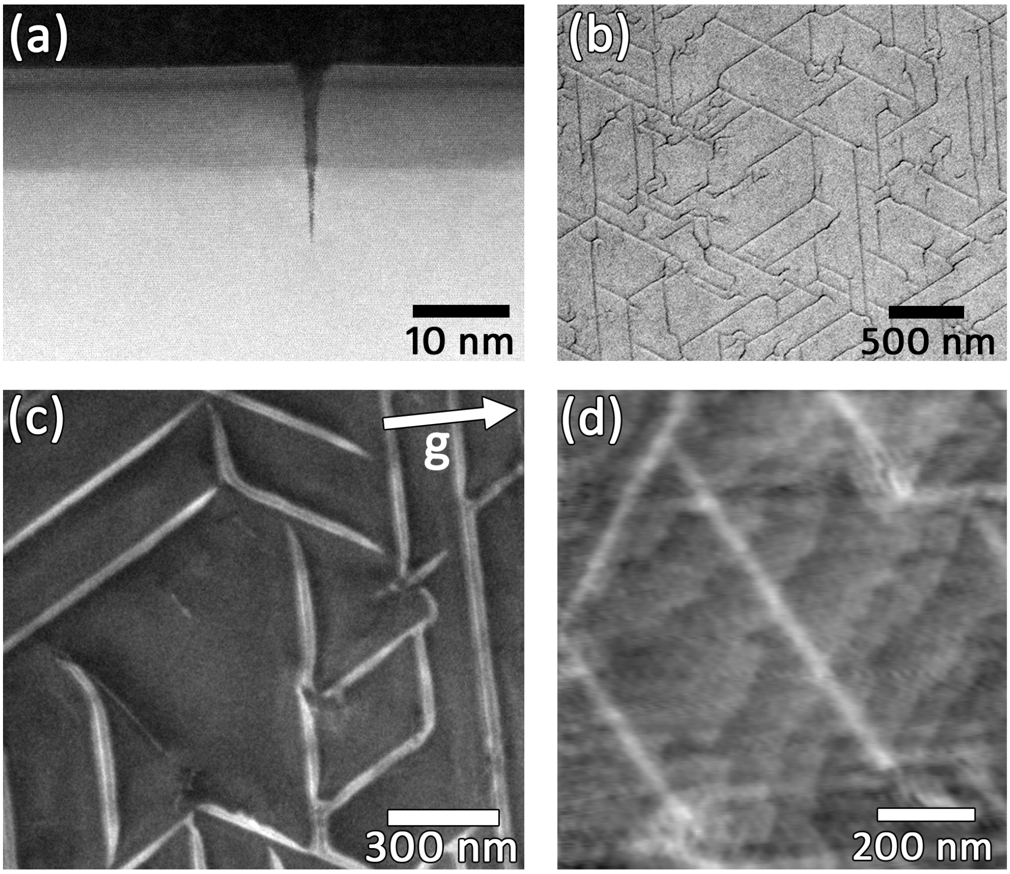

Figure 4.2.: First growth stage of a high temperature $Al_{0.75}Ga_{0.25}N$ interlayer. (a) cross-sectional STEM-HAADF image, (b) SEM image of the surface using secondary electrons (c) plan view weak beam dark field TEM for $\mathbf{g} = 1\bar{1}00$ $\mathbf{g(3g)}$ weak beam conditions and (d) AFM surface topography image (height scale is 2.5 *nm*).

4.2.2.2. First growth stage of a low temperature $Al_xGa_{1-x}N$ interlayer

In contrast to the high temperature $Al_xGa_{1-x}N$ interlayer, the low temperature layer (deposition temperature$\approx$ 800°C) grows 3-dimensionally as can be seen e.g. in the AFM topography image (Fig. 4.3 (d)). Cross-sectional STEM-HAADF imaging reveals a Stranski-Krastanov like growth with a transition towards island growth after an approximately 2 *nm* thin wetting layer (Fig. 4.3 (a)). At this growth stage the islands have a hemispherical shpae with a lateral size of the islands of typically $15-30$ *nm* and approximately 5 *nm* deep trenches between them. Because of the hemispherical shape one might question whether the islands are really crystalline $Al_xGa_{1-x}N$ or whether they have formed from liquid droplets. But high resolution STEM-HAADF imaging in Fig. 4.3 (b) unambiguously shows that the island have crystallised in the wurtzite structure. Same as in the case of the thin high temperature $Al_xGa_{1-x}N$ interlayer, plastic relaxation has not occurred yet for the 7 *nm* thin low temperature $Al_xGa_{1-x}N$ interlayer ($x \approx 0.75$). The contrast in the plan view weak beam image in Fig. 4.3 (c) is caused by local lattice distortions associated with the island edges.

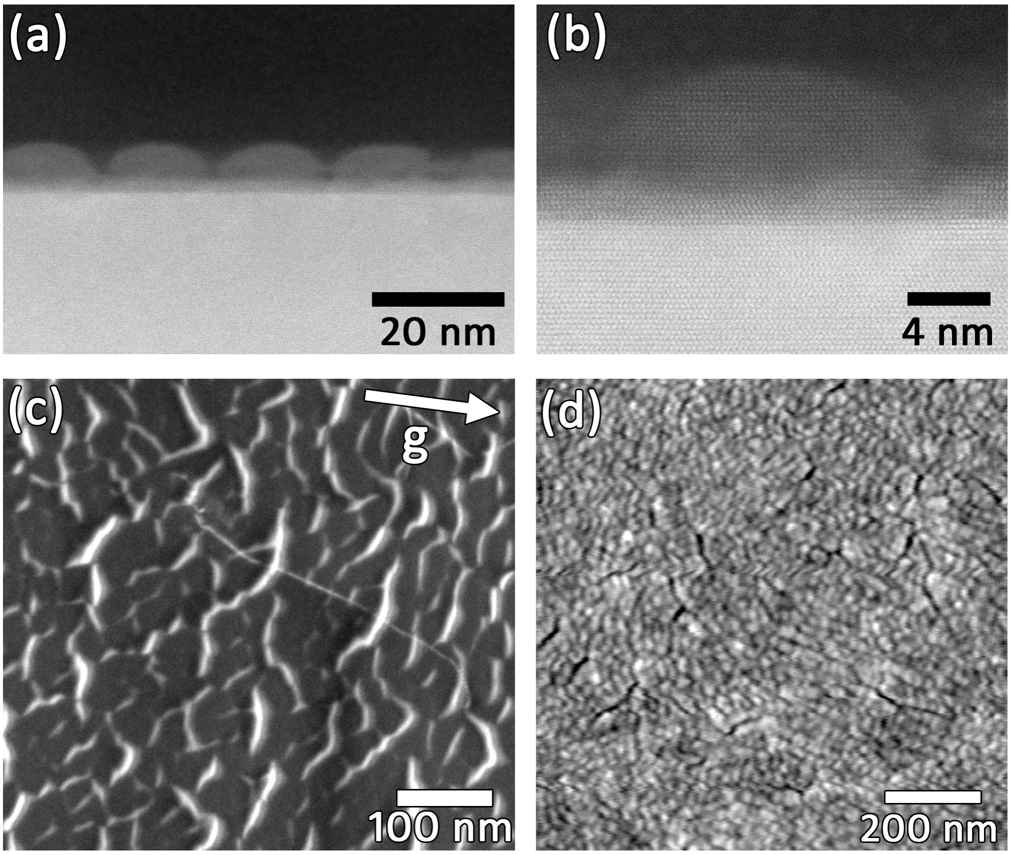

Figure 4.3.: First growth stage of a low temperature $Al_{0.75}Ga_{0.25}N$ interlayer. (a) and (b) cross-sectional STEM-HAADF images, (c) plan view weak beam dark field TEM under $\mathbf{g} = 11\bar{2}0$ **g(3g)** weak beam conditions of the same sample and (d) AFM surface topography image (height scale is 2.5 *nm*).

4.2.2.3. Second growth stage of a high temperature $Al_xGa_{1-x}N$ interlayer

The second growth stage of the high temperature $Al_xGa_{1-x}N$ interlayer corresponding to a layer thickness of approximately 35 nm is displayed in Fig 4.4. This sample has been grown on a sapphire (0001) substrate. In contrast to the first growth stage, we find for this sample a misfit dislocation network at the interface between the $Al_xGa_{1-x}N$ interlayer and GaN buffer. We want to emphasise again that not all misfit dislocations are located exactly at the interface but are vertically spread around it by up to 50 *nm*. However, the misfit dislocations tend to be arranged roughly in 2 planes as indicated by the 2 white triangles in Fig. 4.4 (a). A detailed plan view TEM analysis of the misfit dislocation network has already been carried out for a nominal identical sample, however, grown on a Si (111) substrate, in section 3.2.2 (see Fig. 3.5 on page 36). Just as a quick reminder, in section 3.2.2 we have shown that the misfit dislocation networks are formed mainly by 3 sets of a-type dislocations having bowed dislocation lines.

On the other hand, we find that the surface morphology of the high temperature $Al_xGa_{1-x}N$ interlayer has not much changed compared to the first growth stage, i.e. the

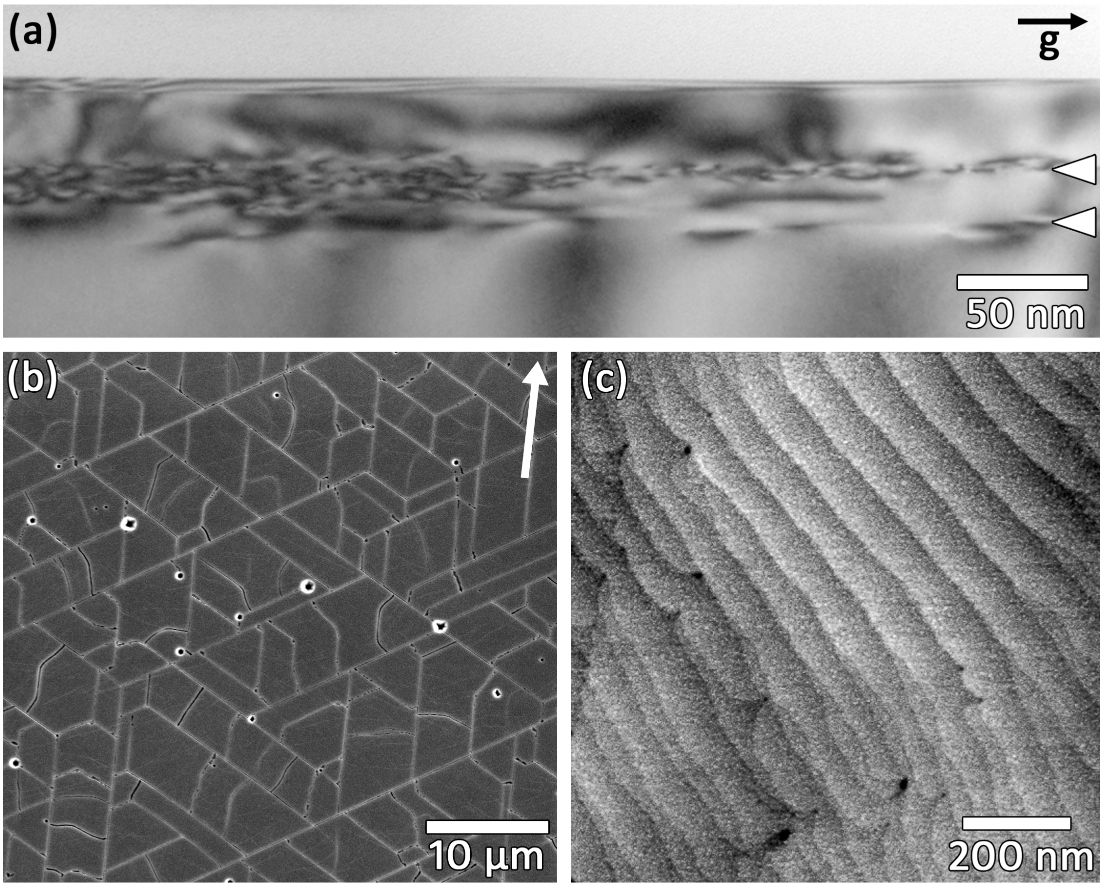

Figure 4.4.: Second stage of the growth of a high temperature $Al_{0.75}Ga_{0.25}N$ interlayer. The sample was depostited on a sapphire (0001) substrate. (a) cross-sectional bright-field TEM image recorded under $\mathbf{g} = 11\bar{2}0$ two-beam conditions, white triangles indicate misfit dislocations. (b) SEM image of the surface using secondary electrons and (c) AFM surface topography image (height scale is 1.3 *nm*). The white arrow in (b) is along $< 11\bar{2}0 >$.

layer is cracked but has still an atomically flat surface between the cracks with a similar average width of the terraces of approximately 70 *nm* (see AFM topography image in Fig. 4.4 (c)). However, SEM imaging (Fig. 4.4 (b)) reveals that the crack pattern deviates from that of the sample with the thinner high temperature $Al_xGa_{1-x}N$ layer. For the present sample, all cracks propagate laterally (predominantly along the $< 11\bar{2}0 >$-directions) until they are bounded by another one. According to common terminology they are called “channelling cracks” [123]. The average spacing of adjacent parallel cracks is approximately 4.5 *µm* for this sample.

4.2.2.4. Second growth stage of a low temperature $Al_xGa_{1-x}N$ interlayer

For the second growth stage of a low temperature $Al_xGa_{1-x}N$ interlayer we have investigated 2 samples - one sample, which has a 16 *nm* thick low temperature $Al_{0.75}Ga_{0.25}N$ interlayer and a second one where the growth was stopped after deposition of a 70 *nm* thick low temperature $Al_{0.75}Ga_{0.25}N$ interlayer. However, the first sample has been grown with a GaN overlayer on top of the $Al_xGa_{1-x}N$ interlayer. Nevertheless, as we will see, the morphology of the low temperature $Al_xGa_{1-x}N$ interlayer is not altered significantly by the deposition of the GaN overlayer. The experimental results are displayed in Fig. 4.5 and Fig. 4.6. Similar to the case of the high temperature $Al_xGa_{1-x}N$ sample an increase of the thickness of the low temperature $Al_xGa_{1-x}N$ interlayer leads to the generation of misfit dislocations at the interface to the GaN buffer (indicated by white triangles in Fig. 4.5 (b)) and for even higher thicknesses a dense misfit dislocation network forms (indicated by a white triangle in Fig. 4.6 (a)). As a reminder: plan-view TEM imaging of the sample with the 70 *nm* thick low temperature $Al_{0.75}Ga_{0.25}N$ interlayer in chapter 3 (see Fig. 4.6 (e) on page 44) has shown that the misfit dislocation network is formed mainly by 3 sets of a-type dislocations having bowed dislocation lines. The average spacing of misfit dislocation lines is approximately 30 *nm* for this sample.

The surface morphology has been examined in the case of the 16 *nm* thin low temperature $Al_{0.75}Ga_{0.25}N$ interlayer by cross-sectional STEM-HAADF imaging (Fig. 4.5 (a)). Compared to the first growth stage the islands have partly coalesced to faceted mesa-like domains with lateral size between $15 - 100$ *nm* in the case of the sample with the 16 *nm* thin low temperature $Al_{0.75}Ga_{0.25}N$ interlayer. These domains are separated by V-shaped trenches, which have an average depth of $6 - 8$ *nm*. At the apex of some of these V-trenches nano-cracks proceed down to the $Al_{0.75}Ga_{0.25}N$/GaN interface. In the case of the sample with the 70 *nm* thick low temperature $Al_{0.75}Ga_{0.25}N$ interlayer without GaN capping cross-sectional TEM bright field imaging (Fig. 4.6 (a)) and AFM topography (Fig. 4.6 (b)) reveals that the mesa-like islands have further coalesced, however, the surface is still rough. After deposition of 70 *nm* low temperature $Al_{0.75}Ga_{0.25}N$, the average depth of the V-trenches is 6 *nm* and the spacing between the trenches is in the range of $50 - 100$ *nm*. However, none of the observed V-trenches reaches the $Al_{0.75}Ga_{0.25}N$/GaN interface. Interestingly, for this sample we also observe cracks in the $Al_xGa_{1-x}N$ interlayer (see left part of Fig. 4.6 (a) or Fig. 4.6 (c)).

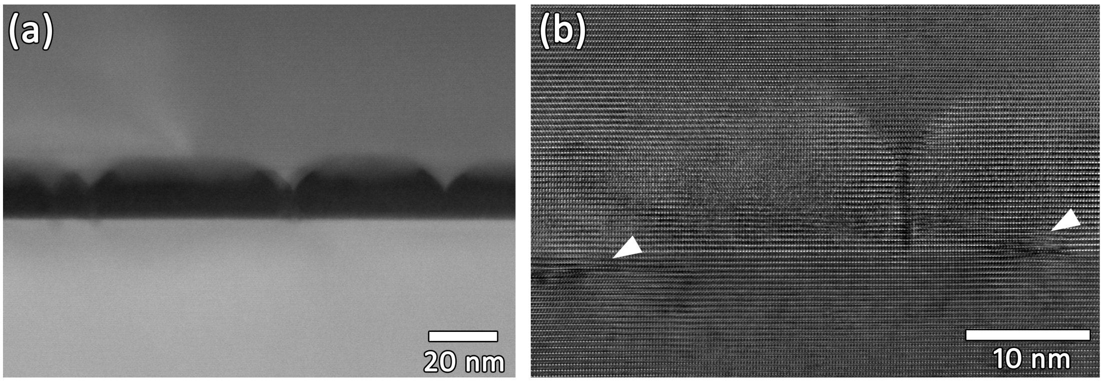

Figure 4.5.: (a) STEM-HAADF and (b) HRTEM images of a 16 *nm* thick low temperature $Al_{0.75}Ga_{0.25}N$ interlayer, which was capped with a GaN overlayer. White triangles in (b) indicate each a misfit dislocation at the lower interface of the low temperature $Al_{0.75}Ga_{0.25}N$ interlayer.

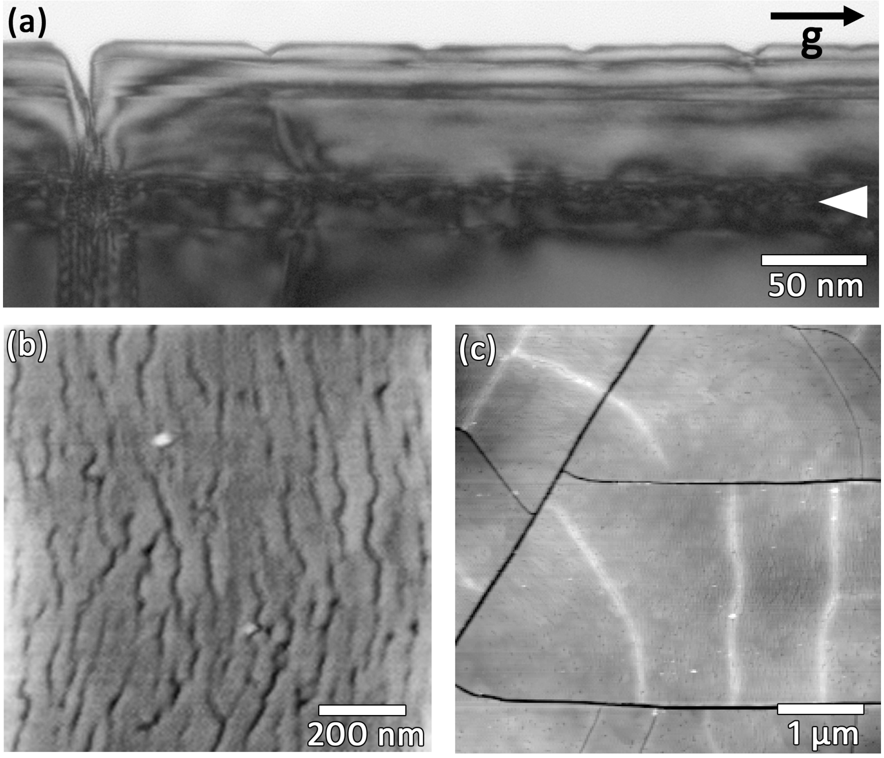

Figure 4.6.: Second stage of the growth of a low temperature $Al_{0.75}Ga_{0.25}N$ interlayer. (a) cross-sectional bright-field TEM image recorded under $\mathbf{g} = 11\bar{2}0$ two-beam conditions, the white triangle indicates the dense misfit dislocation network. (b) 1 x 1 μm^2 (height scale is 5 *nm*) and (c) 5 x 5 μm^2 (height scale is 10 *nm*) AFM surface topography image.

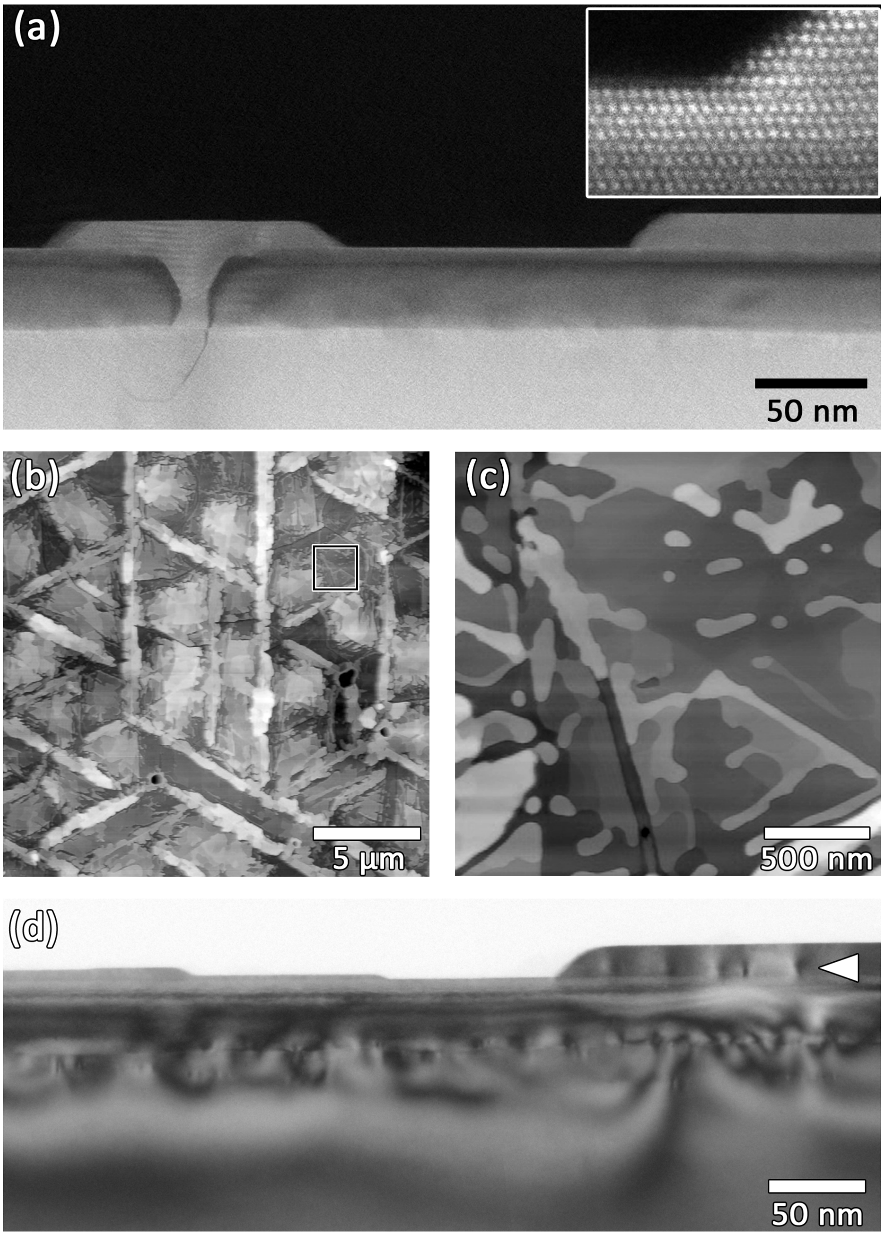

Figure 4.7.: First growth stage of the GaN overlayer on top of a relaxed high temperature $Al_{0.75}Ga_{0.25}N$ interlayer. (a) and (d) are cross-sectional STEM-HAADF and bright field TEM (multibeam conditions) images, respectively. The inset in (a) is a magnified view of an island edge in the GaN overlayer. The white triangle in (d) indicates misfit dislocations, which have just formed at the upper interface of the $Al_{0.75}Ga_{0.25}N$ interlayer. (b) and (c) show AFM surface topography images (height scale is 43 and 26 *nm*, respectively), whereby (c) is a magnified view for the region marked in (b).

4.2.2.5. First growth stage of a GaN overlayer on top of a relaxed high temperature $Al_xGa_{1-x}N$ layer

In the last step of the sample series we have deposited a thin film of GaN with a nominal thickness of 15 *nm* on top of a relaxed high temperature $Al_xGa_{1-x}N$ interlayer. First of all, for the applied growth conditions the GaN overlayer is characterised by a 3-dimensional surface morphology and consists of islands and mesa-like stripes, which are oriented along the three $< 11\bar{2}0 >$- directions (see Fig. 4.7 (b) and (c)). With the help of cross-sectional STEM-HAADF imaging we obtain more detailed information on the growth mode of the GaN overlayer. We find that stripes/islands of the GaN overlayer nucleate at 2 different positions: at cracks as well as on top of flat regions of the high temperature $Al_xGa_{1-x}N$ interlayer. In the second case, the GaN overlayer first completely wets the $Al_xGa_{1-x}N$ interlayer and the thickness of the GaN wetting layer is typically 2-5 monolayers (Fig. 4.7 (a)). Then in a second step, isolated islands nucleate on top of the GaN wetting layer. In contrast to this we attribute the growth of the $< 11\bar{2}0 >$-oriented stripes of the GaN overlayer to nucleation at cracks of the high temperature $Al_xGa_{1-x}N$ interlayer (as a reminder, these cracks are oriented along the three$< 11\bar{2}0 >$- directions). Nucleation of islands and stripes is then followed by lateral growth. Isolated islands as well as the $< 11\bar{2}0 >$-oriented stripes of the GaN overlayer have a faceted mesa-like shape and a lateral size in the range of 50 *nm* – 5 *µm*. The width-to-height aspect ratio is for both typically in the range of $10 - 100$. Additionally, it is worthwhile to note that the crack tips have blunted compared to the atomically sharp cracks during the initial growth stage of the high temperature $Al_xGa_{1-x}N$ interlayer.

Regarding plastic relaxation of the GaN overlayer we observe formation of misfit dislocations in GaN islands/stripes which exceed a height of about 15 *nm* (see white triangle in Fig. 4.7 (d)). In contrast to that, no plastic relaxation has occurred in the wetting layer and in the regions of the GaN overlayer, which consist of flat islands or mesas with a height of less than 10 *nm* (see left part of Fig. 4.7 (d)).

4.2.2.6. First growth stage of a GaN overlayer on top of a relaxed low temperature $Al_xGa_{1-x}N$ layer

The experimental results for the sample with the nominal 15 nm thin GaN overlayer grown on a relaxed low temperature $Al_xGa_{1-x}N$ interlayer are shown in Fig. 4.8. Cross-sectional STEM-HAADF and AFM topography images (see Fig. 4.8 (a) and (b)) illustrate that the GaN overlayer has again a 3-dimensional surface morphology. For the given sample the islands of the GaN overlayer have a width between $50 - 200$ *nm* and the pits between the islands which typically reach down to the GaN/$Al_xGa_{1-x}N$ interface have in average a depth of 10 *nm*. However, the growth mode of the GaN overlayer on top of the low temperature $Al_xGa_{1-x}N$ interlayer differs from that of the aforementioned sample with GaN deposition on a relaxed high temperature $Al_xGa_{1-x}N$ interlayer. Here the GaN islands have already partly coalesced, which is at contrast to the growth of GaN with the the same nominal layer thickness on top of a relaxed high temperature $Al_xGa_{1-x}N$ interlayer. Using Sauvola's method [124] for binarisation of the AFM topography image (Fig. 4.8 (b)) we find that the uncoalesced part (i.e. the pits between coalesced islands) comprises only 7% of the surface area for this sample. From cross-sectional STEM-HAADF images as those shown in Fig. 4.8 (a) one can suppose that for the given case the GaN overlayer nucleates in form of islands at V-shaped trenches at the surface of the low temperature $Al_xGa_{1-x}N$ interlayer. Because of the smaller spacing of these trenches in the low temperature $Al_xGa_{1-x}N$ interlayer (typically in the range of $15-100$ *nm*) compared to the large spacing of cracks in the high temperature $Al_xGa_{1-x}N$ interlayer (typically in the range of several 100 *nm* – µ*m*) the density of nucleation sites for the GaN overlayer is higher for growth on the low temperature $Al_xGa_{1-x}N$ interlayer. Consequently, the growth mode of the GaN overlayer on top of the low temperature $Al_xGa_{1-x}N$ interlayer is characterised by nucleation of islands with a high island density followed by fast coalescence of the layer.

Misfit dislocations can be seen at the interface between GaN overlayer and low temperature $Al_xGa_{1-x}N$ interlayer in cross-sectional dark field images (Fig. 4.8 (c) and (d)). At least some of the observed misfit dislocations probably stem from bended threading dislocations, which originate from the plastic relaxation process at the lower interface of the $Al_xGa_{1-x}N$ interlayer. In addition, it is noteworthy that the density of threading dislocations in the low temperature $Al_xGa_{1-x}N$ interlayer is much higher than for the high temperature $Al_xGa_{1-x}N$ case.

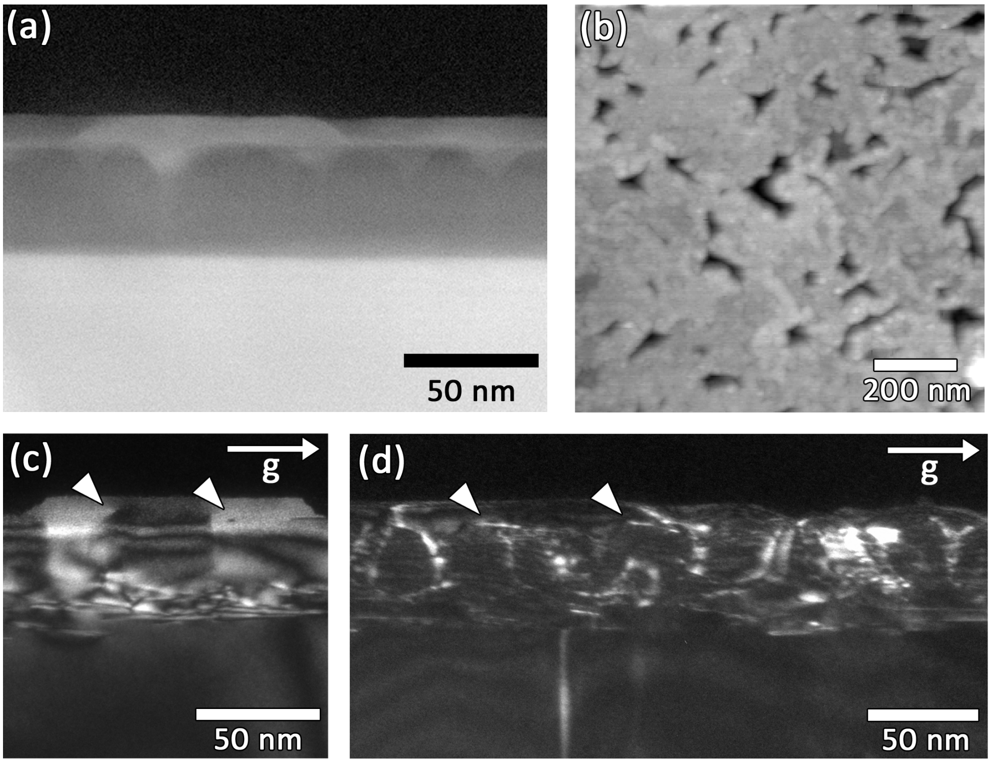

Figure 4.8.: First growth stage of the GaN overlayer on top of a relaxed low temperature $Al_{0.75}Ga_{0.25}N$ interlayer. (a) cross-sectional STEM-HAADF image, (b) AFM surface topography image (height scale is 13 *nm*). (c) and (d) cross-sectional dark field and weak beam dark field images, both recorded for $\mathbf{g} = 1\bar{1}00$. White triangles indicate each a misfit dislocation at the upper interface of the low temperature $Al_{0.75}Ga_{0.25}N$ interlayer.

4.2.3. Summary of experimental results

For sake of clarity we want to briefly summarise the most important experimental observations (from this and the previous chapter 3), which will be in the following relevant for modelling and discussion of the plastic relaxation mechanism. These are:

- During the initial stage of growth of (0001)-oriented $Al_xGa_{1\text{-}x}N$/GaN and GaN/$Al_xGa_{1\text{-}x}N$ heterostructures the strain is elastically relaxed due to either island growth or cracking. Plastic relaxation takes place only beyond a certain critical thickness at a later stage of growth.

- The critical thickness for the onset of plastic relaxation at the $Al_xGa_{1\text{-}x}N$/GaN heterointerface depends on the growth mode of the $Al_xGa_{1\text{-}x}N$ interlayer. For an aluminium content of approximately $x \approx 75\%$ the critical thickness is for samples exhibiting 3-dimensional island growth (in our case for low temperature $Al_xGa_{1\text{-}x}N$) between $5 - 10$ *nm*, and is thus lower than for samples, which show 2-dimensional growth and cracking (in our case high temperature $Al_xGa_{1\text{-}x}N$). In latter case the $Al_xGa_{1\text{-}x}N$/GaN interface is for the same aluminium content coherent even at a thickness of 11 *nm*.

- Plastic relaxation at the interfaces of $Al_xGa_{1\text{-}x}N$ interlayers is caused predominantly by a-type dislocations. Formation of a-type misfit dislocation networks does not require the presence of threading dislocations in the buffer below the $Al_xGa_{1\text{-}x}N$ interlayer.

- The degree of plastic relaxation of the $Al_xGa_{1\text{-}x}N$ interlayer increases with its thickness.

4.3. Quantitative modelling of the strain relaxation process

Plastic relaxation of III-nitride heterostructures has been widely studied in literature [30, 31, 33, 34, 108, 113, 114, 117, 118, 119, 120]. There exist two major models concerning plastic relaxation by a-type misfit dislocations that consider the dislocation formation mechanism. i) Several authors [30, 31, 32, 114, 125] proposed a *"co-operative mechanism"* [30], that starts from a morphology modification followed by introduction of a-type misfit dislocations into the film at island edges, V-pits and/or crack tips, respectively. ii) Liu et al. [33] suggested an alternative model: a *"punch out mechanism",* where simultaneous slip of two a+c-type dislocations having the same a-component but opposite c-component on oppositely inclined pyramidal planes would result in a-type misfit dislocations. Both models, however, treat the dislocation formation process only in a qualitative manner. On the other side, there are models, which treat the problem quantitatively (like Holec et al. [34] using an energy minimisation approach) but neglect the kinetics of formation of a-type misfit dislocations, i.e. nucleation and glide. This is, however, of particular importance for (0001)-oriented biaxially strained heterostructures of III-nitride wurtzite films, since in this case typically no resolved shear stresses are present in the primary slip-systems (prismatic or basal planes) and formation of a-type dislocations is prevented.

Our aim in the following is to go beyond these qualitative considerations and to establish with the help of our experimental results and finite element calculations a quantitative model, which describes relaxation of $Al_xGa_{1-x}N$ interlayers as dependent on the growth morphology and includes nucleation and glide of a-type dislocations into the heterointerface. To develop our model, we will proceed as follows: First we will identify the relevant mechanisms, which dominate plastic relaxation at the interfaces of $Al_xGa_{1-x}N$ interlayers. In the second step we will perform finite element calculations to obtain the lateral distribution of the shear stress on relevant slip planes for typical growth morphologies and to estimate the effect of elastic relaxation. Finally, in the third and forth step we will consider nucleation and glide of a-type dislocation half-loops, respectively, to estimate, on the one side, the critical thickness for plastic relaxation and, on the other side, to analyse, whether strain relaxation is limited in the present case by either the nucleation or glide process.

4.3.1. Identification of the relevant relaxation mechanism

In chapter 3 we have seen that the lattice mismatch at the interfaces of $Al_xGa_{1-x}N$ interlayer is mainly relaxed by a-type misfit dislocations, while a+c-type misfit dislocations typically appear ten times less frequently. We will neglect the latter one therefore in the following considerations and will focus on the formation mechanism of a-type misfit dislocations. In principle there are two possibilities: (i) homogeneous nucleation and glide of dislocation half-loops or (ii) glide of a pre-existing threading dislocations under lattice mismatch induced stress and deposition of a misfit dislocation segment into the heterointerface (Matthews-Blakeslee-model). Though we find experimental hints for both mechanisms there is clear evidence that glide and extension of threading dislocations into the interface is of minor importance. This come from the following two observations: (i) In the case of the sample that was grown on a HVPE GaN substrate a dense network of misfit dislocation forms at the interfaces of the $Al_xGa_{1-x}N$ interlayer despite of the fact that the density of pre-existing threading dislocations is low ($\rho_{TD} \leq 10^7\,cm^{-2}$). Similar results were found by Ren et al. [115] in the case of $Al_xGa_{1-x}N$ layers grown on bulk AlN substrates which had threading dislocation densities of $\rho_{TD} < 10^5\,cm^{-2}$. This suggests that that pre-existing threading dislocations are not a necessary prerequisite for formation of a-type misfit dislocations. (ii) For all samples the density of a-type threading dislocations in the GaN overlayer in the first 200 *nm* directly above the $Al_xGa_{1-x}N$ interlayer is higher than that in the GaN buffer. This is particular obvious for the homoepitaxially grown film (see Fig. 4.1 (c) and (d)). The same phenomenon was also reported in literature [30, 126, 127]. (iii) As mentioned before a-type misfit dislocations appear typically ten times more frequently than a+c-type misfit dislocations. In contrast to that the ratio of a-type vs. a+c-type threading dislocations in the GaN buffer is only about 2:1.

All results taken together show that plastic relaxation at the interfaces of $Al_xGa_{1-x}N$ interlayer is dominated by nucleation of a-type dislocation half-loops if the threading dislocation density in the buffer is small enough ($\leq$ low $10^9\,cm^{-2}$) and if the thickness of the $Al_xGa_{1-x}N$ layer is sufficiently high (more than approximately $10-15$ *nm* for $Al_{0.75}Ga_{0.25}N$).

Let us now identify the relevant slip-system on which nucleation and glide of a-type dislocation half-loops may take place. In the wurtzite lattice a-type dislocations can glide on either $\{1\bar{1}00\}$ prismatic, $\{1\bar{1}0l\}$ pyramidal (with $l = 1,2,...$) or $\{0001\}$ basal planes (see slip-systems in the wurtzite lattice in Fig. 2.1 on page 6). In the first two cases the dislocations could in principle nucleate at the growth surface and then could glide down towards the heterointerface. However, for (0001) oriented wurtzite films there are no driving forces for the $\frac{1}{3} < 11\bar{2}0 > | \{1\bar{1}00\}$ and $\frac{1}{3} < 11\bar{2}0 > | \{1\bar{1}01\}$ slip-systems because the resulting dislocation segment in the interface would have a pure screw character and thus would not relieve misfit strain.

The only remaining possibility is to form a-type misfit dislocations half-loops via the $\frac{1}{3} < 11\bar{2}0 > | \{0001\}$ slip-system. This mechanism is strongly corroborated by the bowed line direction of a-type misfit dislocations in the interfacial plane (see results from the plan view TEM analysis in Fig. 3.5). This is an astonishing finding, since in the case of 2-dimensionally grown (0001)-oriented strained wurtzite films no shear stresses are present in the basal planes. Formation of a-type misfit dislocations via the $\frac{1}{3} < 11\bar{2}0 > | \{0001\}$ slip-system can only be explained if the strained layers' surface or interface deviates from planarity, i.e via a 3-dimensional growth morphology. This is in fact supported by our studies of the initial stages of growth in section 4.2.2. The surface morphology of the $Al_xGa_{1-x}N$ interlayer as well as of the GaN overlayer clearly deviates from a perfect 2-dimensional film during the relevant growth stages: the layers are either cracked or grow in form of hexagonal faceted islands. Moreover, our TEM results suggest that a-type misfit dislocations are generated at both interfaces of the $Al_xGa_{1-x}N$ interlayer either at the edges of islands (see Fig. 4.7 (d) on page 70) or at crack tips (see in the left part of the $Al_xGa_{1-x}N$ interlayer in Fig. 3.2 (c) on page 31). All these findings lead us to conclude that a-type misfit dislocations at the interfaces of $Al_xGa_{1-x}N$ interlayer are introduced via the $\frac{1}{3} < 11\bar{2}0 > | \{0001\}$ slip-system driven by a redistribution of strain due to a 3-dimensional surface morphology.

4.3.2. Finite Element Calculations

In the following we will perform finite element calculations for typical morphologies, which we observe in experiments (i.e. for a crack network and island growth), to obtain the lateral distribution of the shear stress and to estimate the effect of the 3-dimensional morphology on elastic relaxation. Details of the calculation as well as the range of geometry parameters (width-to-height aspect ratio, shape of islands, surface coverage rate of islands, inclination angle of crack facets/island side-facets, propagation depth of cracks), which we consider, are given in appendix B.

Figure 4.9 (a), (b) and (c), (d) show the in-plane strain ε_{xx} and the strain energy density around a crack and around an isolated island having the shape of a hexagonal truncated pyramid, respectively. The effect of the 3-dimensional morphology on elastic relaxation can be clearly seen for both types of geometry. The strongest elastic relaxation occurs at the edges of adjacent free surfaces (crack facets/island side-facets and top (0001) facet). To quantify the degree of strain relaxation as dependent on the geo-

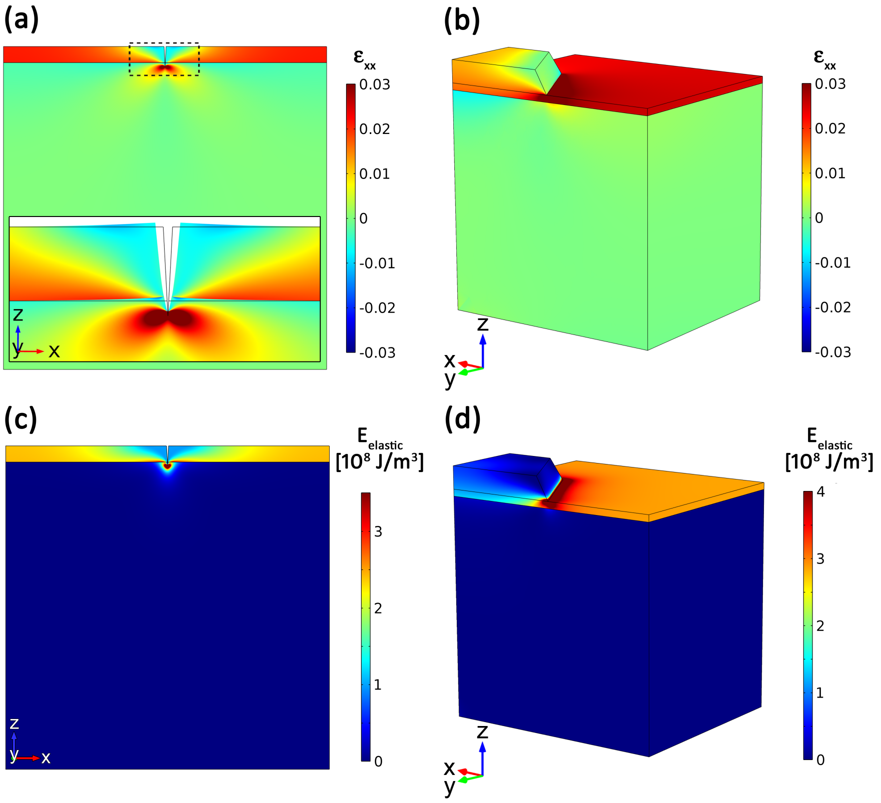

Figure 4.9.: Upper and lower images show the in-plane strain ε_{xx} and the strain energy density for the case of (a) and (c) cracking and (b) and (d) island growth, respectively. The inset in (a) is a magnified view of the crack and shows also the upwards bending of the film in the vicinity of the crack.

metry we have calculated the ratio of the elastic strain energy in the elastically relaxed layer ($E_{elastic}$) the strain energy of a biaxially strained layer in the plain stress state ($E^0_{elastic}$). The elastic energy in the relaxed layer is given by

$$E_{elastic} = \frac{1}{2}\int \sigma \cdot \varepsilon \, dV. \tag{4.1}$$

As can be seen from Fig. 4.10 the degree of elastic relaxation depends mainly on the width-to-height aspect ratio of the geometries: the strain relaxation increases with decreasing aspect ratio w/h. Other parameter like the inclination angle of the island side-walls or crack facets, respectively, the penetration depth of the cracks or the shape of the islands (hexagonal truncated pyramid or hemispheric) each change the degree of elastic strain relaxation typically by less than 5 %.

Fig. 4.11 shows the shear stress $\sigma_{xz}^{crack/island}$ on the $\{0001\}$ planes for the same geometries as considered before. Not surprisingly, in the case of cracking and island growth of the (0001)-oriented $\mathrm{Al_xGa_{1\text{-}x}N}$/GaN heterostructure the redistribution of strain induces significant shear stresses in the $\frac{1}{3} < 11\overline{2}0 > | \{0001\}$ slip-system. Maximum shear stress is found at the crack tip and the island corner, respectively. The

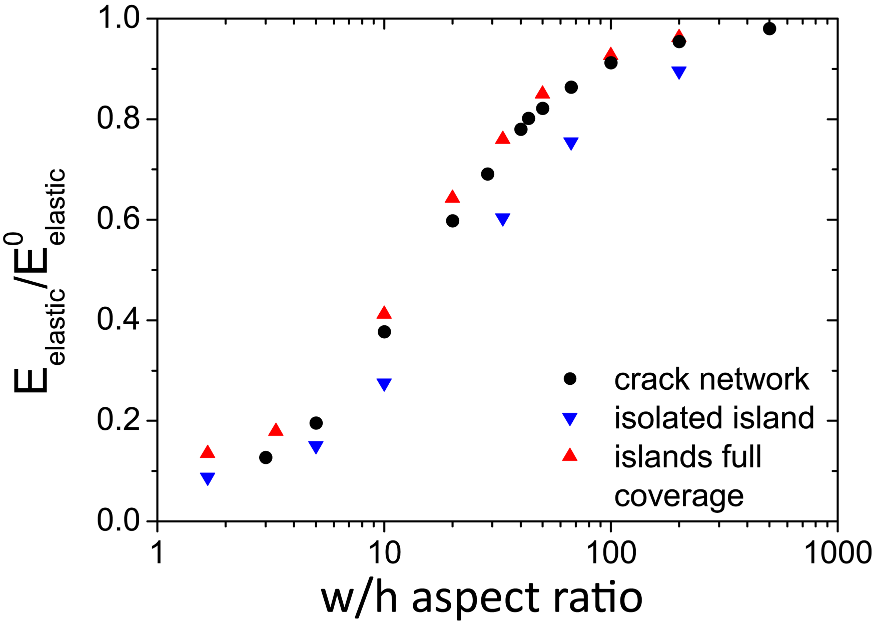

Figure 4.10.: Ratio of the elastic energy $E_{elastic}$ stored in the structure (film+substrate) and the elastic energy stored in the film for biaxial strain conditions (i.e. before elastic relaxation) as a function of the width-to-height aspect ratio.

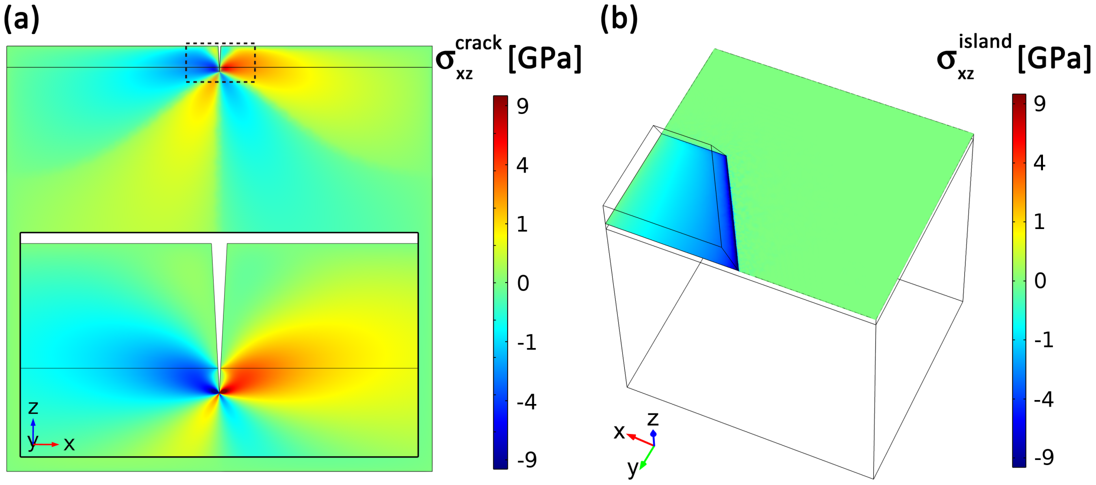
(a)
σ_{xz}^{crack} [GPa]
9
4
1
0
-1
-4
-9
z
y
x
(b)
σ_{xz}^{island} [GPa]
9
4
1
0
-1
-4
-9
x
z
y

Figure 4.11.: Shear stress $\sigma_{xz}^{crack/island}$ in the case of (a) cracking and (b) island growth. The inset in (a) shows a magnified view in the vicinity of the crack (note: the inset has a different color coded scale).

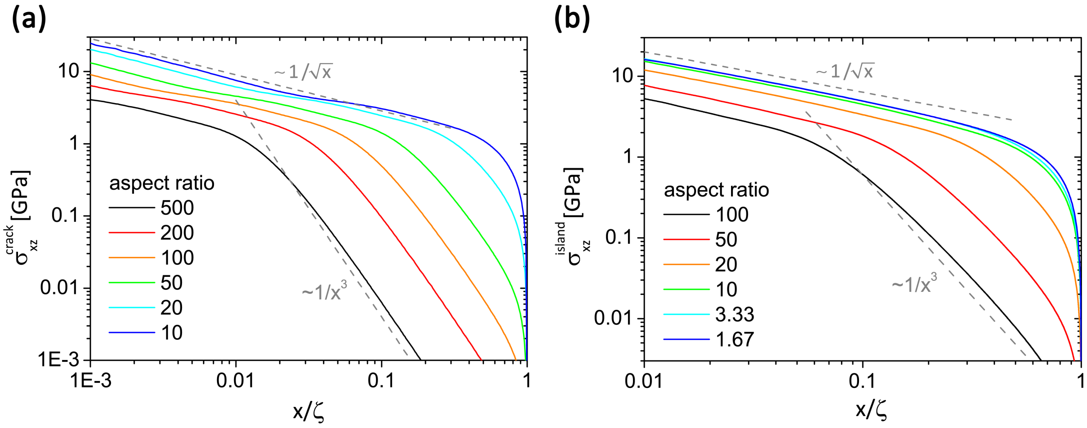

Figure 4.12.: Shear stress $\sigma_{xz}^{crack/island}$ as a function of the normalised distance x/ζ from the (a) crack tip and (b) island edge (along the direction of the island diagonal) for different aspect ratios, whereby $x = 0$ is at the crack tip or island corner, respectively. The normalisation parameter ζ is the half-spacing between adjacent cracks or the half-width of the island, respectively. Aspect ratios are defined as the crack spacing-to-layer thickness and width-to-height ratio for cracking and island growth, respectively.

shear stress $\sigma_{xz}^{crack/island}$ at a normalised distance $\frac{x}{\zeta}$ perpendicular from the crack tip or island corner ($x = 0$ at the crack tip or island corner) is shown in Fig. 4.12. Four major results can be inferred from the diagram, which are qualitatively identical for both geometries:

- in the near vicinity of the crack and island corner/edge the shear stress $\sigma_{xz}^{crack/island}$ decreases with a $\frac{1}{\sqrt{x}}$ dependency; this is in agreement with theoretical predictions [128]
- in this spatial range the strength of the shear stress scales with the square root of the inverse aspect ratio: $\sigma_{xz}^{crack/island} \sim \sqrt{\left(\frac{w}{h}\right)^{-1}}$; in other words, for a fixed average spacing of cracks or island width w the shear stress increases as the layer gets thicker
- at larger distances from the source the shear stress decreases rapidly with a $\frac{1}{x^3}$ dependency
- the transition between the $\frac{1}{\sqrt{x}}$ and $\frac{1}{x^3}$ dependency occurs at a distance x of approximately three times the layer thickness ($x_{transition} \approx 3h$)

The strength of the shear stress also depends to some extend on the explicit geometry like the inclination angle of side facets, the shape of the islands (spherical or hexagonal), the spacing of adjacent islands and the depth of cracks. While the first

3 mentioned parameter typically affect the shear stress by approximately 10% or less we found a strong decrease of the shear stress at a given horizontal distance x from the crack tip if the crack propagates from the heterointerface deeper into the quasi-substrate. E.g. for a crack with a depth of 1.2 times the thickness of the strained film (Fig. 4.13 (b)) the shear stress decreases by approximately 30% compared to a crack which propagates only down to the interface (Fig. 4.13 (a)). For the latter case we can approximate the shear stress in the near vicinity of the crack tip in the $Al_xGa_{1-x}N$/GaN heterointerface by

$$\sigma_{xz}^{crack}(x) = \frac{168\,GPa}{\sqrt{\frac{w}{h}}\sqrt{\frac{x}{\zeta}}} \cdot \varepsilon_{xx}, \tag{4.2}$$

where ε_{xx} denotes the in-plane strain of the layer. For hexagonal islands the shear stress in the (0001) plane along the direction perpendicular to the island edge (y-direction in Fig. 4.13 (c) with $y = 0$ at the island edge) is approximately

$$\sigma_{yz}^{hex\,island}(y) = \frac{182\,GPa}{\sqrt{\frac{w}{h}}\sqrt{\frac{y}{\zeta}}} \cdot \varepsilon_{xx}. \tag{4.3}$$

An even stronger stress concentration at the island corner leads to an approximately 25% higher shear stress in the direction along the island diagonal (x-direction in Fig. 4.13 (d) with $x = 0$ at the island corner)

$$\sigma_{xz}^{hex\,island}(x) = \frac{228\,GPa}{\sqrt{\frac{w}{h}}\sqrt{\frac{x}{\zeta}}} \cdot \varepsilon_{xx}. \tag{4.4}$$

Note that the shear stress around crack tips (eq. (4.2)) and island edges (eq. (4.3)) is almost equivalent. This is not surprising because a crack network is similar to a geometry of adjacent islands with very steep island side-walls. However, eq. (4.2) - (4.4) are only valid for aspect ratios higher than 10. For smaller aspect ratios, e.g. if the height of the island increases, the shear stress at a given normalised distance $\frac{x}{\zeta}$ saturates and actually becomes independent of the aspect ratio

$$\sigma_{xz}^{small\,aspect\,ratio}(x) = \frac{68\,GPa}{\sqrt{\frac{x}{\zeta}}} \cdot \varepsilon_{xx}. \tag{4.5}$$

4.3.3. Nucleation of a-type dislocation half-loops

The general theory of nucleating dislocation half-loops is described in appendix D. It is based on energy minimisation, i.e. a half-loop is nucleated if the release of strain energy stored in the film due to introduction of the dislocation (scales with the area inside the half-loop, i.e. $\sim r^2$) is larger than the line energy of the half-loop (scales approximately with its length, i.e. $\sim r$). Here we follow the approach of Beltz and

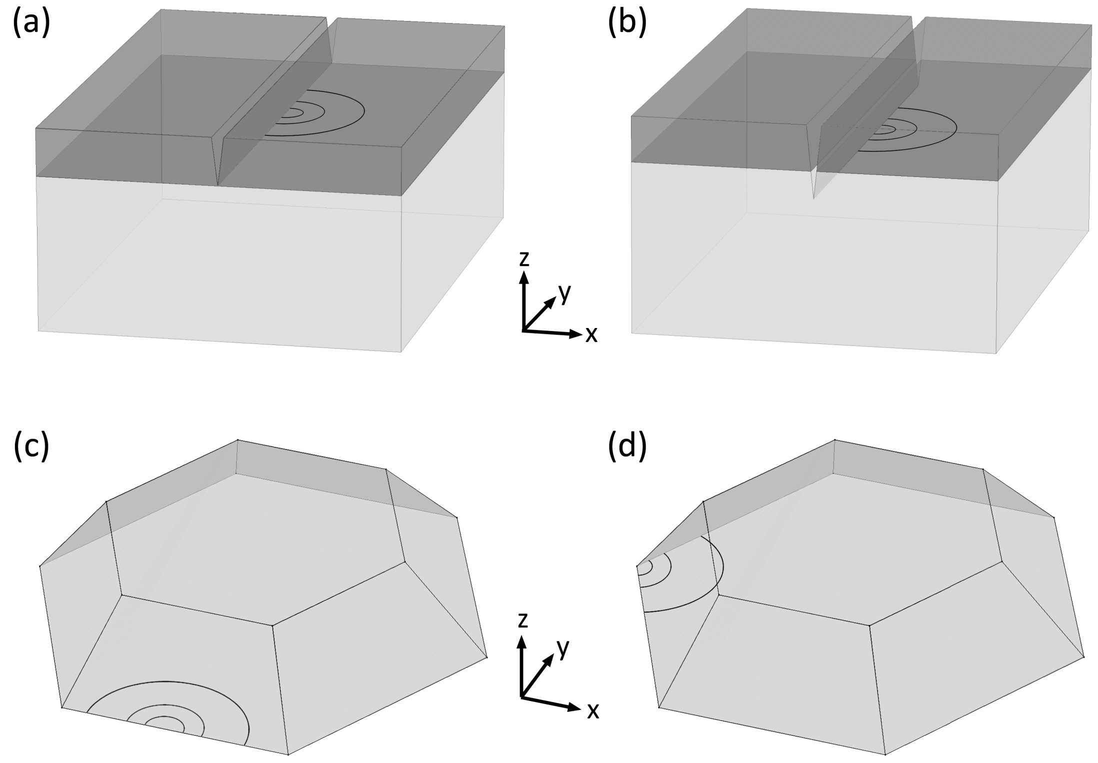

Figure 4.13.: Schematic representation of different possible sites for nucleation of dislocation half-loops in the (0001) plane. (a) Nucleation at a crack tip, which is located in the $Al_xGa_{1\text{-}x}N$/GaN heterointerface or (b) which has propageted into the GaN quasi-substrate, respectively. (c) Nucleation at the edge or (d) in the corner of a hexagonal island. In (a) and (b) the $Al_xGa_{1\text{-}x}N$/GaN heterostructure is displayed in different grey scales for clarity.

Freund [129]. We, however, consider the redistribution of the strain due to a three-dimensional surface geometry of a cracked or islanded film. Since maximum shear stresses on the $\{0001\}$ planes appear around the island edges/corners and at crack tips, we consider in the following nucleation of dislocation half-loops at these sites (schematically depicted in Fig. 4.13).

Replacing the homogeneous shear stress of the general model of Beltz and Freund [129] (see eq. (D.4) on page 143) with the appropriate spatial distribution of the shear stress for the given case of island growth and cracking (as obtained from our FEM calculations), the energy gain due to the work done by the half-loop amounts to

$$\begin{aligned} E_{gain} &= \int \sigma_{\mathbf{ij}} \cdot \overrightarrow{b} \times \overrightarrow{dl} \cdot \overrightarrow{ds} \\ &= \tau^{site} \cdot \sqrt{\frac{h}{2}} \cdot \varepsilon_{xx} \cdot b \cdot \cos\psi \int_0^r \int_0^\pi \frac{r'}{\sqrt{r'} \cdot \sin\varphi} \, d\varphi \, dr' \, , \end{aligned} \tag{4.6}$$

where ψ is the angle between the Burgers-vector and the direction in the interface

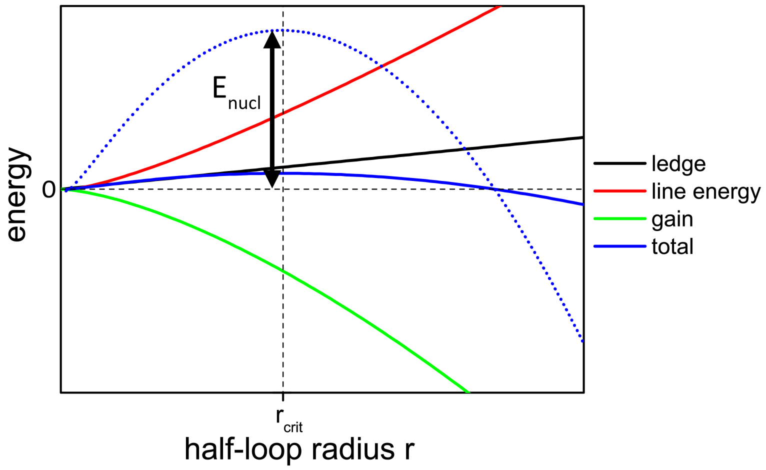

Figure 4.14.: Schematic representation of the different contributions to the total energy for the dislocation nucleation process. The vertical dashed black line denotes the critical radius r_{crit}. The black arrow indicates the nucleation barrier E_{nucl}. The blue dotted line is the same as the blue solid line multiplied by 10.

perpendicular to the crack front or island edge, respectively, and τ^{site} is a pre-factor corresponding to the strength of the shear stress at the respective nucleation site (e.g. 168 *GPa* for nucleation at a crack; compare with eq. (4.2) - (4.5)). Together with the line energy of the dislocation half-loop (eq. (D.1)) and the energy of the ledge created at the surface (eq. (D.6)) we can calculate the total energy of the system according to

$$E_{total}(r) = E_{gain}(r) + E_{half-loop}(r) + E_{ledge}(r)\,. \tag{4.7}$$

The different contributions to the total energy as well as the total energy itself as a function of the dislocation half-loop radius are schematically shown in Fig. 4.14. The energetical barrier for nucleation of an a-type dislocation E_{nucl} then is the total energy of the system at the critical radius r_{crit} of the half-loop. It is defined as the half-loop radius for that the total energy has a maximum (see Fig. 4.14):

$$E_{nucl} = E_{total}(r_{crit}) \;\text{ with }\; r_{crit} = r \iff \frac{\partial E_{total}(r)}{\partial r} = 0. \tag{4.8}$$

In general the nucleation barrier decreases with increasing shear stress on the respective slip plane (see appendix D). In case of a thin layer with perfect 2-dimensional morphology (i.e. plane stress state) the resolved shear stress on slip planes and thus the nucleation barrier is a function of the mismatch strain but is independent of the layer thickness. In our case of a heterostructure with a given certain lattice mismatch but with a three-dimensional modulated surface, however, the shear stress depends essentially on the width-to-height aspect ratio of the structure. Starting from the assumption that the lateral width of the structure (island diameter/crack spacing) is fixed at the beginning of the growth, the increasing thickness determines the shear stress distribution in the structure. We therefore display the nucleation barrier as a function of the thickness of the heterostructure. As we can see from Fig. 4.15 (a), the nucleation energy

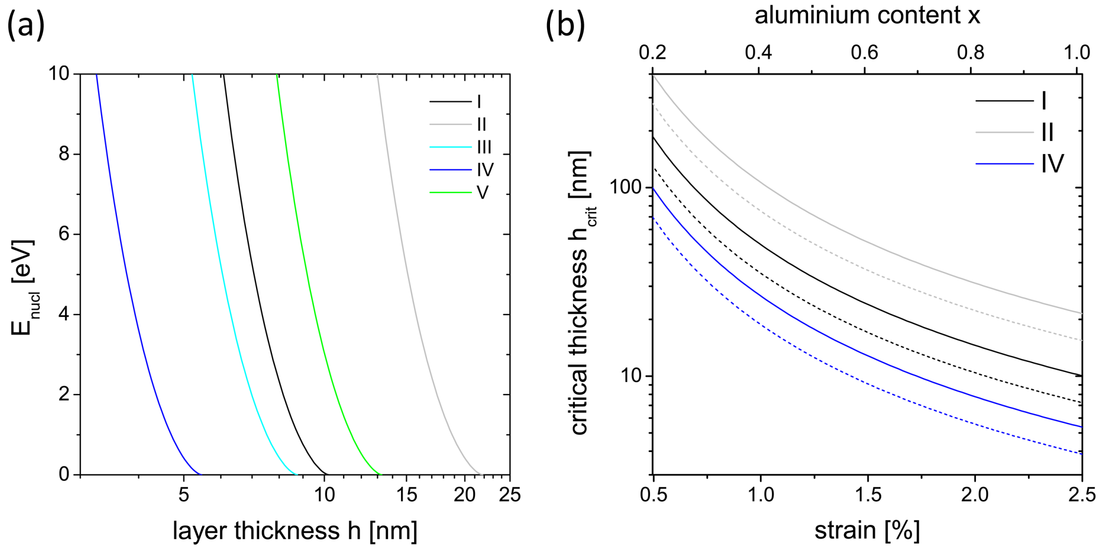

Figure 4.15.: (a) Energetical barrier for nucleation of an a-type dislocation half-loop vs. the thickness of an AlN layer on GaN. (b) Critical thickness for nucleation of an a-type dislocation half-loop as a function of the initial strain (lower axis) or the aluminium content of an $Al_xGa_{1-x}N$/GaN heterostructure (upper axis). The solid and dashed lines denote the case for spontaneous nucleation without an energetical barrier $(E_{nucl} = 0)$ and for a barrier of 4 eV (see explanation in the text), respectively. The different curves in (a) and (b) correspond to the respective considered nucleation sites/geometries: at a crack tip located in the heterointerface (I, compare with Fig. 4.13 (a)) and at tip of a crack which has propageted further into the GaN quasi-substrate with an total crack depth of 1.2 times the thickness of the strained film (II, compare with Fig.(b)); at the edge (III, compare with Fig. 4.13 (c))) and in the corner (IV, compare with Fig. 4.13 (d)) of a hexagonal island; in the corner of a hexagonal island with a fixed aspect ratio of 5 (V).

(E_{nucl}) decreases as the layer gets thicker. This is because with increasing thickness h the shear stress $\sigma_{xz}^{crack/island}$ at a certain distance from the crack tip/island edge increases (compare with eq. (4.2) - (4.4)) until it approaches the critical value where the nucleation barrier vanishes, i.e. $E_{nucl} = 0$. Note that in the case that trenches/pits between islands do not reach the heterointerface, the thickness h corresponds to the depth of these trenches/pits instead of the height of the strained layer. The lowest overall nucleation energy is found for nucleating a dislocation half-loops at the corner of hexagonal islands. This is simply because the shear stress is highest there. One has to remind the reader of the fact that for all cases in Fig. 4.15 (a) except for hexagonal islands with a fixed aspect ratio of 5 (curve V) the island width or the crack spacing, respectively, has to obey the criterion $w/h > 10$ for the whole relevant thickness range. Otherwise, the shear stress will saturate at a given distance from the crack tip/island edge.

Let us now determine the critical thickness at which an a-type dislocation half-loop will nucleate. We will first consider the case of spontaneous nucleation of an a-type dislocation half-loop, i.e. nucleation with no energetical barrier ($E_{nucl} = 0$). Fig. 4.15 (b) (solid lines) shows this relationship as a function of the in-plane strain ε_{xx} for different nucleation sites. The critical thickness decreases with increasing strain ε_{xx} and it is lower for nucleation at island corners than at crack tips.

Since nucleation of dislocations is a thermally activated process, it will occur, however, with a certain probability also at lower thicknesses, when a finite energetical barrier [130] still exists. In this case, the nucleation rate v becomes a function of the energetical barrier E_{nucl} and the available thermal energy. According to Rice and Beltz [130], the rate v for nucleation of dislocation half-loops per unit length of the crack front/island edge can be estimated by

$$v = n \cdot \frac{c_{shear}}{b} \cdot \exp(-\frac{E_{nucl}}{kT}), \tag{4.9}$$

where n is the number of nucleation sites per unit length of the crack front/island edge, here taken as $n = \frac{1}{10b}$, and c_{shear} is the shear wave speed, which can be estimated by [131]

$$c_{shear} = \sqrt{\frac{\mu}{\rho}}, \tag{4.10}$$

where μ is the shear modulus and ρ is the density of the material. Thus, the nucleation rate is the product of an attempt frequency, here $n \cdot \frac{c_{shear}}{b}$, and a temperature dependent Boltzmann probability factor. With these relationships we can now calculate the maximum possible nucleation barrier and by this a lower limit for the thickness of the heterostructures for which the nucleation mechanism has still an reasonable rate. Since there are no literature data available neither for possible energy barriers for nucleation of a-type dislocations in the wurtzite lattice nor for typical nucleation rates we will estimate latter one from our experimental data. Let us therefore assume that after nucleation the half-loops extend by glide and form long dislocation lines which traverse the full island/area bound by neighbouring island side-walls/cracks, respectively. Then the initial number of half-loops nucleated per unit length of the island edge/crack front, respectively, is inversely proportional to the average spacing d of dislocation lines in the final misfit dislocation network. From TEM investigations we know that this spacing is typically in the range of several 10..100 nm (depending on the thickness of the strained layer). We also find by TEM that plastic relaxation occurs only after the strained layer has exceeded a critical thickness and that the degree of strain relaxation increases with the thickness of the layer. Therefore, we assume that the relaxation process occurs roughly gradually in time during the growth of the strained layer. The typical timeframe $t_{relaxation}$ for this process is in the range of 10..100 $seconds$. E.g. for the sample mentioned earlier with a 35 nm thick high temperature $Al_{0.75}Ga_{0.25}N$ interlayer we have found at the lower interface of the $Al_{0.75}Ga_{0.25}N$ interlayer an average spacing of a-type misfit dislocations of about $d = 40$ nm and the time needed for the growth of the $Al_{0.75}Ga_{0.25}N$ layer between a thickness of ≈ 15 nm (estimated thickness for onset of plastic relaxation[3]) and 35 nm was approximately 50 $seconds$. All together we estimate a minimum nucleation frequency in the order of

---

[3] for a sample with a 11 nm thick high temperature $Al_{0.75}Ga_{0.25}N$ interlayer we do not observe misfit

$$\nu \geq \frac{1}{d \cdot t_{relaxation}} \approx 10^6/m \cdot s. \tag{4.11}$$

Note, that this value must be regarded as a lower limit, since expanding half-loops with the same Burgers-vector may join together and form a single extended dislocation line. Together with eq. (4.9) and (4.10) and considering the experimental growth temperature of 1050 °*C* this yields a maximum energetical barrier of $E_{nucl} \approx 35\,kT$, i.e. approximately 4 *eV*. Similar to the case of a vanishing energetical barrier we have calculated the critical thickness for nucleation of an a-type dislocation half-loop with an activation energy of 4 *eV*. The corresponding relationship is shown in Fig. 4.15 (b) for the different nucleation sites with dashed lines. Allowing an energetical barrier of 4 *eV* for nucleating an a-type dislocation half-loop reduces the critical thickness by approximately 30% compared to that for spontaneous nucleation. Note that the strain ε in Fig. 4.15 (b) is the initial strain of the layer and not an effective value after strain redistribution due to elastic relaxation.

4.3.4. Glide of a-type dislocations

As nucleation of half-loops at either cracks or island edges/corner is only the first step of an efficient plastic relaxation process, we will now consider the second important step, i.e. glide of a-type misfit dislocation from the nucleation sites into the heterointerface. A dislocation will glide only if the sum of all shear stresses acting on the dislocation are larger than a certain minimum shear stress, the Peierls stress σ_P

$$|\sigma_{xz}| \geq \sigma_P. \tag{4.12}$$

The Peierls stress is a lattice frictional force the dislocation has to overcome during its motion on the slip plane through the periodic potential of the crystal [132]. In the original form in the framework of the Peierls-Nabarro dislocation model [133, 134] the Peierls stress σ_P is derived from a purely phenomenological consideration and depends essentially on the ratio $\frac{b}{d}$ of the modulus of the Burgers-vector and the interplanar spacing of the slip planes [132]. Chidambarrao et al. [135] have presented a modification which includes also a temperature dependency of the Peierls stress σ_P. For a pure edge dislocation the Peierls stress is given by

$$\sigma_P = \frac{2\mu}{1-\nu}\,\omega \exp\left(-\frac{d}{b}\,\frac{2\pi}{1-\nu}\,\omega\right), \tag{4.13}$$

$$\omega = \exp\left(\frac{4\pi^2 N}{5\mu}\,kT\right), \tag{4.14}$$

where μ is the shear modulus, ν is the Poisson's ratio, b is the modulus of the Burgers-vector, d is the interplanar spacing of the glide planes, N is the number of atoms per unit cell volume, k is the Boltzmann constant and T is the temperature. According to eq. (4.13) and (4.14) the Peierls stress reduces as the temperature increases. For

---

dislocations, whereas a 16 *nm* thick low temperature $Al_{0.75}Ga_{0.25}N$ interlayer is plastically relaxed the $\frac{1}{3} < 11\bar{2}0 > | \{0001\}$ slip-system eq. (4.13) yields a Peierls stress of approximately 0.2 *GPa* at the considered growth temperature of approximately 1000°C. A comparison of the Peierls stress (calculated according to [135]) for different slip-systems is listed in Table 2.1 on page 7 .

The shear stress σ_{xz} on the n-th dislocation is given by

$$\sigma_{xz} = \sigma_{xz}^{crack/island} + \sigma_{xz}^{n,m} + \sigma_{xz}^{image}, \tag{4.15}$$

where $\sigma_{xz}^{crack/island}$ is the shear stress field around cracks and island edges, $\sigma_{xz}^{n,m}$ is the shear stress due to interaction of dislocations with each other and σ_{xz}^{image} is an image stress exerted by the free surface on the dislocation, respectively. The lateral distribution of $\sigma_{xz}^{crack/island}$ can be taken from the FEM calculations in section 4.3.2.

In the case that several a-type misfit dislocations with the same Burgers-vector are present in the heterointerface, the shear stress $\sigma_{xz}^{n,m}$ acting on the n-th dislocation due to interaction with all other dislocations is given by

$$\sigma_{xz}^{n,m} = \sum_{m \neq n} \sigma_{xz}^{m}(d_{nm}) \,, \tag{4.16}$$

where $d_{nm} = x_n - x_m$ is the spacing between dislocation n and m and $x_{n,m}$ is the distance of each dislocation from the crack or island edge, respectively. The term σ_{xz}^{m} is the shear stress field of dislocation m and depending on its location relative to the free surfaces (top surface and crack/island side facets) it is given by [136]

$$\sigma_{xz}^{m}(d_{nm}) = D \begin{cases} \dfrac{1}{d_{nm}} - \dfrac{1}{d_{nm}+2x_m} - 2x_m \dfrac{d_{nm}}{(d_{nm}+2x_m)^3}, & \text{if } x_m < 2h \quad (4.17a) \\[2ex] \dfrac{1}{d_{nm}} - \dfrac{32h^4\, d_{nm} - 4h^2\, {d_{nm}}^3 + {d_{nm}}^5}{(4h^2 + {d_{nm}}^2)^3}, & \text{if } x_m > 2h \quad (4.17b) \end{cases}$$

with

$$D = \frac{\mu\, b}{2\pi\,(1-\nu)} \,. \tag{4.18}$$

Eq. (4.17a) is for the case that the m-th dislocation is much closer to side facet of a crack/island (at a distance x_m from it) than to the (0001) top surface of the film (which has a thickness of h), while eq. (4.17b) is for the case that the m-th dislocation is much closer to the (0001) top surface (at a distance h below the surface) than to a side facet of a crack/island. Note that both equations assume that the interaction is between straight dislocations in a semi-infinite medium, which extends to one side of the free surface [136]. Although this assumption is strictly speaking not completely true in our case, we will use for simplicity in the following approach.

Additionally, the dislocations experience a resolved shear stress σ_{xz}^{image} due to the image effect, which is is a direct consequence of the free surface boundary condition $(\sigma_{ij} \cdot n_j = 0$,i.e. no forces can act normal to a free surface$)$. The mathematical concept is derived in detail e.g. in [132]. Especially for dislocations located in the near vicinity of the nucleation sites ($x_n < 2h$) the image stress σ_{xz}^{image} becomes relevant and drives the dislocation back towards the free surface of cracks or islands, respectively. It is given by

$$\sigma_{xz}^{image} = \frac{\mu\, b}{2\pi\,(1-\nu)} \begin{cases} \dfrac{1}{2x_n}\,, & \text{if } x_n < 2h \qquad (4.19a) \\ \\ \dfrac{2h^2}{x_n^3}\,, & \text{if } x_n > 2h \qquad (4.19b) \end{cases}$$

Note that eq. (4.19b) (a) and(b) are again strictly speaking only valid for straight dislocations in a semi-infinite medium.

Taking all shear stresses together we are able to simulate the motion of a-type dislocations from the nucleation sites into the heterointerface. For this purpose we use an iterative approach according to the following scheme: The starting point of the simulation is a distribution of j dislocations, whereby the first one is located at a distance of 1 nm from the nucleation site (according to our calculations from the previous subsection on nucleation of dislocations this value is approximately the critical radius of a just nucleated a-type dislocation half-loop) and the spacing between adjacent dislocations is 20 nm[4]. In the first step of each iteration cycle we calculate for a given distribution of dislocations for each one the total shear stress with eq. (4.15) and compare it with the Peierls stress. If the modulus of the total shear stress for dislocation n is larger than the Peierls stress ($|\sigma_{xz}| \geq \sigma_P$), then in the second step the n-th dislocation is moved according to the Newton-Raphson method

$$x_n^{(k+1)} = x_n^{(k)} - \frac{\sum \sigma_{xz}(x_n^{(k)})}{\frac{\partial \sum \sigma_{xz}(x_n^{(k)})}{\partial x_n}}, \tag{4.20}$$

where k denotes the iteration number. The cycle is repeated until equilibrium is reached. This is the case if for all dislocations the modulus of the total shear stress is smaller than the Peierls stress.

The simulation of the glide process has been performed for $Al_{0.75}Ga_{0.25}N$/GaN heterostructures ($\varepsilon = 0.018$) to coincide with our experimental samples. We obtain the following results. For aspect ratios $\frac{w}{h} \leq 20$ of the crack or island geometry the driving shear stress of the island edge/crack tip is higher than the Peierls-stress (≈ 0.2 GPa) even at a distance of approximately 70% of half-spacing of the cracks/half-diameter of islands (see Fig. 4.12). This means that a-type misfit dislocations will glide efficiently into the heterostructure. However, for higher aspect ratios the shear stress from cracks/islands alone is not large enough anymore to push misfit dislocations far into the whole heterointerface. This is because further away from crack tips/island edges the shear stress decays with a $\frac{1}{x^3}$ dependency and the shear stress quickly becomes smaller than the Peierls stress. E.g. for an $Al_{0.75}Ga_{0.25}N$/GaN heterostructure with a

---

[4] This value is chosen somehow arbitrary. However, if the initial spacing is chosen smaller or larger (10 and 40 nm) the final distribution of dislocation at equilibrium is not affected (not shown here). Thus the choice of 20 nm as a initial spacing seems reasonable.

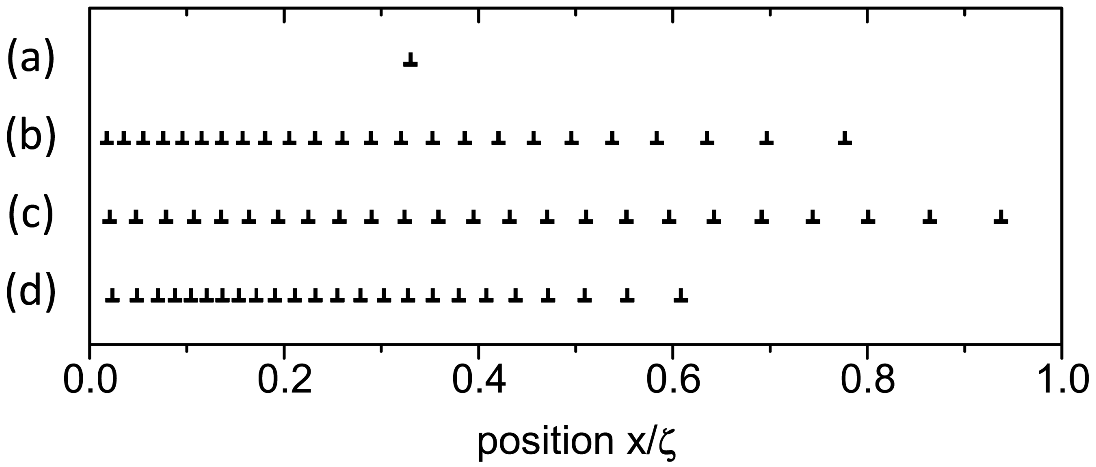

Figure 4.16.: Simulated lateral arrangement of misfit dislocations in the $Al_{0.75}Ga_{0.25}N/GaN$ heterointerface between 2 adjacent cracks seperated by the distance $2\zeta = 1750\,nm$. The thickness of the layer is $h = 35\,nm$ (width-to-height aspect ratio $\frac{w}{h} = 50$). (a) with only 1 misfit dislocation, (b) with 24 misfit dislocations within the half-spacing ζ of the adjacent cracks[6] including dislocation interaction according to eq. (4.16), (c) and (d) same as (b) but with the interaction strength between the dislocations $\sigma_{xz}^{n,m}$ twice and half as strong as in (b), respectively.

crack geometry having an aspect ratio of $\frac{w}{h} = 50$ an isolated misfit dislocation will stop to glide at a distance of only $x \approx 0.3\zeta$ from the crack tip (see Fig. 4.16 (a)). However, a-type dislocations still can glide further because of dislocation-interaction, i.e. the dislocations, which are farthest away from the nucleation sites, are pushed further into the heterostructure by the repelling shear stress field of other a-type dislocations. The distance, how far the dislocations will glide, depends essentially on the strength of the dislocation interaction. Fig. 4.16 (b)-(d) shows the result of a glide process simulation where we have varied the interaction strength[5] and kept all other parameters, e.g. the number of dislocations in the considered array, constant. For higher interaction strength between the dislocations the dislocation pile-up will be pushed further into the interface. According to eq. (4.17b) the strength of the interaction between parallel straight dislocations with Burgers-vectors parallel to the free surface will increase if the distance of the dislocations to the free (0001) top surface, i.e. the thickness h of the layer, increases. Interestingly at force equilibrium the spacing between the misfit dislocations is laterally not constant: it is smallest close to the nucleation sites while it increases for dislocations, which have slipped further into the heterointerface.

---

[6] This number of misfit dislocations would lead to an average residual strain of approximately 1% which corresponds to the equilibrium strain for a 35 nm thick layer with dislocation nucleation at cracks, see Fig. 4.18 in section 4.4.2.2.

[5] The modification of the interaction strength has been implemented in the simulation by varying the virtual thickness of the layer (h in eq. (4.17b)) while the actual thickness (h in eq. (4.2)-(4.4)) responsible for the absolute value of the shear stress around the crack/island $\sigma_{xz}^{crack/island}(x)$ has not been changed.

All together our considerations show that glide of a-type dislocations into the heterointerface does not represent a bottleneck for the plastic relaxation process at the interfaces of $Al_xGa_{1-x}N$ interlayer. If the thickness of the layer is sufficiently high to nucleate a-type dislocations they will also glide away from the nucleation site into the interface. Therefore, the plastic relaxation mechanism will stay active. However, the centre region between two cracks or the centre of islands is typically less plastically relaxed, especially if the width-to-height aspect ratio becomes large (approximately for $\frac{w}{h} \geq 50$).

4.4. Discussion

The discussion is organised as follows. We will first have a view on the microscopic mechanisms responsible for strain relaxation of (0001)-oriented III-nitride heterostructures. In the second part we will focus on the results of our quantitative relaxation model and discuss in particular the influence of the growth mode of the films on the plastic relaxation process. This topic will be addressed first in a more general way. Afterwards, we will discuss explicit implications of the growth mode on strain relaxation process for the case of $Al_xGa_{1-x}N$ interlayers and explain the asymmetry in plastic relaxation between the upper/lower interface of the interlayer. Finally, we will briefly review alternative plastic relaxation mechanisms and discuss their relevance for (0001)-oriented III-nitride heterostructures.

4.4.1. Microscopic model for the growth and strain relaxation mechanism of (0001)-oriented III-nitride heterostructures

In this chapter we have shown that plastic strain relaxation of sufficiently thick $Al_xGa_{1-x}N$/GaN and GaN/$Al_xGa_{1-x}N$ heterostructures grown with a 3-dimensional surface morphology proceeds mainly by nucleation and glide of a-type dislocations in the $\frac{1}{3} < 11\bar{2}0 > |\{0001\}$ slip-system. This is consistent with previous reports in literature. Bethoux et al. [118, 137], Floro et al. [117], Vennegues et al. [30] ($Al_xGa_{1-x}N$ layers on GaN) and Moran et al. [97] (GaN layers on AlN) all observed a dense network of a-type misfit dislocations at the $Al_xGa_{1-x}N$/GaN and GaN/AlN interface, respectively. Also for $In_xGa_{1-x}N$/GaN heterostructures a-type misfit dislocations introduced by basal plane slip have been observed in literature e.g. by Jahnen et al. [31] Liu et al. [138] and Mei et al.[32].

However, the $\frac{1}{3} < 11\bar{2}0 > |\{0001\}$ slip-system becomes only active if the surface morphology deviates from that of a perfect 2-dimensional film. Indeed, we have found in experiments that depending on the growth conditions and on the sign of the strain (tensile or compressive) $Al_xGa_{1-x}N$/GaN as well as GaN/$Al_xGa_{1-x}N$ heterostructures might have either a cracked or islanded surface during the initial growth stage. In both cases part of the elastic energy stored in the strained layers is elastically relaxed. Crack and island geometries, on the other hand, cause also to a redistribution of strain leading to resolved shear stresses on the {0001} slip-planes with a maximum in the vicinity

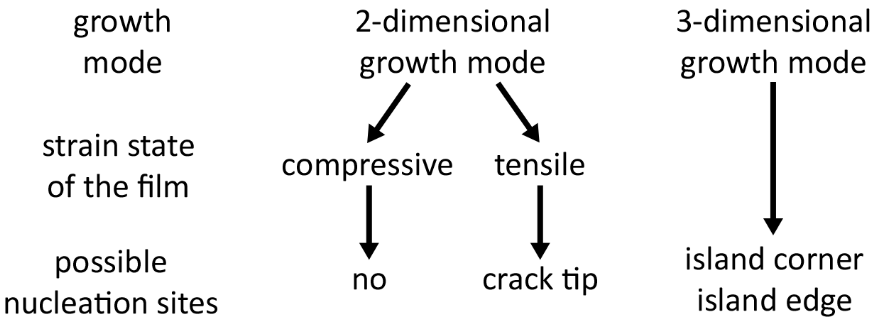

Figure 4.17.: Effect of the growth mode of (0001)-oriented strained wurtzite films on the plastic relaxation process.

of crack tips and island edges/corners, respectively (see results of our finite element calculations in Fig. 4.11). Therefore, if the strained layer has either cracked or grows with an island morphology the $\frac{1}{3} < 11\bar{2}0 > | \{0001\}$ slip-system becomes active and a-type misfit dislocations can be nucleated at these places if the layer thickness exceeds a certain critical value. After nucleation the half-loops then glide laterally on the $\{0001\}$ slip-planes into the layers and form the a-type misfit dislocation networks, which we have described in chapter 29. Because crack tips, island edges or grooves/pits between islands are not always located exactly at the heterointerface a-type misfit dislocations might be nucleated at a certain vertical distance around the interface (see e.g. Fig. 3.2). As soon as the layer has again a 2-dimensional surface morphology, e.g. if the cracks are overgrown or islands have coalesced, or if the heterostructure grows all the time 2-dimensionally the mechanism for plastic relaxation via the $\frac{1}{3} < 11\bar{2}0 > | \{0001\}$ slip-system becomes/is inoperable, respectively, and the residual strain will remain initially unrelaxed.

Such *"cooperative mechanism"* [30], which is characterised by a morphology modification followed by introduction of misfit dislocations from island edges, V-pits and/or crack tips, has already been proposed by other authors [30, 31, 32, 114, 125], though only in a qualitative manner. Our quantitative considerations of the relaxation process presented in the previous section is based on the *"cooperative mechanism"*. However, our model allows for the first time to quantitatively predict relevant values, like e.g. the critical thickness for the onset of plastic relaxation by formation of a-type misfit dislocations, without neglecting the dislocation formation kinetics. Outcomes and results of our model will be discussed in the following sections.

4.4.2. Influence of the growth mode on the plastic relaxation process

We will now discuss the effect of the growth mode of (0001)-oriented strained wurtzite layers on the plastic relaxation process. The crucial point in this consideration is that different growth modes result in different surface morphologies and thus different possible sites for nucleation of a-type misfit dislocations will be available. This is schematically summarised in Fig. 4.17.

4.4.2.1. Critical thickness

Tensile strained layers

Let us first consider tensile strained layers (e.g. $Al_xGa_{1\text{-}x}N$ on GaN). For sufficiently thick[7] tensile strained layers appropriate sites for nucleation of a-type misfit dislocations will be present in any case, independently of the growth mode - either island corners for 3-dimensional growth or crack tips for initial 2-dimensional growth. However, the critical thickness when the first a-type misfit dislocation is introduced into the interface depends on the available nucleation sites and thus on the growth mode of the layer. Our theoretical considerations in section 4.3.3 predict that the critical thickness is approximately 45% lower for nucleation of dislocation half-loops in corners of islands having an aspect ratio of $\frac{w}{h} > 10$ rather than at crack tips (compare dashed blue and red lines in Fig. 4.18). This outcome of our model agrees well with experimental results. While we have found a 10 nm thin $Al_{0.75}Ga_{0.25}N$ interlayer grown with a 3-dimensional morphology on a GaN buffer to be plastically relaxed, we have not observed misfit dislocations in the case of a 11 nm (and thus thicker) $Al_{0.75}Ga_{0.25}N$ interlayer, which has grown 2-dimensionally but has cracked. Similar results can be found in literature reports also for other compositions (see filled blue and open red data points labelled with a and c in Fig. 4.18 at approximately 20% and 40% aluminium content). Note that the aforementioned outcome of our model is only valid if the width-to-height aspect ratio of islands is larger than 10. If the width-to-height aspect ratio becomes smaller than 10 our model predicts that the critical thickness for nucleation of a-type dislocations in island corners starts to increase. For example for $\frac{w}{h} = 5$ the critical thickness has approximately doubled compared to the case of $\frac{w}{h} > 10$ and the value even gets larger than the critical thickness for dislocation nucleation at crack tips.

Another interesting feature which our model predicts is that the growth mode of tensile strained layers does not only affect the critical thickness for the onset of plastic relaxation but also determines whether tensile strained layers will show a brittle or ductile relaxation mechanism. In case of 2-dimensional growth the critical thickness for nucleation of an a-type dislocation at a crack tip is higher than the critical thickness for cracking[8] (compare red dashed and grey solid line in Fig. 4.18). From this we can deduce that for 2-dimensionally grown tensile strained $Al_xGa_{1\text{-}x}N$ layers plastic relaxation by formation of a-type misfit dislocations will not take place until the layer has cracked. Hence such layers will show a brittle relaxation behaviour. This is in agreement with the experimental observation that for a certain thickness window 2-dimensionally grown but cracked films are free of a-type misfit dislocations

---

[7] Sufficiently thick means in this case that the layer thickness exceeds a critical value where cracking would occur if the layer has been grown initially in a 2-dimensional mode.

[8] The critical thickness for cracking has been calculated according to Hutchinson and Suo [123] by $h_{crit}^{cracking} = \frac{2\gamma}{(1+\nu)\,ZM\varepsilon^2}$, where γ is the surface energy of the $\{1\bar{1}00\}$ cleavage planes (118 $meV/\mathring{A}^2$ [139] and 157 $meV/\mathring{A}^2$ [140] for GaN and AlN, respectively), ν is the Poisson's ratio, M is the biaxial modulus of the strained layer ($M = C_{11} + C_{12} - 2\frac{C_{13}}{C_{33}}$), ε is the strain and Z is a dimensionless parameter which amounts according to Hutchinson and Suo [123] for surface cracks to $Z = 3.951$.

(see Fig. 4.2 on page 65). On the other hand, in case of 3-dimensional growth our model predicts that for a given initial strain ε the critical thickness for nucleation of a-type misfit dislocations in island corners (for islands with an aspect ratio of $\frac{w}{h} > 10$) is almost identical with the critical thickness for cracking. However, due to the 3-dimensional morphology part of the initial strain has already been relaxed elastically making cracking less likely than plastic relaxation. Thus the film will show a ductile strain relaxation behaviour.

All together we see that the growth mode has a strong influence on the relaxation process and the growth conditions should be chosen according to the desired goal. If one aims for an as small as possible layer thickness when plastic relaxation sets in then the strained layer should be grown in a 3-dimensional mode with islands having an width-to-height aspect ratio of larger than 10. Such growth mode is also favourable if cracking of tensile strained layers should be avoided.

Compressively strained layers

In contrast to layers being under tension, the growth mode of compressively strained layers (e.g. $\mathrm{Al_xGa_{1\text{-}x}N}$ on AlN or $\mathrm{In_xGa_{1\text{-}x}N}$ on GaN) determines whether plastic relaxation via the $\frac{1}{3} < 11\bar{2}0 > |\{0001\}$ slip-system takes place at all. In case of a 3-dimensional growth of compressively strained layers a-type misfit dislocations can be nucleated at island corners/edges and the relaxation process will proceed in the same way as for tensile strained layers having an islanded surface morphology. Also, in terms of the critical thickness for the onset of plastic relaxation there is no difference compared to tensile strained layers. However, if compressively strained layers grow with a 2-dimensional surface morphology the situation is different. In this case no sites for nucleation of a-type dislocation half-loops will be present and also, as discussed before, resolved shear stresses on the $\{0001\}$ slip-planes will be absent. Therefore, plastic relaxation by nucleation and glide of a-type misfit dislocations will be prevented. As a consequence, compressively strained layers can be grown very thick in a metastable state coherently on a (quasi) substrate, without exhibiting plastic relaxation, if they are deposited 2-dimensionally. E.g. Grandusky et al. [116] demonstrated pseudomorphic growth of $Al_{0.60}Ga_{0.40}$N layers on bulk AlN substrates ($\varepsilon \approx 1.0\%$) up to a thickness of 0.5 μm. This value is approximately 1 order of magnitude more than the critical thickness, which our model predicts in the case when nucleation sites are available.

Comparison with equilibrium critical thickness theory

In Fig. 4.18 we have also plotted the critical thickness for plastic relaxation due to a-type misfit dislocations according to equilibrium critical thickness theory (see black dashed-dotted line). Here we use the model of Holec et al. [34], which is based solely on an energy minimisation approach[9] where the self-energy of the dislocation (elastic energy + core energy) added to the system is compared with the work done by the misfit

---

[9] As shown by Freund and Suresh [39] the solution of the energy minimisation approach coincides with that of a force equilibrium concept (Matthews-Blakeslee-model [122])

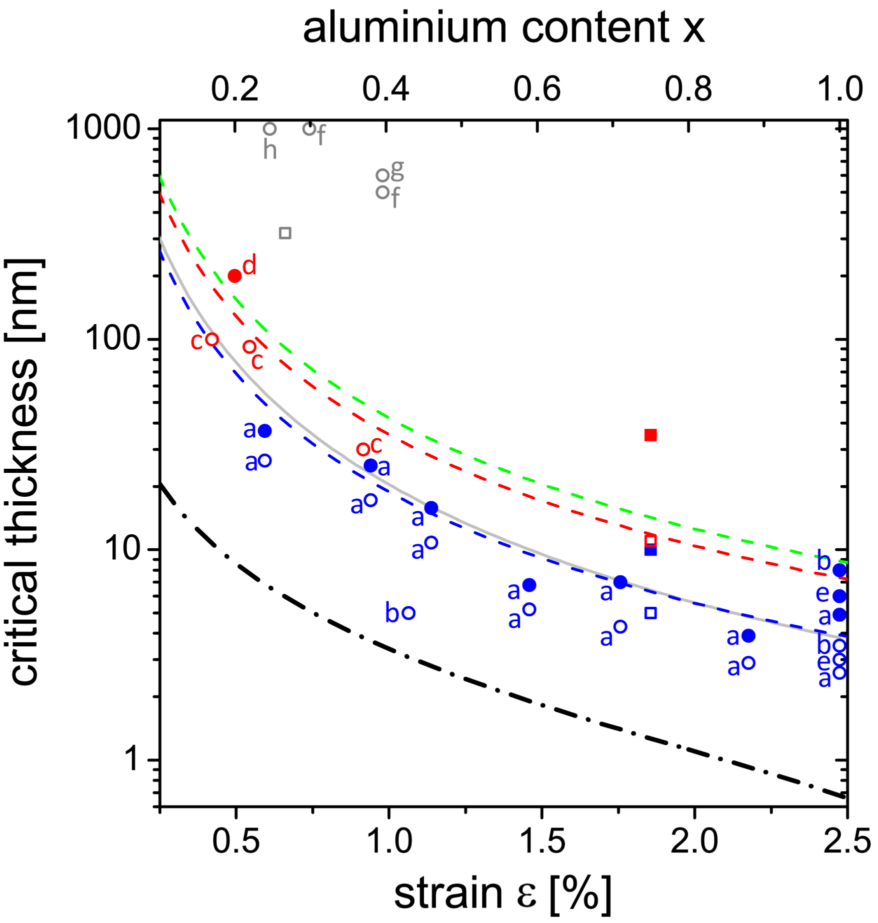

Figure 4.18.: Comparison of critical thickness (CT) curves for strain relaxation of (0001)-oriented III-nitride heterostructures as a function of the strain ε (lower axis) and for $Al_xGa_{1-x}N/GaN$ heterostructure as a function of the aluminium content x (upper axis), respectively. Dashed lines denote the calculated CT for nucleation of a-type dislocation half-loops with an energetical barrier of 4 eV at crack tips (red) and in corners of islands having an aspect ratio of $\frac{w}{h} > 10$ (blue) and $\frac{w}{h} = 5$ (green), respectively. The black dashed-dotted line corresponds to the CT for plastic relaxation by a-type basal plane misfit dislocations according to an energy minimisation concept after Holec et al. [34]. The grey solid curve indicates the CT for surface cracks. Symbols indicate experimental data points, whereby squares/circles denote data from our samples/literature reports, filled/open symbols stand for heterostructures with/without a-type misfit dislocation networks, and red/blue symbols indicate results for 2-dimensional but cracked/3-dimensionally grown $Al_xGa_{1-x}N/GaN$ structures, respectively. The grey circles stand for 2-dimensionally grown $Al_yGa_{1-y}N$ layers on bulk AlN substrates. Literature data are taken from (a) Ref.[119], (b) Ref.[30], (c) Ref.[117], (d) Ref.[118], (e) Ref.[114], (f) Ref.[116], (g) Ref.[141] and (h) Ref.[142].

stress field during the introduction of the dislocation (i.e. the misfit energy relief) [34]. The drawback of the energy minimisation approach is that it does not account for the actual dislocation formation mechanism.

A comparison of the different curves in Fig. 4.18 reveals that the equilibrium theory predicts a critical thickness which is approximately 1 order of magnitude smaller than the critical thickness for nucleating an a-type misfit dislocation at either crack tips or island corners. The experimentally determined range for the onset of plastic relaxation (see filled/open symbols in Fig. 4.18 representing heterostructures with/without a-type misfit dislocation networks, corresponding to an upper and lower bound for the critical thickness of plastic relaxation, respectively) yields a much better agreement with the curve for the critical thickness for nucleation of a-type misfit dislocations at crack tips or island corners rather than with the equilibrium critical thickness graph. All this means that plastic relaxation of (0001)-oriented wurtzite films via the $\frac{1}{3} < 11\bar{2}0 > |\{0001\}$ slip-system is kinetically limited by the nucleation process. Any equilibrium theory, which neglects the dislocation formation mechanism, therefore strongly underestimates the critical thickness for the onset of plastic relaxation.

4.4.2.2. Degree of plastic relaxation

So far we have considered only the critical thickness for which the first a-type misfit dislocation is nucleated. Under the assumption that the $\frac{1}{3} < 11\bar{2}0 > |\{0001\}$ slip-system stays active during further growth more and more misfit dislocations will be formed at the interface as the growth proceeds and the thickness of the heterostructure increases. This will lead to a advancing plastic relaxation of the strain energy stored in the layer. For a given thickness h of the heterostructure one might also be interested in the degree of plastic relaxation or the equilibrium strain state, respectively.

If the relaxation process is limited only by the dislocation nucleation step and lateral glide of just nucleated dislocations into the heterointerface proceeds efficiently, then the equilibrium strain state for a given thickness h will correspond to the critical value $\varepsilon_{crit}^{nucleation}$, for which nucleation of an a-type dislocation will just take place. This value can be read directly from Fig. 4.18 by interpreting the diagram backwards ($\varepsilon_{crit}(h)$ instead $h_{crit}(\varepsilon)$). Note that the thickness h, which is relevant for this consideration, is not always the geometrical height of the strained layer but the depth of trenches between islands or pits in the surface. Similar to the case of the critical thickness before, the value $\varepsilon_{crit}^{nucleation}$ again depends on the surface morphology of the film (due to the available nucleation site).

However, in some cases the plastic relaxation mechanism is not limited by the misfit dislocation nucleation step but by glide of dislocations away from the nucleation site into the layer. If latter process does not proceed efficiently, misfit dislocations will not spread along the whole heterointerface and the misfit strain will be relaxed only in the near vicinity of the nucleation sites. Our FEM calculations and theoretical considerations in section 4.3.4 reveal that glide of a-type dislocations away from the nucleation sites into the heterostructure proceeds effectively and does not limit the plastic relaxation process as long as the width-to-height aspect ratios does not become to large. For $Al_xGa_{1-x}N$/GaN heterostructures typically considered in this work

($x \approx 0.75 \Rightarrow \varepsilon \approx 0.018$) the width-to-height aspect ratio should stay smaller than approximately 50. For geometries with $\frac{w}{h} > 50$ (i.e. very large spacing of cracks/island edges compared to the thickness of the strained layer) the glide process comes to rest in the centre region between cracks/island edges, respectively, and a distribution of a-type misfit dislocations along the whole interface is not be achieved anymore. Actually the critical value of the the width-to-height aspect ratio for which the relaxation mechanism becomes limited by the glide process depends on the initial strain of the heterostructure (this will define how far the dislocations will glide into the interface due to the influence of the shear stress around the nucleation site) and the growth temperature (via the temperature dependency of the Peierls stress). A detailed analysis of the degree of plastic relaxation as a function of all these parameters would go beyond the scope of our work. However, in the case that the plastic relaxation mechanism is limited by the glide process the tendency is as following: the achievable degree of plastic relaxation will decrease if the temperature and/or the initial strain decrease and the width-to-height aspect ratio increases.

In combination with the above discussed effect of the surface morphology on the critical thickness for nucleation of a-type misfit dislocations we conclude that for a given thickness of the heterostructure the highest degree of plastic relaxation is achieved for a 3-dimensional growth mode with islands having an aspect ratio in the range between 10 and approximately 50.

4.4.3. Asymmetry of plastic relaxation at the interfaces of (0001)-oriented $Al_xGa_{1-x}N$ interlayers

Now we will discuss the microscopic origin for the asymmetry in plastic relaxation between the upper and lower interface of $Al_xGa_{1-x}N$ interlayers, which finally leads to the build-up of compressive strain in the subsequent layer. For the following consideration of the asymmetric relaxation behaviour, the actual amount of plastic relaxation at the lower interface of the interlayer and the growth mode of the $Al_xGa_{1-x}N$ interlayer itself do not matter in principle. Let us therefore start the discussion by considering the situation of an GaN buffer/$Al_xGa_{1-x}N$ interlayer structure with a (partly) relaxed $Al_xGa_{1-x}N$ layer. Then the initial compressive strain of a GaN overlayer grown subsequently on top of the interlayer is approximately the amount of strain relaxation δ_{AlGaN} of the $Al_xGa_{1-x}N$ interlayer. Depending on the surface morphology of the GaN overlayer at the initial growth stage one can then divide the situation into 2 cases: 2- or 3-dimensional growth of the GaN overlayer.

2-dimensional growth mode of the GaN overlayer

If the GaN overlayer grows perfectly 2-dimensional, the explanation for the asymmetric relaxation behaviour is rather simple. In this case the $\frac{1}{3} < 11\bar{2}0 > |\{0001\}$ slip-system is not active and plastic relaxation at the upper interface of the $Al_xGa_{1-x}N$ interlayer by nucleation and glide of a-type misfit dislocations will not take place. Plastic relaxation can therefore occur only by some alternative mechanisms. As will be discussed later in section 4.4.5, these mechanism proceed, however, less effectively compared to plastic relaxation via the $\frac{1}{3} < 11\bar{2}0 > |\{0001\}$ slip-system. As a result, the degree of plastic relaxation at the upper interface of the $Al_xGa_{1-x}N$ interlayer will stay close to zero and the initial compressive strain in the GaN overlayer will remain almost unrelaxed.

3-dimensional growth mode of the GaN overlayer

In case of a 3-dimensional growth mode the GaN overlayer will consist at the initial growth stage mainly of individual uncoalesced islands (see schematic illustration in Fig. 4.19 (a)). Due to the islanded surface morphology the $\frac{1}{3} < 11\bar{2}0 > |\{0001\}$ slip-system will be active and a-type misfit dislocations can be nucleated in corners of islands. The critical thickness/height of islands when a-type dislocation nucleation is initiated depends on the initial compressive strain of the GaN overlayer (approximately the amount of strain relaxation δ_{AlGaN} of the $Al_xGa_{1-x}N$ interlayer) and, as discussed in the previous section, if the width-to-height aspect ratio is smaller than 10, also on the specific geometry of the islands. The respective values for the critical thickness can be read from Fig. 4.18.

However, concerning the maximum achievable degree of strain relaxation, it is most important, how the surface morphology develops during further growth. At some point the GaN islands will either coalesce or grow in form of columns and change the overall surface morphology. Depending on the growth mode one can distinguish 3 possible cases: (i) If lateral growth is faster than vertical one, then individual islands will coalesce to a closed film (see Fig. 4.19 (b)). (ii) If lateral and vertical growth rates are comparable, coalescence will not change the surface morphology, i.e. the height of islands and their width-to-height aspect ratio at the surface will stay constant, but the islands will grow on top of a coalesced layer with increasing thickness (see Fig. 4.19 (c)). (iii) If lateral growth is suppressed, islands will not coalesce but grow only vertically and form whiskers (see Fig. 4.19 (d)).

In the first case (i) plastic relaxation comes to rest simply because the layer then grows 2-dimensionally and no shear stresses will be present on the easy slip planes and nucleation sites are not available anymore. If the growth proceeds as in case (ii), then the islands edges/corners still remain as possible nucleation sites for a-type dislocations. However, the height of the islands/depth of trenches between islands stays constant while the layer continues to grow. As a result the plastic relaxation process will not resume with increasing overall thickness of the GaN overlayer. In both cases the degree of plastic relaxation at the upper interface of the $Al_xGa_{1-x}N$ interlayer is determined by the maximum height of islands/depth of trenches between them at the moment of islands coalescence.

In case (iii) islands edges/corners again remain as possible a-type dislocation nucleation sites and the height of the islands increases during further growth. However, at a certain height the plastic relaxation process will cease. This is due to the fact that the width-to-height aspect ratio of the islands decreases during further growth and at an aspect ratio $\frac{w}{h}$ below approximately 10 the shear stress around the islands edges/corners will saturate (see our FEM calculations and compare eq. (4.4) with eq. (4.5)). Below this aspect ratio there is no way to nucleate any further misfit dislocation. Note that in case (iii) the compressive strain in the islands/whiskers of the GaN overlayer will be

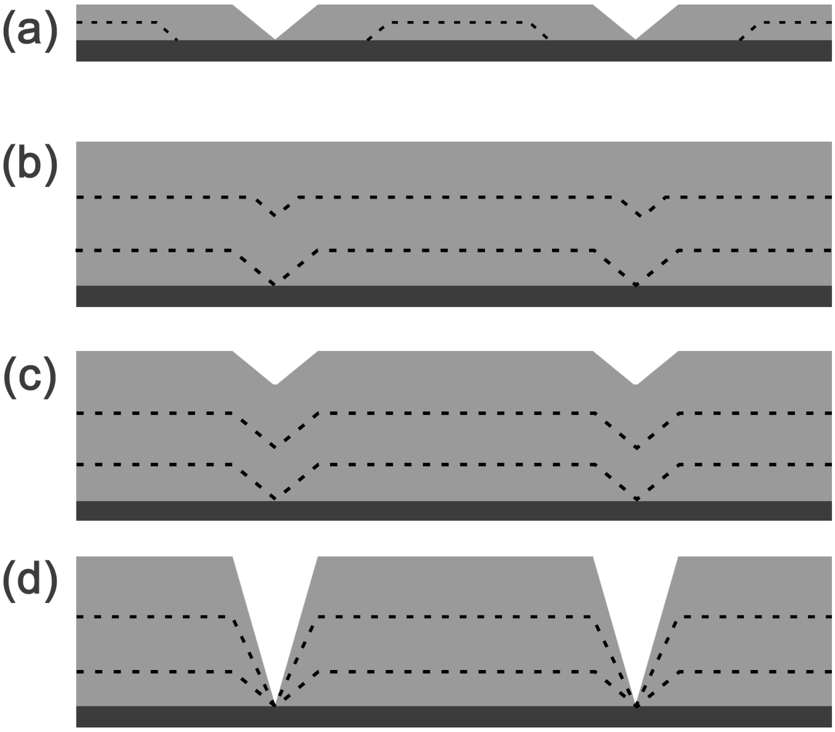

Figure 4.19.: Schematic illustration of possible growth modes of the GaN overlayer (light grey shaded area) on top of an $Al_xGa_{1\text{-}x}N$ interlayer (dark grey shaded area). (a) shows the starting point of non-coalesced individual islands. (b) is the growth mode where islands coalesce to a closed layer (case (i) in the text), (c) represents the case where the surface morphology stays constant but the thickness of the closed layer underneath the islands increases (case (ii) in the text) and (d) illustrates the growth mode where islands do not coalesce and grow only vertically (case (iii) in the text).

significantly relaxed elastically because of the large relative fraction of free surfaces compared to the volume of the islands/whiskers for small width-to-height aspect ratios. E.g. for $\frac{w}{h} = 5$ the degree of elastic strain relaxation is about 50% (corresponding to a ratio of the elastic energies $\frac{E_{elastic}}{E^0_{elastic}}$ of 0.25 in Fig. 4.10).

Following the consideration from above, we can state that the maximum degree of plastic relaxation of a GaN layer grown on top of an $Al_xGa_{1\text{-}x}N$ interlayer is limited, regardless of the actual growth mode, i.e. the chosen growth conditions, of the GaN overlayer. For example, if a GaN overlayer with a maximum height of islands of approximately 15 nm grows on top of a completely relaxed AlN interlayer, the equilibrium strain will be approximately 1.2% (see blue dashed line in Fig. 4.18), i.e. the maximum achievable degree of plastic relaxation at the upper interface of the AlN interlayer is approximately $\frac{1.2\%}{2.4\%} = 0.5$.

It is this inherent asymmetry in plastic relaxation between the upper and lower interface of the $Al_xGa_{1\text{-}x}N$ interlayer that leads to the build-up of compressive strain in the layer grown subsequently on top of the $Al_xGa_{1\text{-}x}N$ interlayer.

4.4.4. Influence of the growth conditions of $Al_xGa_{1-x}N$ interlayers on the strain engineering process

In literature $Al_xGa_{1-x}N$ interlayers, used for strain engineering, are often categorised by their growth temperature - high and low temperature $Al_xGa_{1-x}N$ interlayers. In our experiment an increase of the deposition temperature of $Al_xGa_{1-x}N$ interlayers from 800°C to 1050°C, while all other growth parameters have been nominally kept constant (V/III-ratio=430), leads to a change from a 3- to a 2-dimensional growth mode of $Al_xGa_{1-x}N$ interlayers. However, according to literature reports the same effect can be caused also by varying the V/III ratio for a constant growth temperature [143, 144]. Low/high V/III ratios have been found to lead to 2-/3-dimensional growth of $Al_xGa_{1-x}N$/GaN heterostructures [143, 144].

With respect to plastic relaxation of $Al_xGa_{1-x}N$ interlayers, our considerations of the relaxation mechanism show, however, that not the growth conditions like the deposition temperature themselves are the decisive point but the resulting growth mode of the interlayers. We therefore suggest, to classify $Al_xGa_{1-x}N$ interlayers not by their growth temperature but by their growth mode. As discussed in previous sections, the growth mode of $Al_xGa_{1-x}N$ interlayers has an influence on the critical thickness for the onset of plastic relaxation and on the degree of plastic relaxation. For a given thickness of the interlayer more compressive strain might be built-up in the subsequently grown layer with a 3-dimensionally grown $Al_xGa_{1-x}N$ interlayer. For very thin $Al_xGa_{1-x}N$ interlayers the growth mode even determines, whether strain-engineering works at all. If e.g. a thin 2-dimensionally grown $Al_xGa_{1-x}N$ interlayer had the same thickness as a 3-dimensionally grown $Al_xGa_{1-x}N$ interlayer, which has just started to relax plastically, the 2-dimensionally grown $Al_xGa_{1-x}N$ layer would still be fully strained and thus would not be able to build up any compressive strain. This might be the reason why in some early reports it was claimed that thin high temperature $Al_xGa_{1-x}N$ interlayers are not suited for strain engineering [28, 29, 105].

4.4.5. Alternative plastic relaxation mechanisms

In this section we want to briefly discuss alternative plastic relaxation mechanism and their relevance in relaxation of (0001)-oriented strained wurtzite heterostructures. These relaxation mechanisms may become important if the $\frac{1}{3} < 11\bar{2}0 > |\{0001\}$ slip-system is not active and a-type misfit dislocations cannot be formed by the *"cooperative mechanism"* [30] as discussed above.

In literature some alternative plastic relaxation mechanisms have been reported. The most important ones are: (i) inclination or even complete bending of threading dislocations having an a-component, so that their line segment projected on the basal plane is a misfit dislocation [45, 106, 107, 108, 109, 145, 146] and (ii) formation of a+c-type misfit dislocations by glide on either $\left\{1\bar{1}0\bar{1}\right\}$ (Wu et al. [113]) or $\left\{11\bar{2}2\right\}$ pyramidal slip-planes [33, 117, 118, 120].

Formation of a+c-type misfit dislocations could occur in principle by the classical Matthews-Blakeslee mechanism [147]. For both slip-systems the Schmid-factor is not zero (see Table 2.1 on page 7), meaning that a+c-type dislocations experience on the

$\{1\bar{1}0\bar{1}\}$ or $\{11\bar{2}2\}$ slip-planes even for a perfect 2-dimensional film without cracks or an islanded surface morphology a resolved shear stress. However, this mechanism has very high kinetic barriers. Nucleation of dislocation half-loops correlates with the third power of the Burgers-vector $E_{nucl} \sim b^3$ [129], making nucleation of new a+c-type dislocations at the free surface very unlikely (E_{nucl} would be approximately 7 times higher for a+c-type than for a-type dislocations). Also glide of pre-existing a+c-type dislocations is limited. This is because for the $\frac{1}{3} < 11\bar{2}3 > | \{1\bar{1}0\bar{1}\}$ and $\frac{1}{3} < 11\bar{2}3 > | \{11\bar{2}\bar{2}\}$ slip-system the large Burgers-vector and small spacing of the slip-planes leads to a high Peierls-barrier (see Table 2.1 on page 7), which a+c-type dislocations have to overcome in order that they can glide. As a result the typical spacing of a+c-type misfit dislocations is large compared to that of a-type misfit dislocations if these can be formed, and the amount of strain relaxation caused by a+c-type misfit dislocations stays small.

The other mechanism, i.e. inclination of threading dislocations having an a-component, requires a certain density of pre-existing threading dislocations ρ_{TD} in the film in order to achieve a significant amount of strain relaxation. According to Romanov and Speck [106] the average amount of plastic relaxation can be estimated by

$$\overline{\triangle\varepsilon}(t) = \frac{1}{4} b\, \rho_{TD}\, t \tan\theta_{TD}, \tag{4.21}$$

where t is the thickness of the layer and θ_{TD} is the inclination angle of the threading dislocations. However, this mechanism leads for a 1 μm thick layer with a density of threading dislocations having an a-component of about $\rho_{TD} = 1x\,10^9\,cm^{-2}$ (typical value for heteroepitaxially grown GaN films) and a typical value for the inclination angle of $\theta_{TD} = 25°$(see e.g. Ref. [45, 107, 108, 109, 146]) to a strain relaxation of only $\triangle\varepsilon = 0.04\,\%$. Furthermore, this mechanism has also a certain kinetic barrier. Inclination of a-type dislocations by climb has been theoretically investigated by Romanov and Speck [106] and they have found a typical energy barrier for the inclination mechanism to become operable of several eV per dislocation.

In summary, it can be stated that in the case of (0001)-oriented strained III-nitride heterostructures with a 3-dimensional surface morphology (e.g. island growth, surface pits, macrosteps, cracks) homogeneous nucleation of a-type dislocations is typically the most effective plastic relaxation mechanism. Alternative relaxation mechanism might become relevant only if formation of a-type misfit dislocations is inhibited (e.g. in the case of 2-dimensionally grown compressively strained (0001)-oriented III-nitride heterostructures) or if the threading dislocation density in the film is very high (in the order of $10^{10}\,cm^{-2}$ or higher).

4.5. Conclusions - Optimised growth schema for strain engineering with $Al_xGa_{1-x}N$ interlayers

In the previous sections we have seen that the surface morphology of (0001)-oriented III-nitride heterostructures has a strong influence on the strain relaxation process, not only qualitatively but also quantitatively. This is mainly because of the different energetical barrier for nucleation of a-type misfit dislocations at different available nucleation sites (island corners in case of a 3-dimensional growth mode and crack tips for 2-dimensional growth and cracking). As a direct consequence, the degree of plastic relaxation at the interfaces of $Al_xGa_{1-x}N$ interlayers depends on the growth mode of the $Al_xGa_{1-x}N$ interlayer and the subsequent GaN layer. Hence, the strain engineering process can be influenced by the choice of the growth parameters. With the help of the insight about the relaxation mechanism gained in this work we will develop in the following strategies for an optimised strain engineering process.

$Al_xGa_{1-x}N$ interlayer growth

In principle one can choose 2- as well as 3-dimensionally grown $Al_xGa_{1-x}N$ interlayers. Both have advantages and disadvantages. If a minimum thickness of the $Al_xGa_{1-x}N$ interlayer is crucial for the device structure, a 3-dimensional growth mode is favourable because such interlayers have the advantage of a lower critical thickness for the onset of plastic relaxation and a higher degree of strain relaxation for a given $Al_xGa_{1-x}N$ layer thickness. The width-to-height aspect ratio of the islands should, however, not become much smaller than 10, since in this case nucleation of a-type misfit dislocations will be limited. 2-dimensionally grown $Al_xGa_{1-x}N$ interlayers are also suited for strain engineering. In contrast to 3-dimensionally grown $Al_xGa_{1-x}N$ interlayers they have to be thicker to achieve the same amount of plastic relaxation (and thus to build up the same amount of compressive strain). However, $Al_xGa_{1-x}N$ interlayers grown in a 3-dimensional mode have the potential disadvantage to cause a stronger increase of the threading dislocation density than 2-dimensionally grown $Al_xGa_{1-x}N$ interlayers, even for the same amount of lattice relaxation. This is because for 3-dimensionally grown $Al_xGa_{1-x}N$ interlayers misfit dislocation half-loops in the interfacial plane, causing plastic relaxation, extend initially only as wide as the lateral dimensions of islands of the interlayer are, i.e. typically not more than a few 100 *nm*. In case of 2-dimensionally grown $Al_xGa_{1-x}N$ interlayers a-type dislocation half-loops nucleate at crack tips and then can extend into the whole interface until they reach another crack. This distance is typically in the order of micrometers. Consequently in case of 3-dimensionally grown $Al_xGa_{1-x}N$ interlayers typically a higher number of nucleation events is required to reach the same degree of strain relaxation in the film. Since each nucleated misfit dislocation half-loop initially results in 2 threading dislocations, the threading dislocation density is supposed to be essentially higher in case of 3-dimensionally grown $Al_xGa_{1-x}N$ interlayers.

GaN overlayer growth

In order to build up a maximum amount of compressive strain and also to keep the overall increase of the threading dislocation density as small as possible, any nucleation of a-type dislocations at the upper interface of $Al_xGa_{1-x}N$ interlayers should be avoided. Since the GaN overlayer grows under compressive strain, cracking does not occur at this interface and island edges/corners or surface pits are the only possible sites for nucleation of a-type dislocations in this case. Consequently the GaN overlayer should be grown ideally in a 2-dimensional mode (either layer-by-layer or step-flow growth). If it is not possible to achieve a 2-dimensional surface morphology during the initial growth stage of the GaN overlayer, then an alternative strategy to inhibit plastic relaxation could be to control the growth of the GaN overlayer in such a way that in the first step the height of growing island stays below the critical thickness for nucleation of a-type misfit dislocations. Then in a second step, conditions, which promote fast lateral growth and coalescence of the islands, would be benefitial. Possible growth parameters, which could influence the growth mode are the deposition temperature and the V/III ratio [149], as well as the reactor pressure [150, 151].

5. Anti-surfactant effect of Si in GaN (0001) epitaxy

5.1. Aim of this chapter

It is well known in literature that Si, the donor of choice for GaN, acts as an anti-surfactant[1] in the epitaxial growth of GaN (0001) films [16, 153, 154]. On the one hand, this leads to undesired surface roughening during growth of GaN for high Si doping concentrations (typically beyond a value of $10^{19}\,cm^{-3}$) [154]. On the other hand, the anti-surfactant effect of Si is also intentionally used by exposing the GaN (0001) surface to a Si-flux in order to promote three-dimensional growth and thus to reduce the dislocation density in epitaxial GaN layers [16, 17, 18, 19, 155]. Even quantum dots can be grown with Si as an anti-surfactant [16, 35, 156].

Concerning the origin of the anti-surfactant effect of Si in GaN (0001) epitaxy, the following explanations exist in literature. In case of a lower dose of Si exposure (for an equivalent of 0.039 monolayer of Si), Munkholm et al. [157, 158] concluded from in-situ x-ray investigations that Si changes the growth mode from step-flow to layer-by-layer growth and suggested pinning of step motion by an impurity barrier as a possible explanation. On the other hand, it has been observed that a high dose of Si exposure of the GaN (0001) surface (according to the numbers given in Ref. [17] an equivalent of approximately 1 monolayer of Si and more) leads to a transition from two-dimensional to three-dimensional growth [16, 17, 18, 19, 35, 154]. This has been attributed to a partial "masking"' of the GaN growth surface by Si (commonly called SiN_x-mask). While Tanaka et al. [16] considered a sub-monolayer coverage with Si-N bonds to cause this masking of the surface, Rosa et al. [36, 37] showed with the help of ab-initio calculations that for Si-rich and N-rich growth conditions the GaN (0001) surface is thermodynamically unstable against the formation of β-Si_3N_4 islands, which chemically passivate GaN surfaces.

However, there is no direct experimental proof neither for the SiN_x model proposed by Tanaka et al. [16] nor for the Si_3N_4 model by Rosa et al. [36]. A TEM analysis by Kuwano et al. [38] had indeed shown that the SiN_x-mask is a thin crystalline layer (thickness less than $1\,nm$), which shows an epitaxial relationship with the GaN lattice and contains a certain amount of silicon. However, because aberration correction TEM was not common at that time the exact atomic structure of the SiN_x-mask or SiN_x-interlayer remained unsolved so far. Consequently, any explanation on the physical or chemical mechanism of how the SiN_x-mask prevents growth of GaN growth on top of it remained speculative.

---

[1] In epitaxial growth species are considered as anti-surfactants (surfactant: **surf**ace **act**ive **a**ge**nt**) if they promote three-dimensional growth leading to rougher surfaces in systems that grow two-dimensional under thermodynamic equilibrium conditions [152].

The main goal of this chapter[2] is therefore to resolve this problem. For this purpose we will use in a first step aberration corrected transmission electron microscopy to study the incorporation of Si into the GaN (0001) surface. We will show that the exposure of the GaN (0001) surface to Si leads to the formation of a coherent $SiGaN_3$-monolayer. With the structural information at hand we will afterwards use density functional theory calculations (i) to understand the growth of the $SiGaN_3$-layer itself and (ii) to shed some light onto the behaviour to block growth of GaN on top of this layer. Finally, we will propose an explanation for the anti-surfactant effect of Si in the epitaxy of GaN (0001) films.

5.2. Experimental results

5.2.1. Transition towards 3-dimensional growth

Fig. 5.1 (a) shows a typical cross-sectional transmission electron micrograph of the initial growth stage of a GaN layer (nominal thickness is $10\,nm$) deposited on a Si treated[3] GaN (0001) buffer. The growth conditions of the GaN layer are identical to that of the GaN buffer, which grows 2-dimensionally with a flat surface morphology. The GaN layer on top of the Si treated GaN (0001) buffer, however, exhibits a 3-dimensional growth mode. It consists of isolated islands (compare with AFM image in Fig. 5.1 (b)), which have the shape of truncated hexagonal pyramids. The islands are bound by $\left\{1\bar{1}01\right\}$ facets and have lateral sizes in the order of 100 nm. Using HRTEM imaging a very thin layer becomes visible, which partially covers the GaN buffer surface and is present at the interface between GaN island and the GaN buffer (see Fig. 5.1 (d)). This layer will be hereinafter called the SiN_x-interlayer. HRTEM also shows that nucleation and growth of thick GaN directly on top of the SiN_x-interlayer is inhibited (see Fig. 5.1 (e)). Instead, growth of GaN islands exclusively starts at windows where the GaN buffer is not covered by the SiN_x-interlayer, e.g. at surface steps in the GaN buffer as in Fig. 5.1 (c) or at holes in the SiN_x-interlayer. All these observations are fully consistent with previous reports in literature by other authors (compare references [16, 19, 20, 21, 157]) using Si as an anti-surfactant.

---

[2] Parts of the results shown in this chapter (HR(S)TEM investigation, structural modelling and density functional theory calculations) have been published by myself in Markurt et al. [15].

[3] The Si treatment of the GaN buffer has been performed at a temperature of $1030\,^{\circ}C$ by exposing the GaN (0001) surface for 2 minutes to a silane flux of $400\,nmol/min$ while the Ga flux was stopped. The ammonia flux has remained unchanged the whole time.

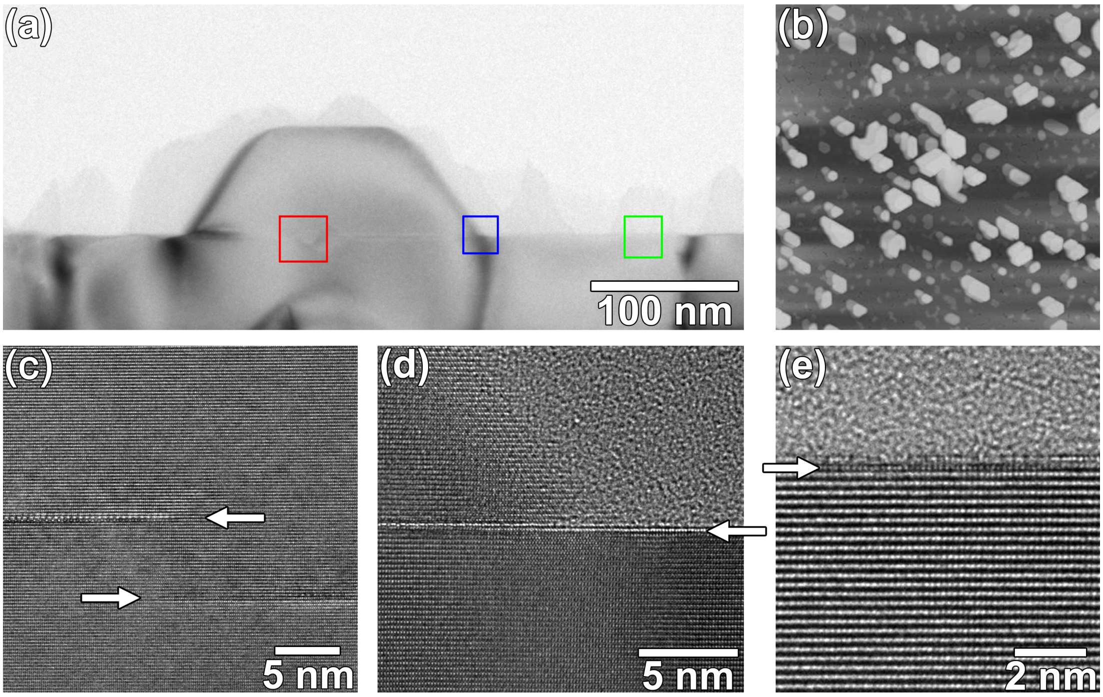

Figure 5.1.: (a) TEM Bright Field image of a GaN island growing on top of the SiN_x-interlayer. (b) 5x5 μm^2 AFM surface topography image (height scale is 150 nm). (c) - (e) show HRTEM images from regions in (a) marked by red, blue and green frames. White arrows indicate the SiN_x-interlayer.

5.2.2. HR(S)TEM investigation of the SiN_x-interlayer

To analyse the atomic structure of the SiN_x-interlayer, we have carried out aberration corrected HRTEM and HRSTEM-ADF imaging in the $\langle 11\bar{2}0 \rangle$ (see Fig. 5.2) and $\langle 1\bar{1}00 \rangle$ projection (see Fig. 5.3). Let us start the detailed contrast analysis with the images recorded in the $\langle 11\bar{2}0 \rangle$ zone axis. Although the HRTEM pattern of the SiN_x-interlayer slightly differs from that of the GaN matrix (see Fig. 5.2 (a)), one can clearly see that the SiN_x-interlayer consists of a single crystalline monolayer, which is coherently grown on the GaN buffer. Along the interface the contrast pattern of the SiN_x-interlayer is constant. From comparison with HRTEM image simulations[4] (see inset in the lower right corner in Fig. 5.2 (a)) we identify bright dots in the GaN matrix as N atomic columns while dark lobes correspond to Ga columns. If we periodically reproduce the (Ab Ba) stacking of the wurtzite lattice across the interface, we find that the SiN_x-interlayer does not interrupt the hexagonal closed package (hcp) stacking of the GaN matrix. As shown in Fig. 5.2 (a) atomic columns of the SiN_x-interlayer even fit into the hcp stacking sequence. Similar results can be found also in the STEM-ADF image (see Fig. 5.2 (b)). However, the reduced ADF intensity of the SiN_x-interlayer points to a reduced effective atomic number Z of its atomic columns compared to that of the GaN matrix. This can be caused e.g. by substitution of Ga atoms with lighter

---

[4] The simulation has been performed according to experimental conditions with a spherical aberration of $C_S = -11\,\mu m$, an overfocus of $\Delta f = +5\,nm$ and a specimen thickness of $t = 7.7\,nm$.

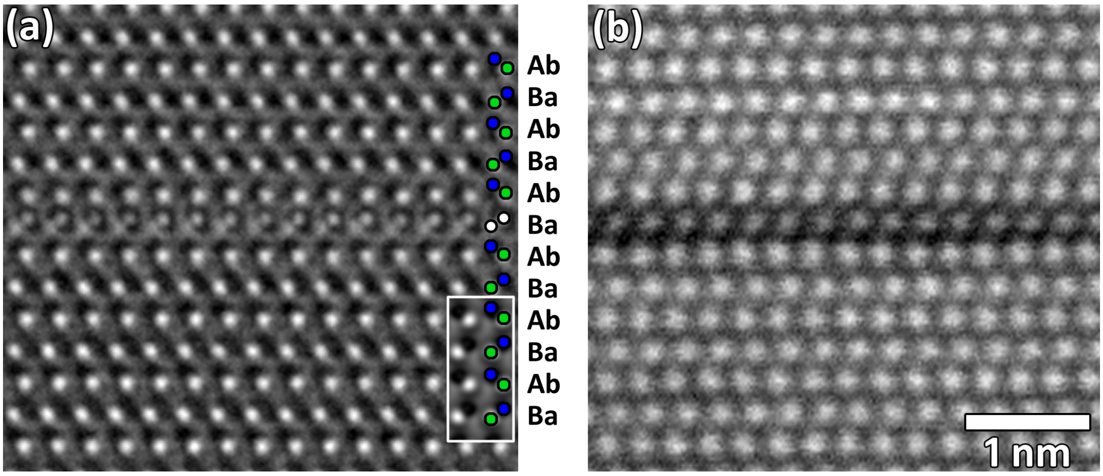

Figure 5.2.: (a) Aberration corrected HRTEM and (b) STEM-ADF images of the SiN_x-interlayer in the $\langle 11\bar{2}0 \rangle$ projection. The inset (indicated by a white frame) in the lower right corner of (a) is a HRTEM image simulation of GaN. Green and blue balls correspond to nitrogen and gallium columns in the GaN matrix. White balls denote atomic columns of the SiN_x-interlayer. Both images are on the same scale.

elements, e.g. Si instead of Ga, and/or a lower density of atoms along the column direction due to e.g. the presence of gallium vacancies V_{Ga}.

The situation is completely different along the $\langle 1\bar{1}00 \rangle$ projection (see Fig. 5.3). There the SiN_x-interlayer is characterised by an in-plane periodicity of three $\{11\bar{2}0\}$ GaN planes. Two experimental findings should be highlighted here. On the one side, the three columns of the periodic unit in the SiN_x-interlayer exhibit different intensities in the phase of the exit wave reconstruction (EWR)[5] and in the ADF image[6] in Fig. 5.3 (b) and (c), respectively. It is particularly noticeable that the intensity of one of the atomic columns in the SiN_x-interlayer basically corresponds to that of the GaN background. Since the phase of the EWR/STEM-ADF image intensity peaks at positions of atomic columns and are proportional to the projected potential of the columns/to their atomic number Z, respectively, these observations suggest that different elements and/or densities of atoms are present in the three columns. On the other side, the three columns of the periodic unit of the SiN_x-interlayer are shifted along the $\langle 0001 \rangle$ direction with respect to each other. The pair formed of the two columns that appear bright in the phase of the EWR/STEM-ADF image forms a buckled configuration. Using the approach of Schulz et al. [162] to locally measure the lattice parameter with a precision of approximately 2 *pm* we find a vertical shift between these two

---

[5] The exit wave reconstruction is an iterative method to retrieve the complex electron wave (i.e. its amplitude and phase, which are otherwise lost during image recording) from a HRTEM defocus series. A detailed description of this method is given e.g. in Ref. [159, 160, 161]

[6] To reduce the noise of the ADF image all spatial frequencies above the resolution limit of the incoherent imaging process (given by the double cut-off frequency of the condenser aperture) have been filtered out. We have further improved the signal to noise ratio by integrating 4 laterally equivalent parts of the image.

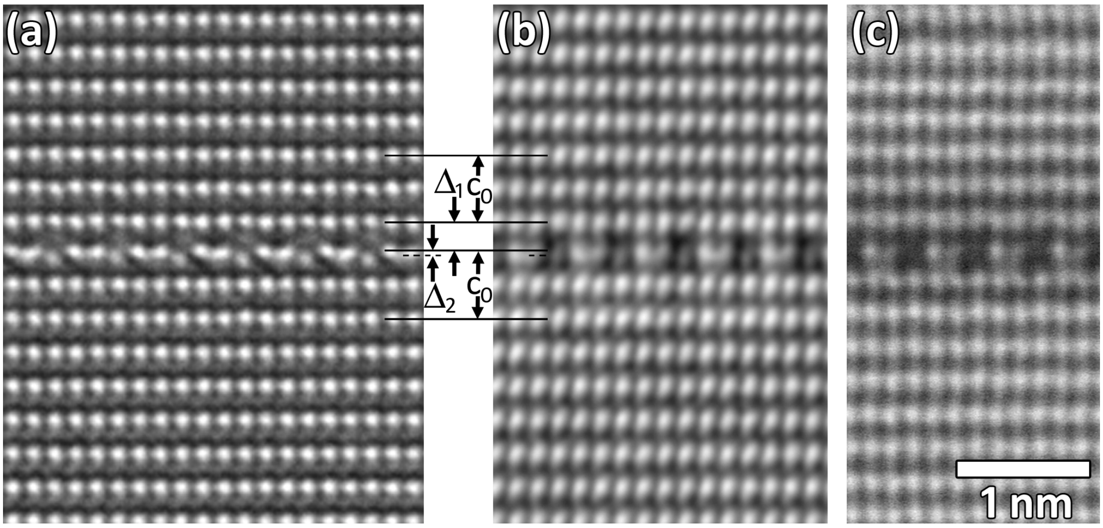

Figure 5.3.: (a) Aberration corrected HRTEM, (b) the phase of an exit wave reconstruction and (c) STEM-ADF images of the SiN$_x$-interlayer in the $\langle 1\bar{1}00 \rangle$ projection. All images are on the same scale.

columns of approximately 12 *pm* (corresponds to $\Delta_2 = 12\ pm$ in Fig. 5.3 (a)). Additionally, this analysis reveals a reduction of the vertical lattice spacing above the SiN$_x$-interlayer by 26 *pm* compared to the out-of-plane-lattice parameter c_0 of the surrounding GaN matrix (corresponds to $\frac{1}{2}c_0 - \Delta_1 = 26\ pm$ in Fig. 5.3 (a)).

5.3. The atomic structure of the SiN$_x$-interlayer

In the following we will use the results obtained from our HR(S)TEM investigation to identify the atomic structure of the SiN$_x$-interlayer. We will first derive a number of possible model structures, then calculate their relaxed atomic condiguration by density functional theory calculations, perform (S)TEM image simulations based on these models and finally identify the atomic structure of the SiN$_x$-interlayer by comparing simulated and experimental HR(S)TEM images.

Let us start with a recapitulation of the two most striking observations: (i) The SiN$_x$-interlayer has a different appearance in the two projections, i.e. it shows a regular wurtzite stacking in the $\langle 11\bar{2}0 \rangle$ projection but an extra periodicity of three $\{11\bar{2}0\}$ planes in the $\langle 1\bar{1}00 \rangle$ projection. (ii) The three cation columns in the SiN$_x$-interlayer seen in the $\langle 1\bar{1}00 \rangle$ projection have a different composition.

These observations can be most easily explained by a $\sqrt{3} \times \sqrt{3}R30°$ reconstruction of the GaN (0001) surface where the three cation positions in the $\sqrt{3} \times \sqrt{3}R30°$ unit cell (see white, dark and light grey balls in Fig. 5.4) are occupied by either Si$_{\mathrm{Ga}}$, V$_{\mathrm{Ga}}$ or Ga. A $\sqrt{3} \times \sqrt{3}R30°$ reconstruction of the SiN$_x$-interlayer is consistent with the observed extra periodicity in the $\langle 1\bar{1}00 \rangle$ projection (see Fig. 5.4 (a)) and with the regular wurtzite appearance if the structure is seen along the $\langle 11\bar{2}0 \rangle$ projection (in this projection all columns have in average the same composition; see Fig. 5.4 (c)).

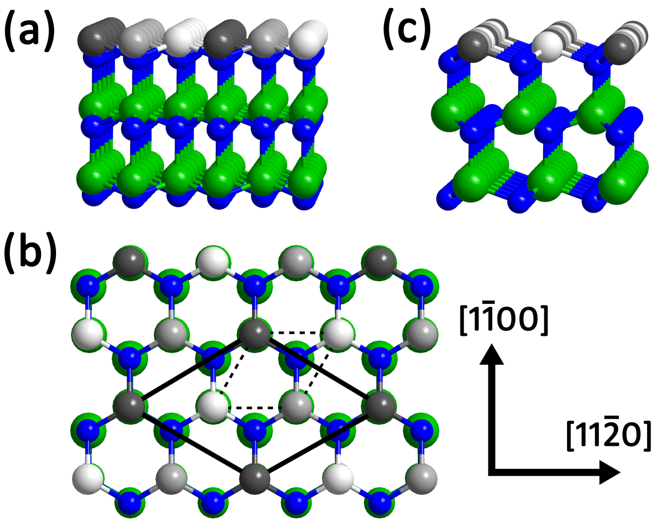

Figure 5.4.: Ball-and-stick model of the SiN_x-interlayer. Blue and green balls represent N and Ga atoms. White, dark and light grey balls denote the cation positions of the SiN_x-interlayer which can be occupied by either Si_{Ga}, V_{Ga} or Ga. (a) Cross-sectional view along $\langle 1\bar{1}00 \rangle$ the projection with the extra periodicity in the SiN_x-interlayer corresponding to three $\{11\bar{2}0\}$ planes. (b) Top view along the $[000\bar{1}]$ direction and (c) cross-sectional view along the $\langle 11\bar{2}0 \rangle$ projection, respectively, of the structure shown in (a). The dashed and solid frame in (b) represent the projected GaN unit cell and the $\sqrt{3} \times \sqrt{3}R30°$ reconstruction, respectively.

If one distributes either Si_{Ga}, V_{Ga} or Ga on the three cation positions, 7 different possible structures consistent with the $\sqrt{3} \times \sqrt{3}R30°$ reconstruction are possible. Since the SiN_x-interlayer forms as a result of an extended silane exposure of the GaN surface and silicon is known to be easily incorporated into GaN [154, 163] (silicon is the donor of choice in GaN) we consider in the following only structures which contain silicon. Due to this restriction, finally five $\sqrt{3} \times \sqrt{3}R30°$ reconstructions, which are listed in Table 5.1 remain for the SiN_x-interlayer.

The atomic geometry of all five model structures has then been relaxed using density functional theory (DFT) calculations. The DFT calculations have been performed by Liverios Lymperakis and Jörg Neugebauer from the Max-Planck-Institut für Eisenforschung. Details of the DFT calculations are given in appendix E. As can be seen in the ball-and-stick representation of the relaxed structures in Fig. 5.5, the difference between the length of the Si-N bond (1.74 Å [164]) and the Ga-N bond (1.95 Å [165]) causes local lattice distortions. Especially the position of N atoms in the SiN_x-interlayer is strongly affected by the presence of Si atoms.

Table 5.1.: Possible structures for the SiN_x-interlayer

structure	cation 1	cation 2	cation 3	stoichiometry	figure
Si-Ga-V_{Ga}	Si	Ga	V_{Ga}	$SiGaN_3$	Fig. 5.5 (a)
Si-Si-V_{Ga}	Si	Si	V_{Ga}	Si_2N_3	Fig. 5.5 (b)
Si-Si-Ga	Si	Si	Ga	Si_2GaN_3	Fig. 5.5 (c)
Si-Ga-Ga	Si	Ga	Ga	$SiGa_2N_3$	Fig. 5.5 (d)
Si-V_{Ga}-V_{Ga}	Si	V_{Ga}	V_{Ga}	SiN_3	Fig. 5.5 (e)

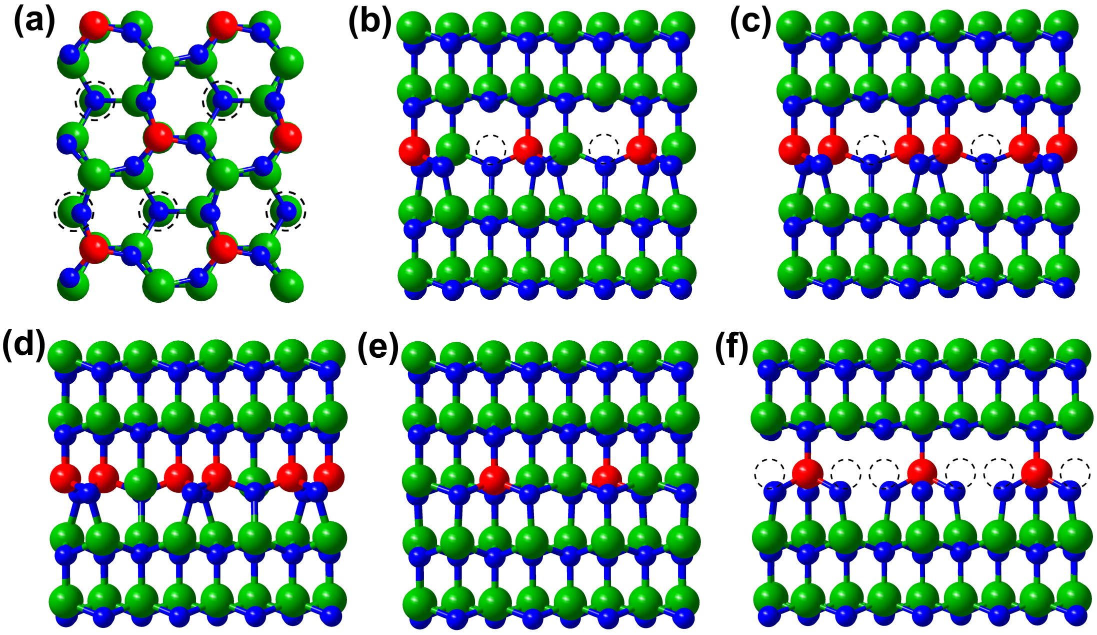

Figure 5.5.: Ball-and-stick representation of the relaxed structures models of the SiN_x-interlayer (see Table 5.1): (a) and (b) Si-Ga-V_{Ga}, (c) Si-Si-V_{Ga}, (d) Si-Si-Ga, (e) Si-Ga-Ga and (f) Si-V_{Ga}-V_{Ga}. (a) is a top view along the $\left[000\bar{1}\right]$ direction, (b)-(f) are cross-sectional view along the $\left\langle 1\bar{1}00\right\rangle$ projection. Blue, green, red and dashed balls indicate N, Ga, Si and V_{Ga}, respectively.

The relaxed structure models have then used to perform (S)TEM image simulations using the multislice method. Simulation parameters have been chosen according to the experimental conditions[7]. In the case of HRTEM simulations the sample thickness and defocus have been adjusted to reproduce the contrast pattern of the GaN matrix in the experimental images while for the STEM-ADF simulations (using the frozen phonon [64, 168, 169] approach with 20 different configurations) the sample thickness has been determined by a quantitative evaluation of the ADF intensity of the GaN matrix in the experimental images [167, 170]. A convolution with a Gaussian with a 1.0 Å full-width at half-maximum to account for the effect of the finite source size [171] has proven to provide the best match between experiment and simulation.

A comparison of experimental and simulated images is shown in Fig. 5.6. An excellent match is found for the Si-Ga-V_{Ga} structure (leftmost column of simulated images) in that it correctly reproduces the intensities of the atomic columns as well as the relaxation of atomic positions leading to the shrinking of the average out-of-plane lattice parameter directly above the SiN_x-interlayer ($\frac{1}{2}c_0 - \Delta_1 = 0.14/0.26$ Å in the DFT calculation/experiment, respectively) and the buckling of the Si and Ga atomic column pair ($\Delta_2 = 0.06/0.12$ Å in the DFT calculation/experiment, respectively). The quantitative difference between the calculated and experimentally determined lattice relaxation is still within the accuracy limit of the used density functional theory method. This difference points to the fact that with modern aberration corrected TEMs one may achieve an accuracy ($\approx 2\ pm$, Ref. [162]) in measuring positions of atomic columns and their shifts even on a local scale that is higher than that, which DFT calculations can predict. For all other assumed structures the simulations show no agreement with the experiment if all experimental images are considered. Thus we conclude that for the applied growth conditions the SiN_x-interlayer consists of three N, one Si, one Ga atom as well as one Ga vacancy arranged within a $\sqrt{3} \times \sqrt{3}R30°$ unit cell on the (0001) growth surface. This structure corresponds to a $SiGaN_3$ stoichiometry. Interestingly, our finding is consistent with previous reports in literature about the GaN (0001) surface symmetry during the Si treatment. Semond et al. observed with in-situ reflection high energy electron diffraction (RHEED) a (1×3) pattern along the $\langle 1\bar{1}00 \rangle$ azimuth for a GaN (0001) surface under a Si flow in molecular beam epitaxy (MBE). The same pattern was also found ex-situ for GaN (0001) templates, which were exposed to a silane flow in a metal-organic vapour phase epitaxy growth process [172, 173, 174].

---

[7] The acceleration voltage was 300 kV in all experiments. For aberration corrected HRTEM imaging/the exit wave reconstruction the spherical aberration has been tuned to $C_S = -11\ \mu m / -35\ \mu m$, respectively. The maximum spatial frequency transferred by the microscope is approximately $12.5\ nm^{-1}$ resulting in an information limit of 0.8 Å. The effect of the modulation transfer function of the imaging system [166] has been taken into account. STEM-ADF imaging has been performed with a spherical aberration of the probe forming lens of $C_S = 1.2\ mm$ and a condenser aperture with a semi-angle of $\alpha = 9.0\ mrad$. The ADF detector inner acceptance semi-angle was $\theta_{det} = 54\ mrad/28\ mrad$ for the images recorded in the $\langle 1\bar{1}00 \rangle / \langle 11\bar{2}0 \rangle$ projection, respectively and the radial sensitivity of the detector has been considered as described in reference [167].

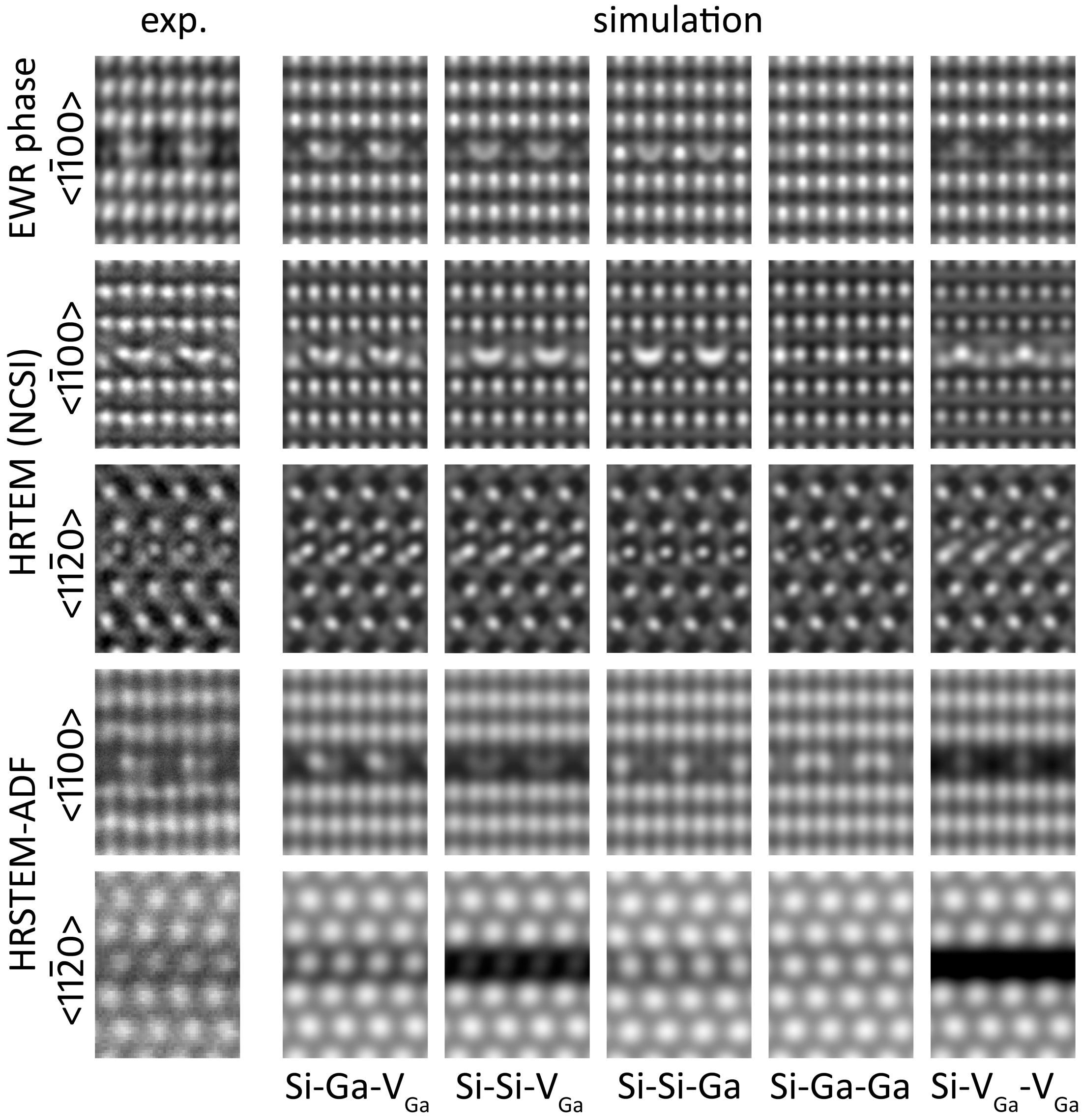
exp.
simulation
EWR phase
<1$\bar{1}$00>
HRTEM (NCSI)
<1$\bar{1}$00>
<11$\bar{2}$0>
HRSTEM-ADF
<1$\bar{1}$00>
<11$\bar{2}$0>
Si-Ga-V$_{Ga}$
Si-Si-V$_{Ga}$
Si-Si-Ga
Si-Ga-Ga
Si-V$_{Ga}$-V$_{Ga}$

Figure 5.6.: Comparison of experimental (left column) and simulated (5 right columns) images of the 5 assumed structure models for the SiN$_x$-interlayer. In case of the HRTEM simulations the defocus is $+6\ nm/+5\ nm$ (overfocus) for the images in the $\langle 1\bar{1}00\rangle/\langle 11\bar{2}0\rangle$ projection, respectively. The sample thickness for the simulated images is from top to bottom $6.1/6.6/7.7/125/40\ nm$. Note that experimental and simulated ADF images are for each row on the same intensity scale: $0.15-0.235/0.075-0.19$ of the incident electron beam for the images in the $\langle 1\bar{1}00\rangle/\langle 11\bar{2}0\rangle$ projection, respectively.

5.4. Discussion

With the help of our HR(S)TEM investigation we have unambiguously identified the atomic structure of the SiN_x-interlayer as a $\sqrt{3} \times \sqrt{3}R30°$ reconstruction having a $SiGaN_3$ stoichiometry. However, two questions concerning the growth of the $SiGaN_3$-layer itself remain unsolved. The first one is why such rather complicated structure containing in its unit cell next to a silicon also a gallium atom as well as a gallium vacancy forms instead of a more simple SiN-/SiN_x-layer. According to previous ab-initio calculations of Rosa and Neugebauer [37] the GaN (0001) surface is thermodynamically unstable against the formation of $\beta - Si_3N_4$ under conditions (N-rich and Si-rich) for that other silicon containing reconstructions would become energetically more favourable than the bare GaN surface. And the second question is why the growth of the $SiGaN_3$-structure is self-limited. For the applied growth conditions we observe in the experiment only a sub-monolayer although the GaN (0001) surface has been exposed to a silane flow for 2 minutes.

In the following discussion we will address both points. For that purpose we have performed extensive first principles calculations on $n\sqrt{3} \times m\sqrt{3}R30°$ $(n,m = 1,2)$ as well as orthogonal $n \times m$ $(n,m = 2,4)$ Si covered GaN (0001) surface reconstructions and compared their surface energies. Methodological details about the DFT calculations together with an overview of all considered structures are given in the appendix E.

5.4.1. Growth of the $SiGaN_3$-interlayer

Fig. 5.7 (a) shows relative surface energies as a function of the silicon chemical potential for a number of surface reconstructions, including the 5 assumed structural models from section 5.3 and structures corresponding to 1 and 2 monolayers of hexagonal SiN. Nitrogen-rich conditions have been applied for the calculations (for further methodological details see appendix E). Note that in Fig. 5.7 (a) only structures free of hydrogen are compared with each other. In the surface phase diagram in Fig. 5.7 (b) also hydrogen containing structures are included.

Looking at these results our DFT calculations reveal that for a wide range of silicon chemical potential a $\sqrt{3} \times \sqrt{3}R30°$ surface reconstruction having a $SiGaN_3$ stoichiometry is the energetically most favourable one. This result is not only in agreement with our experimental finding from the previous section, but it also shows that for a wide range of silicon chemical potential only 1 silicon atom per $\sqrt{3} \times \sqrt{3}$ unit cell can be stabilised on the surface. Only for very Si-rich $(-1.25\ eV \leq \mu_{Si} - \mu_{Si\,bulk} \leq 0)$ and rather H-poor $\left(\mu_H - \frac{1}{2}\mu_{H_2\,molecule} \leq -1.0\ eV\right)$ conditions a surface reconstruction with 2 Si atoms per $\sqrt{3} \times \sqrt{3}$ unit cell on the surface, i.e. a monolayer with Si_2N_3 stoichiometry, will become energetically more favourable. Surface structures with 3 Si atoms per $\sqrt{3} \times \sqrt{3}$ unit cell, i.e. a coherent hexagonal monolayer or bilayer of SiN, is even at very Si-rich conditions from thermodynamic point of view highly unfavourable (see solid and dashed lines in Fig. 5.7 (a)). This means that coherent growth of thick SiN-layers is inhibited. Consequently, the Si treatment of the GaN (0001) surface in MOVPE/MBE experiments (moderate Si-flux, Ga-flux off and N-flux as for typical GaN growth conditions) can be considered as self-limited growth and results in

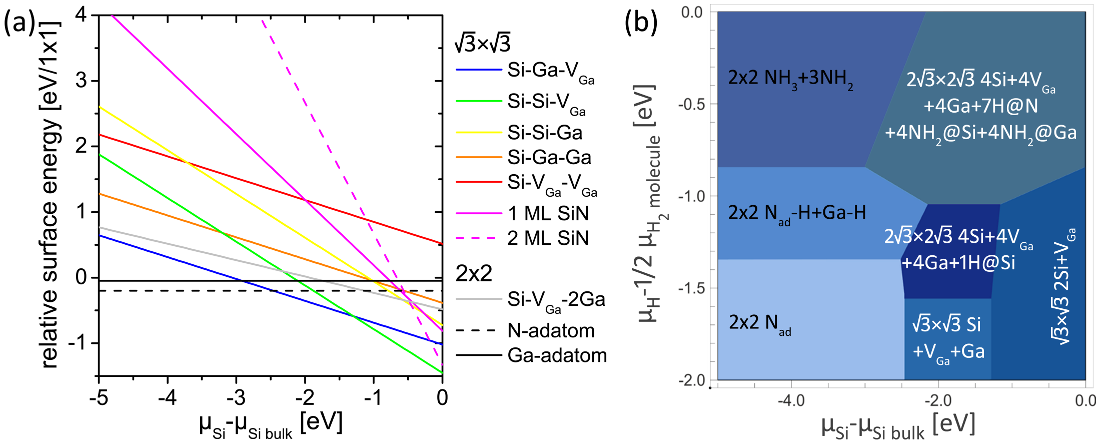

Figure 5.7.: (a) Relative surface energies for a variety of considered structures as a function of the silicon chemical potential. (b) Surface phase diagram showing stable surface reconstructions as a function of the hydrogen and silicon chemical potentials. Each contour in the phase diagram denotes a different surface reconstruction which is the energetically most favourable one for the respective range of hydrogen and silicon chemical potentials. For more details about the structure of the GaN reconstructions indicated by black labels in (b) and the hydrogen containing adsorbates see Ref. [175] and Ref.[176], respectively.

accordance with our DFT calculations for moderate Si-rich conditions in the formation of 1 monolayer of $SiGaN_3$. A longer duration of the Si treatment thus only increases the surface coverage rate with the $SiGaN_3$-monolayer but does not lead to growth of a thicker layer.

The reason for the higher surface energy of coherent SiN-layers compared to that of the $SiGaN_3$ structure is understood when considering the large difference between the Si-N (1.74 Å [164]) and Ga-N (1.95 Å [165]) bond length. While for the $SiGaN_3$-monolayer structure different in-plane and out-of-plane relaxation of individual atoms (see relaxed structure model in Fig. 5.5 (a) and (b)) leads to rather unstrained bonds, this is impossible for SiN layers. Thus a coherent layer of SiN on top of GaN would be highly strained, making it energetically unfavourable compared to the $SiGaN_3$-structure.

Let us finally address the question of the stability of the GaN (0001) surface against formation of $\beta - Si_3N_4$ during the Si treatment. Our DFT calculations predict that the $SiGaN_3$-monolayer will become energetically more favourable than silicon free GaN surface reconstructions if the silicon chemical potential increases about a value of approximately

$$\mu_{Si} - \mu_{Si\ bulk} \geq -2.5\ eV, \tag{5.1}$$

i.e. beginning from moderate Si-rich conditions. According to previous ab-initio calculations of Rosa and Neugebauer [37] this value is for N-rich conditions $\left(\mu_N - \frac{1}{2}\mu_{N_2 molecule} = 0\right)$, as we have assumed in our considerations, already above the limit

$$\mu_{Si} - \mu_{Si\,bulk} \leq \frac{1}{3}\Delta H^{f}_{Si_3N_4} = -3.32\,eV \tag{5.2}$$

where the system should become thermodynamically unstable against formation of $\beta - Si_3N_4$. This means that $\beta - Si_3N_4$ might form e.g. as small particles in the growth atmosphere above the surface. However, for the applied growth conditions we obviously observe in the experiment only the $SiGaN_3$-monolayer but no epitaxial growth of coherent $\beta - Si_3N_4$-layers. Similarly as discussed before for the coherent growth of SiN-monolayers on top of GaN, it is the high lattice mismatch between $\beta - Si_3N_4$ and GaN that inhibits formation of a coherent layer of crystalline $\beta - Si_3N_4$ on the GaN (0001) surface for typical growth conditions for that the $SiGaN_3$-monolayer is deposited.

5.4.2. Anti-surfactant effect of Si in the growth of GaN

Having identified the atomic geometry of the SiN_x-interlayer as $SiGaN_3$ we will now use this information to shed some light onto the behaviour of this layer to block growth of GaN on top of it. In order to understand how the $SiGaN_3$ layer blocks growth we calculate the change in relative surface energy when depositing additional GaN monolayers on top of this surface. For the calculations we assume thermodynamical equilibrium with bulk GaN under nitrogen rich conditions according to typical growth conditions in MOVPE experiments. For further methodological details of the calculations see appendix E.

The corresponding relative surface energies are shown in Fig. 5.8. We find that the thermodynamic minimum is for a single GaN monolayer on top of the $SiGaN_3$ terminated surface. Adding further GaN monolayers steeply and linearly increases the surface energy, making the additional monolayers and thus the growth of a thick GaN film thermodynamically highly unfavourable. Interestingly, the blocking mask does not contain Si in the top surface layer as conventionally assumed, but terminates in a single GaN monolayer.

In order to understand the driving forces underlying this anti-surfactant effect we have performed a detailed analysis of these surface structures. We find that there is a strong competition between chemistry and charge compensation by the Ga vacancies: The growth of 1 monolayer of GaN on top of the $SiGaN_3$-monolayer will result in charge transfer from the surface cation dangling bonds (dbs) to the Ga vacancies in the $SiGaN_3$-layer to saturate nitrogen dangling bonds. This leads to formation of an electrical dipole between the $SiGaN_3$-layer and the surface (see schematic representation in the right inset in Fig. 5.8), which initially increases the energy of the system. However, owing to the large cohesive energy of bulk Si_3N_4 (74.3 $eV/cell$, Ref. [177]), the energy increase due to the built in electrical dipole moment is overcompensated by the energy gain due to the passivation of all the Si dangling bonds by N of the GaN overlayer grown on top of the $SiGaN_3$ layer. Depositing additional monolayers of GaN, however, further increases the distance between the surface and the Ga vacancy and thus also the electrical dipole moment. This results in an energetically highly unfavourable surface that prevents further growth of GaN.

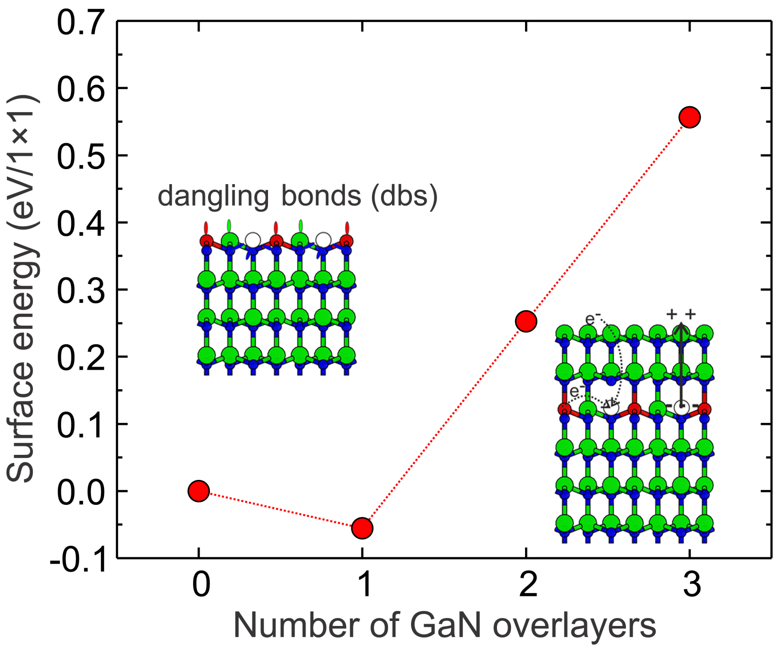

Figure 5.8.: Relative surface energies versus number of GaN overlayers on top of the $SiGaN_3$ monolayer. The energies are referenced with respect to the $SiGaN_3$ terminated surface. The dashed red line is a guide for the eye. Insets: Schematic ball-and-stick representation of no (left) and 2 GaN overlayers (right) configurations. Green, blue, red, and white balls indicate Ga, N, Si atoms and Ga vacancies, respectively. In the case of no and one GaN overlayer the dangling bonds are schematically shown. In the case of 2 GaN overlayers the charge transfer and the build in electrical dipole moment are indicated. Dashed black arrows denote the charge transfer from the Si atoms and the surface cations to the vacancies. Plus (+) and minus (-) symbols schematically represent the charge distribution after the charge transfer and the solid arrow indicates the direction of the dipole moment.

Thus, we conclude that the anti-surfactant effect of Si in the growth of GaN (0001) is based on the formation of a single monolayer of $SiGaN_3$ buried in the subsurface. The presence of this buried and electrically active layer shifts the chemical potential at the GaN surface and thus inhibits further growth. This shift of the chemical potential originates from the dipole moment caused by charge transfer between the surface cation dangling bonds to the acceptor states of the Ga vacancies in the electrically active buried monolayer. Eventually, the growth of thick GaN layers occurs initially exclusively at locations where the $SiGaN_3$ layer is not present, e.g. at surface steps or at holes in the $SiGaN_3$ mask and proceeds then by lateral overgrowth.

6. Summary and conclusions

In this work we have investigated mainly by means of transmission electron microscopy the following two aspects that are of particular importance in the growth of heteroepitaxial GaN layers: Plastic relaxation processes in strained (0001) III-nitride films and the effect of silicon, as the donor of choice in GaN, on the surface morphology in the epitaxial growth of (0001)-oriented GaN films. Our studies have revealed the following main results:

Mechanism of plastic relaxation of strained (0001) wurtzite films:

Our experimental results reveal that efficient plastic relaxation of strained (0001)-oriented wurtzite films proceeds mainly by nucleation and glide of a-type misfit dislocations in the $\frac{1}{3} < 11\bar{2}0 > |\{0001\}$ slip-system. Our experimental observations and theoretical considerations show that other mechanisms like the inclination of pre-existing a-type threading dislocations and formation of a+c-type misfit dislocations are kinetically inhibited and their contribution to plastic relaxation of strained (0001)-oriented wurtzite heterostructures is typically of minor importance. Nucleation of a-type misfit dislocations is, however, due to the particular slip geometry of the wurtzite lattice, suppressed for (0001)-oriented thin films, as long as they are grown with a perfect 2-dimensional morphology. In this case the films are in a plane stress condition and therefore the resolved shear stresses on the $\{0001\}$ slip planes, necessary for dislocation nucleation and glide, are zero. In case the surface of the strained films undergoes a transition towards a 3-dimensional surface morphology (e.g. due to island growth, cracking, the presence of macroscopic surface steps or surface pits), the strain redistributes, leading to resolved shear stresses on the $\{0001\}$ planes and a-type misfit dislocations may form in the basal plane.

Quantitative modelling of the plastic relaxation process

With the help of our experimental results and numerical calculations using the finite element method we have developed a quantitative model for plastic relaxation of (0001)-oriented strained wurtzite films. In contrast to previous work in literature (e.g. Holec et al. [34, 121]) our model considers the crucial process of misfit dislocation formation, i.e. nucleation and glide of a-type dislocation half-loops. Critical thickness values predicted by our model are in excellent agreement with our experimental results and those of other authors. However, the main benefit of our model is that it allows to understand quantitatively how plastic relaxation is linked to the growth process of the film. Our analysis reveals that the critical thickness for the onset of plastic relaxation of strained (0001)-oriented wurtzite films depends next to the strain also essentially on the surface morphology, i.e. the growth mode, of the film. For a given strain, a-type dislocations nucleate at the corners of growth islands at lower layer thicknesses than at the tip of cracks in a 2-dimensionally grown but cracked layer.

Conclusions for optimised growth conditions

As mentioned before, the choice of growth parameter affects the growth mode of the film and thus also the strain relaxation behaviour. Depending on the desired goal, different growth strategies should be applied. If one aims for a pseudomorphic heterostructures with maximum thickness, growth conditions favouring a 2-dimensional morphology should be chosen. In case of compressively strained layers it is thus possible to deposit pseudomorphic layers up to thicknesses that are more than one order of magnitude higher than equilibrium critical thickness theory (e.g. Matthews-Blakeslee-model) predicts. In contrast to that, if one aims for efficient plastic relaxation of misfit strain for the lowest possible layer thickness, e.g. at the $Al_xGa_{1\text{-}x}N$/GaN buffer interface in case of strain-engineering with $Al_xGa_{1\text{-}x}N$ interlayers, then 3-dimensional growth is favourable.

Strain-engineering with $Al_xGa_{1\text{-}x}N$ interlayers

Strain engineering in GaN films by means of $Al_xGa_{1\text{-}x}N$ interlayer is based on an asymmetry in plastic relaxation between the two interfaces of $Al_xGa_{1\text{-}x}N$ interlayers. Although misfit dislocation networks form at both interfaces of the interlayer, the smaller average spacing of dislocation lines at the lower interface of $Al_xGa_{1\text{-}x}N$ interlayers compared to that at the upper one finally leads to a build-up of compressive strain in the subsequent GaN layer. Our studies reveal that this phenomenon occurs qualitatively independent on growth parameters of the $Al_xGa_{1\text{-}x}N$ interlayer such as the thickness and deposition temperature. However, as shown in this work, different deposition temperatures of the $Al_xGa_{1\text{-}x}N$ interlayer might change its growth mode. This in turn, as discussed before, influences the critical thickness for the onset of plastic relaxation of the $Al_xGa_{1\text{-}x}N$ interlayer and the degree of strain relaxation at a given thickness. To achieve a build-up of compressive strain in the subsequent layer at all (or a certain amount of compressive strain) thicker $Al_xGa_{1\text{-}x}N$ interlayers are required if they are grown 2-dimensionally instead of 3-dimensionally, e.g. if higher deposition temperatures are chosen. This fact might explain why in some of the earlier work (see e.g. Ref. [28, 29]) it was assumed that thin high temperature $Al_xGa_{1\text{-}x}N$ interlayer are not suitable for strain-engineering. However, not only that strain-engineering is possible with high temperature $Al_xGa_{1\text{-}x}N$ interlayer as well they have the potential advantage to result at the end in a smaller threading dislocation density in the subsequent GaN film than in case of 3-dimensionally grown low temperature $Al_xGa_{1\text{-}x}N$ interlayers.

Effect of Silicon on the epitaxial growth of GaN (0001)

Silicon delta-doping of the GaN (0001) surface leads to the growth of a coherent submonolayer that corresponds with respect to the GaN lattice to a $\sqrt{3} \times \sqrt{3}R30^\circ$ reconstruction where the three cation positions are occupied by a silicon and a gallium atom and a gallium vacancy. Accordingly the stoichiometry of this layer is $SiGaN_3$.

Since growth of thick GaN layers directly on top of the $SiGaN_3$-monolayer (commonly called SiN_x-mask in the literature) is inhibited a transition towards 3-dimensional island growth occurs. GaN islands exclusively nucleate at windows not covered by the $SiGaN_3$-monolayer and growth then proceeds laterally over the $SiGaN_3$-monolayer. A high concentration of silicon on the GaN (0001) surface thus acts as an anti-surfactant in the epitaxial growth of GaN. Our density functional theory calculations reveal that the blocking of direct growth of thick GaN layers on top of the $SiGaN_3$-monolayer is caused by a shift of the chemical potential at the GaN (0001) growth surface. This shift of the chemical potential originates from a dipole moment caused by charge transfer between the surface cation dangling bonds and the acceptor states (Ga vacancies) in the electrically active $SiGaN_3$-monolayer. Since this energetically unfavourable dipole moment would increase with each additional GaN monolayer direct nucleation of thick GaN films or islands on top of the $SiGaN_3$-monolayer is suppressed.

7. Acknowledgements

First of all, I would like to express my greatest thanks to my supervisor Dr. Martin Albrecht who has made this work possible. I would like to thank him for all the support, hours of fruitful discussions about any topic of my work and for his helpful comments on this thesis. I have always appreciated the working atmosphere in his group allowing to study with a state-of-the-art instrument basic problems of material science.

Many thanks belong to all members of our electron microscopy group at the Leibniz institute of crystal growth (Dr. Tobias Schulz, Thilo Remmele, Robert Schewski, Stefan Mohn, Philipp Müller, Natalia Stolyarchuk, Kerstin Banse, Dr. Maxim Korytov, Dr. Mutong Niu). I have very much appreciate your excellent company during the past years! Special thanks go to Kerstin Banse for her help in TEM sample preparation, Tobias Schulz for countless fruitful as well as entertaining conversations and Thilo Remmele for his help to solve any technical problem with the TEM and for providing excellent software for TEM data analysis and simulation.

I am also very thankful to Professor Dr. Henning Riechert, Professor Sir Colin Humphreys and Professor Dr. Armin Dadgar for their willingness to review this thesis.

Many thanks belong to Dr. Philipp Drechsel and Dr. Peter Stauss from Osram Opto Semiconductors in Regensburg for providing us with high quality samples and introducing me into the challenges of MOVPE growth. I would also like to acknowledge the cooperation with Prof. Armin Dadgar (Otto von Guericke University Magdeburg) and the former AZZURRO Semiconductors Inc. Both shared samples with us in the framework of the "GaNonSi" BMBF project.

A special thank belongs to Dr. Liverios Lymperakis and Professor Jörg Neugebauer from the Max-Planck-Institut für Eisenforschung (MPIE) in Düsseldorf for performing the density functional calculations shown in this work and for many interesting conversations about ab-initio modelling of growth processes.

Further, I am very thankful to Albert Kwasniewski, Dr. Martin Schmidbauer and Dr. Stephanie Fritze (former Otto von Guericke University Magdeburg now Laytec Inc.) for XRD measurements and extended discussions about and sometime probably also in the reciprocal space.

I thank Frank Langhans, Roman Bansen and Dr. Andreas Duk for performing AFM measurements shown in this work.

I would also like to acknowledge the financial support within the framework of the "GaNonSi" BMBF project and the "Sinople" EU-project.

Great thanks go to all my friends and my family, who supported me during my PhD time.

Finally, I am incredibly thankful especially to my loving wife for her endless encouragement, her patience and her trust in me in the past years.

Bibliography

[1] H. Amano, Jpn. J. Appl. Phys. 52, 050001 (2013)

[2] A. Dadgar, C. Hums, A. Diez, J. Bläsing, and A. Krost, J. Crystl Growth **297**, 279 (2006)

[3] J.-Y. Kim, Y. Tak, J. Kim, H.-G. Hong, S. Chae, J. W. Lee, H. Choi, Y. Park, U.-I. Chung, J.-R. Kim, and J.-I. Shim, Proc. SPIE **8262**, 82621D (2012)

[4] S. Arulkumaran, G. I. Ng, S. Vicknesh, H. Wang, K. S. Ang, J. P. Y. Tan, V. K. Lin, S. Todd, G. Q. Lo, and S. Tripathy, Jpn. J. Appl. Phys. **51**, 111001 (2012)

[5] Christy D., Egawa T., Yano Y., Tokunaga H., Shimamura H., Yamaoka Y., Ubukata A., Tabuchi T. and Matsumoto K., Appl. Phys. Express **6**, 026501 (2013)

[6] Press release Osram Opto Semiconductors, “Success in research: First gallium-nitride LED chips on silicon in pilot stage”, 12th January 2012

[7] D. Zhu, C. McAleese, M. Häberlen, C. Salcianu, Te. Thrush, M. J. Kappers, A. Phillips, P. Lane, M. Kane, D. Wallis, T. Martin, M. Astles, N. Hylton, P. Dawson, and C. J. Humphreys, J. Appl. Phys. **109**, 014502 (2011)

[8] P. Drechsel, H. Riechert , J. Cryst. Growth **315**, 211 (2011)

[9] D. Zhu, D. J. Wallis, and C. J. Humphreys, Rep. Prog. Phys. **76**, 106501 (2013)

[10] C. Roder, S. Einfeldt, S. Figge, and D. Hommel, Phys. Rev. B **72**, 085218 (2005)

[11] Y. Okada and Y. Tokumaru, J. Appl. Phys. **56**, 314 (1984)

[12] C. Roder, “Analyse struktureller Eigenschaften von GaN mittels hochauflösender Röntgenbeugung bei variabler Meßtemperatur”, PhD thesis, Universität Bremen, 2007

[13] A. Dadgar, J. Bläsing, A. Diez, A. Alam, M. Heuken, and A. Krost, Jpn. J. Appl. Phys. **39**, L1183 (2000)

[14] P. R. Hageman, S. Haffouz, V. Kirilyuk, A. Grzegorczyk, and P. K. Larsen, phys. stat. sol. (a) **188**, 523 (2001)

[15] T. Markurt, L. Lymperakis, J. Neugebauer, P. Drechsel, P. Stauss, T. Schulz, T. Remmele, V. Grillo, E. Rotunno, and M. Albrecht, Phys. Rev. Lett. **110**, 036103 (2013)

[16] S. Tanaka, M. Takeuchi, and Y. Aoyagi, Jpn. J. Appl. Phys. **39**, L831 (2000)

[17] H. Lahreche, P. Vennegues, B. Beaumont, and P. Gibart, J. Cryst. Growth **205**, 245 (1999)

[18] M. J. Kappers, R. Datta, R. A. Oliver, F. D. G. Rayment, M. E. Vickers, and C. J. Humphreys, J. Cryst. Growth **300**, 70 (2007)

[19] J. Hertkorn, F. Lipski, P. Brückner, T. Wunderer, S. B. Thapa, F. Scholz, A. Chuvilin, U. Kaiser, M. Beer, and J. Zweck, J. Cryst. Growth **310**, 4867 (2008)

[20] M. Hijikuro, N. Kuwano, M. Takeuchi, and Y. Aoyagi, phys. stat. sol. (c) **3**, 1832 (2006)

[21] K. Pakula, R. Bozek, J. M. Baranowski, J. Jasinski, and Z. Liliental-Weber, J. Cryst. Growth **267**, 1 (2004)

[22] H. Amano, M. Iwaya, T.i Kashima, M. Katsuragawa, I. Akasaki, J. Han, S. Hearne, J. A. Floro, E. Chason, and J. Figiel, Jpn. J. Appl. Phys. **37**, L1540 (1998)

[23] A. Dadgar, M. Poschenrieder, J. Bläsing, K. Fehse, A. Diez, and A. Krost, Appl. Phys. Lett. **80**, 3670 (2002)

[24] I.-H. Lee, T. G. Kim, and Y. Park, J. Cryst. Growth **234**, 305 (2002)

[25] S. Raghavan, X. Weng, E. Dickey, and J. M. Redwing, Appl. Phys. Lett. **87**, 142101 (2005)

[26] Q. Sun, J. T. Wang, H. Wang, R. Q. Jin, D. S. Jiang, J. J. Zhu, D. G. Zhao, H. Yang, S. Q. Zhou, M. F. Wu, D. Smeets, and A. Vantomme, J. Appl. Phys. **104**, 043516 (2008)

[27] A. Krost and A. Dadgar, phys. stat. sol. (a) **194**, 361 (2002)

[28] J. Bläsing, A. Reiher, A. Dadgar, A. Diez, and A. Krost, Appl. Phys. Lett. **81**, 2722 (2002)

[29] A. Reiher, J. Bläsing, A. Dadgar, A. Diez, A. Krost, J. Cryst. Growth **248**, 563 (2003)

[30] P. Vennegues, Z. Bougrioua, J.-M. Bethoux, M. Azize, and O. Tottereau, J. Appl. Phys. **97**, 024912 (2005)

[31] B. Jahnen, M. Albrecht, W. Dorsch, S. Christiansen, H. P. Strunk, D. Hanser, and Robert F. Davis, MRS Internet J. Nitride Semicond. Res. **3**, 39 (1998)

[32] J. Mei, R. Liu, F. A. Ponce, H. Omiya, and T. Mukai, Appl. Phys. Lett. **90**, 171922 (2007)

[33] R. Liu, J. Mei, S. Srinivasan, H. Omiya, F. A. Ponce, D. Cherns, Y. Narukawa, and T. Mukai, Jpn. J. Appl. Phys. **45**, L549 (2006)

[34] D. Holec, Y. Zhang, D. V. S. Rao, M. J. Kappers, C. McAleese, and C. J. Humphreys, J. Appl. Phys. **104**, 123514 (2008)

[35] S. Tanaka, S. Iwai, and Y. Aoyagi, Appl. Phys. Lett. **69**, 4096 (1996)

[36] A. L. Rosa, J. Neugebauer, J. E. Northrup, C.-D. Lee, and R. M. Feenstra, Appl. Phys. Lett. **80**, 2008 (2002)

[37] A. L. Rosa and J. Neugebauer, Phys. Rev. B **73**, 205314 (2006)

[38] N. Kuwano, M. Hijikuro, S. Hata, M. Takeuchi,d, Y. Aoyagi, J. Cryst. Growth **298**, 284 (2007)

[39] L. B. Freund and S. Suresh in “Thin film materials: stress, defect formation, and surface evolution”, Cambridge University Press, Cambridge (2003)

[40] G. B. Stringfellow in ”Organometallic Vapor-Phase Epitaxy, Second Edition: Theory and Practice”, Academic Press, San Diego (1999)

[41] D. T. J. Hurle in “Handbook of Crstal growth”, North-Holland, Amsterdam (1994)

[42] J. E Ayers in “Heteroepitaxy of Semiconductors: Theory, Growth, and Characterization”, CRC Press, Boca Raton (2007)

[43] G. Dhanaraj, K. Byrappa, V. Prasad, and M. Dudley in ”Springer handbook of crystal growth”, Springer, Berlin (2010)

[44] E. Bauer and J. H. van der Merwe, Phys. Rev. B **33**, 3657 (1986)

[45] P. Drechsel, P. Stauss, W. Bergbauer, P. Rode, S. Fritze, A. Krost, T. Markurt, T. Schulz, M. Albrecht, H. Riechert, and U. Steegmüller, phys. stat. sol. (a) **209**, 427 (2012)

[46] H. Ishikawa, K. Yamamoto, T. Egawa, T. Soga, T. Jimbo, and M. Umeno, J. Cryst. Growth **189**, 178 (1998)

[47] A. Krost and A. Dadgar, Mater. Sci. Eng. B, **93**, 77 (2002)

[48] S. Raghavan , X. Weng , E. Dickey, and J. M. Redwing, Appl. Phys. Lett. **88** , 041904 (2006)

[49] K. Cheng, M. Leys, S. Degroote, B. Van Daele, S. Boeykens, J. Derluyn, M. Germain, G. Van Tendeloo, J. Engelen, and G. Borghs, J. Electron. Mater. **35**, 592 (2006)

[50] M. Haeberlen, D. Zhu, C. McAleese, M. J. Kappers and C. J. Humphreys, J. Phys.: Conf. Ser. **209**, 012017 (2010)

[51] A. Able, W. Wegscheider, K. Engl, and J. Zweck, J. Cryst. Growth **276**, 415 (2005)

[52] D. B. Williams and C. B. Carter in “Transmission electron Microscopy”, Plenum Press, New York (1996)

[53] B. Fultz and J. Howe in “Transmission Electron Microscopy and Diffractometry of Materials”, Springer, New York (2009)

[54] H. Bethge and J. Heydenreich in “Electron microscopy in solid state physics”, Elsevier, Amsterdam (1987)

[55] S. J. Pennycook and P. Nellist D. in “Scanning Transmission Electron Microscopy: Imaging and Analysis”, Springer, New York (2011)

[56] C. Kisielowski et al., Microscopy and Microanalysis **14**, 469 (2008)

[57] O. Scherzer, J. Appl. Phys. **20** , 20 (1949)

[58] H. Rose, Optik **85**, 19 (1990)

[59] H. Rose, Ultramicroscopy **56**, 11 (1994)

[60] S. Uhlemann and M. Haider, Ultramicroscopy **72**, 109 (1998)

[61] H. Lichte, Ultramicroscopy **38**, 13 (1991)

[62] C. L. Jia, M. Lentzen, and K. Urban, Microscopy and Microanalysis **10**, 174 (2004)

[63] C. L. Jia and K. Urban, Science **303**, 2001 (2004)

[64] E. J. Kirkland in “Advanced Computing in Electron Microscopy”, Springer, New York (2010)

[65] J. M. Cowley and A. F. Moodie, Acta Cryst. A **10**, 609 (1957)

[66] P.A. Stadelmann, Ultramicroscopy **21**, 131 (1987)

[67] M. Lentzen, Ultramicroscopy **99**, 211 (2004)

[68] D. J. H. Cockayne, L. F. Ray and M. J. Whelan, Philosophical Magazine **20**, 1265 (1969)

[69] A. Howie, Journal of Microscopy **117**, 11 (1979)

[70] Z. L. Wang, Micron **34**, 141 (2003)

[71] Z. L. Wang and J. M. Cowley, Ultramicroscopy **31**, 437 (1989)

[72] C. R. Hall and P. B. Hirsch, Proc. Roy. Soc. A, **286**, 158 (1965)

[73] L. M. Peng, Micron **30**, 625 (1999)

[74] P. M. Voyles , J. L. Grazul, and D. A. Muller, Ultramicroscopy **96**, 251 (2003)

[75] V. Grillo, K. Mueller, K. Volz, F. Glas, T. Grieb, and A. Rosenauer, J. Phys.: Conf. Ser. **326**, 012006 (2011)

[76] V. Grillo, E. Carlino, and F. Glas, Phys. Rev. B **77**, 054103 (2008)

[77] A. Rosenauer et al., Ultramicroscopy **111**, 1316 (2011)

[78] V. Grillo and F. Rossi, J. Cryst. Growth **318**, 1151 (2011)

[79] V. Grillo, Ultramicroscopy **109**, 1453 (2009)

[80] Z. L. Wang, Ultramicroscopy **53**, 73 (1994)

[81] P. D. Nellist and S. J. Pennycook, Ultramicroscopy **78**, 111 (1999)

[82] S. Hillyard and J. Silcox, Ultramicroscopy **58**, 6 (1995)

[83] J. C. H. Spence and J. M. Zuo, Ultramicroscopy **31**, 233 (1989)

[84] A. P. Pogany and P. S. Turner, Acta Cryst. A **24**, 103 (1968)

[85] J. M Cowley, Appl. Phys. Lett. **15**, 58 (1969)

[86] M. Weyland and D. A. Muller, Nano Sol. **1**, 24 (2005)

[87] W. Van den Broek, S. Van Aert, and D. Van Dyck, Microscopy and Microanalysis **18**, 336 (2012)

[88] T. M. Smeeton , M. J. Kappers , J. S. Barnard , M. E. Vickers , and C. J. Humphreys, Appl. Phys. Lett. **83**, 5419 (2003)

[89] G. G. Stoney, Proc. Roy. Soc. London A, **82**, 172 (1909)

[90] L. B. Freund , J. A. Floro , and E. Chason , Appl. Phys. Lett. **74**, 1987 (1999)

[91] C. Stampfl and C. G. Van de Walle, Phys. Rev. B **57**, R15052 (1998)

[92] D. N. Zakharov, Z. Liliental-Weber, B. Wagner, Z. J. Reitmeier, E. A. Preble, and R. F. Davis, Phys. Rev. B **71**, 235334 (2005)

[93] I. Belabbas, J. Chen, Ph. Komninou, and G. Nouet, phys. stat. sol. (c) **10**, 84 (2013)

[94] I. Belabbas, G. Mimitrakopulos, J. Kioseoglou, A. Bere, J. Chen, Ph. Komninou, P. Ruterana, G. Nouet, Superlattices and Microstructures **40**, 458 (2006)

[95] J. Kioseoglou, G. P. Dimitrakopulos, Ph. Komninou, and Th. Karakostas, Phys. Rev.B **70**, 035309 (2004)

[96] Ph. Komninou, J. Kioseoglou, G. P. Dimitrakopulos, Th. Kehagias, and Th. Karakostas, phys. stat. sol. (a) **202**, 2888 (2005)

[97] B. Moran, F. Wu, A.E. Romanov, U.K. Mishra, S.P. Denbaars, and J.S. Speck, J. Cryst. Growth **273**, 38 (2004)

[98] M. Albrecht, H. P. Strunk, J. L. Weyher, I. Grzegory, S. Porowski, and T. Wosinski, J. Appl. Physics **92**, 2000 (2002)

[99] J. G. Lozano, A. M. Sanchez, R. Garcia, D. Gonzalez, M. Herrera, N. D. Browning, S. Ruffenach, and O. Briot, Appl. Phys. Lett. **91**, 071915 (2007)

[100] J. Kioseoglou, E. Kalesaki, G. P. Dimitrakopulos, Th. Kehagias, Ph. Komninou, and Th. Karakostas, Appl. Surf. Sci. **260**, 23 (2012)

[101] L. Zhang, W. E. McMahon, Y. Liu, Y. Cai, M. H. Xie, N. Wang, and S. B. Zhang, Surf. Sci. **606**, 1728 (2012)

[102] S.N. Filimonov, V. Cherepanov, N. Paul, H. Asaoka, J. Brona, and B. Voigtländer, Surf. Sci. **599**, 76 (2005)

[103] F. Ernst, P. Porouz, and E. Bauser, phys. stat. sol. (a) **131**, 651 (1992)

[104] H. Yamaguchi, J. G. Belk, X. M. Zhang, J. L. Sudijono, M. R. Fahy, S. Jones, D. W. Pashley, and B. A. Joyce, Phys. Rev. B **55**, 1337 (1997)

[105] A. Krost, A. Dadgar, G. Strassburger, and R. Clos, phys. stat. sol. (a) **200**, 26 (2003)

[106] A. E. Romanov and J. S. Speck, Appl. Phys. Lett. **83**, 2569 (2003)

[107] D. M. Follstaedt, S. R. Lee, A. A. Allerman, and J. A. Floro, J. Appl. Phys. **105**, 083507 (2009)

[108] P. Cantu, F. Wu, P. Waltereit, S. Keller, A. E. Romanov, U. K. Mishra, S. P. DenBaars, and J. S. Speck, Appl. Phys. Lett. **83**, 674 (2003)

[109] I. C. Manning, X. Weng, J. D. Acord, M. A. Fanton, D. W. Snyder, and J. M. Redwing, J. Appl. Phys. **106**, 023506 (2009)

[110] I. C. Manning, X. Weng, M. A. Fanton, D. W. Snyder, J. M. Redwing, J. Cryst. Growth **312**, 1301 (2010)

[111] J. F. Wang, D. Z. Yao, J. Chen, J. J. Zhu, D. G. Zhao, D. S. Jiang, H. Yang, and J. W. Liang, Appl. Phys. Lett. **89**, 152105 2006

[112] J.-S. Xue, Y. Hao, J.-C. Zhang, and J.-Y. Ni, Chin. Phys. B **19**, 057203 (2010)

[113] Z. Wu, K. Nonaka, Y. Kawai, T. Asai, F. A. Ponce, C. Chen, M. Iwaya, S. Kamiyama, H. Amano, and I. Akasaki, Appl. Phys. Express **3**, 111003 (2010)

[114] A. Bourret, C. Adelmann, B. Daudin, J.-L. Rouviere, G. Feuillet, and G. Mula, Phys. Rev. B **63**, 245307 (2001)

[115] Z. Ren, Q. Sun, S.-Y. Kwon, J. Han, K. Davitt, Y. K. Song, A. V. Nurmikko, H.-K. Cho, W. Liu, J. A. Smart, and L. J. Schowalter, Appl. Phys. Lett. **91**, 051116 (2007)

[116] J. R. Grandusky, J. A. Smart, M. C. Mendrick, L. J. Schowalter, K. X.Chen, E. F.Schubert, J. Cryst. Growth **311**, 2864 (2009)

[117] J. A. Floro, D. M. Follstaedt, P. Provencio, S. J. Hearne, and S. R. Lee, J. Appl. Phys. **96**, 7087 (2004)

[118] J.-M. Bethoux and P. Vennegues, J. Appl. Phys. **97**, 123505 (2005)

[119] S. R. Lee, D. D. Koleske, K. C. Cross, J. A. Floro, K. E. Waldrip, A. T. Wise, and S. Mahajan, Appl. Phys. Lett. **85**, 6164 (2004)

[120] S. Srinivasan, L. Geng, R. Liu, F. A. Ponce, Y. Narukawa, and S. Tanaka, Appl. Phys. Lett. **83**, 5187 (2003)

[121] PhD thesis D. Holec, Selwyn College, University of Cambridge, Cambridge (2006)

[122] J. W. Matthews and A. E. Blakeslee, J. Cryst. Growth **27**, 118 (1974)

[123] J.W. Hutchinson and Z. Suo, Adv. Appl. Mech. **29**, 63 (1992)

[124] J. Sauvola and M. Pietikäinen, Pattern Recognition **33**, 225 (2000)

[125] S. J. Hearne, J. Han, S. R. Lee, J. A. Floro, D. M. Follstaedt, E. Chason, and I. S. T. Tsong, Appl. Phys. Lett. **76**, 1534 (2000)

[126] G. P. Dimitrakopulos, E. Kalesaki, Ph. Komninou, Th. Kehagias, J. Kioseoglou, and Th. Karakostas, Cryst. Res. Technol. **44**, 1170 (2009)

[127] J. F. Wang , D. Z. Yao , J. Chen , J. J. Zhu , D. G. Zhao , D. S. Jiang , H. Yang , and J. W. Liang, Appl. Phys. Lett. **89**, 152105 (2006)

[128] G. R. Irwin, J. Appl. Mech. **24**, 361 (1957)

[129] G. E. Beltz and L. B. Freund, phys. stat. sol. (b) **180**, 303 (1993)

[130] J. R. Rice and G. E. Beltz, J. Mech. Phys. Solids **42**, 333 (1994)

[131] J. McLaughlin and D. Renzi, Inverse Problems **22**, 681 (2006) 681

[132] J. P. Hirth and J. Lothe, in “Theory of Dislocations”, McGraw-Hill, New York 1968

[133] R. Peierls, Proc. Phys. Soc. London **52**, 34 (1940)

[134] F. R. N. Nabarro, Proc. Phys. Soc. London **59**, 256 (1947)

[135] D. Chidambarrao, G. R. Srinivasan, B. Cunningham, and C. S. Murthy, Appl. Phys. Lett. **57**, 1001 (1990)

[136] A. K. Head, Proc. Phys. Soc. B, **66**, 793 (1953)

[137] J.-M. Bethoux, P. Vennegues, F. Natali, E. Feltin, O. Tottereau, G. Nataf, P. De Mierry, and F. Semond, J. Appl. Phys. **94**, 6499 (2003)

[138] R. Liu , J. Mei , S. Srinivasan , F. A. Ponce , H. Omiya , Y. Narukawa , and T. Mukai, Appl. Phys. Lett. **89** , 201911 (2006)

[139] J. E. Northrup and J. Neugebauer, Phys. Rev. B **53**, R10477 (1996)

[140] J. E. Northrup, R. Di Felice, and J. Neugebauer, Phys. Rev. B **55**, 13878 (1997)

[141] F. Asif, H.-C. Chen, A. Coleman, I. Ahmad, B. Zhang, J. Dion, A. Heidari, V. Adivarahan, and A. Khan, phys. stat. sol. (c) **11**, 798 (2014)

[142] T. Kinoshita, K. Hironaka, T. Obata, T. Nagashima, R. Dalmau, R. Schlesser, B. Moody, J. Xie, S. Inoue, Y. Kumagai, A. Koukitu, and Z. Sitar, Appl. Phys. Express **5**, 122101 (2012)

[143] S. Keller, G. Parish, P. T. Fini, S. Heikman, C.-H. Chen, N. Zhang, S. P. DenBaars, U. K. Mishra, and Y.-F. Wu, J. Appl. Phys. **86**, 5850 (1999)

[144] M. Gherasimova, G. Cui, Z. Ren, J. Su, X.-L. Wang, J. Han, K. Higashimine, and N. Otsuka, J. Appl. Phys. **95**, 2921 (2004)

[145] S. Raghavan, X. Weng, E. Dickey, and J. M. Redwing, Appl. Phys. Lett. **87**, 142101 (2005)

[146] S. Fritze, P. Drechsel, P. Stauss, P. Rode, T. Markurt, T. Schulz, M. Albrecht, J. Bläsing, A. Dadgar, and A. Krost, J. Appl. Phys. **111**, 124505 (2012)

[147] J. W. Matthews, A. E. Blakeslee, and S. Mader, Thin Solid Films **33**, 253 (1976)

[148] T. M. Katona , P. Cantu , S. Keller , Y. Wu , J. S. Speck , and S. P. DenBaars, Appl. Phys. Lett. **84**, 5025 (2004)

[149] D. Kapolnek , S. Keller , R. Vetury , R. D. Underwood , P. Kozodoy , S. P. Den Baars , and U. K. Mishra, Appl. Phys. Lett. **71**, 1204 (1997)

[150] K. Hiramatsu, K. Nishiyama, A. Motogaito, H. Miyake, Y. Iyechika, and T. Maeda, phys. stat. sol. (a) **176** , 535 (1999)

[151] C. E. Dreyer, A. Janotti, and C. G. Van de Walle, Phys. Rev. B **89**, 081305 (2014)

[152] J. Neugebauer, phys. stat. sol. (c) **0**, 1651 (2003)

[153] A. Dadgar et al., Adv. Solid State Phys. **44**, 313 (2004)

[154] S. Fritze, A. Dadgar, H. Witte, M. Bügler, A. Rohrbeck, J. Bläsing, A. Hoffmann, and A. Krost, Appl. Phys. Lett. **100**, 122104 (2012)

[155] O. Contreras, F. A. Ponce, J. Christen, A. Dadgar, and A. Krost, Appl. Phys. Lett. **81**, 4712 (2002)

[156] R. Tu, C. Tun, C. Chou, B. Lee, C. Tsai, T. Wang, J. Chi, C. Lee, and G. Chi, Jpn. J. Appl. Phys. **43**, L264 (2004)

[157] A. Munkholm, C. Thompson, M. V. Ramana Murty, J. A. Eastman, O. Auciello, G. B. Stephenson, P. Fini, S. P. DenBaars, and J. S. Speck, Appl. Phys. Lett. **77**, 1626 (2000)

[158] A. Munkholm, G. B. Stephenson, J. A. Eastman, O. Auciello, M. V. Ramana Murty, C. Thompson, P. Fini, J. S. Speck, and S. P. DenBaars, J. Cryst. Growth **221**, 98 (2000)

[159] W. Coene, G. Janssen, M. Op de Beeck, and D. Van Dyck, Phys. Rev. Lett. **69**, 3743 (1992)

[160] W. Coene, A. Thust, M. Op de Beeck, and D. Van Dyck, Ultramicroscopy **64**, 109 (1996)

[161] L. J. Allen, W. McBride, N. L. O'Leary, and M. P. Oxley, Ultramicroscopy **100**, 91 (2004)

[162] T. Schulz, T. Remmele, T. Markurt, M. Korytov, and M. Albrecht, J. Appl. Phys. **112**, 033106 (2012)

[163] C. G. Van de Walle and J. Neugebauer, J. Appl. Phys. **95**, 3851 (2004)

[164] A. Y. Liu and M. L. Cohen, Phys. Rev. B **41**, 10727 (1990)

[165] Q. Yan , P. Rinke , M. Scheffler, and C. G. Van de Walle, Appl. Phys. Lett. **95**, 121111 (2009)

[166] A. Thust, Phys. Rev. Lett. **102**, 220801 (2009)

[167] A. Rosenauer, K. Gries, K. Müller, A. Pretorius, M. Schowalter, A. Avramescu, K. Engl, and S. Lutgen, Ultramicroscopy **109**, 1171 (2009)

[168] R. F. Loane, P. Xu, and J. Silcox, Acta Cryst. A **47**, 267 (1991)

[169] D. A. Muller, B. Edwards, E. J. Kirkland, and J. Silcox, Ultramicroscopy **86**, 371 (2001)

[170] J. M. LeBeau and S. Stemmer, Ultramicroscopy **108**, 1653 (2008)

[171] J. M. LeBeau,S. D. Findlay, L. J. Allen, and S. Stemmer, Phys. Rev. Lett. **100**, 206101 (2008)

[172] F. Semond, E. Frayssinet, M. Leroux, Y. Cordier, M. Reda Ramdani, J.C. Moreno, S. Sergent, B. Damilano, P. Vennegues, O. Tottereau, and J. Massies, 16th European Molecular Beam Epitaxy Workshop (Euro-MBE 2011), L'Alpe d'Huez (2011), Contributed talk (Mo 3.6.)

[173] M. J. Rashid, E. Frayssinet, S. Vezian, M. Leroux, O. Tottereau, P. Vennegues, M. Nemoz, J. Massies, and F. Semond, 9th International Conference on Nitride Semiconductors (ICNS-9), Glasgow (2011), Poster presentation PB 1.71.

[174] F. Semond (private communication)

[175] C. G. Van de Walle and J. Neugebauer, Phys. Rev. Lett. **88**, 066103 (2002)

[176] A. R. Smith, R. M. Feenstra, D. W. Greve, J. Neugebauer, and J. E. Northrup, Phys. Rev. Lett. **79**, 3934 (1997)

[177] A. Y. Liu and M. L. Cohen, Phys. Rev. B **41**, 10727 (1990)

[178] D. Hull and D. J. Bacon in "Introduction to Dislocations", Butterworth-Heinemann, Oxford (2011)

[179] E. Schmid, Z. Elektrochemie **37**, 447 (1931)

[180] A. F. Wright, J. Appl. Phys. **82**, 2833 (1997)

[181] A. Rosenauer, S. Kaiser, T. Reisinger, J. Zweck, W. Gebhardt, and D. Gerthsen, Optik **102**, 63 (1996)

[182] P.L. Galindo, S. Kret, A.M. Sanchez, J.-Y. Laval, A. Yanez, J. Pizarro, E. Guerrero, T. Ben, S.I. Molina, Ultramicroscopy **107**, 1186 (2007)

[183] M.J. Hÿtch, E. Snoeck, and R. Kilaas, Ultramicroscopy **74**, 131 (1998)

[184] P. Ruterana , S. Kret , A. Vivet , G. Maciejewski , and P. Dluzewski, J. Appl. Phys. **91**, 8979 (2002)

[185] R. Erni, H. Heinrich, and G. Kostorz, Ultramicroscopy **94**, 125 (2003)

[186] T. Grieb, K. Müller, R. Fritz, M. Schowalter, N. Neugebohrn, N. Knaub, K. Volz, and A. Rosenauer, Ultramicroscopy **117**, 15 (2012)

[187] Schowalter et al., "Composition quantification from HAADF-STEM in AlGaN/GaN heterostructures revised", 18th Microscopy of Semiconducting Materials Meeting (MSM-XIIX), Oxford (2013), Poster presentation PA10

[188] J. P. Hirth, in "The Relation between the Structure and Mechanical Properties of Metals", H. M. Stationary Office, London (1963)

[189] E. A. Fitzgerald, G. P. Watson, R. E. Proano, D. G. Aas, P. D. Kirchner, G. D. Petit, and J. M. Woodall, J. appl. Phys. **65**, 2220 (1989)

[190] G. Kresse and J. Hafner, Phys. Rev. B **49**, 14251 (1994)

[191] G. Kresse and J. Furthmüller, Comput. Mater. Sci. **6**, 15 (1996)

[192] J. E. Northrup, J. Neugebauer, R. M. Feenstra, and A. R. Smith, Phys. Rev. B **61**, 9932 (2000)

A. Coherent elastic scattering

We will now consider coherent elastic scattering of an incident plane wave with the periodic potential of a crystalline specimen. Since this scattering process essentially relies on the wave nature of the incident beam and moving electrons as well as photons can be regarded as waves, the basic principles of coherent elastic scattering can be applied to electron and X-ray diffraction. The process is schematically depicted in Fig. A.1 (a). Assume that a plane wave with an amplitude A_0 and wave vector $\vec{k_0}$ is incident upon a crystal

$$\Psi_0 = A_0 \exp\left[2\pi i\left(\vec{k_0}\cdot\vec{r}\right)\right]. \tag{A.1}$$

The periodically arranged atoms scatter the incident wave and according to Huygens' principle the atoms can be considered as a source of secondary spherical wavelets (indicated by light grey circle segments in Fig. A.1 (a)). The scattered waves can be expressed by

$$\Psi_{sc} = \Psi_0 f(\theta) \frac{\exp[2\pi ikR]}{R}, \tag{A.2}$$

where R is the distance from the scattering centre and $f(\theta)$ is the so called atomic scattering amplitude, which is a measure for the scattering strength as a function of the scattering angle θ. These spherical waves then spread out and superimpose on each other either constructively or destructively. In the far-field the amplitude of the resulting new wave will peak only if the difference in the path length between spherical waves emitted from atoms of adjacent planes is an integer multiple of the wavelength λ. In this case the amplitudes of different spherical waves are added constructively. This criterion is well known as Bragg's law and can be expressed by

$$2d_{hkl}\sin\theta = n\lambda, \tag{A.3}$$

where n is an integer number and d_{hkl} is the interplanar spacing of the (hkl) lattice planes (see Fig. A.1 (a)). The analogue of Bragg's law in the reciprocal space is the equation

$$\vec{k_g} - \vec{k_0} = \vec{g}, \tag{A.4}$$

where $\vec{k_g}$ and $\vec{k_0}$ (with $\left|\vec{k_g}\right| = \left|\vec{k_0}\right| = \frac{1}{\lambda}$) are the wave-vectors of the diffracted and incident beam and $\vec{g}$ is the diffraction vector ($|\vec{g}| = \frac{1}{d_{hkl}}$). This equation states that the condition for diffraction to occur is that the change of the wave vectors must be a

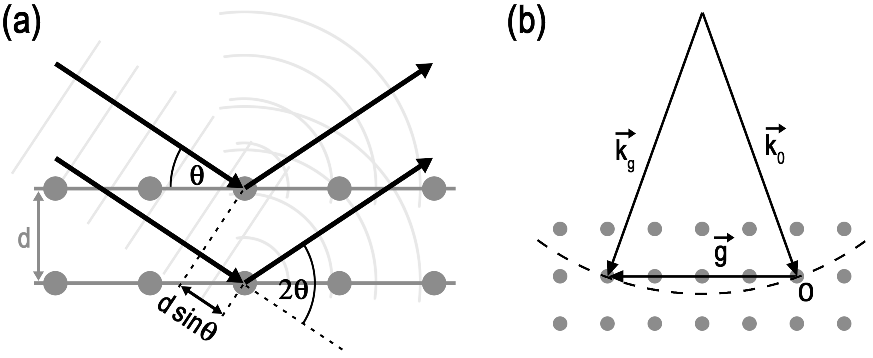

Figure A.1.: Schematic representation of diffraction of a plane wave at a crystal (a) in the real space and (b) in the reciprocal space. In (a) grey balls and horizontal grey lines denote atoms and planes at which the incident wave is diffracted. Light grey lines and circle segments represent wave fronts of the incident and scattered spherical waves, respectively. Black arrows indicate the direction of the wave vectors of the incident and diffracted beam. In (b) grey spheres denote reciprocal lattice points of a crystalline specimen. Black arrows indicate the wave vector of the incident ($\vec{k_0}$) and diffracted beam ($\vec{k_g}$) and the diffraction vector ($\vec{g}$), respectively. The dashed black line represents the Ewald sphere which has a radius of $\frac{1}{\lambda}$. The reciprocal lattice point labeled with "0" denotes the origin of the reciprocal lattice.

reciprocal lattice vector. Thinking in terms of the Ewald construction[1] the Bragg condition will be satisfied if the Ewald sphere passes through a reciprocal lattice point (see Fig. A.1 (b)). Note that in case of thin films the reciprocal lattice points are elongated along the direction of the film normal and diffracted beams, whose corresponding reciprocal lattice rods are cut by the Ewald sphere, will still have some intensity even if the Bragg condition is not exactly satisfied for the respective lattice planes.

---

[1] For the Ewald construction a sphere with radius of $\frac{1}{\lambda}$ is drawn through the origin of the reciprocal lattice (denoted by “O” in Fig. A.1 (b)). The centre of the Ewald sphere is given by the wave vector of the incident beam which points to the origin of the reciprocal lattice. A tilt of the lattice/incident beam corresponds to a rotation of the reciprocal lattice/Ewald sphere around the origin of the reciprocal lattice, respectively.

B. Details of the finite element calculation

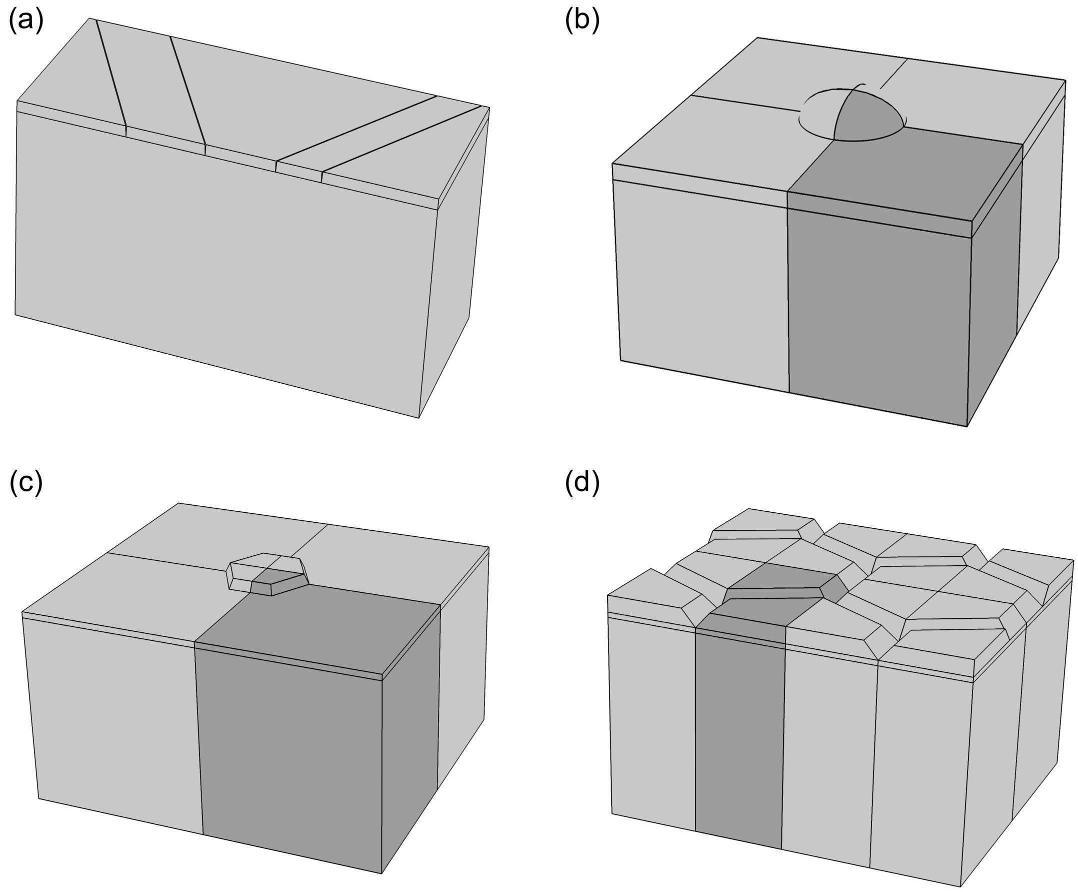

Figure B.1.: Models used for finite element calculations. The $Al_xGa_{1\text{-}x}N$ film on top of the GaN quasi-substrate has the geometry of (a) crack network, (b) isolated hemispheric island, (c) isolated hexagonal truncated pyramid and (d) hexagonal islands with full surface coverage. According to the experimental results we add a thin wetting layer underneath the islands in the case of the models (b)-(d). Using the symmetrie of the structure it is sufficient to calculate only a part of the full structure (the dark grey shaded areas in (b)-(d)).

The finite element analysis has been performed with the COMSOL Multiphysics® software package version 4.2 a. The geometry of the models, which we consider for the calculations in section 4.3.2, is depicted in Fig. B.1. Parameters like the depth of the cracks, shape of islands, inclination angle of islands side-facets and the width-to-height aspect ratio have been systematically varied (see Table B.1 for an overview about the considered parameter range). The thickness of the GaN quasi-substrate has been chosen to be at least 10 times larger than the thickness of the $Al_xGa_{1\text{-}x}N$ film. The models are meshed with typically 100000 tetrahedra, whereby the element size at boundaries and edges is typically 10-50 times finer than in the matrix. The side surfaces of the cells have to satisfy the constraint of symmetric boundaries (i.e. the geometry and mechanical loads have to be symmetric across the surface). All the other surfaces like the top surfaces, island side-facets and crack facets are free to relax. To account for the anisotropy of the material we have implemented anisotropic properties in our finite element calculations. The elastic stiffness tensor C, which connects the stress-tensor σ and the strain-tensor ε according to (using the Voigt notation)

$$\sigma = C\,\varepsilon \tag{B.1}$$

is given by

$$\begin{aligned}\mathbf{C} &= \begin{pmatrix} C_{11} & C_{12} & C_{13} & C_{14} & C_{15} & C_{16} \\ C_{21} & C_{22} & C_{23} & C_{24} & C_{25} & C_{26} \\ C_{31} & C_{32} & C_{33} & C_{34} & C_{35} & C_{36} \\ C_{41} & C_{42} & C_{43} & C_{44} & C_{45} & C_{46} \\ C_{51} & C_{52} & C_{53} & C_{54} & C_{55} & C_{56} \\ C_{61} & C_{62} & C_{63} & C_{64} & C_{65} & C_{66} \end{pmatrix} \\ &= \begin{pmatrix} \begin{matrix}367\\+29\cdot x\end{matrix} & \begin{matrix}135\\+2\cdot x\end{matrix} & \begin{matrix}103\\+5\cdot x\end{matrix} & 0 & 0 & 0 \\ \begin{matrix}135\\+2\cdot x\end{matrix} & \begin{matrix}367\\29\cdot x\end{matrix} & \begin{matrix}103\\+5\cdot x\end{matrix} & 0 & 0 & 0 \\ \begin{matrix}103\\+5\cdot x\end{matrix} & \begin{matrix}103\\+5\cdot x\end{matrix} & \begin{matrix}405\\-32\cdot x\end{matrix} & 0 & 0 & 0 \\ 0 & 0 & 0 & \begin{matrix}95\\+21\cdot x\end{matrix} & 0 & 0 \\ 0 & 0 & 0 & 0 & \begin{matrix}95\\+21\cdot x\end{matrix} & 0 \\ 0 & 0 & 0 & 0 & 0 & \begin{matrix}116\\+13\cdot x\end{matrix} \end{pmatrix} \text{GPa}\,,\end{aligned} \tag{B.2}$$

where x is the AlN mole fraction in $Al_xGa_{1-x}N$ alloys. The full set of elastic constants for GaN and AlN has been taken from the work of Wright [180].

Table B.1.: Overview about the considered parameter range of the finite element analysis

geometry	parameter	considered values
cracks	depth of cracks	1.0, 1.1, 1.2, 1.3, 1.4, 1.6, 2.0 times the thickness of the strained layer
	aspect ratio $\left(\frac{\text{average spacing of parallel cracks}}{\text{height of strained layer}}\right)$	500, 200, 100, 66.7, 50, 43.3, 40, 28.6, 20, 10, 5, 3
islands	shape of islands	hemispherical, hexagonal truncated pyramid
	surface coverage rate with islands	100% (full coverage), 25%, 1% (isolated island)
	inclination angle of island sidefacets to (0001)	30°, 40°, 50°, 60°
	aspect ratio $\left(\frac{\text{island diameter}}{\text{height of island}}\right)$	200, 100, 66.7, 50, 33.3, 20, 10, 5, 3.33, 1.67

C. Analysis of the $Al_xGa_{1\text{-}x}N$ interlayer composition

Quantitative modelling of the relaxation process (e.g. determination of the critical thickness for cracking and the onset of plastic relaxation) requires the knowledge of the composition of the $Al_xGa_{1\text{-}x}N$ interlayer. As the actual composition of the $Al_xGa_{1\text{-}x}N$ interlayer can deviate from the nominal value, an experimental verification of the composition is necessary. It has been reported that the interlayer can contain a significant amount of gallium even if they have been grown as nominal pure AlN interlayer [26, 29]. A possible reasons for this could be, especially in the case of very thin interlayer, the presence of residual Ga-precursors in the gas ambience in the MOVPE reactor.

In this work we use two different methods to determine the real composition of $Al_xGa_{1\text{-}x}N$ interlayers - local strain analysis from HR(S)TEM images and quantitative evaluation of STEM-HAADF intensities. In the following we will use these two methods to evaluate exemplarily the composition of a 11 *nm* thin high temperature $Al_xGa_{1\text{-}x}N$ layer (see Fig. 4.2 on page 65). This sample offers the advantage that the $Al_xGa_{1\text{-}x}N$ layer is not plastically relaxed and has grown 2-dimensionally with an atomically flat surface. Thus the strain-state of the $Al_xGa_{1\text{-}x}N$ interlayer is laterally almost constant (except in the near vicinity of cracks). Otherwise, locally varying strain fields around misfit dislocations or island edges would either directly (in case of HR(S)TEM strain mapping) or indirectly (STEM-HAADF intensity via changing electron channelling conditions) affect the composition analysis.

C.1. Strain analysis from high resolution (S)TEM lattice images

A local strain analysis can be performed by evaluating high resolution TEM and STEM lattice images. This can be done either as a real space or Fourier space approach. In the first case (see e.g. Ref. [162, 181, 182]) the strain analysis is based on the following steps: (i) intensity maxima/minima corresponding to atomic columns are identified in the image by a peak finding algorithm, (ii) the distances between the image intensity maxima/minima are measured (iii) which provides the local in-plane and out-of-plane lattice parameter/strain state, respectively. In case of the Fourier space approach the local strain is obtained by the following steps [183]: (i) a small mask is placed around a reflection in the Fourier transform of an HRTEM lattice image, (ii) an inverse Fourier transform is performed, (iii) the phase of the resulting complex image is determined; changes of the phase correspond to local displacements of atomic planes, and (iv) the

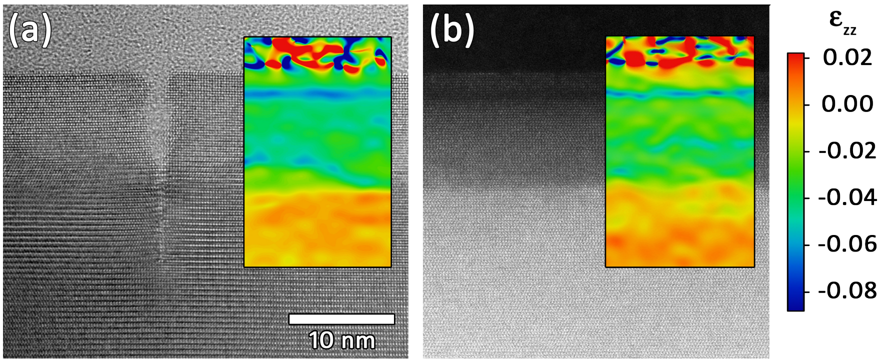

Figure C.1.: Quantitative composition analysis of an $Al_xGa_{1-x}N$ interlayer by means of strain mapping by geometric phase analysis at the heterointerface between a 11 *nm* thin high temperature $Al_{0.75}Ga_{0.25}N$ layer and GaN buffer.(a) HRTEM and (b) HRSTEM-HAADF images. Both images are on the same lenght scale. The insets show the out-of-plane strain ε_{zz}.

derivative of the phase gives the local strain. This method is known as geometric phase analysis (GPA) and has been proposed by Hÿtch et al. [183]. The composition of the $Al_xGa_{1-x}N$ interlayer is finally calculated by means of Vegard's law and assuming biaxial/uniaxial distortion [184], respectively.

Fig. C.1 shows the result of a geometric phase analysis of high resolution TEM and STEM images. We obtain consistent results for both cases. The strain analysis of the HRTEM image yields an average composition for the 11 *nm* thin high temperature $Al_xGa_{1-x}N$ layer of $x = 0.73 \pm 0.06$ while the strain analysis of the HRSTEM-HAADF image gives an average composition of $x = 0.7 \pm 0.1$. Notably, an Al-rich region in the upper part of the $Al_xGa_{1-x}N$ layer (see blue horizontal layer in Fig. C.1) with a composition of $x = 0.90 \pm 0.04$ is seen in both strain maps. The errors are given by the standard deviation of the fluctuations in the GPA result.

C.2. Quantitative analysis of STEM-HAADF image intensities

In the past years there have been several reports in literature [77, 167, 185, 186] which demonstrate a quantitative composition analysis of heterostructures by evaluating the intensity of STEM-HAADF images. STEM Z-contrast can thus be used as a complementary technique to strain analysis methods. Following the approach of LeBeau et al. [170, 171], quantitative STEM imaging is based on a normalisation of the measured raw intensity (I_{raw}) with respect to the intensity of the incident electron probe $\left(I_{probe}\right)$

$$I_{normalised} = \frac{I_{raw} - I_{vacuum}}{I_{probe}} , \tag{C.1}$$

where I_{vacuum} is the vacuum intensity (i.e. the detector signal when the electron beam is not scattered onto the detector at all). The intensity of the incident probe I_{probe} can be easily measured by placing the unscattered direct electron beam on the

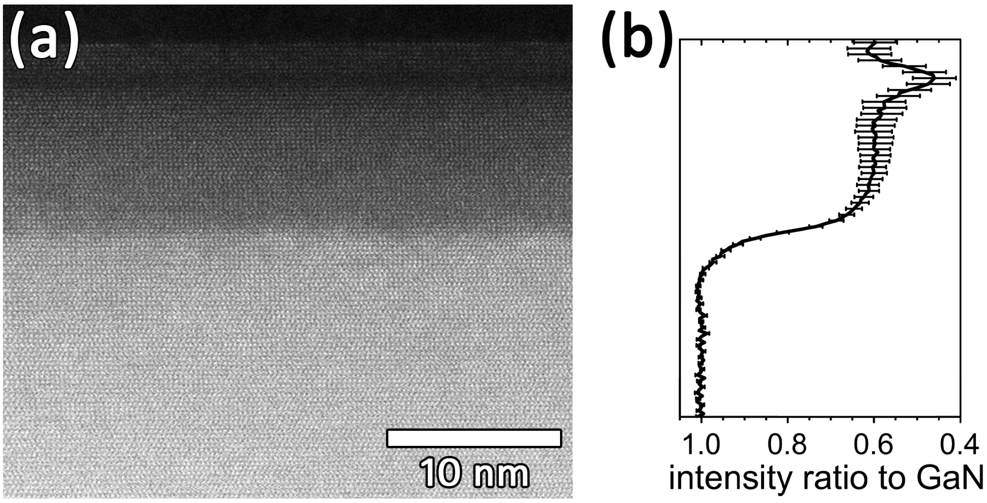

Figure C.2.: Quantitative composition analysis of an $Al_xGa_{1-x}N$ interlayer by means of the STEM-HAADF image intensity. (a) STEM-HAADF image of the heterointerface between a 11 *nm* thin high temperature $Al_xGa_{1-x}N$ layer and GaN buffer (same image as before in Fig. C.1(b)). (b) Intensity ratio to GaN.

HAADF detector (usually the direct beam is centred in the inner hole of the HAADF detector). To obtain correct results, it is important that the detector pre-amplifier and analog-to-digital converter system do not cut off the vacuum level and also do not saturate for higher intensities. The experimental normalised intensity of the layer or its intensity ratio towards a reference material can then be compared with frozen phonon simulations [64, 168, 169] to determine the composition of the heterostructure. For the case of $Al_xGa_{1-x}N$/GaN heterostructures this has been demonstrated by Rosenauer et al. [167]. Including also static displacements of individual atoms in the $Al_xGa_{1-x}N$ alloy into the HAADF simulations Schowalter et al. [187] reported a good quantitative agreement between the composition analysis by means of STEM-HAADF and other methods with errors typically not more than a few %.

Such composition evaluation has been performed exemplarily for the same sample as before, i.e. a heterostructure of a 11 *nm* thin high temperature $Al_xGa_{1-x}N$ interlayer grown on a GaN buffer. Fig. C.2 (b) shows the ratio of the measured intensity (laterally average over the field of view in Fig. C.2 (a)) with respect to the intensity of the GaN background. The error bars correspond to the uncertainty in fitting the background. According to the work by Rosenauer et al. [167] and Schowalter et al. [187] we calculate an average composition of the $Al_xGa_{1-x}N$ layer of $x = 0.77 \pm 0.09$ and for the Al-rich region in the upper part of the $Al_xGa_{1-x}N$ layer (appears as darker layer) $x = 0.93 \pm 0.05$. These results are in good agreement with that of the strain analysis.

A systematic evaluation of the composition of $Al_xGa_{1-x}N$ interlayer from other samples has revealed that the average aluminium content of $Al_xGa_{1-x}N$ interlayer amounts typically to $x = 0.75 \pm 0.05$.

D. Nucleation of dislocations

The theory of homogeneous nucleation of dislocation half-loops at free surfaces has been considered e.g. by Hirth [188], Matthews et al. [147], Fitzgerald et al. [189] and Beltz and Freund [129]. The basic idea of this concept is rather simple and is based on an energy minimisation approach. A dislocation is nucleated if the release of strain energy stored in the film is larger than the energy of the nucleated dislocation. Hereinafter we will follow the approach of Beltz and Freund [129]. In their model it is assumed that the nucleated dislocations are semi-circular. The energy of the half-loop with radius r is then given by

$$E_{half-loop} = \frac{r}{2} \cdot \frac{\mu b^2}{4} \frac{2-\nu}{1-\nu} \left[\ln\left(\frac{8mr}{e^2 b} \right) + 1 \right] , \tag{D.1}$$

where μ is the shear modulus, ν is Poisson's ratio and m is a geometry dependent correction factor $(0 < m < 1)$. According to Beltz and Freund [129] the correction factor yields for a Poisson's ratio of $\nu = 0.21$ the value of $m \approx 0.535$.

The elastic energy released by the half-loop is the work done by the stress field $\sigma_{\mathbf{ij}}$ (2nd-order tensor) while moving the dislocation with Burgers-vector $\vec{b}$ and line direction $\vec{dl}$ the distance $\vec{ds}$. It is calculated according to

$$E_{gain} = \int \sigma_{\mathbf{ij}} \cdot \vec{b} \times \vec{dl} \cdot \vec{ds}. \tag{D.2}$$

If $\sigma_{\mathbf{ij}}$ is spatially constant, the energy gain due to introduction of a half-loop with radius r amounts to

$$E_{gain} = -\frac{\pi}{2} r^2 \tau b, \tag{D.3}$$

where τ is the resolved shear stress, which acts on the dislocation. In the case of biaxially strained, isotropic films τ is given by

$$\tau = 2\mu \frac{1+\nu}{1-\nu} \varepsilon \cos\alpha \cos\beta + \tau_{ext} \tag{D.4}$$

where ε is the strain of the film, α is the angle between the Burgers-vector and the direction in the strained interface, perpendicular to the dislocation line, β is the angle between the slip plane and the normal of the strained interface and τ_{ext} is a possible external resolved shear stress on the relevant slip-plane. The term

$$\cos\alpha \cos\beta = S \tag{D.5}$$

in eq. (D.4) is the so-called the Schmid-factor S [179]. It defines the resolved shear stress, which acts on a dislocation in a given slip system caused by the misfit stress [132].

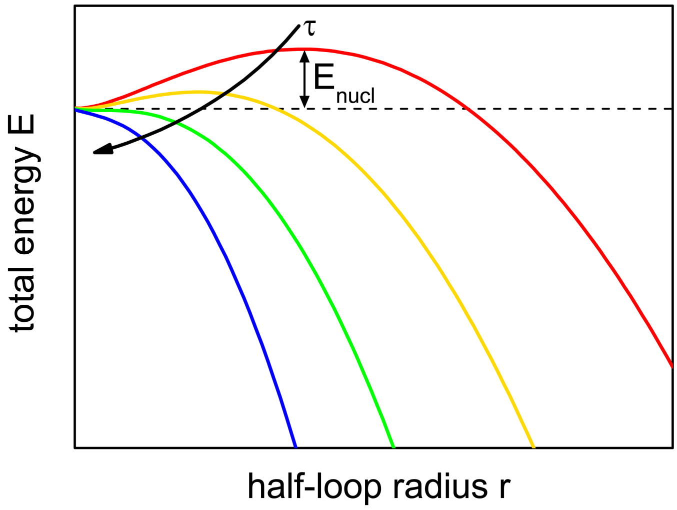

Figure D.1.: Schematic representation of the total energy E_{total} as a function of the dislocation half-loop radius r for increasing resolved shear stress τ. For the case of the lowest shear stress (red curve) the energetical barrier for nucleation of the half-loop E_{nucl} is indicated in the graph.

If the Burgers-vector of the half-loop has a component perpendicular to the surface, where the half-loop is nucleated, then a ledge will be created or removed at the surface and the energy associated with this ledge is given by [189]

$$E_{ledge} = \pm \frac{\mu}{4} r b^2 \cos\gamma \,, \tag{D.6}$$

where γ is the angle between Burgers-vector and the surface normal. A positive/negative sign means creation/removal of a ledge, respectively. The sum of all three energies gives the total energy of the system. Its evolution with the radius of the half-loop is schematically shown in Fig. D.1. The total energy is 0 for $r = 0$, then increases to a local maximum for $r = r_{crit}$ and for $r > r_{crit}$ the half-loop becomes unstable against enlargement and the total energy E_{total} decreases as the radius of the half-loop increases. The total energy at the critical radius of the half-loop defines the energetical barrier (activation energy) for nucleation E_{nucl} of the half-loop

$$E_{nucl} = E_{total}(r_{crit}) \tag{D.7}$$

The critical radius r_{crit} is defined by the condition

$$\left.\frac{\partial E_{total}}{\partial r}\right|_{r=r_{crit}} = 0. \tag{D.8}$$

The critical radius as well as the nucleation barrier decrease for increasing shear stress τ (see Fig. D.1). Therefore, one can also calculate the critical shear stress τ_{crit} for which spontaneous nucleation and enlargement of the half-loop will occur. This will be the case if the nucleation barrier just vanishes. Mathematically this can be expressed by

$$\begin{aligned}\left.\frac{\partial E_{total}}{\partial r}\right|_{r=r_{crit}} &= 0\\ \left.\frac{\partial^2 E_{total}}{\partial r^2}\right|_{r=r_{crit}} &= 0.\end{aligned} \tag{D.9}$$

If the local shear stress τ is lower than the critical value τ_{crit} nucleation of half-loops can be considered as a thermally activated process with an energy barrier of E_{nucl}. The nucleation rate (number of nucleated half-loops per time) then depends on the temperature during the growth of the film and the resolved shear stress [189].

E. Density functional theory calculations

In order (i) to account for relaxation of bonds of assumed structural models and (ii) to investigate and explain the self-limited growth and the anti-surfactant effect of the $SiGaN_3$-layer we have performed first principles projected augmented wave calculations within density functional theory (DFT) for a variety of models and compared the surface energies of these reconstructions. The calculations have been performed by Liverios Lymperakis and Jörg Neugebauer at the Max-Planck-Institut für Eisenforschung (MPIE) in Düsseldorf.

For the DFT calculations we have used the Vienna ab-initio simulation package (VASP [190, 191]). Exchange and correlation have been described within the generalized gradient approximation. The surfaces have been modelled using a slab geometry consisting of 9 GaN monolayers and a vacuum of thickness equivalent of 11 Å. Periodic boundary conditions have been applied. The anion dangling bonds at the bottom side of the slab have been passivated by partially charged pseudo-hydrogen. The plane wave cut-off has been set to 500 eV and the Brillouin zone has been sampled by an equivalent $4 \times 4 \times 1$ Monkhorst-Pack mesh for the $\sqrt{3} \times \sqrt{3}R30^\circ$ unit cell. Relaxation of the lattice along the $\langle 0001 \rangle$ direction has been fully taken into account.

The surface energy per unit area A of each reconstruction has been calculated according to

$$\gamma_{surface} = \frac{E_{total}^{cell} - \sum_i n_i \mu_i}{A}, \tag{E.1}$$

where E_{total}^{cell} is the total energy of the cell obtained from the DFT calculations, n_i is the number and μ_i is the chemical potential of the involved atomic species i. Note that due to the absence of an inversion symmetry in the wurtzite lattice we can not calculate absolute surface energies for the (0001) planes. Instead we use relative values with the clean Ga-terminated (0001) surface as a reference.

From eq. (E.1) one can see that the surface energies are dependent on the chemical potentials of all involved species. For the present case we consider gallium, nitrogen, silicon and hydrogen in our calculations. The chemical potentials, in turn, vary with the chosen growth parameters like the partial pressure of the respective species and the temperature. However, in order to avoid that the system becomes unstable against formation of elementary phases of involved species, their chemical potentials have to obey the boundary conditions

$$\begin{aligned}
\mu_{Ga} &\leq \mu_{Ga\,bulk} \\
\mu_{Si} &\leq \mu_{Si\,bulk} \\
\mu_{N} &\leq \frac{1}{2}\mu_{N_2\,molecule} \\
\mu_{H} &\leq \frac{1}{2}\mu_{H_2\,molecule}\,.
\end{aligned} \tag{E.2}$$

For the analysis of the surface reconstructions during the Si treatment of the GaN (0001) surface a further limitation for the chemical potentials can be deduced from the following consideration. Since during this process the Ga-flux is off but a sufficiently high ammonia flow (i.e. a supply of active nitrogen) is kept to avoid GaN decomposition, we neither expect a significant positive nor negative growth of GaN. Hence we assume the surface to be in thermodynamic equilibrium with bulk GaN under N-rich/Ga-poor conditions. For the studies of the anti-surfactant effect where we deposit additional GaN monolayers on top of the $SiGaN_3$-interlayer we also assume, corresponding to typical MOVPE growth conditions, thermodynamic equilibrium with bulk GaN under N-rich/Ga-poor conditions. For the given situation the N and Ga chemical potentials are thus given by

$$\mu_N - \frac{1}{2}\mu_{N_2 molecule} = 0\,, \tag{E.3}$$

$$\begin{aligned}
\mu_{Ga} - \mu_{Ga\,bulk} + \mu_N - \frac{1}{2}\mu_{N_2\,molecule} \leq H_f^{GaN\,bulk} &= -1.25\;eV\;[37] \\
\mu_{Ga} - \mu_{Ga\,bulk} &= -1.25\;eV.
\end{aligned} \tag{E.4}$$

To mimic and to understand the growth process during the Si treatment, first principles calculations of a large variety of $n\sqrt{3}\times m\sqrt{3}R30^\circ$ $(n,m = 1,2)$ as well as orthogonal $n\times m$ $(n,m = 2,4)$ Si covered GaN (0001) surface reconstructions have been performed. Following is a list of all surface reconstructions considered for this purpose together with their relative surface energies for Si-rich and N-rich (= Ga-poor) conditions and for a hydrogen chemical potential of $\mu_H - \frac{1}{2}\mu_{H_2}^{molecule} = -1.0\,eV$[1]. Adsorbates like H, NH_x $(x \leq 3)$, which have been reported for hydrogenated GaN (0001) surfaces [175], have also been been included in the calculations. These adsorbates are distributed on the surface to obey the electron counting rule. The nomenclature n[A]@B in Table E.1 denotes n times adsorbate A (A: H, NH, NH_2 or NH_3) bound to n surface atoms B (B: Ga, Si, or N). Grey shaded rows in Table E.1 indicate structures with $\sqrt{3}\times\sqrt{3}R30^\circ$ periodicity which have a $SiGaN_3$ stoichiometry. Additionally we included surface reconstructions without Si in our calculations to allow a comparison with previous literature studies.

---

[1] According to Van de Walle and Neugebauer [175] the hydrogen chemical potential amounts to approximately this value for a growth temperature of about 1000°C and typical pressures in MOVPE experiments.

Table E.1.: Considered GaN (0001) surface reconstructions

periodicity	Ga substitutions in the layer	adsorbates/comments	surface energy per 1×1 [eV]
$\sqrt{3}\times\sqrt{3}$	2Si+1V$_{Ga}$/$\sqrt{3}\times\sqrt{3}$	no adsorbate	-1.452
$\sqrt{3}\times\sqrt{3}$	6Si/$\sqrt{3}\times\sqrt{3}$	2 monolayers of SiN	-1.329
$2\sqrt{3}\times2\sqrt{3}$	1Si+1V$_{Ga}$/$\sqrt{3}\times\sqrt{3}$	7[H]@N+4[NH$_2$]@Si+4[NH$_2$]@Ga	-1.155
$2\sqrt{3}\times2\sqrt{3}$	1Si+1V$_{Ga}$/$\sqrt{3}\times\sqrt{3}$	6[H]@N+4[NH$_2$]@Si +3[NH$_2$]@Ga+[NH$_3$]@Ga	-1.135
$2\sqrt{3}\times2\sqrt{3}$	1Si+1V$_{Ga}$/$\sqrt{3}\times\sqrt{3}$	7[H]@N+3[NH$_2$]@Si+[NH]@Si +3[NH$_2$]@Ga+[NH$_3$]@Ga	-1.114
$2\sqrt{3}\times2\sqrt{3}$	1Si+1V$_{Ga}$/$\sqrt{3}\times\sqrt{3}$	6[H]@N+3[NH$_2$]@Si +[NH$_3$]@Si+4[NH$_2$]@Ga	-1.099
$2\sqrt{3}\times2\sqrt{3}$	1Si+1V$_{Ga}$/$\sqrt{3}\times\sqrt{3}$	5[H]@N+3[NH$_2$]@Si+[NH$_3$]@Si]@Ga +3[NH$_2$]@Ga+[NH$_3$]@Ga	-1.094
$2\sqrt{3}\times2\sqrt{3}$	1Si+1V$_{Ga}$/$\sqrt{3}\times\sqrt{3}$	6[H]@N+3[NH$_2$]@Si +[NH$_3$]@Si+4[H]@Ga	-1.073
$2\sqrt{3}\times2\sqrt{3}$	1Si+1V$_{Ga}$/$\sqrt{3}\times\sqrt{3}$	8[H]@N+3[NH$_2$]@Si +[NH]@Si+4[NH$_2$]@Ga	-1.069
$2\sqrt{3}\times2\sqrt{3}$	1Si+1V$_{Ga}$/$\sqrt{3}\times\sqrt{3}$	1[H]@Si	-1.066
$2\sqrt{3}\times2\sqrt{3}$	1Si+1V$_{Ga}$/$\sqrt{3}\times\sqrt{3}$	7[H]@N+3[NH$_2$]@Si+[NH$_3$]@Si +3[NH$_2$]@Ga+[NH]@Ga	-1.029
$\sqrt{3}\times\sqrt{3}$	1Si+1V$_{Ga}$/$\sqrt{3}\times\sqrt{3}$	no adsorbate	-1.020
$2\sqrt{3}\times2\sqrt{3}$	1Si+1V$_{Ga}$/$\sqrt{3}\times\sqrt{3}$	8[H]@N+4[NH$_2$]@Si +3[NH$_2$]@Ga+[NH]@Ga	-1.017
$2\sqrt{3}\times2\sqrt{3}$	1Si+1V$_{Ga}$/$\sqrt{3}\times\sqrt{3}$	+2[NH$_2$]@Ga+2[NH$_3$]@Ga 4[H]@N+3[NH$_2$]@Si+[NH$_3$]@Si	-1.012
$2\sqrt{3}\times2\sqrt{3}$	1Si+1V$_{Ga}$/$\sqrt{3}\times\sqrt{3}$	+[NH$_3$]@Ga+4[H]@Si 6[H]@N+3[NH$_2$]@Ga	-0.952
$2\sqrt{3}\times2\sqrt{3}$	1Si+1V$_{Ga}$/$\sqrt{3}\times\sqrt{3}$	+2[NH]@Si+4[NH$_2$]@Ga 9[H]@N+2[NH$_2$]@Si	-0.942
$2\sqrt{3}\times2\sqrt{3}$	1Si+1V$_{Ga}$/$\sqrt{3}\times\sqrt{3}$	+2[NH$_2$]@Ga+2[NH$_3$]@Ga 4[H]@N+3[NH$_2$]@Si+[NH$_3$]@Si	-0.924
$2\sqrt{3}\times2\sqrt{3}$	1Si+1V$_{Ga}$/$\sqrt{3}\times\sqrt{3}$	3[H]@N	-0.894
$2\sqrt{3}\times2\sqrt{3}$	1Si+1V$_{Ga}$/$\sqrt{3}\times\sqrt{3}$	3[H]@Si	-0.887
$2\sqrt{3}\times2\sqrt{3}$	1Si+1V$_{Ga}$/$\sqrt{3}\times\sqrt{3}$	6[H]@N+4[H]@Si+3[H]@Ga	-0.875
$2\sqrt{3}\times2\sqrt{3}$	1Si+1V$_{Ga}$/$\sqrt{3}\times\sqrt{3}$	7[H]@N+3[H]@Si+3[H]@Ga	-0.871
$2\sqrt{3}\times2\sqrt{3}$	1Si+1V$_{Ga}$/$\sqrt{3}\times\sqrt{3}$	6[H]@N+3[H]@Si+4[H]@Ga	-0.871
2×2	1[Si]+1V$_{Ga}$/2×2	2[H]@N+3[NH$_2$]@N	-0.851
$2\sqrt{3}\times2\sqrt{3}$	1Si+1V$_{Ga}$/$\sqrt{3}\times\sqrt{3}$	+2[NH$_2$]@Ga+2[NH]@Ga 9[H]@N+4[NH$_2$]@Si	-0.836
$\sqrt{3}\times\sqrt{3}$	3Si/$\sqrt{3}\times\sqrt{3}$	1 monolayer of SiN	-0.812
$2\sqrt{3}\times2\sqrt{3}$	1Si+1V$_{Ga}$/$\sqrt{3}\times\sqrt{3}$	+[NH$_3$]@Si+4[H]@Ga 8[H]@N+3[NH$_2$]@Si	-0.772
$2\sqrt{3}\times2\sqrt{3}$	1Si+1V$_{Ga}$/$\sqrt{3}\times\sqrt{3}$	+[NH$_3$]@Ga+4[H]@Si 8[H]@N+3[NH$_2$]@Ga	-0.762
$2\sqrt{3}\times2\sqrt{3}$	1Si+1V$_{Ga}$/$\sqrt{3}\times\sqrt{3}$	6[H]@N+3[H]@Ga	-0.758

2×2	1Si+1V$_{Ga}$/2×2	1[H]@N+1[H]@Ga+1[H]@Si	-0.754
$\sqrt{3}\times\sqrt{3}$	2Si/$\sqrt{3}\times\sqrt{3}$	no adsorbate	-0.724
$2\sqrt{3}\times2\sqrt{3}$	1Si+1V$_{Ga}$/$\sqrt{3}\times\sqrt{3}$	7[H]@N+4[H]@Ga	-0.689
2×2	1Si+1V$_{Ga}$/2×2	1[H]@Si	-0.686
2×2	1Si+1V$_{Ga}$/2×2	2[H]@N+1[H]@Si	-0.679
$2\sqrt{3}\times2\sqrt{3}$	1Si+1V$_{Ga}$/$\sqrt{3}\times\sqrt{3}$	12[H]@N+3[NH$_2$]@Si+[NH$_3$]@Si	-0.620
$2\sqrt{3}\times2\sqrt{3}$	1Si+1V$_{Ga}$/$\sqrt{3}\times\sqrt{3}$	12[H]@N+3[H]@Si	-0.609
2×2	1Si+1V$_{Ga}$/2×2	1[H]@N	-0.550
4×2	1Si+2V$_{Ga}$/4×2	4[H]@N+[NH$_2$]@Si +4[NH$_2$]@Ga+[NH$_3$]@Ga	-0.523
2×2	1Si+1V$_{Ga}$/2×2	1[H]@Ga	-0.522
$2\sqrt{3}\times2\sqrt{3}$	2Si/$\sqrt{3}\times\sqrt{3}$	8[H]@Ga+1[H]@Si	-0.519
2×2	1Si+1V$_{Ga}$/2×2	no adsorbate	-0.483
$2\sqrt{3}\times2\sqrt{3}$	1Si+1V$_{Ga}$/$\sqrt{3}\times\sqrt{3}$	12[H]@N + 1[H]@Si	-0.467
2×2	1Si+1V$_{Ga}$/2×2	2[H]@N+1[H]@Ga	-0.445
$2\sqrt{3}\times2\sqrt{3}$	1Si+1V$_{Ga}$/$\sqrt{3}\times\sqrt{3}$	+[NH$_3$]@Si+4[NH]@Ga 12[H]@N+3[NH$_2$]@Si	-0.393
$2\sqrt{3}\times2\sqrt{3}$	1Si+1V$_{Ga}$/$\sqrt{3}\times\sqrt{3}$	12[H]@N+1[H]@Ga	-0.386
$\sqrt{3}\times\sqrt{3}$	1Si/$\sqrt{3}\times\sqrt{3}$	no adsorbate	-0.385
2×2	no SiN$_x$-mask	[Nad-H]+[Ga-H], see Ref.[175]	-0.373
$2\sqrt{3}\times2\sqrt{3}$	1Si+1V$_{Ga}$/$\sqrt{3}\times\sqrt{3}$	+3[NH$_2$]@Ga+[NH]@Ga 12[H]@N+4[NH]@Si	-0.361
$2\sqrt{3}\times2\sqrt{3}$	1Si+1V$_{Ga}$]/$\sqrt{3}\times\sqrt{3}$	+[NH$_3$]@Si+4[NH$_2$]@Ga 12[H]@N+3[NH$_2$]@Si	-0.358
2×2	1Si/2×2	[NH$_3$] + 2[NH$_2$]+[NH$_2$]@Si	-0.346
$2\sqrt{3}\times2\sqrt{3}$	1Si+1V$_{Ga}$/$\sqrt{3}\times\sqrt{3}$	+[NH]@Si+4[NH]@Ga 12[H]@N+3[NH$_2$]@Si	-0.268
$2\sqrt{3}\times2\sqrt{3}$	1Si+1V$_{Ga}$/$\sqrt{3}\times\sqrt{3}$	+4[NH$_2$]@Ga+[NH]@Ga 12[H]@N+4[NH$_2$]@Si	-0.264
2×2	1Si+1V$_{Ga}$/2×2	3[H]@N	-0.262
$2\sqrt{3}\times2\sqrt{3}$	1Si+1V$_{Ga}$/$\sqrt{3}\times\sqrt{3}$	12[H]@N+3[NH$_2$]@Ga+[NH$_3$]@Ga	-0.245
2×2	no SiN$_x$-mask	[Nad-H]+[NH$_2$], see Ref.[175]	-0.207
2×2	no SiN$_x$-mask	N-Adatom, see Ref.[176]	-0.198
2×2	no SiN$_x$-mask	3[Ga-H], see Ref.[175]	-0.151
2×2	no SiN$_x$-mask	[NH$_3$]+3[NH$_2$], see Ref.[175]	-0.104
2×2	no SiN$_x$-mask	[NH$_3$]+3[GaH], see Ref.[175]	-0.068
2×2	no SiN$_x$-mask	Ga-Adatom, see Ref.[176]	-0.048
$\sqrt{3}\times\sqrt{3}$	1Si+1V$_{Ga}$+1N$_{Ga}$/$\sqrt{3}\times\sqrt{3}$	no adsorbate	0.484
$\sqrt{3}\times\sqrt{3}$	1Si+2V$_{Ga}$/$\sqrt{3}\times\sqrt{3}$	no adsorbate	0.516
$\sqrt{3}\times\sqrt{3}$	1Si+1N$_{Ga}$/$\sqrt{3}\times\sqrt{3}$	no adsorbate	1.063
$\sqrt{3}\times\sqrt{3}$	no SiN$_x$-mask	laterally contracted Ga bilayer, see Ref.[192]	1.646
$\sqrt{3}\times\sqrt{3}$	1Si+2N$_{Ga}$/$\sqrt{3}\times\sqrt{3}$	no adsorbate	2.719

Publications

Peer-Review (ordered by date of publication)

1. R. Schewski, G. Wagner, M. Baldini, D. Gogova, Z. Galazka, T. Schulz, T. Remmele, T. Markurt, H. von Wenckstern, M. Grundmann, O. Bierwagen, P. Vogt, and M. Albrecht, “Epitaxial stabilization of pseudomorphic α-Ga_2O_3 on sapphire (0001)”, Appl. Phys. Express **8**, 011101 (2014)

2. T. Schulz, A. Nirschl, P. Drechsel, F. Nippert, T. Markurt, M. Albrecht, and A. Hoffmann, “Recombination dynamics in $In_xGa_{1-x}N$ quantum wells - Contribution of excited subband recombination to carrier leakage”, Appl. Phys. Lett. **105**, 181109 (2014)

3. E. Rotunno, M. Albrecht, T. Markurt, T. Remmele, and V.Grillo , “Three dimensional analysis of the composition in solid alloys by variable probe in scanning transmission electron microscopy”, Ultramicroscopy **146**, 62 (2014)

4. M. Albrecht, R. Schewski, K. Irmscher, Z. Galazka, T. Markurt, M. Naumann, T. Schulz, R. Uecker, R. Fornari1, S. Meuret, and M. Kociak, “Coloration and oxygen vacancies in wide band gap oxide semiconductors: Absorption at metallic nanoparticles induced by vacancy clustering - A case study on indium oxide”, J. Appl. Phys. **115**, 053504 (2014)

5. T. Schulz, A. Duff, T. Remmele, M. Korytov, T. Markurt, M. Albrecht, L. Lymperakis, J. Neugebauer, C. Cheze, and C. Skierbiszewski, “Separating strain from composition in unit cell parameter maps obtained from aberration corrected high resolution transmission electron microscopy imaging”, J. Appl. Phys. **115**, 033113 (2014)

6. R. Bansen, J. Schmidtbauer, U. Juda, T. Markurt, T. Teubner, R. Heimburger, and T. Boeck, “Influence of surface roughness on Ge nanowire growth by MBE”, phys. stat. sol. (rrl) **7**, 831 (2013)

7. T. Markurt, L. Lymperakis, J. Neugebauer, P. Drechsel, P. Stauss, T. Schulz, T. Remmele, V. Grillo, E. Rotunno, and M. Albrecht, “Blocking Growth by an Electrically Active Subsurface Layer: The Effect of Si as an Antisurfactant in the Growth of GaN”, Phys. Rev. Lett. **110**, 036103 (2013)

8. T. Schulz, T. Remmele, T. Markurt, M. Korytov, and M. Albrecht, “Analysis of statistical compositional alloy fluctuations in InGaN from aberration corrected transmission electron microscopy image series”, J. Appl. Phys. **112**, 033106 (2012)

9. S. Fritze, P. Drechsel, P. Stauss, P. Rode, T. Markurt, T. Schulz, M. Albrecht, J. Bläsing, A. Dadgar, and A. Krost, “Role of low-temperature AlGaN interlayers in thick GaN on silicon by metalorganic vapor phase epitaxy ”, J. Appl. Phys. **111**, 124505 (2012)
10. P. Drechsel, P. Stauss, W. Bergbauer, P. Rode, S. Fritze, A. Krost, T. Markurt, T. Schulz, M. Albrecht, H. Riechert, and U. Steegmüller, “Impact of buffer growth on crystalline quality of GaN grown on Si (111) substrates”, phys. stat. sol. (a) **209**, 427 (2012)

Proceeding papers

1. D. Klimm, J. Philippen, T. Markurt, and A. Kwasniewski, “Ce3+:CaSc2O4 Crystal Fibers for Green Light Emission: Growth Issues and Characterization”, Proceedings of the Materials Research Society (MRS) Fall Meeting, Boston, 2013; arXiv:1311.5460
2. R. Heimburger, R. Bansen, T. Markurt, J. Schmidtbauer, T. Teubner, and T. Boeck, "Solvent-induced growth of crystalline silicon on glass ", Proceedings of the 38th Photovoltaic Specialists Conference (PVSC), Austin, 2012

Own conference contributions (ordered by date of presentation)

1. Invited talk: T. Markurt, T. Schulz, P. Drechsel, P. Stauss, and M. Albrecht, “A predictive model for plastic strain relaxation in (0001)-oriented III-Nitride wurtzite films”, Materials Research Society (MRS) Fall Meeting, Boston, 2014
2. Contributed talk: T. Markurt, T. Schulz, N. Christensen, X. Q. Wang, X. T. Zheng, D. Y. Ma, T. Suski, I. Gorczyca, M. Albrecht, T. Remmele, and A. Svane, “InN/GaN Superlattices - Resolving the Discrepancies between Theory and Experiment”, XII International Conference on Nanostructured Materials (NANO 2014), Moscow, 2014
3. Contributed talk: T. Markurt, L. Lymperakis, J. Neugebauer, T. Schulz, T. Remmele, E. Rotunno, V. Grillo, P. Drechsel, P. Stauss, and M. Albrecht, “Unveiling the anti-surfactant effect of Si in GaN epitaxy by aberration corrected transmission electron microscopy”, 10th International Conference on Nitride Semiconductors (ICNS-10), Washington, 2013
4. Poster presentation: T. Markurt, R. Ravash, A. Dadgar, A. Krost, and M. Albrecht, “Pinning of stacking faults by AlN-interlayer in semi-polar GaN films studied by transmission electron microscopy”, 10th International Conference on Nitride Semiconductors (ICNS-10), Washington, 2013
5. Poster presentation: T. Markurt, T. Schulz, P. Drechsel, P. Stauss, and M. Albrecht, “Growth and relaxation mechanisms of AlGaN-interlayers for thermal strain compensation in GaN on silicon substrates”, 10th International Conference on Nitride Semiconductors (ICNS-10), Washington, 2013

6. Contributed talk: T. Markurt, L. Lymperakis, J. Neugebauer, T. Schulz, T. Remmele, E. Rotunno, V. Grillo, P. Drechsel, P. Stauss, and M. Albrecht, “Unveiling the anti-surfactant effect of Si in GaN epitaxy by aberration corrected transmission electron microscopy”, 18th Conference Microscopy of Semi-conducting Materials (MSM-XVIII), Oxford, 2013

7. Contributed talk: T. Markurt, L. Lymperakis, J. Neugebauer, T. Schulz, T. Remmele, E. Rotunno, V. Grillo, and M. Albrecht, "Structure determination of in-situ deposited SiN_x nano-mask in GaN (0001) films by transmission electron microscopy", 15th European Microscopy Congress (EMC), Manchester, 2012

8. Poster presentation: T. Markurt, E. Rotunno, V. Grillo, A. Duff, L. Lymperakis, T. Schulz, T. Remmele, and M. Albrecht, "Composition analysis of InGaN quantum wells by STEM-HAADF", 15th European Microscopy Congress (EMC), Manchester, 2012

9. Poster presentation: T. Markurt, L. Lymperakis, J. Neugebauer, T. Schulz, T. Remmele, P. Drechsel, P. Stauss, E. Rotunno, V. Grillo, and M. Albrecht, “Investigation of self-terminated growth of in-situ deposited SiN_x nano-mask”, 4th International Symposium on Growth of III-Nitrides (ISGN-4), St. Petersburg, 2012

10. Contributed talk: T. Markurt, T. Schulz, P. Drechsel, P. Stauss, M. Albrecht, and R. Fornari, “Growth and relaxation mechanisms of AlN-interlayers for thermal mismatch accommodation in GaN on silicon substrates”, 9th International Conference on Nitride Semiconductors (ICNS-9), Glasgow, 2011

Selbständigkeitserklärung

Hiermit erkläre ich, dass ich die vorliegende Arbeit selbständig ohne fremde Hilfe und nur unter Verwendung der angegebenen Literatur und Hilfsmittel angefertigt habe.

Des Weiteren bestätige ich hiermit, dass ich mich an keiner anderen Universität um einen Doktorgrad beworben habe und keinen entsprechenden Doktorgrad besitze. Ich habe Kenntnis über die dem Verfahren zugrunde liegende Promotionsordnung der Mathematisch-Naturwissenschaftlichen Fakultät der Humboldt-Universität zu Berlin.

Berlin, den 8. Januar 2016

Toni Markurt